Post Asymptotic Giant Branch and Central Stars of Planetary Nebulae in the Galactic Halo

Simon Weston

Submitted to the University of Hertfordshire in partial fulfilment of the requirements of the degree of PhD by research

Research Supervisors : Dr Ralf Napiwotzki & Dr Silvia Catalán

January 2012

Contents

Abstract

Post asymptotic giant branch (post-AGB) stars, central stars of planetary nebulae (CSPNe) and planetary nebulae (PNe) are important phases of stellar evolution as the material they feedback is the seed of subsequent star formation in a galaxy. The majority of low and intermediate mass stars are expected to evolve through these channels, however, it is uncertain how many actually do, and at what rate. The Galactic halo, with its older population, provides a direct test of evolutionary models for low mass stars.

Birthrate estimates of PNe are uncertain and worse still, are in contradiction with accepted white dwarf (WD) birthrate estimates. Much of the uncertainty stems from the lack of complete samples and poorly determined distance estimates. New surveys such as the Sloan Digital Sky Survey (SDSS), Galaxy Evolutionary Explorer (GALEX) and the INT Photometric Hα Survey (IPHAS) have discovered many new PNe and have observed the far edges of the Galaxy. Improved methods of determining distances to CSPNe are presented here, using model atmospheres, evolutionary tracks and high resolution reddening maps utilising these revolutionary surveys.

Locating the CSPN is non-trivial particularly for evolved PNe, as they are extended with their central star often displaced from the centre of the nebula. Therefore, photometric criteria are required to locate the CSPN in the nebula's field. Synthetic photometry of the CSPNe is derived from spectral energy distributions (SEDs) computed from a grid of model atmospheres covering the parameter range of CSPNe. The SEDs are convolved with filter transmission curves to compute

synthetic magnitudes for a given photometric system which are then calibrated with standard stars and WDs.

A further project borne out of a search for luminous central stars of faint PNe, resulted in a systematic search for post-AGB stars in the Galactic halo. In this work, new candidate halo post-AGB stars are discovered from a search through the SDSS spectroscopic database. Combined with previously identified halo post-AGB stars, including the results of a sub-sample from the Palomar-Green (PG) survey, the number of observed and predicted populations are compared. The number of observed post-AGB candidates shows a remarkable deficit to expectations. A survey within a subset of the photometric database of SDSS supports the findings of the PG and SDSS spectroscopic surveys.

These findings provide strong evidence for a lack of post-AGB stars in the Galactic halo and thick disc. A plausible explanation is that a large fraction of stars in these old, metal-poor populations are evolving via alternative channels. The implications of such a result are far reaching with knock on effects for stellar evolutionary theory, galactic evolution and extragalactic redshift estimates.

Acknowledgements

There are a number of people who have helped make this thesis a reality and I am indebted to all of my colleagues within CAR at the University of Hertfordshire, who have given me helpful advice, support and discussions. My utmost gratitude is to my principal supervisor, Ralf Napiwotzki, who has been my guidance and support since the fateful day I knocked on his office door and asked him to supervise my undergraduate final year project. Five years later and his limitless knowledge and impartial advice saw me through the dark days and to the end of my PhD. As my second supervisor, Silvia Catalán has been a driving force since she became part of my supervisory team and has made invaluable contributions. Kieran Forde has helped in a number of ways from latex problem solving to stress-releasing (sometimes inducing) games of football. I would like to thank my colleague, long time housemate and close friend, Andy Gallagher, who has sparked endless discussions from questions which at a first glance seemed so simple. The number of lengthy discussions, sometimes lasting days, made everything clearer eventually. My family have been the backbone of my time at University and their unrelenting support has enabled me to concentrate on my studies, in particular my Father who has encouraged me to follow the career paths I have chosen. Finally, I would never have finished my thesis without my girlfriend, Gemma, who proof-read each chapter, put up with my grumpy days and cracked the whip when it was needed for the final deadline. All the while, keeping me smiling and making an agonising period of writing up significantly less painful.

List of Figures

List of Tables

Chapter 1

Introduction

In the standard single star evolutionary scenario, all low and intermediate mass stars begin their lives as hydrogen (H) core burning main sequence (MS) stars. Subsequent H shell burning (first red giant branch) and later helium (He) core burning on the horizontal branch (HB) alter the elemental abundances and structure of the star. These phases enrich the core, first producing He through the various channels of the p-p chain before carbon (C) and oxygen (O) are formed from triple-alpha processes. Shells of H and He lay on top of the enriched core. A cycle of H and He shell burning is maintained as a star evolves up the asymptotic giant branch (AGB). Thermal pulses in the shell burning phases are accompanied by mass loss which discards much of the stellar matter before a final superwind ejects the majority of the remaining envelope in a single mass loss episode as the star leaves the AGB. A fast wind sets in, sweeping up the shell as the star becomes a post-AGB object. The short-lived phase of rapidly increasing temperature may illuminate the ejected envelope via ionisation as a planetary nebula (PN) if the post-AGB star evolves quickly enough. Finally the PN (if visible) disperses and the remnant central star of the planetary nebula (CSPN) enters the white dwarf (WD) cooling sequence. This evolutionary process is illustrated for a $M = 2M_{\odot}$ star, in a Hertzsprung-Russell (H-R) diagram (Fig. 1.1).

In 1756, Charles Messier observed the first PNe and included four such objects
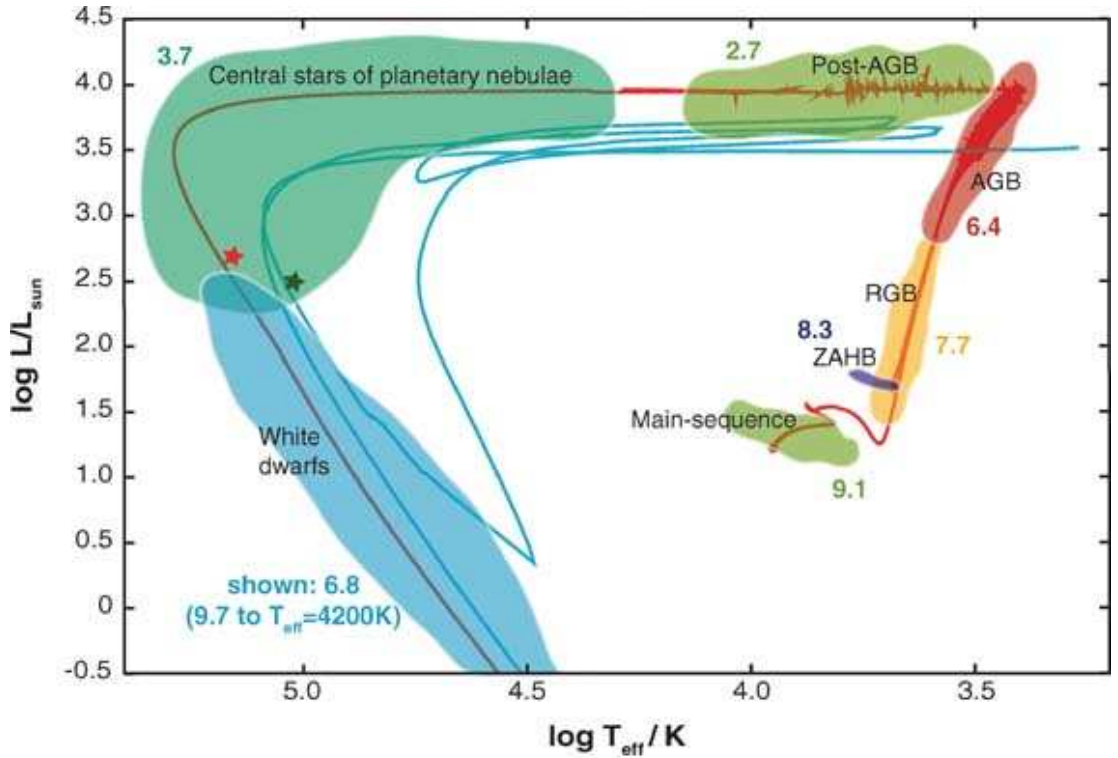
Figure 1.1: An H-R diagram showing the evolution of a $2M_\odot$ star. The red line follows the standard evolutionary channel with the shaded regions highlighting specific phases of evolution. The numbers are log times (in years) the duration in each phase, for example, the main sequence phase lasts $10^{9.1} \approx 1.26$Gyrs. The blue line shows the offset track of a 'born-again' AGB object. The figure is taken from Herwig (2005).

in his first catalogue. It took until 1927 for Zanstra to determine the physical processes that enable the observation of a PN, and that the energy driving this mechanism originates from the CSPN. The evolutionary status of the central star and its PN was unknown until 1956 when Shklovsky proposed that the nebula is ejected from the central star and represents the connecting phase between the AGB and WDs. Paczyński (1971) computed the first detailed model of the nuclei of PNe and later the name post-AGB was borne as the evolutionary stage commencing at the tip of the AGB before the PN is observed in the optical and continuing after the nebula is dispersed.

These final phases of stellar evolution are the shortest lived within a stellar lifetime, but have the greatest impact on galactic evolution as they are the primary contributor of enriched material making up the interstellar medium (ISM) which provides the seed for subsequent star formation. Post-AGB stars, CSPNe and

PNe are direct descendants of AGB stars and are an essential element in understanding the stellar material returned back into the ISM. Although much time has been spent in modelling these phases, many problems remain with mass loss mechanisms due to a lack of physical understanding of the empirical relationships found. PNe provide direct observations of material returned to the ISM through this evolutionary channel which can be quantified via their birthrate and average nebula mass. The detection of circumstellar material as PNe is not always possible as slow evolving post-AGB stars reach ionisation temperatures only after the PN has dispersed and become optically thin to the CSPN radiation. A Post-AGB status is an indication that a star has evolved though the standard evolutionary channel via thermal pulses which result in high mass loss and chemical mixing at the tip of the AGB. The material ejected into the ISM from this channel is more enriched than the alternative lower mass evolutionary paths, such as the post-early AGB (post-EAGB) and post-extended HB (post-EHB), which do not undergo thermal pulses or ascened the AGB at all, respectively. This has a knock-on effect for stellar evolutionary theory, the chemical enrichment of the Galaxy and subsequently, Galactic evolution. Therefore, the determination of the fraction of stars going through the post-AGB phase is essential.

A detailed understanding of stellar evolution is a key factor in determining the star formation history and origins of the Galaxy. Spiral galaxies (such as our own) contain billions of stars but unlike their more massive elliptical counterparts contain a large contribution of gas and dust and are still evolving with continuous star formation. Star formation occurs when over-dense regions in a gas cloud gravitationally collapse and ignite nuclear fusion in the core. The evolution of a star is dependent on its initial mass and metallicity, which are set at formation and determine the stars evolutionary track. A star will not deviate from its evolutionary path unless it experiences external influences such as an interaction with a binary companion. The first-formed stars known as population III, formed as high mass objects with a low metal content and consequently ejected nucleosyn-

thesised heavier elements into the surrounding gases producing an enriched ISM. Stars that formed from the enriched ISM (pop. II) dominate low metallicity environments such as the Galactic halo and thick disc. The formation of lower-mass stars is possible with higher metallicity and these stars are dominant, as their higher mass counterparts have evolved, similarly to the pop. III objects. The thin disc is dominated by metal-rich pop. I stars with a range of masses and are part of a population with ongoing star formation. Stellar evolution due to the feedback from synthesised elements is the driving force behind continuous star formation and subsequent galactic evolution, therefore, much work has gone into understanding and constraining evolutionary models. Low and intermediate mass stars provide a significant portion of the feedback material to the ISM ($\sim 50\%$, Busso et al., 1999) and it is important to determine the quantity of different elements within this material, and also when stars no longer evolve through this channel for galactic evolution. The majority of feedback material comes from the AGB mass loss phase with the ejected gas and dust later ionised by the central star as it contracts and increases in effective temperature (T_{eff}), resulting in a PN. Direct observations and determinations of the Galactic PN space density through volume or magnitude limited samples are carried out using average nebula lifetimes to estimate birthrates. The WD birthrate should be greater than the PN birthrate as all PNe end their lives as WDs, however, WDs are also formed through other evolutionary channels. Recent determinations have produced the implausible result of a greater post-AGB birthrate (Pottasch, 1996; Liebert et al., 2005). The WD birthrate is likely to be more reliable, as WDs have significantly higher space densities than post-AGB stars and PNe, resulting in a more complete local sample (Holberg & Bergeron, 2006). Furthermore, investigations of PNe are hindered by incomplete samples and uncertain distance estimates. It is not possible to observe a complete Galactic PN population as some PNe have low surface brightness, which proves even more problematic when looking into the Galactic plane. Therefore, a global PN estimate is made by compiling a local complete

sample, determining a local density and extrapolating it to a total Galactic population. A sample of evolved PNe is particularly susceptible to incompleteness as they are extended with lower surface brightness, however, a volume limited sample can be expected to be dominated by evolved, low surface brightness PNe (Frew & Parker, 2006). Many different methods of distance determinations have been employed for PNe with results varying between different investigations (Pottasch, 1996). Improved distance estimates with highly spatially resolved and deeper surveys reduce uncertainties and could assist in bringing the post-AGB and WD birthrates in agreement. A revision of the PN birthrate is also required as a significant number of PNe have been observed in new surveys with no detailed follow-up on the CSPN and so distance estimates of these objects will be based on the nebula alone. PN birthrate estimates are heavily reliant on the local density (Daub, 1982; Kwok, 2000) which relies on accurate distance estimates. Using the CSPN in distance estimates has proved to be more consistent where estimates using the nebula flux and statistical methods differ greatly and are sensitive to assumptions of the nebula mass. Locating the central star and using its observed magnitude gives a fair distance estimate using the distance modulus, as the CSPN absolute magnitude has a narrow range for evolved PNe. Once detected, the central star can be analysed further using photometry or spectroscopy for such things as determining distance methods using reddening, and determining atmospheric parameters, removing assumptions about the star.

A search of low surface brightness profile PNe can be undertaken by identifying a central star and subsequently searching for its nebula. CSPN have unique photometric properties in pop. II environments and candidates can be identified with optical colours. If a candidate matches photometric criteria then follow up analysis of the object may confirm it to be a CSPN, and a deep Hα observation of the stellar field may detect a low surface brightness nebula. Few low surface brightness PNe are known even though all PNe become fainter as they evolve. However, low mass CSPNe start as low surface brightness PNe. For all extended

PNe their central star should be luminous even if the nebula is not detectable. A search for stand-alone central stars and their progenitors (post-AGB stars) in pop. II environments such as the Galactic halo may result in the identification of previously undetected PNe and will provide direct observations to test models of low mass and metallicity objects.

If we assume that the aforementioned evolution is standard for all low and intermediate mass stars, then all phases of evolution should be observed in older Galactic populations like the halo. However, the number of known PNe and post-AGB stars in the halo is small with only 14 PNe (Otsuka et al., 2010) and approximately 30 high Galactic latitude ($|b| > 20°$) post-AGB stars (Szczerba et al., 2007) observed to date. This may be an observational bias as it is difficult to detect PNe around low mass progenitors as they have much lower mass loss rates producing lower surface brightness nebulae (Kaeufl et al., 1993) and reach ionisation temperatures at a slower rate (Weiss & Ferguson, 2009). Although slowly evolving post-AGB stars may explain the lack of observed PNe, luminous CSPNe should still be detected. The lack of known post-AGB objects in pop. II environments may also be due to observational biases. Carrying out a systematic survey removing this bias should either find a large number of new post-AGB stars or give evidence indicating that the majority of low mass and metallicity objects may not be evolving through the AGB. This leads to an absence of AGB mass loss which has ramifications for the enrichment of the ISM leading to subsequent lower metallicity star formation. Results from a detailed search of evolved objects in older populations will have implications for the PN birthrate and stellar evolutionary models, thus affecting galactic evolution.

1.1 The Aim of the Thesis

This thesis consists of two well defined projects. The first is to use photometry to locate the central star of previously known PNe in each nebula's field. Synthetic

photometry of the CSPNe is derived from spectral energy distributions (SEDs) computed from a grid of model atmospheres covering the parameter range of CSPNe. The SEDs are convolved with filter transmission curves to compute synthetic magnitudes for a given photometric system which are then calibrated with standard stars and WDs. After the CSPN is located, the observed magnitude is used with a range of hypothetical distances to determine absolute magnitudes. The same hypothetical distances are applied to the angular diameter of the PNe with the known expansion velocity to determine a kinematic age. The range of CSPN absolute magnitudes and the kinematic ages of the nebula are used in conjunction with post-AGB evolutionary tracks to reduced the range of possible distances. Where available, the distance is further restricted with high spectral resolution 3D reddening maps. Improving PN distance estimates is essential to improving PN birthrates and Galactic population estimates. The distance methods will provide a useful tool when constructing a volume limited complete sample using photometry alone.

A spin-off project which subsequently became the bulk of the thesis was formed from an inverse of the above. CSPNe are luminous and easier to detect than evolved PNe which have expanded and dissipated to become low surface brightness nebula. Deep Hα observations around the CSPNe may identify the faint PNe. The study was broadened to include post-AGB type objects (without a previously known nebulae), and a search for post-AGB stars and CSPNe in the Galactic halo was undertaken. A synthetic Galactic population of post-AGB stars is produced to compare with observations. The observed sample is taken from an old Palomar-Green (PG) study of hot, high Galactic latitude stars (Saffer et al., 1997) and a new spectroscopic and photometric search in the Sloan Digital Sky Survey (SDSS). The detection of such objects would locate the hidden population expected by population synthesis models, whereas the non-detection raises questions over the models of low mass and metallicity stellar evolution.

Chapter 2

The Evolution of Post-AGB Stars and Central Stars of Planetary Nebulae

Post-AGB stars are an evolutionary phase common to all low and intermediate mass stars as they evolve across the top of the H-R diagram from the tip of the AGB to the WD cooling track. The post-AGB phase begins after turbulent and significant mass-loss phases on the AGB. Details of a star's evolution during this phase ar important to its subsequent composition.

As described in Sect. 1, the evolution of a star begins at the H core burning, MS phase which is the longest nuclear burning stage for all stars. As H core burning ceases, the inert core is predominantly composed of He with H burning shell as the star ascends the (first) red giant branch (RGB). This leads to a core contraction and an expanding envelope which soon becomes convective, and if deep enough can cause the first dredge up of the products of H burning to the stellar surface. H shell burning adds He to the core until conditions for He burning are reached at the tip of the RGB. He core burning stars can be identified with HB or clump stars. When He core burning ceases at the end of the HB the star is left with a contracting, increasingly degenerate C and O core surrounded by layers of He

and H. Subsequently, the He shell increases in temperature which causes He shell burning to ignite through the triple alpha process at the base of the shell, which drives the expansion of the shell and envelope. These phases cause a significant increase in luminosity via the expansion of the envelope and the more massive stars undergo a second dredge up. When the He shell depletes, the thermal pulse cycle commences with alternating phases of quiescent H shell burning and violent He burning. Steady H shell burning, which radiates much of its energy away, deposits He 'ash' on top of the He shell. The He shell increases in mass and begins He burning at the bottom of the shell. The high energy production rate of the triple alpha process and retention of much of the stellar energy by the thick He shell causes violent, runaway He burning (He shell flash) which becomes the dominant energy source. The luminosity rapidly increases before the He burning shell expands and the burning ceases. Deep convection in the envelope can now penetrate into regions enriched with α processed material (third dredge up of C-enhanced material). He burning stops and H burning becomes the dominant energy source again. The low temperature of the envelope allows for the formation of molecules and dust grains through condensation. The dust grains have significantly larger absorption cross sections than atoms and molecules and are more likely to absorb or scatter emitted photons from the stellar core converting much of the energy into momentum. This process is known as radiatively driven wind and increases the velocity of the dust in the tenuous atmosphere so that its expansion velocity is high enough to exceed the escape velocity and the material becomes detached from the star. The H and He shell burning cycle continues until the envelope is sufficiently thin and starts to contract causing the star to increase its temperature and leave the AGB. Nuclear shell burning continues to operate until the evolutionary track reaches its hottest point and the star descends the WD cooling track which is observable through the emission of thermal energy.

2.1 Mass-Loss Relationships

There are two major mass-loss phases in the evolution of low- and intermediate-mass stars. The first is on the RGB and empirical relationships have been developed based on spectroscopic observations of late type giants. Reimers (1975) uses the expansion velocity of circumstellar lines (in particular Ca II, H and K lines) at different radii from the stellar surface to determine the mass-loss and plots the findings against stellar parameters for the observed stars. Reimers (1975) found the empirical relationship:

$$\dot{M}(M_\odot/\mathrm{yr}) = 4 \times 10^{-13} \frac{(L/L_\odot)(R/R_\odot)}{(M/M_\odot)} \tag{2.1}$$

and it was employed for all phases of mass-loss at the time. The second and significantly more important mass-loss phase takes place on the AGB. The Reimers relation was applied to AGB mass-loss until other relationships were found which brought the predicted mass-loss in line with observations. Recent derivations of the AGB mass-loss have used empirical, physical and numerical models (Habing & Olofsson, 2003). The dust-driven wind depends on the opacity of the circumstellar material which in turn relies on the composition of the dust. AGB stars are classified as C-rich (C/O > 1, C-type), O-rich (C/O < 1, M-type) and S-types (C/O≈1) and as CO molecules are present in all types, the more abundant element forms molecules and dust with the remaining elements. Weiss & Ferguson (2009) apply one of two AGB mass-loss relationships to their evolutionary tracks. For C-rich AGB stars the mass-loss rate of Wachter et al. (2002) is applied based on theoretical radiation-hydrodynamical models to produce:

$$\log \dot{M}(M_\odot/\mathrm{yr}) = -4.52 - 6.81 \log(T_{\mathrm{eff}}/2600\mathrm{K}) + 2.474 \log(L/10^4 L_\odot)$$

$$-1.95 \log(M/M_\odot) \tag{2.2}$$

For O-rich AGB stars the empirical formula of van Loon et al. (2005) is applied:

$$\log \dot{M}(M_\odot/\mathrm{yr}) = -5.65 + 1.05 \log(L/10^4 L_\odot) - 6.3 \log(T_\mathrm{eff}/3500\mathrm{K}) \qquad (2.3)$$

On the AGB, mass-loss increases as the luminosity increases in time and the third dredge up provides a C-enhancement which increases opacities. A significant drop off of the temperature is followed by the last thermal pulse which results in the removal of most of the circumstellar envelope. An overview of the tip of the AGB evolution is shown in Fig. 2.1 for a solar metallicity, $M = 2M_\odot$ star. Mass-loss after this is insignificant in terms of the final mass of the star but still has an effect on the envelope mass and subsequently the evolutionary speed. The rates of mass-loss during the post-AGB phase are unknown with several empirical relationships being applied by different authors. Any one of the above three equations have been employed for different studies, although it is generally agreed that the Reimers relationship or the radiative driven wind formula of Pauldrach et al. (1988),

$$\log \dot{M}(M_\odot/\mathrm{yr}) = -1.29 \times 10^{-15}(L/L_\odot)^{1.86} \qquad (2.4)$$

are used when $T_\mathrm{eff} > 10,000\mathrm{K}$.

The superwind marks the end of the AGB evolution, although observationally this is not clear as the central star is obscured by the circumstellar material and only the dusty envelope is observable in the infra-red (IR). The IR signature of the thermal emission from dust in the envelope is yet to cool significantly since it was detached from the central star. On the scale of a few hundred years the circumstellar envelope expands so that it is optically thin and the exposed star may be detectable again. This results in two distinct features in the object's spectra, the optical central star and IR circumstellar envelope (Fig. 2.2). The central star evolves independently of its ejected envelope and its evolutionary speed is solely reliant on the mass of the remaining outer shell and the consumption of that mass through shell burning ($\dot{M}_H \sim 10^{-7} M_\odot/\mathrm{yr}$; van Winckel, 2003) and/or a
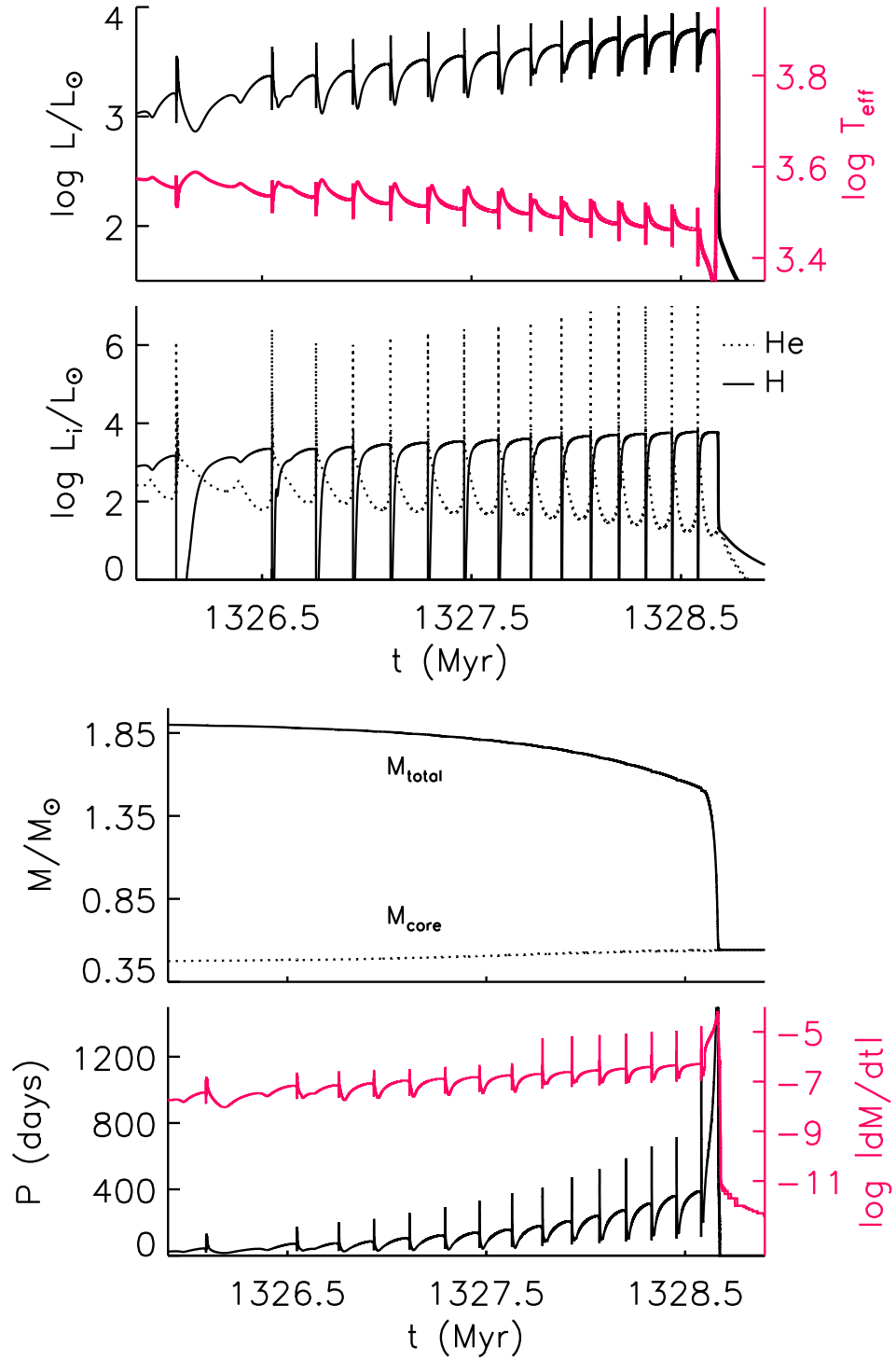
Figure 2.1: The AGB thermal pulsing phase of a $M = 2M_\odot$, solar metallicity star. From top to bottom the panels show $\log L_\odot$ and $\log T_{\text{eff}}$, log H burning luminosity (L_H, solid) and log He burning luminosity (L_He, dotted), total and core mass, pulsation period, P, and log mass-loss rate, dM/dt, all against time. This figure is taken from Weiss & Ferguson (2009).
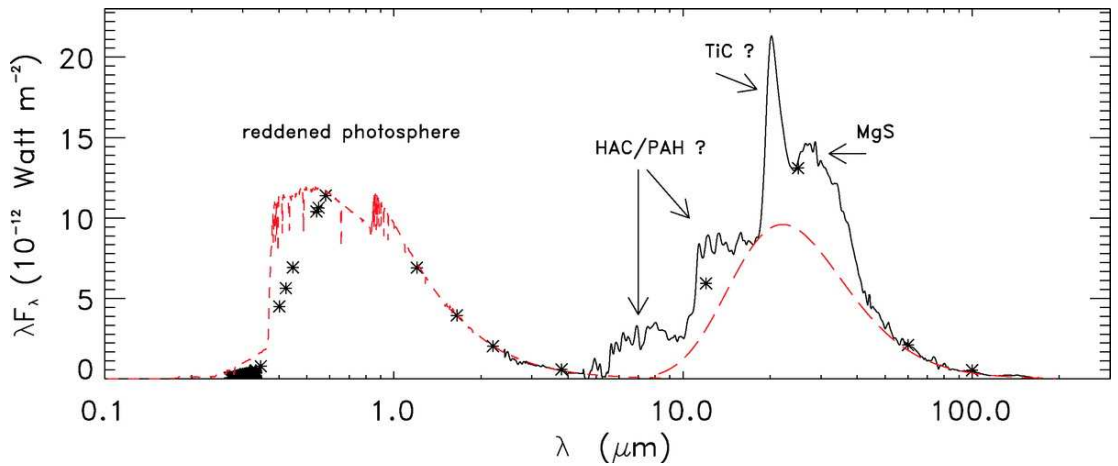
Figure 2.2: The double peaked energy disturibution of the post-AGB star, HD 56126. Figure from van Winckel (2003).

dust-driven wind causing mass-loss on the post-AGB ($\dot{M}_{\mathrm{AGB}} \sim 10^{-8} - 10^{-7} M_{\odot}/\mathrm{yr}$; Trams et al., 1989). Thus, the evolutionary timescale is given by $t_{\mathrm{tr}} = M_{\mathrm{env}}/(\dot{M}_H + \dot{M}_{\mathrm{AGB}})$ where M_{env} is the initial envelope mass. With the burning rate (and luminosity) staying fairly constant for post-AGB stars, the envelope mass and mass-loss are essential for evolutionary timescales. High mass stars lose almost all of their envelope in the mass-loss phase and so their post-AGB evolution is quick ($t_{\mathrm{tr}} \sim 100$yrs), with a high mass-loss and burning rate diminishing the envelope quickly. Low mass stars have significantly less luminosity which means the radiative driven wind is less effective with residual envelope burning dominant in burning up the envelope (Trams et al., 1989). The timescale of the post-AGB evolution is a balance between the two envelope consuming processes. Essentially, observing PNe is reliant upon the central star evolving fast enough to ionisation temperatures so that the nebula is not too dispersed and too faint to detect. The end of the post-AGB phase (with or without a PN) is reached when only a thin H envelope remains which is unable to sustain further shell burning, leaving a WD.

2.2 What is a post-AGB star?

Some confusion exists as to what is meant by the term 'post-AGB star' with more specific synonyms used to define the star's subsequent evolution. Furthermore,

different authors use different definitions of the beginning of the post-AGB phase. In this work, a post-AGB star is defined as a star that has evolved from the AGB and is not yet a WD (with or without the detection of a PN). This definition incorporates stars in their transition to becoming a CSPN, or a so-called 'proto-PN'. The moment the star leaves the AGB is not observable and even if it were, would not be obvious if mass-loss continues. Blöcker (1995) models continuous mass-loss after the superwind and uses a start point of the pulsational period of less than 50 days. Vassiliadis & Wood (1994) use $T_{\mathrm{eff}} = 10,000$K as a start age but also state a transition time of each model from $\Delta \log T_{\mathrm{eff}} = 0.3 - T_{\mathrm{eff}} = 10,000$K. Lower mass progenitors evolve at a slower rate, losing less mass and the PNe surrounding them have a lower surface brightness (Marigo et al., 2004, in particular Fig. 10) leading to two possible outcomes:

1. the star has a PN but with low surface brightness

2. the nebula disperses before the central star is hot enough to ionise it

BD+33°2642 is an example of a slowly evolving CSPN with a very faint nebula in spite of the star having T_{eff}=22,000K (Napiwotzki et al., 1994). PHL 1580 and 174 are both post-AGB stars which are hot enough to ionise a nebula and although no nebula is detected, the possibility of the stars previously having a nebula can not be ruled out (Conlon et al., 1991). Recent studies of PN luminosity functions (PNLF) show a decrease in the number of PNe expected in early-type galaxies (Buzzoni et al., 2006, Tab. 4) which are dominated by old population stars which is emphasised in Marigo et al. (2004), Fig. 25. The observed sample of PNe in the Galactic halo is a direct confirmation of the reduced numbers of PNe observed for old populations with only 14 known (Otsuka et al., 2010). Post-AGB stars in the halo are low mass and slowly evolving and are easier to detect than their dispersed PN with approximately 30 known (Conlon et al., 1991; Szczerba et al., 2007).

2.3   PN Formation and Morphology

As described above, the material of a PN is expelled from the central star near the end of the AGB where much of the mass-loss takes place via a dust-driven wind. The ejected matter in these phases are later illuminated as a PN, however, direct observations are difficult as the optically thick circumstellar material absorbs most of the stellar radiation. At this phase, model simulations can only be constrained by IR observations of the circumstellar material. Furthermore, although one can see the post-AGB object when the ejected material disperses, the nebula is only observable in the optical through scattered light of the central star until the central star heats enough to photoionise the nebula gas at $T_{\text{eff}} \sim 20,000$K. The early shaping of the nebula must be constrained by IR spectroscopic observations and the H_2 emission of the molecular gas. The evolution of the morphology is described by the interacting stellar wind (ISW) model of Kwok et al. (1978) which consists of a fast wind, interacting with the circumstellar material from the slower AGB wind. If a spherical stellar wind is assumed, a shell is formed and remains intact until it is shaped due to the varying densities in the ISM. However, detailed structure is seen in nebulae prior to ISM interaction and the shaping mechanism for these objects is not clear. The varying morphologies are classified into three different types, round, elliptical and bipolar (including multi-pole shapes) in Stanghellini et al. (2002). Proposed single star shaping mechanisms which produce axisymmetric nebulae include stellar rotation (Reimers et al., 2000) and magnetic fields (Blackman et al., 2001), however, they fail to reproduce PNe in detail and systematically. Binary evolution has been considered as the only feasible shaping mechanism to produce the morphology found in PNe (de Marco, 2009).

2.4   The Binary Scenario

Soker (1997) strongly argue that stellar rotation is not significant for later phases of evolution and that post-AGB stars do not produce a strong enough magnetic
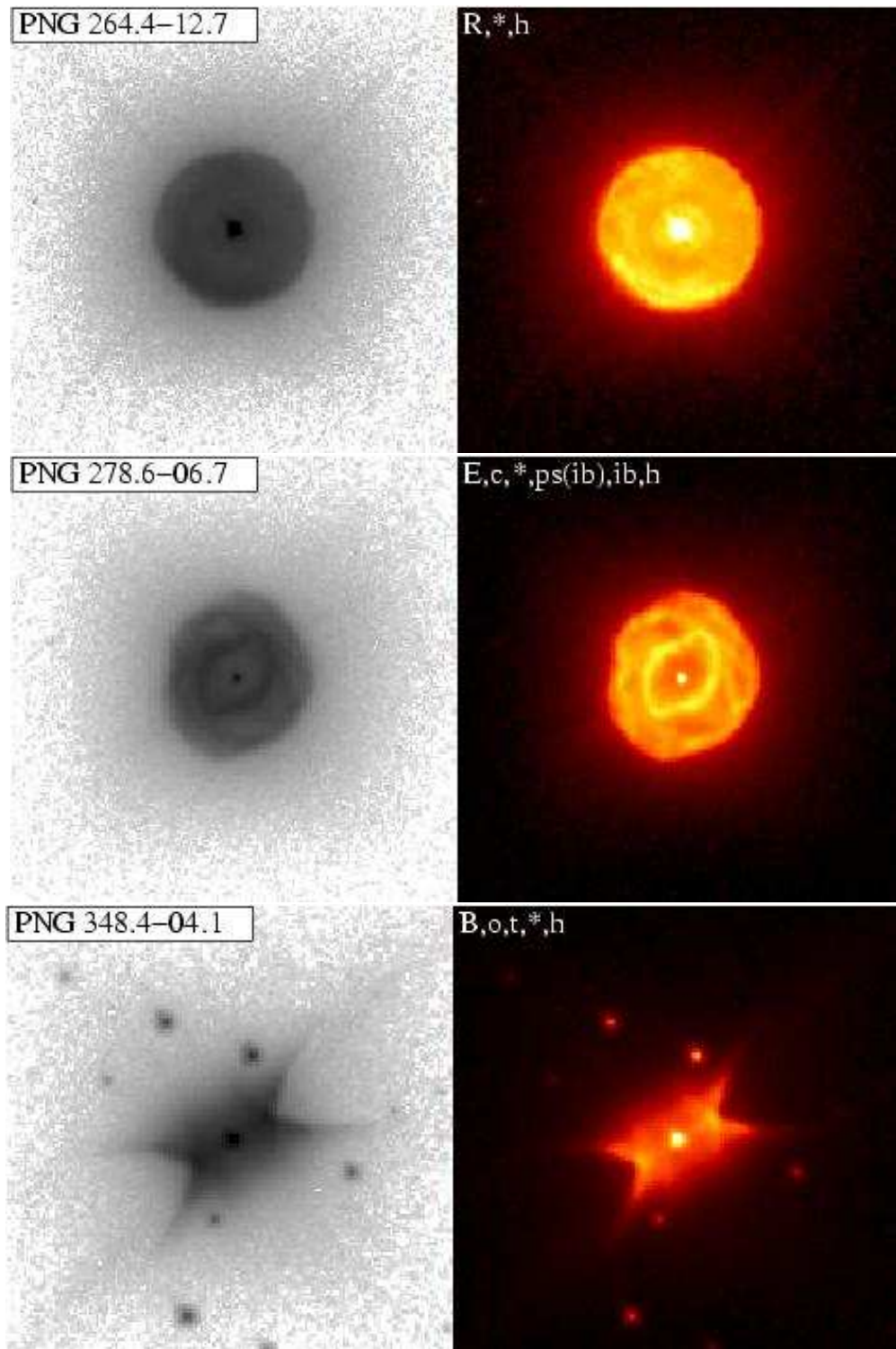
Figure 2.3: The three morphological types of PNe from the Hubble Space Telescope in Sahai et al. (2011). Both images are with Hα filters, one in gray scale and the other in false colour to emphasise the fine structure. From top to bottom they are round, elliptical and multipolar.

field to shape nebulae. They state that all asymmetric PNe require a companion to dynamically shape their shell before being driven by the fast wind and subsequent shaping via ISM interaction. Soker (1997) adds that a companion can be a stellar binary component or a substellar object, such as a brown dwarf or planet. Their analysis of 458 PNe had a 46% (stellar) and 54% (substellar) split of companion type. The asymmetric PNe within the study are sub-divided into three categories, non-interacting (10%), interacting without a common envelope (11%) and interacting with a common envelope (23%). Soker (1997) showed that the shaping of asymmetric nebula requires a companion, however, 64% of their PNe evolve on a single star evolutionary channel (non-interacting) and when this result is combined with observed spherical nebulae, it implies a dominant single star evolutionary channel.

In the standard single star scenario, described earlier, the central star reaches temperatures of more than 20,000K and begins to ionise its circumstellar cloud which then emits photons when the electrons recombine. The re-radiation makes it possible to observe PNe in the optical. Alternatively, De Marco & Moe (2005) and Moe & De Marco (2006) suggest that the PNe are largely created by binary stars and argue that if the single star scenario is dominant, a higher number of PNe will be formed in the Galaxy with respect to the number observed even after corrections for incompleteness.

Moe & De Marco (2006) modelled synthetic population estimates using the hypotheses of binary dominated CSPNe to drive down the extrapolated numbers for PN birthrates. The model reproduces the PN birthrate using determinations of Galactic structure and stellar formation and evolution from the literature. By using estimates of the Galactic mass and star counts, the number of stars that go on to produce PNe greatly reduces with the stipulation that they must be part of a binary system. The theoretical PN birthrate value from their work is $1.1 \pm 0.5 \times 10^{-12}\,\mathrm{yr}^{-1}\,\mathrm{pc}^{-3}$, which is in agreement with WD birthrates, therefore, the observed CSPN binary ratio was followed-up by different authors using vari-

ous methods. Searches for photometric variations (Bond, 2000), direct detections (Ciardullo et al., 1999) and radial velocity (RV) variations (Méndez, 1989) of CSPNe have been undertaken and the results suggest that the minority of central stars are binaries. De Marco et al. (2004) argue that more detailed RV surveys are required and carried out an ongoing survey with initial results showing that ten out of eleven CSPNe show RV variations implying a binary dominated scenario. This high fraction from the biased sample has since been an isolated result with subsequent follow-up observations showing no clear evidence for most CSPNe being binaries.

In a binary scenario, closely orbiting stars come into contact as the primary evolves up the AGB and fills its Roche lobe. Once the Roche lobe of either star is filled, their envelope overspills and begins to dump matter on the companion. The companion accretes matter until its maximum accretion rate is exceeded and the donated material overspills forming a common envelope around the system. Orbital energy lost to the common envelope is used to eject the surrounding gas and drives the expansion of the nebula. Further support for a binary theory comes from the non-spherical morphology of most PNe (Balick & Frank, 2002). If PNe are formed solely by interacting binary systems then they can be considered atypical as only ∼10% of WDs are observed to have closely orbiting companions (Napiwotzki et al., 2004). This would devalue PNe as tools to test AGB evolution in general. It is possible that PN shaping may be dependent on a companion but the single star evolution channel remains dominant and thus the CSPN/WD birthrate contradiction still exists.

2.5 Evolution of Low Mass stars

Evolutionary models of low mass stars ($M < 0.85 M_\odot$) do not evolve through the thermal pulse phase before they reach the post-AGB phase. The mass at which this cut off occurs is hard to define as the evolution is sensitive to envelope mass

which decreases as a star evolves up the AGB. Dorman et al. (1993) models show that a transition between post-AGB and post early AGB (EAGB) occurs at a remnant mass of $M \sim 0.52 M_\odot$. Post-EAGB stars lose enough envelope mass to leave the AGB early, evolving across the H-R diagram before thermal pulses takes place. This argument is supported by globular clusters (GCs) where the average turn-off mass is $M \sim 0.85 M_\odot$ (Jacoby et al., 1997) and evolved objects are observed to follow the low mass post-AGB and post-EAGB tracks.

Lower mass objects, fail to begin He shell burning and do not ascend the AGB at all. The majority of the Dorman et al. (1993) tracks with a core mass of $M < 0.5 M_\odot$ do not ascend the AGB, instead evolving along the HB and extreme horizontal branch (EHB) and traversing straight across the H-R diagram as post-EHB objects before descending the WD cooling track. A core mass of $M = 0.5 M_\odot$ corresponds to an initial mass of $M \sim 0.74 M_\odot$ (Catalán et al., 2008) but with a progenitor evolutionary age older than the Galaxy (Girardi et al., 2000), their numbers are estimated to be low ($\sim 1\%$; Drilling & Schönberner, 1985; Heber, 1986; Saffer et al., 1994) with their appearance explained by binary interactions (Maxted et al., 2001). All three channels of post-HB evolution are shown in Fig. 2.4.

By probing the old, evolved populations of the Galaxy, one can determine the threshold when PNe become too faint to observe and appear simply as stand alone post-AGB stars. With the low number of known population II post-AGB objects, identifying more will provide direct evidence for this expected, but largely unknown phase. A non-detection of these objects may imply that evolved stars with low mass and metallicity are not fully ascending the AGB, and instead are predominately following the post-EHB channel.
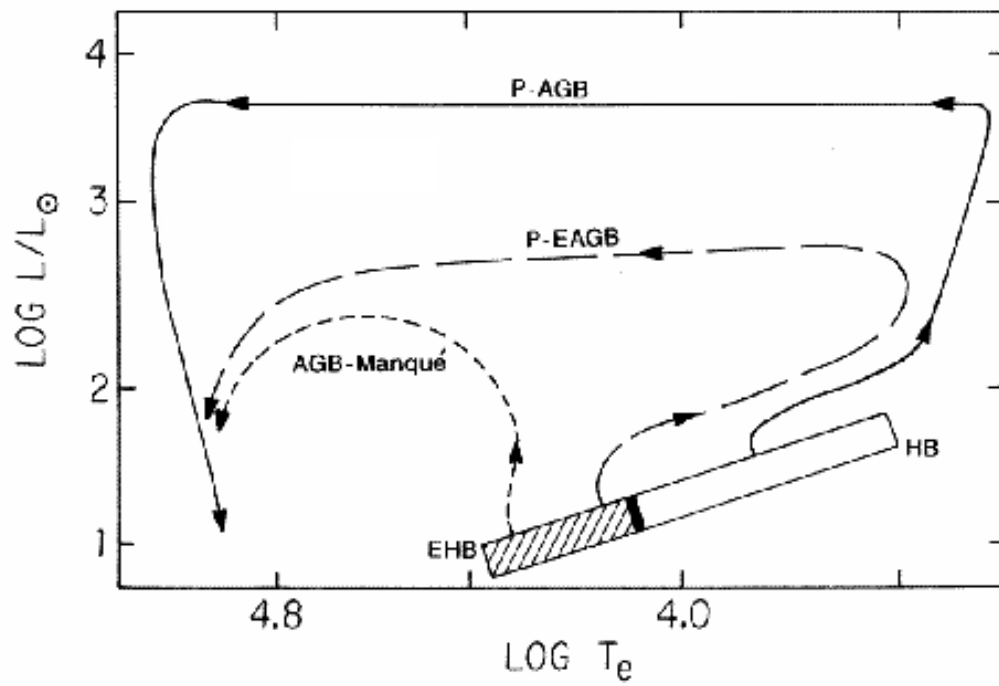
Figure 2.4: The three post horizontal branch channels, the standard post-AGB channel, post-EAGB and post-EHB (AGB-Manqué). This figure is taken from O'Connell (1999).

Chapter 3

PN Birthrates

PN birthrates are an important tool in determining the extent of the role PNe play in the feedback process of the Galaxy but are notoriously difficult to constrain. Studies by various authors yield a magnitude spread in birthrates with estimates ranging from 0.4 (Jacoby, 1980) to 8.0 (Ishida & Weinberger, 1987) $\times 10^{-12}\,\mathrm{PNe\,yr^{-1}\,pc^{-3}}$. The uncertainty in these values is due to a combination of incompleteness in samples, and difficulties in deriving PNe distances. Removing, or certainly decreasing the above uncertainties can improve upon the PNe birthrate estimates, however, the best recent estimates of $2.1 \times 10^{-12}\,\mathrm{yr^{-1}\,pc^{-3}}$ (Phillips, 2002) and $3.0 \times 10^{-12}\,\mathrm{yr^{-1}\,pc^{-3}}$ (Pottasch, 1996) are larger than the well determined WD birthrate of $1.0 \pm 0.25 \times 10^{-12}\,\mathrm{yr^{-1}\,pc^{-3}}$ from the PG survey (Liebert et al., 2005). The PN birthrate clearly needs to be revised as all PNe form a WD yet WDs also form from other evolutionary processes such as post-EAGB stars, which leave the AGB before the onset of thermal pulses and post-EHB stars, which do not ascend the AGB at all. As these objects do not go through a PN phase to become WDs one would expect the WD birthrate to be larger than that of PNe. Recent surveys of PNe such as The Macquarie/AAO Strasbourg Hα planetary nebula catalogue, (MASH, Parker et al. 2006), MASH-II (Miszalski et al., 2008) and The INT (Isaac Newton Telescope) Photometric Hα Survey (IPHAS, Drew et al. 2005), have added a significant number of new discov-
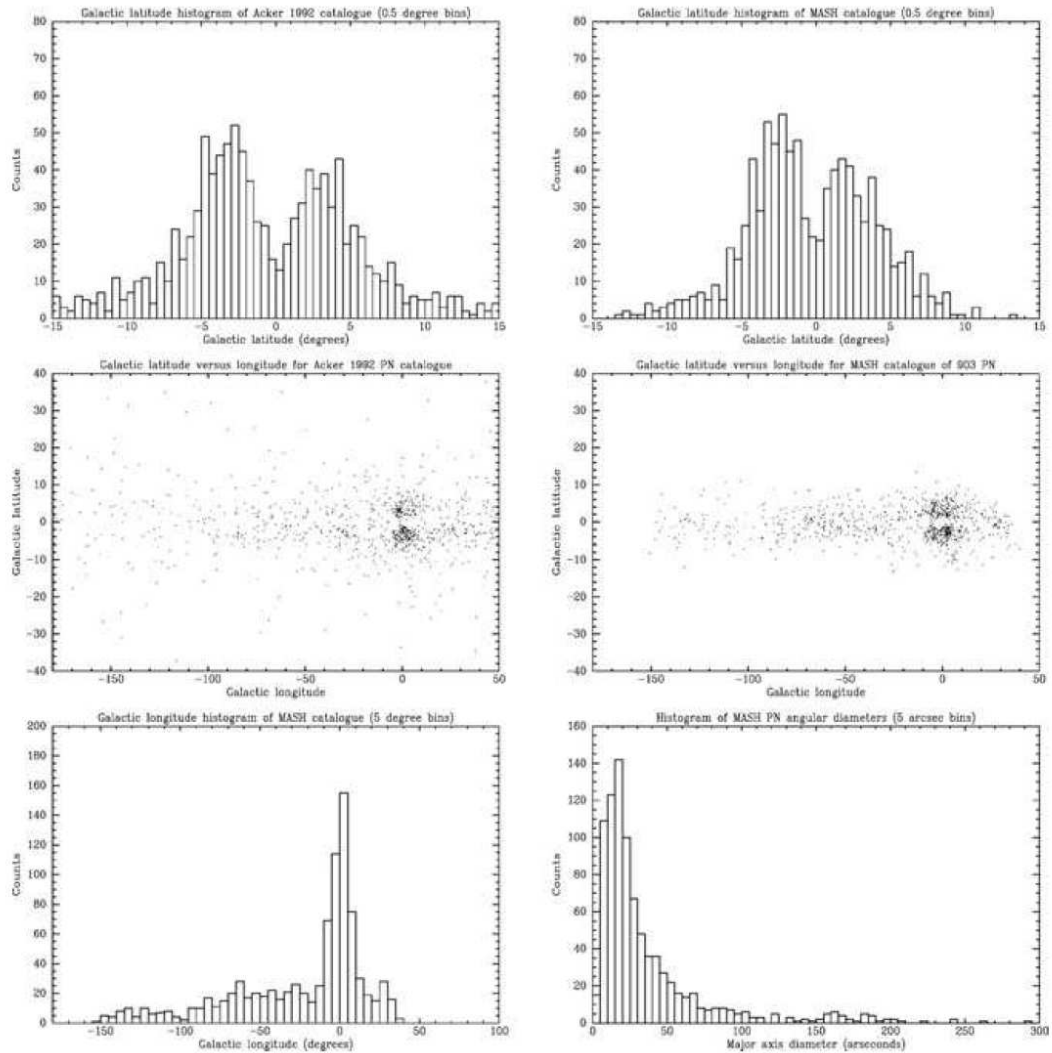
Figure 3.1: The Galactic distribution of PN and comparisons between the ESO/Strasbourg catalogue (Acker et al., 1992) and MASH (Parker et al., 2006). The figure is taken from (Parker et al., 2006).

eries to the previous database of the Strasbourg/ESO catalogue of Galactic PNe (Acker et al., 1992). However, incompleteness can be seen near the Galactic centre ($|b| < 2°$) and at the far reaches of the Galaxy ($l > 40°$) for MASH even with the noticeable improvements compared to the Strasbourg catalogue (Fig. 3.1). There is also a considerable bias in favour of compact PNe. IPHAS has found a significant number of new PNe in the Galactic plane. Younger compact PNe have been found (Viironen et al., 2009) as well as the more elusive extended nebulae (Sabin et al., 2010), however, with only three colours, Hα, r' and i', IPHAS can identify candidate objects but follow-up spectra or cross matching with IR surveys

is needed to confirm the PN classification. Hα emission is a key identifier of PNe however it is also observed in young stellar objects, novae and symbiotic stars and can be misclassified. The new surveys have more than doubled the known PNe sample to $\sim$3000 objects but this is still expected to be only $\sim$10% of the Galactic population (Pottasch, 1996; Phillips, 2002). The above estimates are based on observed local samples and extrapolated to the entire Galaxy so it is important that the local sample is correct. Methods used and errors found for observational PN birthrates are discussed later in Sect. 3.1 and highlight the importance and difficulties of determining distances to PNe.

3.1   PN Birthrate Determination

PN birthrates are determined through extrapolations of a complete local sample to the Galaxy. These estimates vary from author to author due to uncertainties caused by incorrectly classified PNe, incompleteness and inaccurate distances. These errors are more apparent when looking into the Galactic plane due to extinction and the dense environment (low surface brightness nebulae can be indistinguishable from the ISM) and for large distances (observed magnitudes are fainter as $f_\lambda \propto d^{-2}$). As such, the local space density must be accurate, as any errors will be propagated and emphasised through the extrapolation. The distribution of PNe projected on the Galactic plane (ρ_1) can be approximated as a function of the local density (ρ_0), perpendicular distance above the Galactic plane (z) and the scale height (k^{-1}):

$$\rho = \rho_0 e^{-kz} \tag{3.1}$$

$$\rho_1 = 2 \times \int_0^\infty \rho dz = \frac{2\rho_0}{k} \tag{3.2}$$

This was proposed in Daub (1982) and applied for local density estimates at the time including that of Ishida & Weinberger (1987). The number of PNe given

within a fixed volume of maximum distance (D) from the sun is:

$$N(D) = 2 \times \int_0^D 2\pi \mathrm{dp} \int_0^{\sqrt{D^2 - p^2}} \rho(z)\mathrm{dz} \qquad (3.3)$$

where p, is the projected radius along the Galactic plane. Expanding the integral gives:

$$N(D) = 2\pi\rho_0 \left[\frac{D^2}{k} - \frac{2}{k^3} + e^{-kD}\left(\frac{2D}{k^2} + \frac{2}{k^3} \right) \right] \qquad (3.4)$$

which in turn can be used inversely to determine a local density through a number of PNe in a complete local sample for a limited distance (Daub, 1982). The birthrate of PNe, r, is determined using the space density per radius interval, derived from the local density normalised to a nebula with a 1 pc radius, $\tilde{\rho}_0$ and the average expansion velocity, v, by:

$$r[\mathrm{kpc}^{-3}\,\mathrm{yr}^{-1}] = 1.02 \times 10^{-6} \tilde{\rho}_0 [\mathrm{kpc}^{-3}\mathrm{pc}^{-1}]\, v[\mathrm{km\,s}^{-1}] \qquad (3.5)$$

Daub (1982) determine a PN birthrate of $5 \pm 2 \times 10^{-3}\,\mathrm{kpc}^{-3}\,\mathrm{yr}^{-1}$ using the values of $\tilde{\rho}_0$ for each radius interval and v of 20-30km s^{-1}. A total number of PNe in the Galaxy is estimated by taking the ratio of the PN surface density to the Galactic mass surface density along the Galactic plane (giving a PN number per unit mass) and multiplying by the Galaxy mass. Daub (1982) determines a value of $\rho_1 = 13\mathrm{kpc}^{-2}$, using $\rho_0 = 53\mathrm{kpc}^{-3}$ and $k = 8^{-1}$, which for a local mass density of $0.019\,\mathrm{g\,cm}^{-2}$ and a Galactic mass of $10^{11}M_\odot$, gives 14,000 as a total number of PNe. The birthrate was in agreement with literature at the time (if not smaller) but, like today, was in contradiction to the WD birthrate. Other methods include the specific mass or luminosity (i.e. PNe per solar mass or PNe per solar luminosity) extrapolated to give the Galactic value. All Galactic samples suffer from the distance problem which was realised then, but it is still not fully resolved today. Extragalactic samples of the local group can be used for a Galactic estimate which greatly reduce the distance problem but suffer from

other difficulties discussed later. Eq. 3.4 shows that the local density is sensitive to distances, both directly and through the determination of the scale height and a complete local sample. With the aforementioned errors in mind, distance determination techniques are imperative and the methods implemented must be improved.

3.2   Distance Determination Methods

Many PN distance determination methods have been proposed and applied within the past 40 years with varying success. The most prominent methods are estimates which assume properties of the nebula and are used with direct measurements. These methods are called statistical methods and the methods are improved by empirically determined relationships which have produced spin-off techniques, although they are less reliable for older, evolved nebulae. Methods which involved the central star can only be used for evolved objects when the nebula is expanded and optically thin to the stellar radiation. Other methods are useful as additional checks but are rarely readily available.

3.2.1   The Shklovsky Method

The most popular method applied in estimating PN distances was proposed by Shklovsky (1956), which uses direct measurements of a nebula's flux (F) and angular radius (θ) with theoretically derived values of the filling factor (ϵ), and the PN ionisation mass (M_i). The distance can be determined using the flux of the nebula with either the Hβ recombination line or free-free emission at a frequency of 5GHz. The Hβ flux requires a H-rich nebula which is ionised by its central star and as the nebula is in thermal equilibrium, each ionisation is balanced by a recombination. The effects of varying ϵ and M_i are determined in Boffi & Stanghellini (1994) with a discussion on the range of values for different populations of PNe. They determine the mean for ϵ by the flux detected on Earth

from a spherical, isotropic nebula as:

$$F_{\mathrm{H}\beta} = \frac{\alpha_\beta h \nu_\beta}{4\pi D^2} \int_0^{R_i} \epsilon n_e n_p 4\pi r^2 dr \; [\mathrm{erg\,cm^{-2}\,s^{-1}}] \tag{3.6}$$

where $F_{\mathrm{H}\beta}$ is the Hβ flux, h is the Planck constant, ν_β is the frequency of the Hβ line, D is the distance to the PN, n_e and n_p are the number densities of electrons and ions, respectively, and R_i is the radius of the ionised gas in the nebula. The recombination coefficient for Hβ, α_β, is determined from the nebula's electron temperature, T_e:

$$\alpha_\beta = 9.69 \times 10^{-11} \times T_e^{-0.88} \; [\mathrm{cm^3\,s^{-1}}] \tag{3.7}$$

which for the vast majority of PNe is $T_e \approx 10,000$K. Applying the assumptions of a pure H nebula, $n_e \approx n_p$, the small angle approximation, $R_i \approx \theta D$, and rearranging Eq. 3.6 for ϵ gives:

$$\epsilon = 2.47 \times 10^6 F_{\mathrm{H}\beta} \left(\frac{1}{\alpha_\beta \theta^3 n_e^2 D} \right) \tag{3.8}$$

As with any ideal gas a mass in a given volume is expressed by:

$$M_i = \frac{4\pi R_i^3}{3} n_e \mu_e m_{\mathrm{H}} \epsilon \; [g] \tag{3.9}$$

where μ_e is the mean atomic weight per electron, $\mu_e = \frac{2}{1+X}$ where X is the H fraction in the nebula and m_{H} is the mass of a H atom. Substituting Eq. 3.9 into Eq. 3.6 gives the nebula ionised mass independent of θ:

$$M_i = 3.45 \times 10^{-2} \left(\frac{F_{\mathrm{H}\beta} D^2}{\alpha_\beta n_e} \right) \; [M_\odot] \tag{3.10}$$

Equations 3.8 and 3.10 are used in Boffi & Stanghellini (1994) to derive empirical values of ϵ and M_i for PNe with previously determined n_e and D. Re-arranging

Eq. 3.8 for n_e and substituting into Eq. 3.10 gives:

$$M_i = 2.195 \times 10^{-5} F_{\mathrm{H}\beta}^{1/2} D^{5/2} \alpha_\beta^{-1/2} \theta^{3/2} \epsilon^{1/5} \qquad (3.11)$$

Re-arranging for D and assuming an electron temperature of $T_e = 10,000$K provides a distance with the empirically derived relationships of ϵ and M_i from Boffi & Stanghellini (1994) and direct observations of $F_{\mathrm{H}\beta}$ and θ:

$$D = 0.014(M_i/M_\odot)^{2/5} F_{\mathrm{H}\beta}^{-1/5} \epsilon^{-1/5} \theta^{-3/5} \text{ [kpc]} \qquad (3.12)$$

The free-free continuum flux is well represented at 5GHz and is often used as the Hβ line can be weak and difficult to observe in dense regions of the ISM. The electron density in terms of the 5-GHz flux can be expressed as:

$$n_e = 2.8 \times 10^{19} F_{\mathrm{5GHz}}^{1/2} \epsilon^{-1/2} R_i^{-3/2} D \text{ [cm}^{-3}] \qquad (3.13)$$

(Kwok, 2000). Assuming a H/He and ionised/neutral ratio an electron temperature, $\theta = R_i/D$ and substituting into Eq. 3.9 one can deduce a distance:

$$D = 46 \left[F_{\mathrm{5GHz}}(\mathrm{mJy}) \right]^{-1/5} \epsilon^{-1/5} (\theta/\mathrm{arcsec})^{-3/5} (\mathrm{M_i/M_\odot})^{2/5} \text{ [kpc]} \qquad (3.14)$$

The preference for radio measurements over Hβ is laid out in Pottasch & Zijlstra (1992) when compared to a similar sample by Stasińska et al. (1991). Pottasch & Zijlstra (1992) explain this is due to the inaccuracy of nebula radii when using photographic plates for optical images. However, both methods are reliant upon the nebula mass which is unrealistically assumed to be constant. This assumption is known to be worse for low surface brightness and distant PNe. Mendez et al. (1988) determine distances using atmospheric parameters derived from spectroscopy and the divergence increases for large distances when comparing distances solely based on statistical estimates by Daub (1982) (Fig.3.2). Subsequent
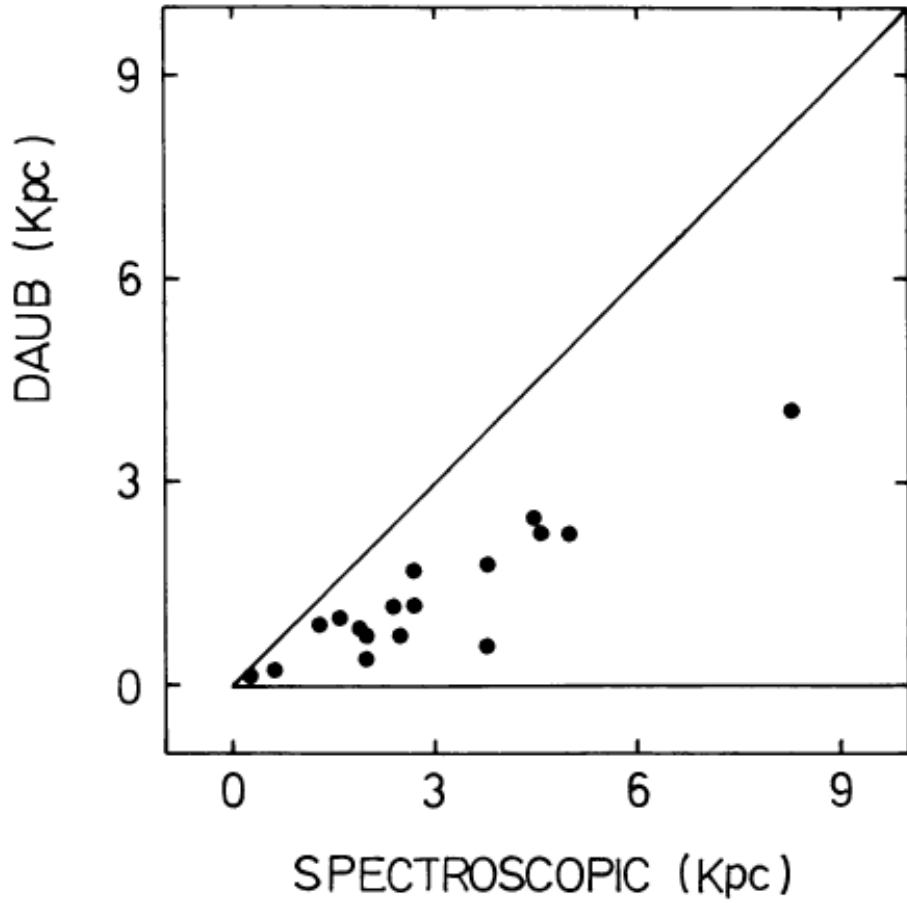
Figure 3.2: This figure demonstrates the difference between spectroscopic and statistical distances. The solid line showing the one to one ratio. Statistical distances underestimate the true measurement. The figure is from Mendez et al. (1988).

statistical methods (discussed later) improve the assumptions through empirical relationships but are derived from the principles of the Sklovsky method.

3.2.2 Forbidden Line Ratio Method

The greatest source of error in the Shklovsky method is the assumed nebula ionised mass. This can be removed if the electron density of the nebula can be determined independently of the mass (see Eq. 3.10). In 1987, Barlow determine ionised masses of nebulae in the Magellanic Clouds using the intensity ratio of the forbidden [OII] doublet line (3,726/3,739 Å). A doublet originates from levels which only differ in electron spin and thus have similar energies and wavelengths. For [OII], the transitions $^2D_{5/2}$ and $^2D_{3/2}$ to the electron level $^4S_{3/2}$ are observed

at 3,726 Å and 3,729 Å, respectively. The emissions from a nebula arise from collisional excitation, followed by a subsequent collisional de-excitation or spontaneous emission. The excitation rate is balanced between the two emission processes such that:

$$n_e n_i q_{ij} = n_e n_j q_{ji} + n_j A_{ji} \tag{3.15}$$

where n is the number density of atoms with electrons in the lower (i) and higher (j) energy levels, A_{ji} is the radiation transition probability where $j > i$. q_{12} and q_{21} are the collisional excitation and de-excitation rate coefficients. In a low density environment, where $n_e \rightarrow 0$, every collisional excitation is followed by an emitted photon and so there is no collisional de-excitation and the radiative transition probability has no impact. In fact, only the statistical weights of the exciting collisions contribute, so the ratio of the two line strengths is given by j_{3729}/j_{3726} which in the case of [OII] is 6/4 = 1.5. In the high density limit, $n_e \rightarrow \infty$, collisional de-excitations dominate setting up a Boltzmann ratio so that (Osterbrock, 1974):

$$\frac{j_{3729}}{j_{3726}} = \frac{N_{^2D_{5/2}} A_{3729}}{N_{^2D_{3/2}} A_{3726}} \tag{3.16}$$

The same processes can be followed for other forbidden lines and Stanghellini & Kaler (1989) also use single-ionised sulphur, [SII] 6,717/6,730 Å, double-ionised chlorine, [ClIII] 5,517/5,537 Å and triple-ionised argon [ArIV] 4,711/4,740 Å to determine nebula electron densities. The line strength ratios calculated as a function of electron density are shown in Fig. 3.3. Difficulties associated with the forbidden line ratio method are that the lines can be weak and often require high resolution spectroscopy to identify the two components of the doublet. Furthermore, the ratio and densities often vary within individual PNe and a variation in number densities is given for different elements (Pottasch, 1980) which can be seen in Fig. 3.3 as well. The errors are significantly increased with older low surface brightness PNe similarly to the Shklovsky method.
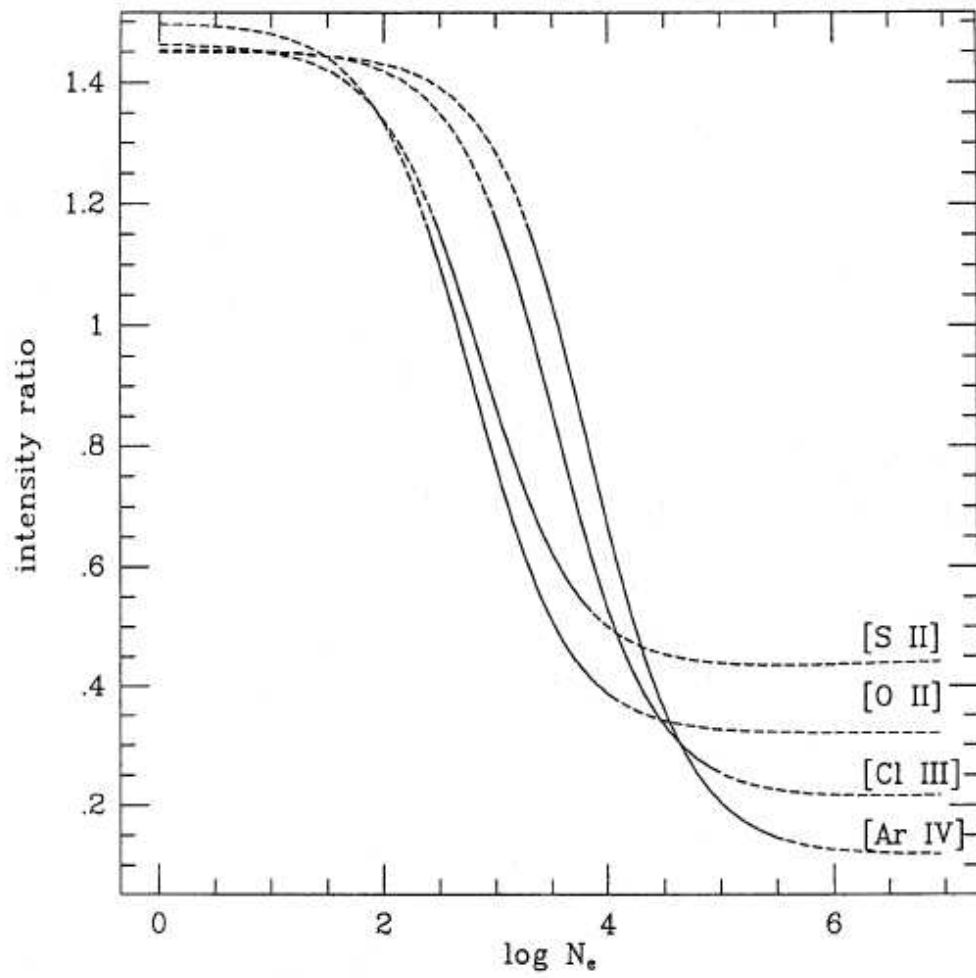
Figure 3.3: The electron density for the labelled forbidden line ratios. The broken lines show parts of the curve that lie within 20% of the flat part of the curve, increasing uncertainty. The figure is from Stanghellini & Kaler (1989).

3.2.3 PN Surface Brightness-Radius Relationship

Further attempts to improve the Shklovsky distance were made by applying a PN mass-radius relationship empirically. Maciel & Pottasch (1980) take previous work in the literature of nebulae electron densities from forbidden line ratios, angular diameters and distance determinations. Using the empirical mass-radius relationship they determine the masses and then distances of 121 PNe and plot physical parameters against one another to determine additional empirical relationships. Their first-order least-squares straight line approximation of the mass-radius relation implies that $M(M_\odot) = 1.225R[\text{pc}] - 0.0123$, subsequently replacing a fixed mass in Eq. 3.9. Alternatively, Milne (1982) suggests that for optically thick nebulae (i.e. high densities) the number density is unimportant and empirically determines a radio flux-distance relation of $S_{5\text{GHz}}d^2 = 8.1 \times 10^5 \text{Jy pc}^2$ from 13 nebulae. This implies for optically thick nebulae $M_i \propto R^{3/2}$ as $V \propto N_e^{-2}$ and this is used in conjuction with Eq. 3.9. Milne (1982) uses the assumption of a constant mass for the optically thin nebulae and uses the same assumed values of $\epsilon = 0.6$ and $M = 0.16M_\odot$ as Milne & Aller (1975) to derive the distance using Eq. 3.14. Equating the optically thin and thick nebulae:

$$d = 6180F_{5\text{GHz}}^{-1/5}\theta^{-3/5} = 900F_{5\text{GHz}}^{1/2} \qquad (3.17)$$

one can determine the distance with the observed radio flux and angular diameter using Fig. 3.4. Although both methods improve on the assumption of a constant nebula mass, both relationships are tenuous and have large errors attached to them statistically even for the nebulae they were derived from. The errors have been reduced in the recent study of Phillips (2002) but are still significant. Furthermore, many of the assumptions used for the Shklovsky method are applied again and are biased against large distance, low surface brightness nebulae.
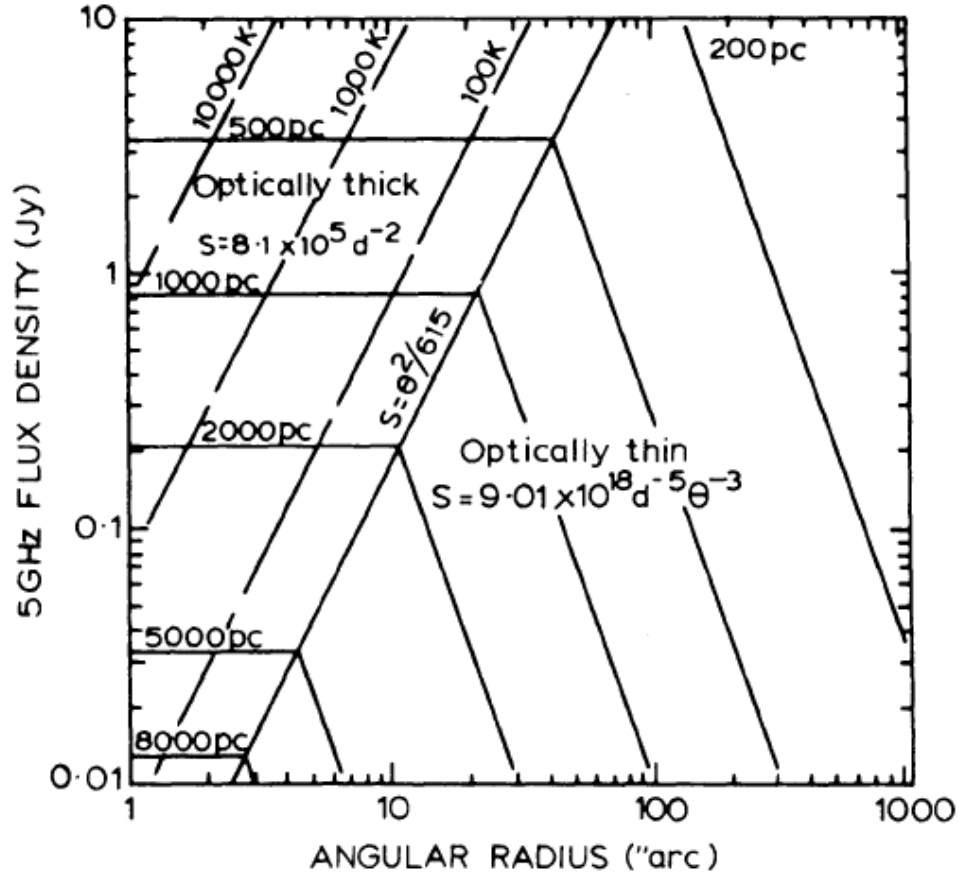
Figure 3.4: The radio surface brightness of the nebula plotted against its radius. The figure is from Milne (1982).

3.2.4 Spectroscopy of the Central Star

The distances of any astronomical object can be determined if the intrinsic properties can be established to give a surface flux. This was first done for a survey of CSPNe by Mendez et al. (1988), who obtained high resolution spectroscopy of 22 objects. The atmospheric parameters are determined by fitting theoretical non-LTE, plane-parallel H and He only model atmospheres. The best fit is determined using Hδ (and sometimes Hβ) with the He II lines 4200Å, 4541Å, 4686Å and the He I line 4471Å. Equating the apparent and absolute fluxes, Mendez et al. (1988) derive:

$$D^2 = 3.82 \times 10^{-11} \frac{M}{M_\odot} \frac{F}{g} 10^{0.4 V_0} \qquad (3.18)$$

where M is the CSPN mass in solar masses, F is the stellar surface flux taken from model atmospheres in $\mathrm{erg\,cm^{-2}\,s^{-1}}$ and g is the gravity in $\mathrm{cm\,s^{-2}}$. The apparent magnitude, V_0 is corrected for interstellar extinction by using interstellar lines. The distance is determined from the calculated gravity and de-reddened observed magnitude in conjuction with the model flux. The mass can be inferred based on the CSPN mean mass or from T_{eff}-$\log g$ space from evolutionary tracks. This method has been used in significantly larger surveys like that of Napiwotzki (1999, 2001). The advantages of this method are that properties of the nebula are not applied for the distance estimate and so no assumptions have to be made about it. Additionally, with high resolution spectra the errors are minimised on T_{eff} and $\log g$ which propagates through to the CSPN mass. However, there is a heavy reliance on the model atmospheres which are complicated by the fact LTE can not be assumed. Furthermore, circumstellar reddening is significant for younger PNe and it is difficult to determine the apparent stellar magnitude with this added complication.

3.2.5   Properties of a Binary Companion

Many PNe are known to have a binary central star and a distance can be inferred using the companion if it is observable. NGC 246 was the first CSPN to have a distance determined using its companion, confirmed as a binary component from RV and proper motions (Minkowski, 1965). A survey of 113 PNe using the HST was carried out by Ciardullo et al. (1999) and determined the binarity of a CSPN by a direct observation of a nearby star without using other information (i.e. RV or proper motion). The assumption was made that the star is associated with the CSPN if it is close to it in a sparsely populated region of the Galaxy. If the binary is a MS star then the absolute magnitude can be determined using the de-reddened colours and fitting to the MS. The distance modulus is then used to estimate a distance to the companion and therefore the PN. Other detections of companions have been through RV and proper motion surveys. Pottasch (1996)

summarises nine PNe with distance determinations from the photometry of companions and DS1, a nebula with a double lined spectroscopic binary, where both components can be used to estimate a distance (Drilling, 1985). Distances derived from companions are very reliable, particularly with MS secondaries, but are difficult to detect and rely on being able to resolve the individual components as well as a heavy reliance upon a correct determination of interstellar extinction. Known CSPNe with usable companions are still quite rare to date.

3.2.6 Trigonometric Parallax of the Central Star

Trigonometric parallaxes, π, have been used to measure the distance to stars using the orbit of the instrumentation (the Earth for ground based telescopes) as a baseline and the angular difference for two or more epochs, $D = 1/\pi$. In 1989 ESA launched the High Precision Parallax Collecting Satellite, Hipparcos, which was expected to improve distance estimates with its larger baseline. However, PNe are often distant and many of the 19 CSPNe selected in the Hipparcos input catalogue are near the magnitude limit (Acker et al., 1998) resulting in a significant error in the parallax measurement for the majority of the programme stars. This has meant the best recent parallax determinations for PNe stem from the ground based US Naval Observatory (USNO), a 1.55m telescope based at the Flagstaff station in Arizona dedicated to proper motion and parallax studies. The significantly improved CCD detectors and an improved sample selection in the USNO survey provide the most extensive, accurate CSPNe parallax measurements with 16 PNe (Harris et al., 2007). The Hubble space telescope can be used for astrometric purposes and the parallax for the PN, NGC 6853, was determined (Benedict et al., 2003). Benedict et al. (2009) went on to determine parallax distances for four more PNe with the HST but due to limited observing time is unlikely to provide a notable statistical sample (Harris et al., 2007). Parallaxes are accurate when the correct targets are selected with the right instrumentation but are very time intensive to derive. The small sample from the above surveys is from several

epochs spanning up to ten years. The launch and then wait for subsequent results from the ESA mission, GAIA, will allow for more accurate measurements of distant PNe but the local parallax sample will not significantly increase until then.

3.2.7 Expansion Parallax of the Nebula

Direct observations of the nebula expansion in different epochs can be used with the radial velocity (RV) of the nebula to determine a distance:

$$D = 211 \frac{V [\text{kms}^{-1}]}{\dot{\theta} [\text{mas/yr}]} \, [\text{pc}] \tag{3.19}$$

where V is the RV and $\dot{\theta}$ is the proper motion (Kwok, 2000). This is reliant upon significant expansion to have occurred between two epoch measurements. Optical observations for $\sim$15 PNe were done by Liller et al. (1966) and Liller & Liller (1968) comparing nebula proper motions at epochs $\sim$50 years apart. They find significant proper motion allowing the determination of accurate distances for four PNe. Hajian et al. (1993) and Hajian et al. (1995) use the Very Large Array (VLA) in New Mexico to determine proper motions at radio wavelengths. The higher signal to noise ratio and resolution means that the epoch difference can be significantly reduced and unlike the optical studies both observations are done with the same telescope and detectors decreasing the chance of calibration errors. With six year baselines the radio survey determined distances for five of the six PNe observed. The expansion method, particularly for radio observations, is reliable and in agreement with other distance measurements where they exist in the literature, however, one has to assume a constant velocity for a spherical nebula. Furthermore, the assumption that the proper motion velocity described by θ is identical to the RV may not stand. Marten & Schoenberner (1991) show that stellar winds are not constant which in turn will affect the RV measurements. The result is an RV measurement likely to be inconsistent with the proper motion of the outer rim. Even with these questionable assumptions the success in obtaining

expansion velocities with optical measurements is significantly less than 50%, although this fraction is increased for radio surveys.

3.2.8   Interstellar Reddening Distances

All Galactic objects have intrinsic colours and depending on the amount of material between the observer and the source, observed colours are affected by the ISM. This is due to the interstellar dust that absorbs the radiation having a larger cross section in the blue region of the optical spectrum and therefore making objects appear redder than they are intrinsically. Maps of the ISM are created in two ways, either by the direct detection of dust through IR surveys, or by semi-empirical studies of a large sample of stars with spectral classifications which have a known intrinsic colour. The most well known IR map of interstellar reddening is by Schlegel et al. (1998) and directly observes the reflected light using the Infrared Astronomical Satellite (IRAS) and the Cosmic Background Explorer (COBE) to produce a composite 100μm map. Removing all point sources gives a map of the Galactic dust structure with high column densities observed to have high 100μm flux. The IR maps are useful for objects outside of the galactic plane where all of the absorption along the line of sight has taken place but can not be used for nearby or Galactic plane objects. The Schlegel et al. (1998) IR extinction map is shown in Fig. 3.5. 3D maps were developed by using 2D maps and adding an absorption depth along a line of sight, essentially producing plots of distance against extinction. This was developed by Fitzgerald (1968) and Lucke (1978) who determine the extinction for a given region in the sky by taking all stars in that region and after spectral classification determining reddening of MS stars by comparing their observed and intrinsic colours. Once the Galaxy is fully mapped the distance to any object can be deduced assuming the reddening can be determined. Additionally, spectra can be used to measure the Na D equivalent widths to determine reddening (Napiwotzki & Schönberner, 1995). An example is shown in Fig. 3.6 for six PNe using the extinction maps of IPHAS created by Sale

et al. (2009) and applied in Giammanco et al. (2011). PN distances determined from extinction are used in conjuction with other methods rather than on their own. This is due to the large uncertainty involved in distinguishing the interstellar reddening, which is especially difficult for compact nebula where circumstellar reddening is non-negligible. However, CSPNe have a small range of colours in the red part of the optical spectrum and so a reasonable approximation of intrinsic photometry can be made. Unfortunately, the location of a PN within the Galaxy may mean that little information can be extracted if it lies within an extinction-distance plateau. This is particularly apparent when extending out of the Galactic plane or other dust free regions. For these reasons reddening distance estimates are used as checks rather than primary determinations.
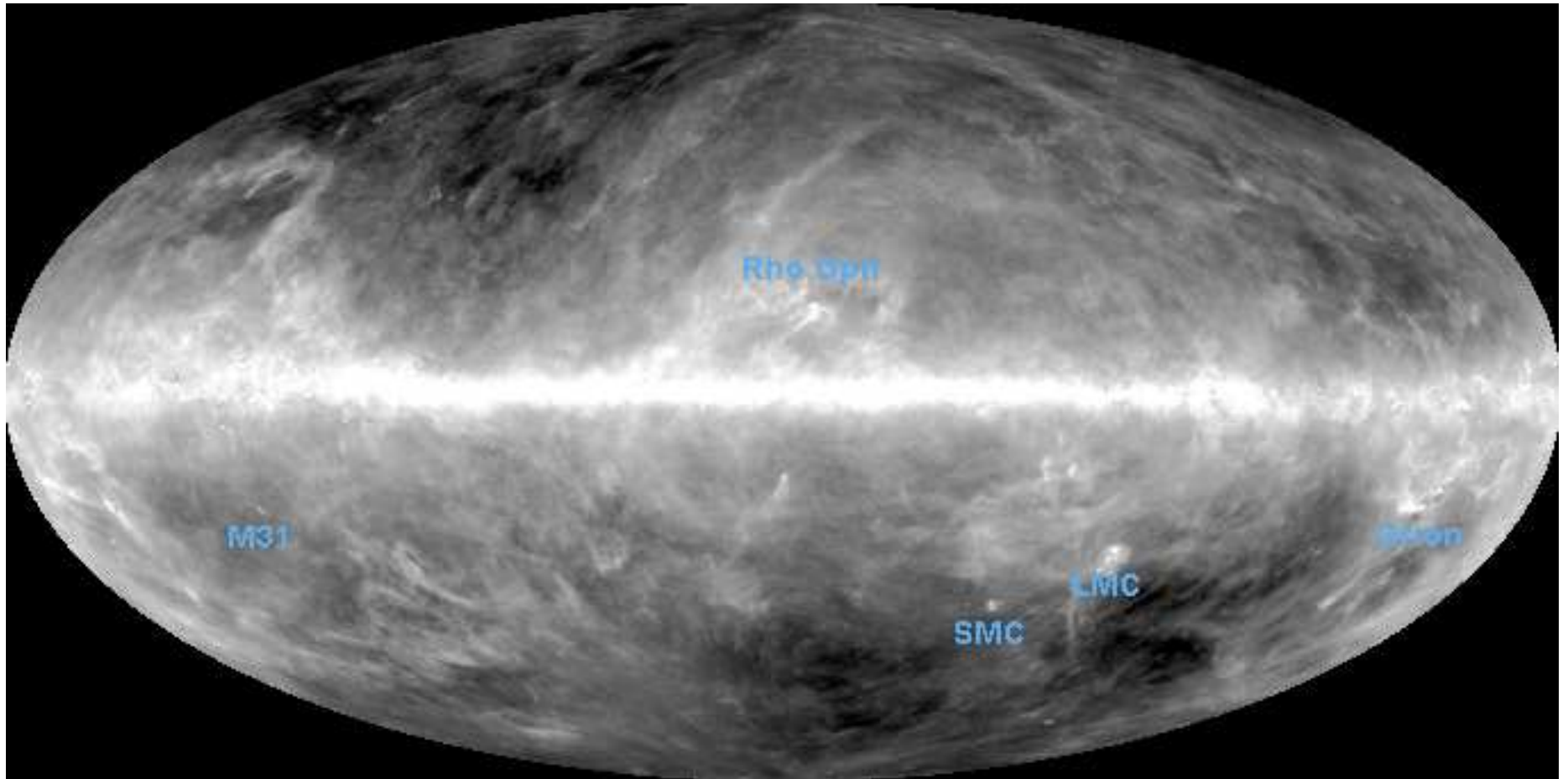
Figure 3.5: Extinction 100μm map from IRAS and COBE. Figure taken from IRSA (2011) based on the work of Schlegel et al. (1998).

3.3 PN Luminosity Functions and Extragalactic PNe

PN birthrates derived from local space densities are extrapolated to Galactic space densities to give a total Galactic PN estimate. Total numbers rely on the distribution to be constant for PNe throughout the Galaxy and population estimates are limited to local samples which are sensitive to the error-strewn distance determinations as well as containing a small statistical sample. In order to overcome the problems associated with Galactic PNe samples a study of other nearby galaxies has been carried out. PN luminosity functions (PNLFs) are a useful tool to compare extragalactic and local PNe populations. Jacoby (1980) derives a PNLF for the Magellanic Clouds using the brightest observable nebulae. The sample incompleteness is greatly reduced as the cutoff is easy to identify (as it is magnitude dependent and not distance) and problems with interstellar reddening are greatly reduced as both galaxies are face on and have a smaller line of sight absorption effect. The observed PNLF for the Small and Large Magellanic Clouds are similar and so are combined to give extra statistical weight. Jacoby (1980) compared the PNLF with that of a theoretical prediction and a sample of local Galactic optically thin nebula (see Fig. 3.7). The lack of Galactic PNe at the bright end was attributed to the sample being limited to optically thin PNe and the local population. With this correction and comparisons to other local group galaxies, Jacoby (1980) suggest using the same PNLF for all galaxies. This was tested for NGC 3377, NGC 3379 and NGC 3384, three different spectral type galaxies by Ciardullo et al. (1989) and they found similar PNLFs with the three galaxies a similar distance away. The PN abolute magnitude for a given initial mass star has a definite maximum brightness (Marigo et al., 2004). The $2.5M_\odot$ initial mass star has the brightest peak luminosity and can be used as a standard candle to
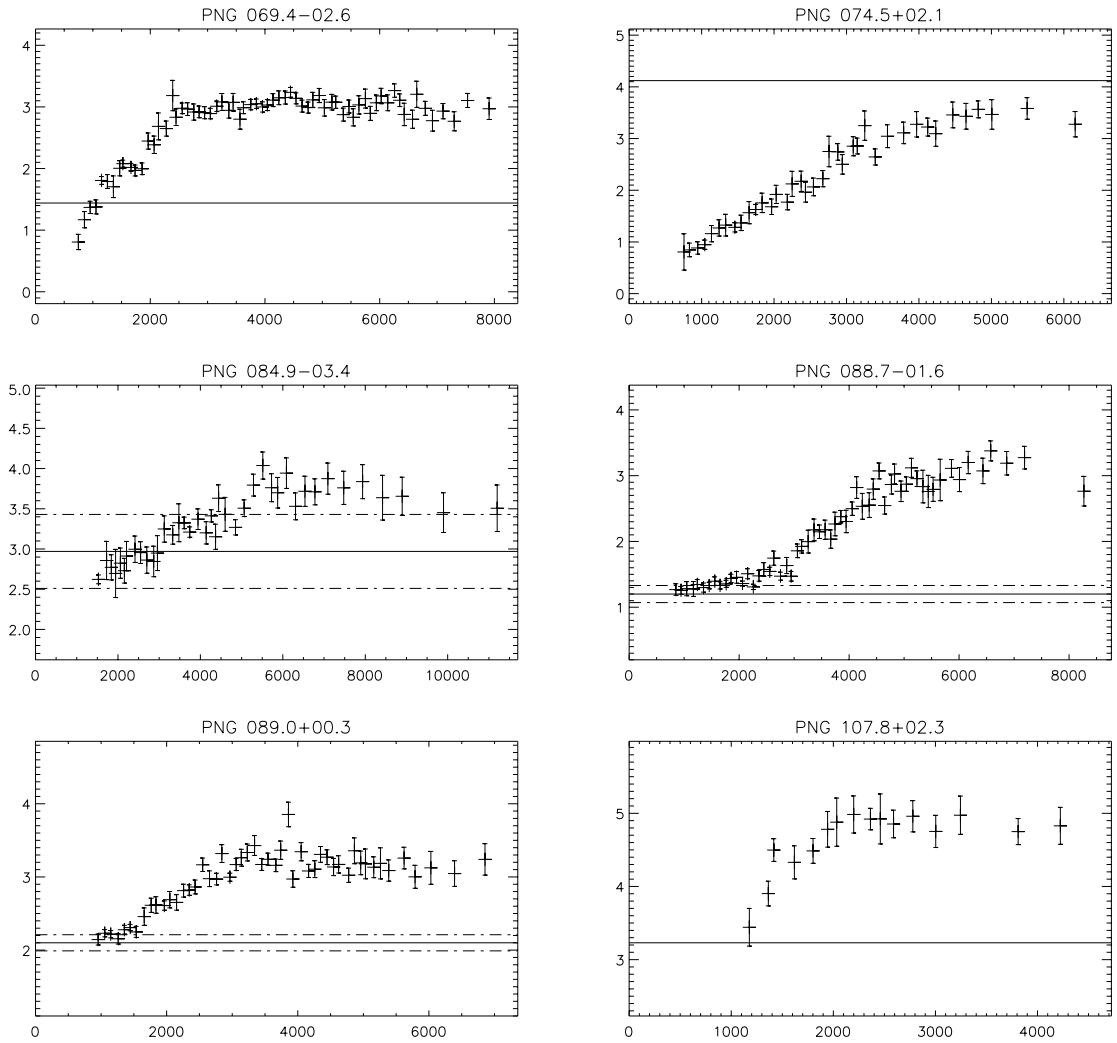
Figure 3.6: An extinction-distance plot of six PNe in IPHAS from Giammanco et al. (2011) using the algortithm developed by Sale et al. (2009). The x-axis is the distance in pc and the y-axis is A_V.

determine a PNLF using the relation:

$$N(m_{5007}) = e^{0.307m_{5007}}[1 - e^{3(m^* - m_{5007})}] \tag{3.20}$$

where $N(m_{5007})$ is the number of PNe for a given magnitude bin, m_{5007}, and a PN peak magnitude, m^*. For M31, the brightest observed PN is $m_{5007} = 20.17$, and the PNLF is displayed in Fig. 3.8. The PNLF is used for a complete sample to define a luminosity or mass specific PN density. The extrapolation to the whole galaxy is simply estimated using the total galaxy mass or luminosity. The Milky Way total PN population may be approximated by assuming M31's mass specific
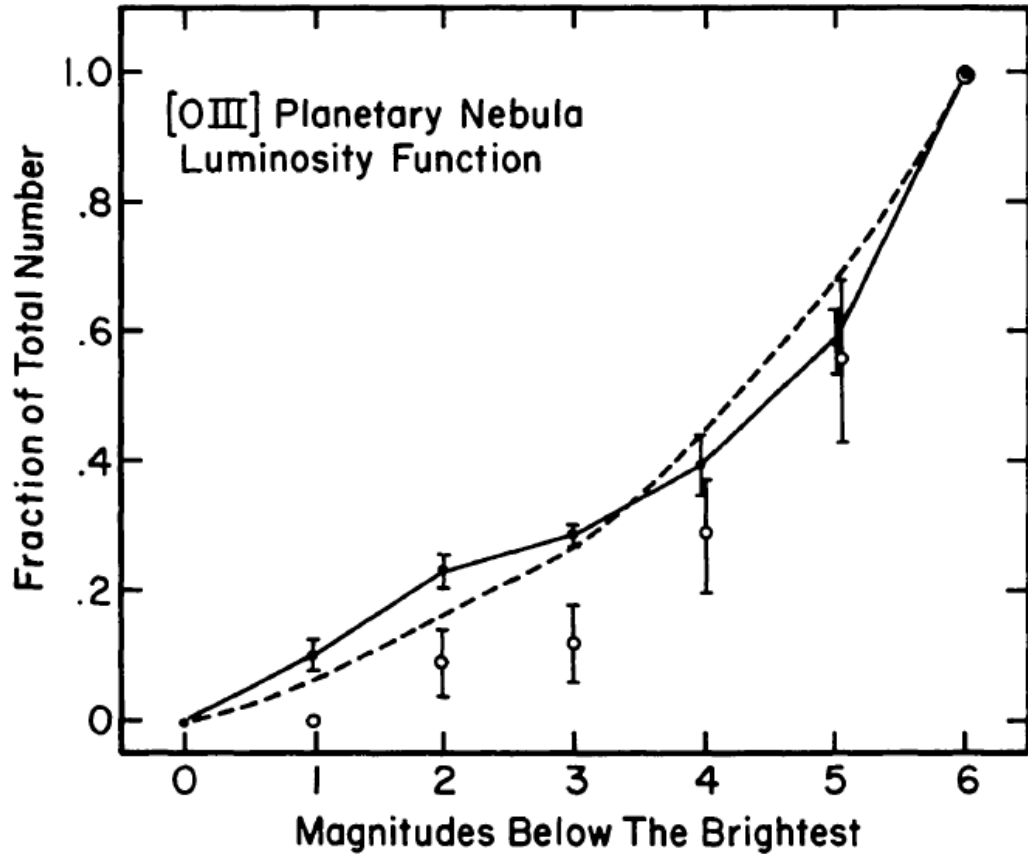
Figure 3.7: The [OIII] luminosity function for the Magellanic Clouds (solid lines). The dashed line is a theoretical PNLF. The open circles are optically thin Galactic PN. Figure taken from Jacoby (1980).

density and applying its own mass or by taking a mean value of the local group (Jacoby, 1980). The two methods give differing results and this is due to the different type of PNLF for a given galaxy type. Marigo et al. (2004) show the extreme example of a simulated PNLF for a large elliptical and a spiral (Fig. 3.9). Therefore, the type of galaxy is important when inferring a relationship and M31 which is similar to the Milky Way is a better comparison than the LMC and SMC which are irregular dwarfs. The study of PN numbers in other galaxies eliminates the matter of distances, but increases the issue of incompleteness. Complications, as well as the incompleteness, include the assumption of uniform distribution and the galaxy mass or luminosity assumptions.
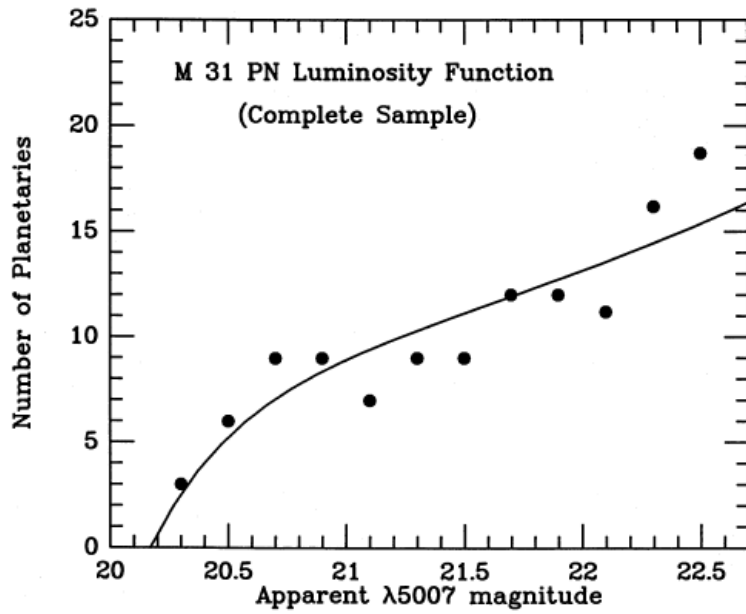
Figure 3.8: The PNLF of M31. The filled dots show a binned number of PNe with a theoretical fit based on Eq. 3.20. Figure taken from Ciardullo et al. (1989).
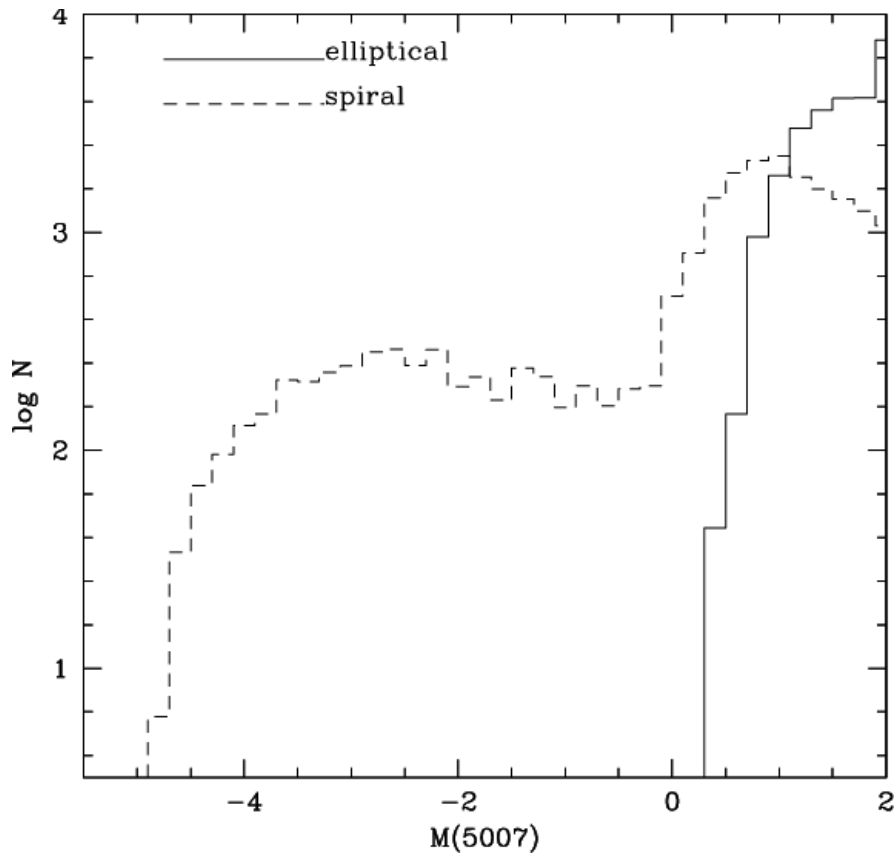
Figure 3.9: Two template PNLFs for a model elliptical (solid line) and a spiral galaxy (dashed line). Figure taken from Marigo et al. (2004).

3.4 Summary of Previous PN Birthrate Estimates

The differing methods of determining PN birthrates and total Galactic population have been applied by a number of different authors. A summary of PN and WD birthrates is listed in Table 3.1. All have been compared with the best known WD estimates at the time and nearly all exceed the WD number. Jacoby (1980) use extragalactic PN populations and scale to the Milky Way to make a magnitude limited complete sub-sample and correct for the brightness limit by using a local incomplete Galactic population. Although not directly comparable, the Galactic PN birthrate derived from the PNLF by Jacoby (1980) is the only birthrate in agreement with the WDs. This may be due to the removal of significant Galactic difficulties such as distance estimates and a non-biased local sample. The calculation does rely on assumptions like the Milky Way having a similar distribution to nearby similar galaxies and on non-observed low surface brightness nebulae. Direct observations of a more distant and complete local sample will test the low mass assumption. Galactic PN birthrate estimates that rely on statistical distances like Daub (1982) and Ishida & Weinberger (1987) use constant values of $\epsilon \sim 0.6$ and $M_i \sim 0.2 M_\odot$ and are thought to be underestimates based on the nebula mass assumption, paricularly for low surface brightness PNe. Ishida & Weinberger (1987) carried out a 'complete' sample of PNe using a limited volume (D$\leq$ 500pc) and a range of distance determination techniques. They compiled their catalogue of PNe from the literature and included over 1,000 PNe, however, only 31 made their complete sample. As mentioned earlier, statistical estimates have been shown to underestimate distances thus over predicting local samples and subsequently, Galatic estimates. A noticeable difference in the total predicted number of PNe is found by Daub (1982) and Ishida & Weinberger (1987), with respect to their birthrates. The difference stems from the distance cap of a complete sample and the knock on effects from this assumption. Noticeable differences

in the scale height and surface densities are seen for Ishida & Weinberger (1987) when compared to Daub (1982) and Zijlstra & Pottasch (1991) which give largely different total numbers. In order to remove such discrepancies Pottasch (1996) use a sample of known PNe, excluding distance estimates, made using statistical methods. The most prevalent method in their sample is determining the central star gravity spectroscopically and deriving a distance. Other methods used include parallaxes and spectroscopic distances to a resolved companion of a central star, however, both are limited by time and the rarity of these objects fulfilling such criteria. A final method used by Pottasch (1996) is distances via extinction. However, this is restricted to Galactic plane PNe and the 3D extinction plots have since been superseded. Their distances for individual PN were compared with multiple methods and the distances are in agreement, however, incompleteness can be seen from 600pc outwards (their Fig. 2). Pottasch (1996) correct for the various sources of incompleteness by limiting to a cylindrical volume with a radius of 700pc and a height of 320pc. Phillips (2002), using a cylinder region of 1kpc found a smaller birthrate deriving distances through calibrating the PN angular diameter and surface brightness. The calibrating nebulae were limited to a distance of $D \leq 0.7 \sec b$ [kpc] (where b is the Galactic latitude) and had well determined distances using non-statistical methods. Errors in this technique consist of the assumption of well-known calibration nebula and different angular diameters in different bands. Over a period of time, it is noticeable that PNe birthrate estimates have reduced the error and improved required assumptions but the WD/PNe contradiction still exists. The estimate of Pottasch (1996) suggests an accurate local sample with accurate distances but is at odds with the extragalactic approach of Jacoby (1980). Probing further into the Galactic plane and to the outer reaches of the halo will provide a direct test of the extrapolated projected populations.

Author(s)	Methods Used	χ $[10^{-12}\mathrm{yr}^{-1}\mathrm{pc}^{-3}]$	$\mathrm{N_{PN}}$
Jacoby (1980)	PNLF	0.4[a]	10,000
Daub (1982)	Statistical	5.0 ± 2.0	14,000
Ishida & Weinberger (1987)	Statistical	8.0	140,000
Zijlstra & Pottasch (1991)	Mixed	8.0	23,000[b]
Pottasch (1996)	Mixed	3.0	35,000
Phillips (2002)	Statistical	2.1	30,000
Moe & De Marco (2006)	Theoretical	1.1 ± 0.5	46,000
WD Birthrates			
Weidemann (1977)	Spectroscopic	2.0	–
Liebert et al. (2005)	Spectroscopic	1.0 ± 0.25	–

[a] Estimate made using PN per solar mass of $2.1 \times 10^{-7}\,\mathrm{PNe\,M_\odot}^{-1}$.
[b] Total number of Galactic **disc** PNe.

Table 3.1: A summary of PN birthrate estimates

3.5 Estimating Distances Using Central Stars for New Surveys

With only 13% of the known PNe having central star spectroscopic information (Weidmann & Gamen, 2011) and an even smaller fraction for the recently added ($\sim$1500) PNe found through Hα surveys, the central star has not been used to derive distance estimates to most PNe. With more telescopes and surveys at the community's disposal much of the sky has been observed photometrically at a broad range of wavelengths. The Galaxy Evolutionary Explorer (GALEX) is a 0.5m UV space telescope launched by NASA in 2003 and has been utilised to look for hot stars in the Milky Way in an all-sky survey (Morrissey et al., 2007). With two filters with central wavelengths of $FUV(1530\,\text{Å})$ and $NUV(2270\,\text{Å})$, GALEX is an ideal tool to locate hot point sources such as post-AGB stars, CSPNe and WDs. When used in conjunction with optical telescopes and surveys it is possible to classify individual sources with a degree of confidence without the need for spectroscopy, and atmospheric parameters may be determined. SDSS (York et al., 2000) is a 2.5m telescope in New Mexico dedicated to the survey of the north Galactic pole (NGP) with five optical and near-IR filters with central wavelengths of $u'(3540\,\text{Å})$, $g'(4750\,\text{Å})$, $r'(6220\,\text{Å})$, $i'(7630\,\text{Å})$ and $z'(9050\,\text{Å})$. GALEX

and SDSS are both deep surveys with limiting magnitudes observing out to the far reaches of the Milky Way which will detect central stars for known PNe, as well as potentially identifying bright CSPNe for low surface brightness nebulae yet to be observed. Cross matching SDSS and GALEX sources gives a large baseline of seven filters (21 colours) covering the UV, optical and near-IR allowing for the identification of a CSPN with the unique seven filter photometry within a nebula's field. The photometry can be used with evolutionary tracks to estimate distances, described in Sect. 5. IPHAS (Drew et al., 2005) may be used with GALEX in the same way as SDSS but in the Galactic plane. IPHAS uses the 2.5m telescope based on La Palma, to survey the Galactic plane in $H\alpha$ (6563 Å), and Sloan r' (6220 Å) and i' (7630 Å) bands to a depth of $r' < 20$. In order to determine colours for CSPNe, atmospheric models are required to make spectral energy distributions (SEDs) which in turn have the throughput of the survey filters folded on to them. The magnitudes must then be calibrated so that the theoretical atmospheric parameters are corrected to the observed. The calibration is key so that results are not erroneous and so a thorough process is essential described in Sect.4.

Chapter 4

Synthetic Photometry and Calibration

Synthetic model atmospheres are used to correlate the physics of a star to an observable photosphere. Spectroscopy is the best method to determine the parameters and evolutionary status for a given object, however, spectroscopic surveys take significantly longer to observe the same region of sky as their photometric counterparts and the object must be identified prior to the submission of a spectroscopic proposal. However, it is often possible to use a broad range of photometric filters to ascertain the nature of an astrophysical object and deduce parameters without the need for follow-up spectroscopy. The recent discovery of ~1500 previously unknown PNe in photometric surveys (Sabin et al., 2010) contains many older extended nebulae which are likely to have a resolved central star, which is not necessarily in the centre of such PNe due to interaction with the ISM. Furthermore, a considerable number of PNe have been found in high density environments (like the Galactic plane) and locating the CSPN can be non-trivial. Some CSPNe are the only blue object within a nebula's field and are easily identified, however, many central stars have similar photometric characteristics as other objects such as Galactic HB and extragalactic sources like quasar stellar objects (QSOs) and emission line galaxies. Multi-band photometry using colour-colour plots identifies

the CSPNe by their unique region in each plot. SDSS (York et al., 2000) and GALEX (Morrissey et al., 2007) are ideal for identifying candidate CSPNe as they observe a large region of sky surrounding the NGP in multiple bands and up to limiting magnitudes of $g' < 23$ for SDSS and $m_{AV} < 21$ for GALEX. The bands in these surveys cover the Balmer jump and lines which are sensitive to $\log g$ and the Rayleigh-Jeans tail, which represents a $T_{\rm eff}$ profile. A model SED for a $T_{\rm eff}$=10,000K, $\log g$=2.00, solar metallicity star is shown in Fig. 4.1 with GALEX and SDSS filter throughputs over plotted. To determine the colours of the CSPNe in the two systems for a given $T_{\rm eff}$-$\log g$, model atmospheres replicating the central star are required. The INT (Isaac Newton Telecope) Photometric Hα survey (IPHAS, Drew et al., 2005) provides high resolution covergae of the Galactic plane and can be used in conjunction with GALEX in a similar manner to SDSS. This chapter will describe the computation of synthetic photometry for parameters typical for post-AGB stars and CSPNe. The range of atmospheric parameters is displayed in $T_{\rm eff}$-$\log g$ space together with evolutionary tracks (Fig. 4.2). A grid of model atmospheres (and SEDs) are created for a range of effective temperatures and gravities and synthetic photometry is deduced by folding the SEDs with filter throughputs in the two systems. The model atmosphere and the filter throughput are theoretical determinations producing synthetic photometry which must be calibrated with a well studied set of standard stars. There are few known CSPNe or post-AGB stars in the Galactic halo and well studied objects of this kind are often saturated in deep field surveys like SDSS and GALEX. Therefore, calibrating a synthetic grid to observed data is non-trivial. WDs represent the evolved phase of post-AGB stars, have simple spectra and have dimmed sufficiently with age to be observed reliably in the aforementioned surveys. WDs are used initially to correct for any systematic offsets in the filters of the survey telescopes and also any additional scatter (on top of the quoted errors in the database). The small halo population of post-AGB stars with available photometry is used to confirm and refine the calibration.
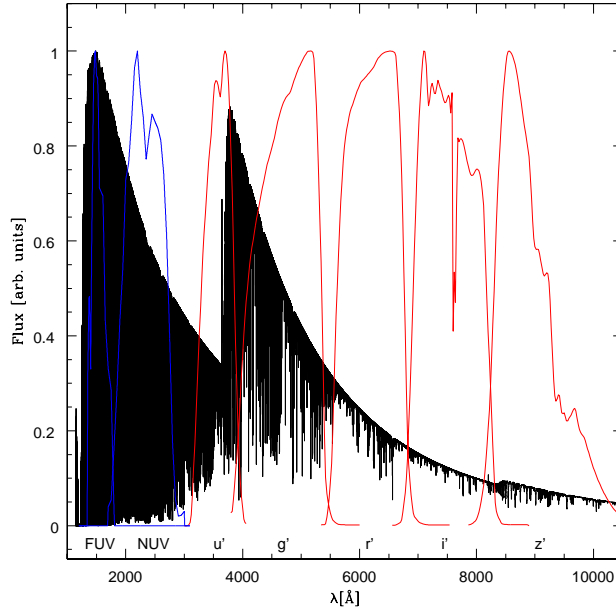
Figure 4.1: A T_{eff}=10,000K $\log g$=2.00 model spectrum with the labelled GALEX (blue) and SDSS (red) filters overplotted. The SED and filter throughputs are normalised to a flux of arbitrary units independent of each other.
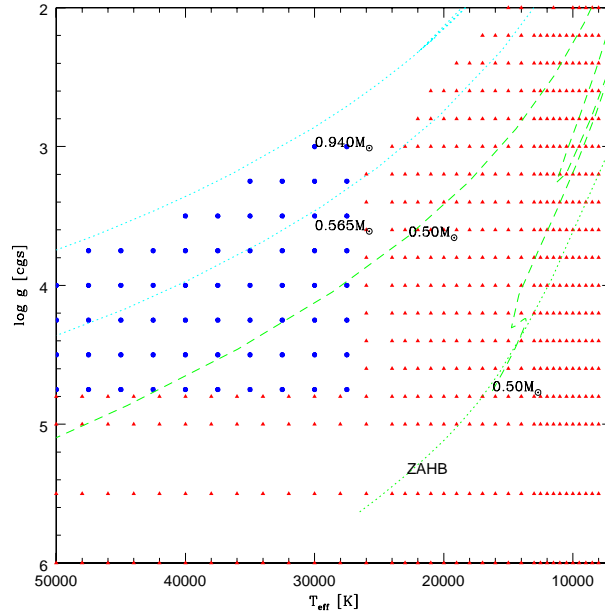
Figure 4.2: The model grid data points used for post-AGB stars. The blue dots are TLUSTY (Lanz & Hubeny, 2003) points and red triangles are ATLAS9 (Kurucz, 1991). The tracks indicate the expected parameter range of post-AGB/CSPNe (cyan, short dashed; Schönberner 1983,Blöcker 1995), post-EAGB (green, long dashed; Dorman 1992) and the zero-age HB (green, short dashed).

49

4.1 CSPN Model Atmospheres

CSPNe exhibit a range of atmospheric parameters and undergo a significant change in structure and photosphere appearance with a range of temperatures from $T_{\text{eff}} \sim 20,000$K when the nebula is first ionised, up to $T_{\text{eff}} \sim 200,000$K before descending the WD cooling track. The spectral types of CSPNe vary and can be classified in many ways. Mendez (1991) uses the simple broad criteria of H-rich, if H lines are detected, or H-poor with approximately four subcategories in each case depending on spectral features in emission or absorption. The most common H-rich subtypes are denoted hgO(H) (high-gravity) and O(H) and have spectra similar to WDs and massive young O-type stars, respectively. They are thought to evolve through standard single-star evolutionary paths. The H-poor CSPNe are mainly Wolf-Rayet type central stars. Although their origin is uncertain, they are thought to be the result of a late He flash and may be constrained to high mass nuclei. Weidmann & Gamen (2011) produced a catalogue containing more detailed classifications of 492 CSPNe. Both studies show a broad range of emission and absorption patterns found in the stars but both show a H-rich majority, most of which have classifications of O(H), B and hgO(H) type stars as well as pure hydrogen WDs (DAs). Furthermore, most emission or absorption features in the other H-rich spectral types are narrow and may not contribute significantly to a broadband magnitude. The majority of CSPNe are H-rich and so the focus is on these classes.

Three sets of model atmospheres are used to create a CSPN grid of synthetic photometry. They represent the three most common spectral types, O, B and DA WDs and are described in detail individually below.

1. Low T_{eff} CSPNe and post-AGB stars have similar spectral features and model atmospheres as B type MS stars. The assumption of local thermodynamic equilibrium (LTE) still holds and is applied to B type CSPNe. ATLAS9 (Kurucz, 1991) is a model atmosphere code which assumes local ther-

modynamic equilibrium (LTE), line blanketed, static, plane-parallel model atmospheres. The grid has a fixed solar metallicity and is created in this study for a range of T_{eff} ($8,000\text{K} \leq T_{\text{eff}} \leq 50,000\text{K}$) and $\log g$ ($2.00\,\text{cm}\,\text{s}^{-2} \leq \log g \leq 6.50\,\text{cm}\,\text{s}^{-2}$) of differing step sizes (Fig. 4.2). SEDs are produced using the linfor program from the Kiel/Bamberg group which assumes LTE for radiative transfer equations (Lemke, 1997). The SEDs spread a broad range of wavelengths from UV to near IR ($1150\,\text{Å}$-$12,000\,\text{Å}$).

2. O type CSPNe have higher T_{eff} and departures from LTE are observed. Low gravity models (in ATLAS9 and TLUSTY) close to the Eddington limit do not converge to solutions due to problems caused by high radiation pressure. O star models were computed with TLUSTY, a non-LTE, plane-parallel metal-line blanketed hydrostatic equilibrium model atmosphere program (Hubeny & Lanz, 1995). OSTAR2002 is a grid of SEDs derived from TLUSTY model atmospheres applying non-LTE radiative transfer (Lanz & Hubeny, 2003). TLUSTY is used for high temperatures as collisions no longer dominate because of the high radiation field. The effect of LTE versus non-LTE for sdB stars is summarised in Kudritzki (1976) and Napiwotzki (1997). For both sets of model grids only solar metallicity is considered for simplicity. The effect on broadband fluxes is minimal as displayed in Lanz & Hubeny (2003). The OSTAR2002 grid has effective temperatures, $27,500\text{K} \leq T_{\text{eff}} \leq 55,000\text{K}$ in steps of 2500K and gravities of, $3.0 \leq \log g \leq 4.75$ in 0.25dex steps (Fig 4.2). The SEDs span a broad range of wavelengths from the near-UV to the far-IR ($50\,\text{Å}$-$3,000,000\,\text{Å}$).

3. A grid of DA WD model atmospheres was provided by D. Koester (priv. comm.) and represent hot, high $\log g$ CSPNe which are found in fast evolving PNe. The WD model atmospheres were computed for a composition of pure H assuming static, plane-parallel stellar atmospheres in radiative, hydrostatic and LTE (Finley et al., 1997). The radiative transfer is han-

dled assuming LTE. The grid contains a T_{eff} range of $10{,}000\,\text{K} - 100{,}000\,\text{K}$ and $\log g = 7.00 - 9.00\,\text{cm}\,\text{s}^{-2}$ with varying temperature steps and fixed δ $\log g = 0.25$ steps for each temperature. The model spectra span across UV, optical and near IR wavelengths ($1150\,\text{Å}$-$10{,}000\,\text{Å}$).

The photometric properties of these stars can be determined with filters folded on top of the SEDs.

4.2   Grids of Synthetic Photometry for CSPNe

The SEDs created from the model atmospheres are combined with a filter through-put to determine a star's absolute magnitude. Converting from fluxes to magnitudes varies depending on the photometric system used and the filter itself. The systems are calibrated using either a standard star or a fixed zero-point. The Vega system assumes the magnitude for every filter is zero for Vega so that the flux corresponding to the flux of Vega is the zero-point. The AB system (Oke & Gunn, 1983) used for the SDSS photometric system use 3631 Jy (1 Jy = 1 Jansky $= 10^{-26}\,\text{W}\,\text{m}^{-2}\,\text{Hz}^{-1} = 10^{-23}\,\text{erg}\,\text{cm}^{-2}\,\text{s}^{-1}\,\text{Hz}^{-1}$) as the zero-point for every filter, removing any reliance on Vega. Once the synthetic magnitude is determined for a given filter, the system must be calibrated to standard stars observed in the same filters. The calibration removes any systematic errors introduced by either the model atmospheres, observed magnitudes or subsequent pipeline. A calibration is carried out for SDSS, IPHAS and GALEX using CALSPEC standards where applicable and an observed sample of DA WDs. CALSPEC is a compilation of high resolution spectra of standard stars used to calibrate the HST. Vega is included in the list which contains a significant number of WDs. DA WDs are used as they have very simple atmospheres with just a continuum and Balmer lines in absorption, which makes them ideal calibrators. The CALSPEC spectra consist of wavelength in Å and the observed fluxes in $\text{erg}\,\text{cm}^{-2}\,\text{s}^{-1}\,\text{Å}^{-1}$ which are converted to observed magnitudes. The surface fluxes of the WDs (H_λ) are converted to

absolute magnitudes on the Earth from a source at a distance of 10pc:

$$f_{\text{obs}}(\lambda) = \pi \left(\frac{R}{d}\right)^2 H_\lambda \tag{4.1}$$

where the radius (R) is determined using the known gravity of each object and the mass-radius relation of Fontaine et al. (2001).

4.2.1 Sloan Digital Sky Survey

The SDSS is a deep field survey aimed at the NGP ($b > 15°$) in five optical and near-IR bands (filters shown in Fig. 4.1). The saturation limit for each filter is $m_{\text{AB}} \sim 14$ with brightness limits of 22.3, 23.3, 23.1, 22.3, and 20.8 for the u', g', r', i' and z' filters, respectively. The Sloan system is defined by AB_ν magnitudes so that:

$$m_\nu = -2.5\log\left\{\frac{\int S_\nu f_\nu d[\log(\nu)]}{\int S_\nu d[\log(\nu)]} \Big/ 3631 \times 10^{-23}\right\} \tag{4.2}$$

where m_ν is the brightness in magnitudes, S_ν is the system response at an air mass of 1.3 for a point source and f_ν is the flux in $\text{erg}\,\text{cm}^{-2}\,\text{s}^{-1}\,\text{Hz}^{-1}$. The synthetic spectra are convolved with the SDSS photometric telescope (PT) filters to produce $u'g'r'i'z'$ magnitudes. The SDSS 0.5m PT is located next to the main survey telescope and is used as a calibrator for the bright CALSPEC WDs. The photometric system is comparable with Vega near 5480 Å only (where AB=Vega). Therefore, the brightness of Vega is non-zero for $u'g'r'i'z'$. In this study, three other observed HST CALSPEC standard WD spectra are used to finely adjust the calibration of the r' band. Subsequently, the r' band is used as a calibrator for the rest of the filters using the colour (i.e. $m - r'$) from a list of 175 WDs with well known atmospheric parameters taken from the WD database (McCook & Sion, 1999). The WDs contain additional statistical weight to the CALSPEC standards due to the larger dataset with offsets calculated using colours.

Table 4.1: SDSS magnitudes of HST CALSPEC Standards

Star	u'_{CAL}	g'_{CAL}	r'_{CAL}	i'_{CAL}	z'_{CAL}	File Name
Vega	0.926	−0.106	0.143	0.357	0.519	alpha_lyr_stis_003.fits
GD71	12.423	12.771	13.262	13.629	13.979	gd71_mod_005.fits
GD153	12.660	13.067	13.577	13.953	14.308	gd153_mod_004.fits
G191-B2B	10.989	11.467	12.007	12.394	12.753	g191b2b_mod_004.fits

Table 4.2: SDSS offsets using the primary WDs

Star	u'_{off}	g'_{off}	r'_{off}	i'_{off}	z'_{off}
GD71	0.015	−0.019	−0.020	−0.018	−0.007
GD153	0.040	−0.045	−0.004	−0.003	−0.001
G191-B2B	0.044	0.003	−0.000	−0.006	−0.013
Mean	0.033	−0.020	−0.008	−0.009	−0.007
σ_{Mean}	0.013	0.020	0.009	0.006	0.005

Primary Standard & WDs - Vega, GD71, GD153, G191-B2B

HST CALSPEC stars are ideal for calibrating filters as detailed UV, optical and IR spectrophotometry exists. Additionally, as they are observed with HST there is no contamination from the Earth's atmosphere. The observed Vega, GD71, GD153 and G191-B2B spectra are taken from the CALSPEC website (Bohlin, 2007). The SDSS magnitudes are computed by convolving the filter transmission with the spectra and are displayed in Table 4.1. Offsets are calculated by comparing the HST CALSPEC SDSS magnitudes with the observed SDSS measurements (i.e. $m'_{\text{off}} = m'_{\text{obs}} - m'_{\text{CAL}}$). The offsets are calculated from the actual observed SDSS magnitudes (taken from Holberg & Bergeron 2006, Table 9) and are given in Table 4.2.

Other WDs

A calibration of the SDSS filters can be carried out using WDs with well known T_{eff} and $\log g$. 175 WDs are observed in SDSS with well known T_{eff} and $\log g$ in the WD database (McCook & Sion, 1999), selected by Holberg & Bergeron (2006) with the caveat of having magnitudes $g' > 13.55$ and avoiding magnetic and binary WDs. Taking the u' band as an example, the synthetic absolute $M_{g'}$ and $M_{u'}$, along with

Table 4.3: SDSS colour offsets using the g' magnitude as the calibrating band for the secondary WDs

	u'_{off}	r'_{off}	i'_{off}	z'_{off}	Notes
Mean	0.071	-0.026	-0.056	-0.071	g' calibration, All 175 WDs
σ_{Mean}	0.111	0.093	0.148	0.187	g' calibration, All 175 WDs
Mean	0.053	-0.005	-0.021	-0.024	g' calibration, 1σ
σ_{Mean}	0.044	0.033	0.045	0.058	g' calibration, 1σ
Mean	0.054	-0.007	-0.027	-0.027	g' calibration, $T_{\mathrm{eff}}>15{,}000$K
σ_{Mean}	0.088	0.043	0.055	0.066	g' calibration, $T_{\mathrm{eff}}>15{,}000$K
Mean	0.046	-0.006	-0.026	-0.024	g' calibration, $T_{\mathrm{eff}}>15{,}000$K, 1σ
σ_{Mean}	0.036	0.021	0.028	0.031	g' calibration, $T_{\mathrm{eff}}>15{,}000$K, 1σ

Table 4.4: SDSS colour offsets using the r' magnitude as the calibrating band for the secondary WDs

	u'_{off}	g'_{off}	i'_{off}	z'_{off}	Notes
Mean	0.035	0.019	-0.010	-0.025	r' calibration, All 175 WDs
σ_{Mean}	0.189	0.093	0.068	0.101	r' calibration, All 175 WDs
Mean	0.058	0.005	-0.020	-0.021	r' calibration, 1σ
σ_{Mean}	0.055	0.033	0.024	0.036	r' calibration, 1σ
Mean	0.061	0.007	-0.020	-0.020	r' calibration, $T_{\mathrm{eff}}>15{,}000$K
σ_{Mean}	0.116	0.043	0.026	0.045	r' calibration, $T_{\mathrm{eff}}>15{,}000$K
Mean	0.055	0.006	-0.019	-0.019	r' calibration, $T_{\mathrm{eff}}>15{,}000$K, 1σ
σ_{Mean}	0.044	0.021	0.014	0.023	r' calibration, $T_{\mathrm{eff}}>15{,}000$K, 1σ

the observed g'_{obs} give a synthetic observed magnitude, $u'_{\mathrm{syn}} = g'_{\mathrm{obs}} - (M_{g'} - M_{u'})$. This is compared to the actual observed u' to find an offset (i.e. $u'_{\mathrm{off}} = u'_{\mathrm{obs}} - u'_{\mathrm{syn}}$). The offset and scatter in each band are shown in Table 4.3. This was repeated with r' replacing g' as the calibration band as an additional test, with the offset and scatter listed in Table 4.4. The g' and r' bands are used as the g' band is used in Holberg & Bergeron (2006) but the r' magnitude shows less offset and scatter in Table 4.2. A further check was carried out by filtering out the WDs with $T_{\mathrm{eff}}<15{,}000$K. This removes the model atmospheres of lower temperatures which may be affected by collision induced absorption (CIA, Tremblay & Bergeron 2008). For each check, the data points lying outside of the 1σ confidence limit are rejected and the offsets and scatter are determined from the cleaned data. The offsets are shown in Tables 4.3 and 4.4.

Table 4.5: Final SDSS offsets using the r' band calibration from the CALSPEC primary WDs and the colour offsets from the secondary WDs

	u'_{off}	g'_{off}	r'_{off}	i'_{off}	z'_{off}	Notes
Mean	0.047	-0.002	-0.008	-0.027	-0.027	r'_{off} from Table 4.2 + Table 4.4
σ_{Mean}	0.044	0.023	0.009	0.016	0.025	$\sqrt{\sigma_{r'}^2 + \sigma_{m'}^2}$

SDSS Offset Conclusion

The synthetic magnitudes of the CALSPEC standards are in general agreement with the value of Holberg & Bergeron (2006), within 0.01 magnitudes. The same WDs are used in both studies but different model grids are applied. Using either g' or r' as the calibrating band makes little difference and these offsets can be combined with the primary WDs but all yield the same result within 0.01 magnitudes. The r' band is used as the calibrating filter and the offsets for all filters are shown in Table 4.5. The plots of the corrected secondary WD offsets are shown in Figs. 4.3 and 4.4. The observed WD colours are shown again with the corresponding model grid in Fig. 4.5. The u' band has a relatively larger offset in both investigations thought to be caused by detector sensitivity issues at smaller wavelengths. The colour calibration with the 175 secondary WDs is likely to be more accurate for the finer calibration due to its larger sample and therefore statistical weight. The bluer colours show some scatter but most WDs sit on the model grid where expected. The photometric errors in the redder colours show that in most cases they are as large as the model grid itself. Therefore, the red colours can only be used as confirmation of the WD classification. The scatter is significant, particularly for u' and z' and must be considered in addition to the stated observational errors in the database. The correction applied to the
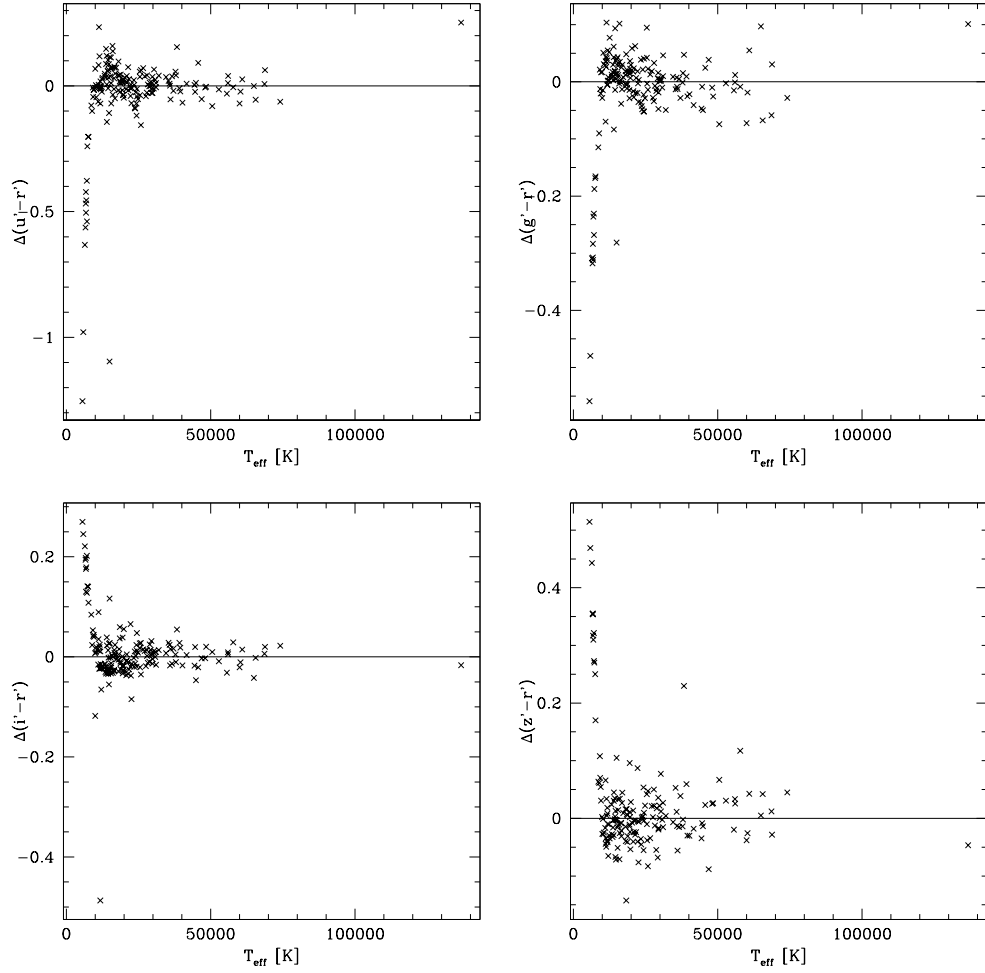
Figure 4.3: The SDSS offsets of the 175 Secondary WDs in each magnitude plotted against temperature. The large offsets for the low $T_{\rm eff}$ WDs could be due to bad observations or poor $T_{\rm eff}$ determinations but do not affect the final offset as they are removed as 1σ outliers.

synthetic magnitudes with scatter are:

$$u'_{\rm obs} = u' + 0.047 \pm 0.040 \tag{4.3}$$

$$g'_{\rm obs} = g' - 0.002 \pm 0.023 \tag{4.4}$$

$$r'_{\rm obs} = r' - 0.008 \pm 0.009 \tag{4.5}$$

$$i'_{\rm obs} = i' - 0.027 \pm 0.016 \tag{4.6}$$

$$z'_{\rm obs} = z' - 0.027 \pm 0.025 \tag{4.7}$$
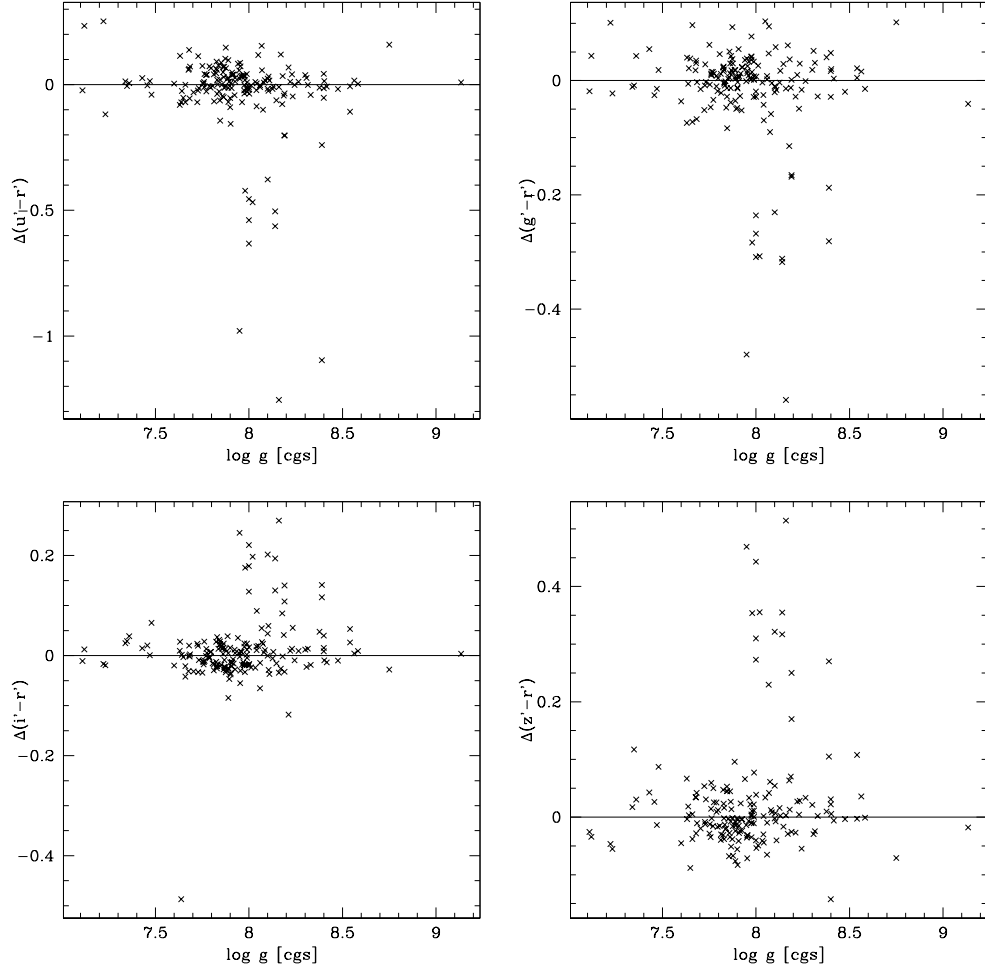
Figure 4.4: The SDSS offsets of the 175 Secondary WDs in each magnitude plotted against gravity. The large offsets are due to the low T_{eff} WDs (see Fig. 4.3) and are removed as 1σ outliers.
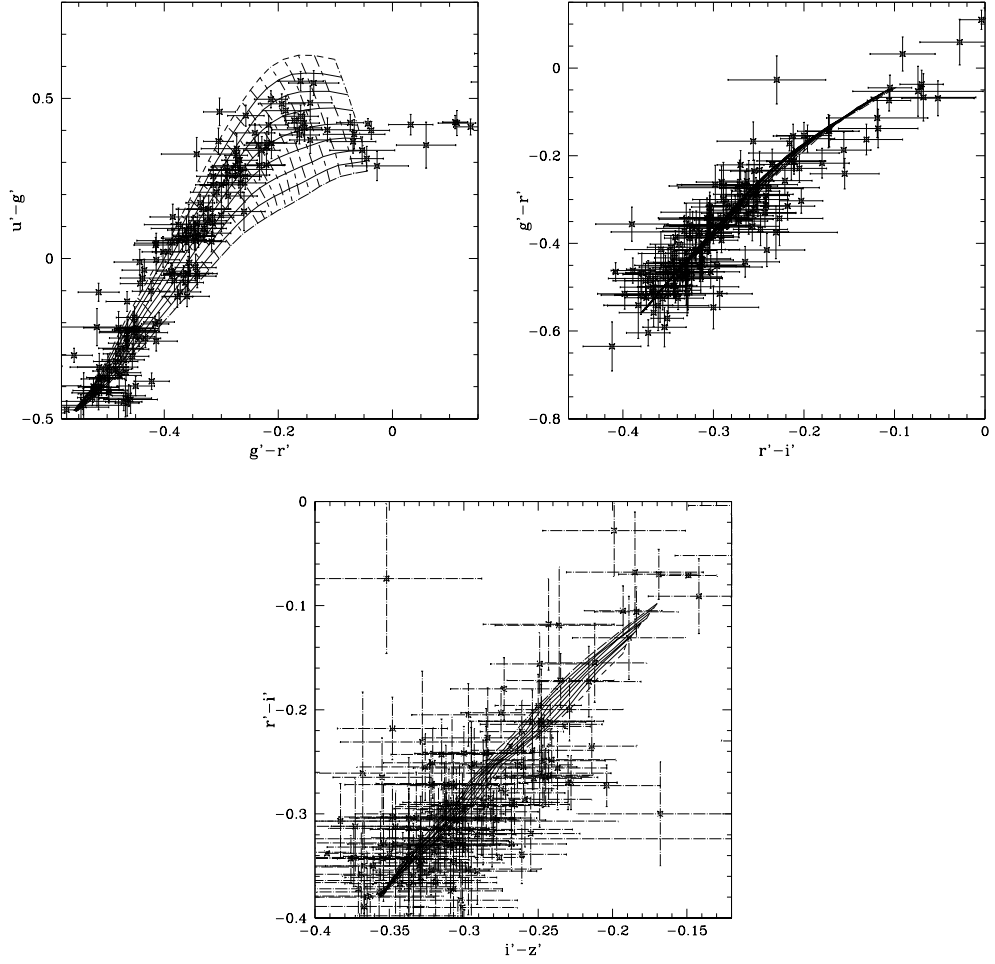
Figure 4.5: The colour-colour plots of Secondary WDs with the model grid. The crosses are observational errors taken from the SDSS database. The solid lines are colours of constant $\log g$ and the long dash, short dash are colours of constant T_{eff}. The T_{eff} ranges from left to right from 10,000K to 100,000K. The $\log g$ ranges from $7.00\mathrm{cm\,s}^{-2}$ to $9.00\mathrm{cm\,s}^{-2}$ from top to bottom.

4.2.2 IPHAS

IPHAS (Drew et al., 2005) is a northern Galactic plane survey of the Milky Way in Hα, and Sloan r' and i' bands (Fig. 4.6). Each filter has an approximate brightness range of $13 < m < 20$ and the survey covers a latitude range of $|b| < 5°$. Many previously unknown PNe obscured within the plane have been discovered using IPHAS and have added considerably to the previously known Galactic sample (Viironen et al., 2006). A disadvantage of the three filters when searching for CSPNe is that there is little information in the continuum dominated $r' - i'$ colour and so bluer optical magnitudes are needed especially where there are no observations in GALEX. The UV excess survey (UVEX, Groot et al., 2009) using the INT covers the same area in U, g' and r', however, the survey is far from complete and so UVEX filters are not calibrated here. IPHAS magnitudes are in the Vega system, however, Vega is too bright to be observed in IPHAS, although, the synthetic Vega magnitudes are used here to convert from AB magnitudes. Eight other CALSPEC standards are observed and will be the primary calibrators. A colour check is performed using WDs observed in IPHAS from the supernova type Ia progenitor survey (SPY; Napiwotzki et al., 2001).

Calibration with Primary Standard & WDs - Vega, Feige110, Feige34, G191B2B, GD50, EGGR 102, HZ21, HZ4, LTT9491

Similarly to the SDSS r' band calibration (described in Sec. 4.2.1), all three IPHAS magnitudes were calibrated using eight CALSPEC standards observed in IPHAS plus Vega. Convolving the CALSPEC Vega spectrum with IPHAS filters gives the r', i' and Hα magnitudes in Table 4.6. This is comparable to the Vega AB magnitude quoted by González-Solares et al. (2008) which is determined numerically. The synthetic observed AB r' magnitude for each WD is calibrated with an observed magnitude from multiple observations. The magnitude and offsets are given in Table 4.7. The observed magnitudes are reduced in number to include only good observations. Bad data is filtered out due to photometric conditions
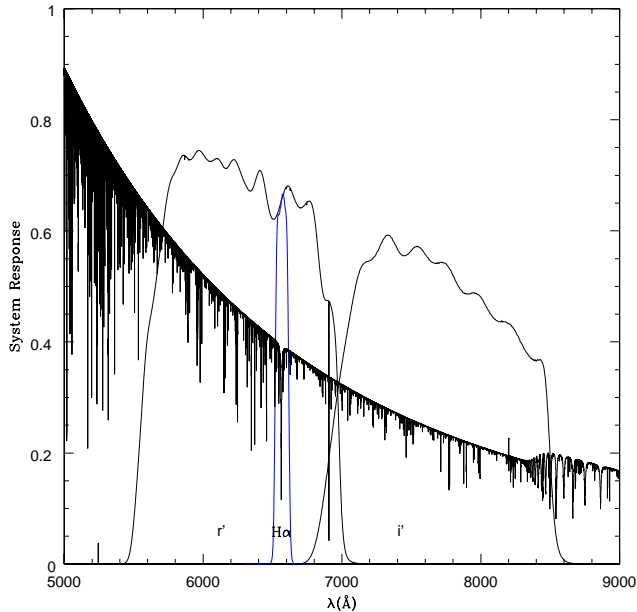
Figure 4.6: A T_{eff}=10,000K $\log g$=2.00 model spectra with the IPHAS filters over-plotted. The SED and filter throughputs are normalised to a flux of arbitrary units independent of each other.

Table 4.6: IPHAS AB magnitudes of HST CALSPEC Vega

Star	r'	i'	Hα	File Name
Vega	0.151	0.383	0.360	alpha_lyr_stis_003.fits

for the night, saturation and 1σ outliers. The good observations are averaged to determine a photometric observed magnitude for each WD and an offset is taken from the average of the eight WD offsets. An offset is also determined using the offsets of the 104 observations of the eight standards giving an equal weighting to each point and then by removing the 1σ outliers. A scatter was calculated for all observations and the cleaned sample of the CALSPEC standards.

Calibration with WDs in SPY

A selection of WDs was required to calibrate the IPHAS colours in a similar process to SDSS (Sect. 4.2.1). A compilation of WDs with reliable T_{eff} and $\log g$ determined by high resolution spectra in IPHAS's field was carried out by SPY (Napiwotzki et al., 2001). SPY is a RV survey searching for double degenerate systems which exceed the Chandrasekhar limit and will merge in a Hubble time.

Table 4.7: IPHAS AB magnitudes of HST CALSPEC WDs

Star	r'_{obs} [a]	r'_{CAL}	i'_{obs} [a]	i'_{CAL}	$H\alpha_{\mathrm{obs}}$ [a]	$H\alpha_{\mathrm{CAL}}$
Feige110	11.935	11.923	12.096	12.073	12.024	11.898
Feige34	11.270	11.253	11.430	11.398	11.393	11.191
G191B2B	11.899	11.873	12.070	12.053	11.993	11.829
GD50	14.168	14.162	14.335	14.309	14.253	14.207
EGGR 102	12.852	12.816	12.964	12.924	13.122	12.926
HZ21	14.802	14.765	14.947	14.940	14.847	14.725
HZ4	14.561	14.535	14.600	14.586	14.903	14.744
LTT9491	14.060	14.029	13.992	13.975	14.063	13.898
Offset average 8 WDs	0.022		0.030		0.147	
Scatter 8 WDs	±0.011		±0.010		±0.047	
Offset average all	0.021		0.023		0.137	
Scatter all	±0.032		±0.0447		±0.114	
Offset 1σ cleaned	0.020		0.023		0.135	
Scatter 1σ cleaned	±0.055		±0.063		±0.095	

[a] Observed magnitudes are an average over a number of observations.

SPY observes optical spectra, and T_{eff} and $\log g$ can be obtained using the Balmer line fitting method (Koester et al., 2001). Eleven WDs with well defined parameters in SPY have been observed in IPHAS. The offsets from the CALSPEC WDs are applied and then checked using the r' band as the calibration filter. They are used with the known T_{eff} and $\log g$ to create synthetic $M_{r'}-M_{i'}$ and $M_{r'}-M_{H\alpha}$ to find an $r'-i'$ and $r'-H\alpha$ offset. The results are summarised in Table 4.8. Even with the low number of WDs observed in both SPY and IPHAS and the effects of reddening not being accounted for, the scatter in the both colours is surprisingly low. Furthermore, the results are in agreement with the CALSPEC standards for the r' and i' bands. The $H\alpha$ offset is not consistent and may be due to the sensitivity to the determined $\log g$. For that reason the CALSPEC offsets are used to correct the synthetic photometry.

IPHAS Offset Conclusion

The Vega to AB magnitude conversion and calibration is best using the CALSPEC WDs. Although the SPY WDs are in agreement with the CALSPEC WDs for $r'-i'$ the $H\alpha$ measurements are inconsistent, therefore, the SPY offsets are not used.

Table 4.8: IPHAS WDs in SPY

Star	T_{eff}	$\log g$	r'	i'	Hα	$(r'-i')_{\text{off}}$	$(r'-\text{H}\alpha)_{\text{off}}$
WD0556+172	18090	8.15	15.879	15.980	16.029	-0.009	0.118
WD0558+165	16040	8.20	15.764	15.821	15.947	0.016	0.114
WD0612+177	25269	7.86	13.461	13.609	13.535	-0.007	0.128
WD1840+042	8960	8.33	14.714	14.584	14.699	-0.000	0.129
WD1845+019	29806	7.83	12.915	13.088	13.081	-0.013	0.006
WD1857+119	9800	8.04	15.518	15.430	15.582	0.006	0.143
WD1911+135	13393	7.85	14.287	14.287	14.249	0.040	0.342
WD1914+094	33086	7.85	15.544	15.769	15.569	-0.058	0.122
WD1918+110	19045	7.84	16.210	16.325	16.309	-0.013	0.139
WD1919+145	14550	8.04	13.036	13.113	13.563	-0.020	-0.222
WD1943+163	19272	7.84	14.171	14.238	14.277	0.036	0.130
Mean offset						-0.002	0.114
Scatter						±0.026	±0.039

As with SDSS the scatter must not be ignored and it is high due to the ongoing calibration for IPHAS. The calculated scatter is likely to be over cautious and caused by some bad observations which are not flagged. The following corrections are applied to IPHAS synthetic magnitudes:

$$r'_{\text{obs}} = r' - 0.151 + 0.020 \pm 0.055 \tag{4.8}$$

$$i'_{\text{obs}} = i' - 0.383 + 0.023 \pm 0.063 \tag{4.9}$$

$$\text{H}\alpha_{\text{obs}} = \text{H}\alpha - 0.360 + 0.135 \pm 0.095 \tag{4.10}$$

4.2.3 GALEX

GALEX is a space-based UV telescope with two imaging bands, NUV ($\lambda_{\text{eff}} = 1528$Å) and FUV ($\lambda_{\text{eff}} = 2271$Å) (Morrissey et al., 2007). The primary goal of GALEX is an all sky survey in the UV with limiting magnitudes of 19.9 and 20.8 for FUV and NUV, respectively. The filters provide a large photometric base line when combined with optical magnitudes which is useful for detecting hot stars and determining temperatures (Fig. 4.1). GALEX uses AB magnitudes like Sloan

Table 4.9: GALEX offsets using CALSPEC standards

Star	FUV_{obs}	FUV_{CAL}	FUV_{off}	NUV_{obs}	NUV_{CAL}	NUV_{off}
Vega	–	2.141	–	–	1.671	–
HZ4	14.59	14.47	+0.12	14.57	14.51	+0.06
LDS749B	15.65	15.60	+0.05	14.72	14.76	−0.04
LTT9491	16.14	16.12	+0.02	14.64	14.61	+0.03
Mean offset		0.06±0.04				0.02±0.04

but in wavelength space:

$$FUV_\nu = -2.5\log\left\{\frac{\int S_\nu f_\nu d[\log(\nu)]}{\int S_\nu d[\log(\nu)]}\bigg/ 1.40 \times 10^{-15}\right\} + 18.82 \qquad (4.11)$$

$$NUV_\nu = -2.5\log\left\{\frac{\int S_\nu f_\nu d[\log(\nu)]}{\int S_\nu d[\log(\nu)]}\bigg/ 2.06 \times 10^{-16}\right\} + 20.08 \qquad (4.12)$$

The photometric offsets are determined using CALSPEC standards and the WDs from SDSS where they are observed in GALEX.

Primary Star & WDs - Vega, HZ4, LDS749B, LTT9491

GALEX has observed 17 of the CALSPEC standard stars (Morrissey et al., 2007) and so a similar calibration as Vega and the three WDs in SDSS (see Sect. 4.2.1) can be done. However, eleven of the sample are saturated and have unreliable photometry and three others only have near-UV data and are not WDs. This leaves HZ4, LDS749B and LTT9491 which are all close to or dimmer than the suggested bright magnitude limit ($m_{AB} \sim 15$) from Morrissey et al. (2007). The Vega synthetic magnitude and the individual and average offsets are given in Table 4.9.

GALEX offsets with WDs in Sloan

The secondary WDs used with the Sloan calibration are applied to calibrate GALEX colours with the Sloan r' band for the 131 Sloan WDs observed with GALEX. The strong impact of CIA on the UV flux and uncertain modelling of this in the model atmospheres leads to a minimum temperature limit of 15,000K.

Table 4.10: GALEX offsets using the secondary WDs

	FUV_off	NUV_off	Notes
Mean	0.150	0.043	r' calibration, All 131 WDs
σ_Mean	0.310	0.145	r' calibration, All 131 WDs
Mean	0.120	0.037	r' calibration, 1σ
σ_Mean	0.130	0.063	r' calibration, 1σ
Mean	0.138	0.065	r' calibration, $T_\mathrm{eff}>15,000$K
σ_Mean	0.161	0.137	r' calibration, $T_\mathrm{eff}>15,000$K
Mean	0.123	0.052	r' calibration, $T_\mathrm{eff}>15,000$K, 1σ
σ_Mean	0.071	0.055	r' calibration, $T_\mathrm{eff}>15,000$K, 1σ
Mean	0.080	0.002	r' calibration, $T_\mathrm{eff}>15,000$K, m>15
σ_Mean	0.158	0.110	r' calibration, $T_\mathrm{eff}>15,000$K, m>15
Mean	0.080	0.006	r' calibration, $T_\mathrm{eff}>15,000$K, 1σ, m>15
σ_Mean	0.077	0.045	r' calibration, $T_\mathrm{eff}>15,000$K, 1σ, m>15

Finally, the detectors are known to saturate at $m \sim 15$ for both bands so a brightness limit was applied. As with the SDSS calibration described earlier, a synthetic observed magnitude is determined using, $FUV_\mathrm{syn} = r'_\mathrm{obs} - (M_{r'} - M_{FUV})$. This is compared to the actual observed FUV to find an offset (i.e. $FUV_\mathrm{off} = FUV_\mathrm{obs} - FUV_\mathrm{syn}$). The derived average offset and scatter are used to remove 1σ outliers. The remaining 40 WDs are used to determine a more accurate offset and are summarised in Table 4.10.

GALEX Offset Conclusion

The offsets from the primary WDs can be used, however, with the well determined r' magnitudes from Sloan, the secondary WDs give more statistical weight and should improve the calibration. The colour offset is applied to the corresponding magnitude and the scatter is noticeably larger than the error quoted in the GALEX database. The large scatter for the FUV filter is not unexpected as it suffered from calibration issues before being shut down. The correction applied to the synthetic photometry is:

$$\mathrm{NUV}_\mathrm{obs} = \mathrm{NUV} + 0.006 \pm 0.045 \tag{4.13}$$

$$\mathrm{FUV}_\mathrm{obs} = \mathrm{FUV} + 0.080 \pm 0.077 \tag{4.14}$$

and the offsets are shown in Figs. 4.7 and 4.8. The GALEX and SDSS observed WD colours are shown with the model grid in Fig. 4.9. The colours show that although GALEX is sensitive to temperatures and $\log g$ between 10,000K and 15,000K, for hotter temperatures the UV observed errors are as large as the grid and the sensitivity to $\log g$ is lost. Therefore, GALEX colours can only be used as a T_{eff} determination and confirmatory observations for WDs.

4.2.4 Colour-Colour plots of CSPNe

The filter calibrations enable a direct comparison with observed magnitudes from SDSS, IPHAS and GALEX to the synthetic photometry model grids. Colour-colour plots have been produced with a combination of the aforementioned sytems and bands to establish a unique region to locate CSPNe. By defining a colour-colour region which surrounds the model grids a central star can be located within its nebula's field. The regions can be shifted accordingly for reddening and so can be used in regions with strong extinction. Atmospheric parameters may be determined using the grids depending on the band observed and the quality of the photometry. The SDSS plots (Figs. 4.10- 4.12) display some temperature sensitivity but highlight the lack of $\log g$ sensitivity with optical photometry. Fig. 4.13 shows that when optical photometry is combined with UV, T_{eff} and $\log g$ can be determined for CSPNe. GALEX UV photometry may be combined with IPHAS bands but $r' - i'$ is not sensitive to T_{eff} or $\log g$ so a colour must be defined using both systems (Fig. 4.14). The colour-colour plots give a region of colour space where CSPNe reside, and imply that atmospheric parameters may be deduced with accurate photometry. The calibration must be confirmed for non-WD CSPNe.

Figure 4.7: The GALEX offset from the 40 secondary WDs with $m > 15$ and $T_{\text{eff}} > 15,000$K in FUV and NUV with respect to r' plotted against temperature.
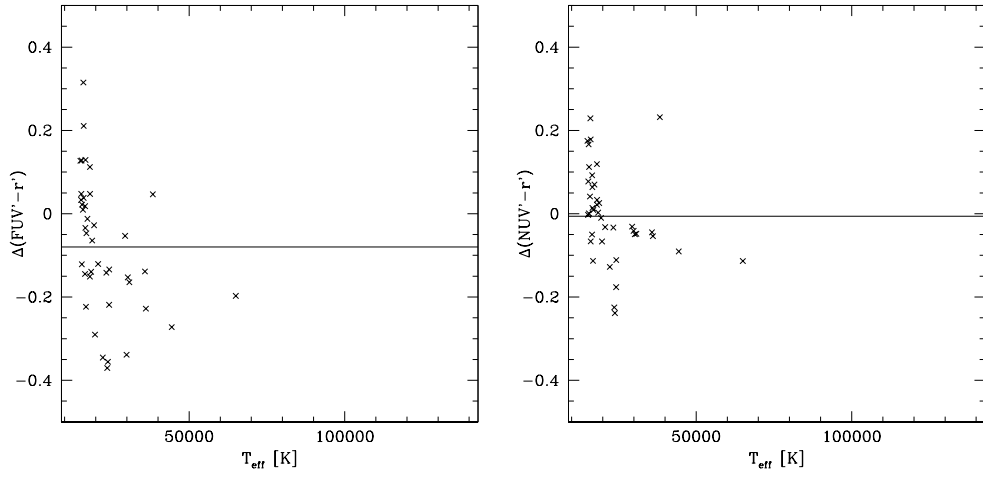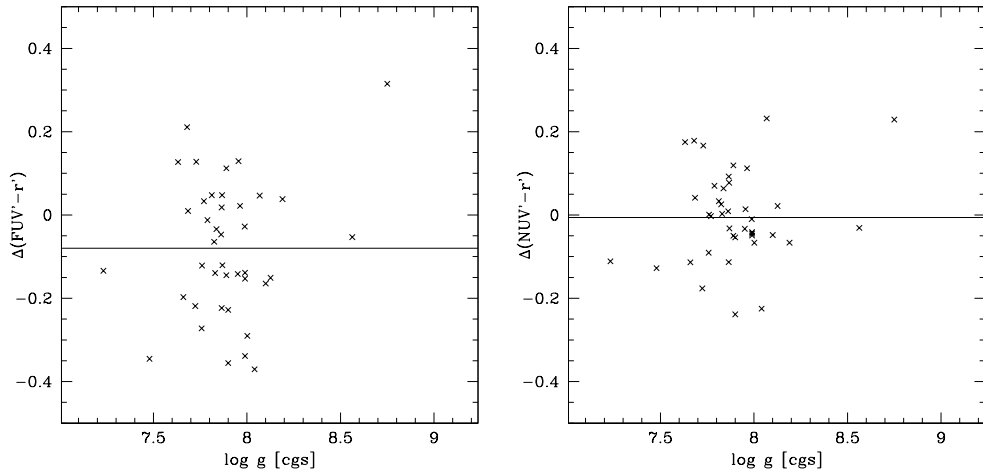

Figure 4.8: The GALEX offset from the 40 secondary WDs with $m > 15$ and $T_{\text{eff}} > 15,000$K in FUV and NUV with respect to r' plotted against gravity.
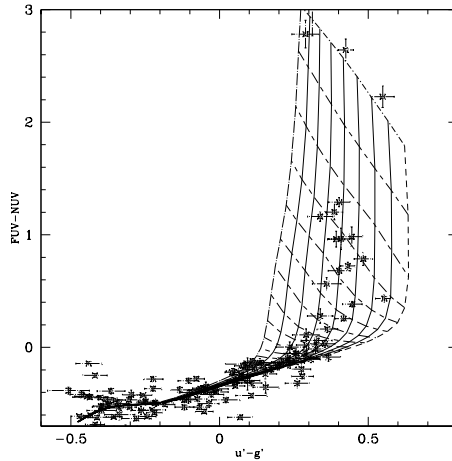
Figure 4.9: The secondary WDs in GALEX and SDSS colour-colour space. The crosses show the photometric errors quoted in the SDSS and GALEX databases, respectively.

4.3 Calibration Confirmation

The calibrations of SDSS, IPHAS and GALEX use WDs as the model atmospheres are relatively simple and so the offsets are mainly correcting the filter throughputs. These can be directly applied to WD central stars found in old PNe, but the calibration must be confirmed for central stars with other spectral types like O and B stars. CSPNe and post-AGBs have significantly lower space densities then WDs and so the nearest objects are more distant and in the case of the Galactic plane suffer from interstellar reddening. Therefore, objects perpendicular to the plane are best used. However, only a few CSPNe or post-AGB stars with known parameters are faint enough not to saturate SDSS filters. The study of Saffer et al. (1997) identify ten possible post-AGB candidates at high Galactic latitudes and eight of these objects are observed in SDSS. Three of these objects have magnitudes ($m < 14$) in at least one filter and are saturated. The five remaining objects PG1208+224, PG1314+442, PG1332+281, PG1356+242 and PG2120+062 have their spectroscopically determined T_{eff}, $\log g$ and observed magnitudes summarised in Table 4.11. Additionally, four of the five objects have GALEX magnitudes. The observed SDSS magnitudes are de-reddened applying the interstellar reddening maps of Schlegel et al. (1998), whereas the FUV−NUV
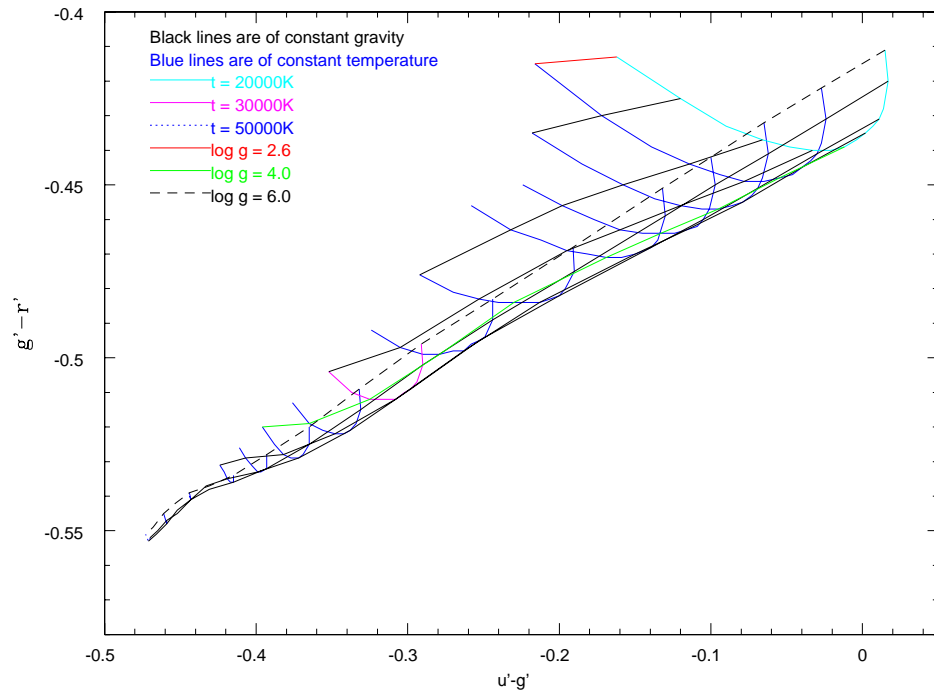
Figure 4.10: CSPN model grid in a SDSS, $u' - g'/g' - r'$, colour-colour plot.

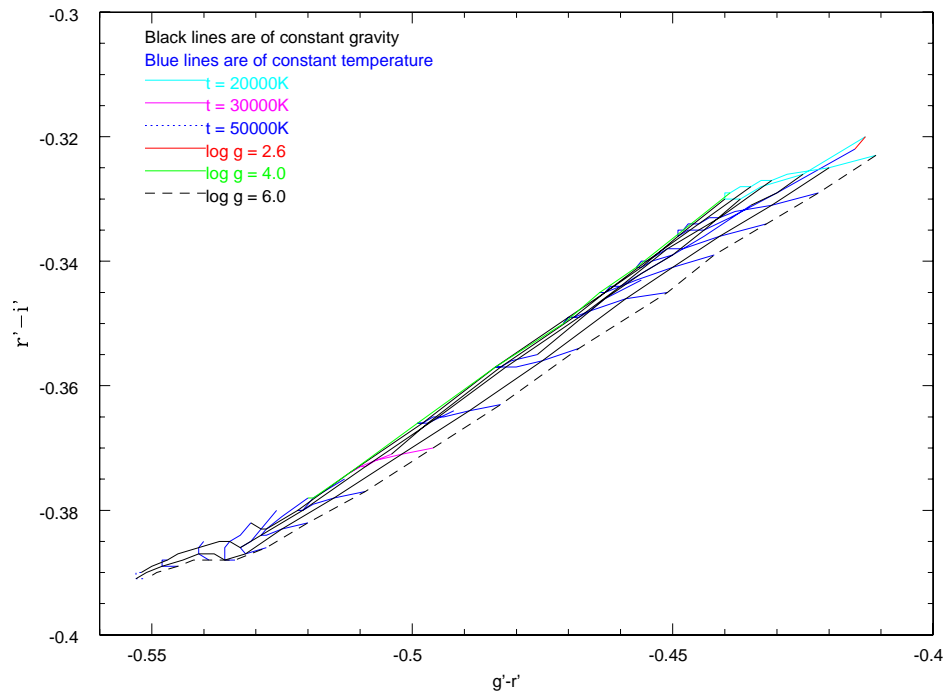
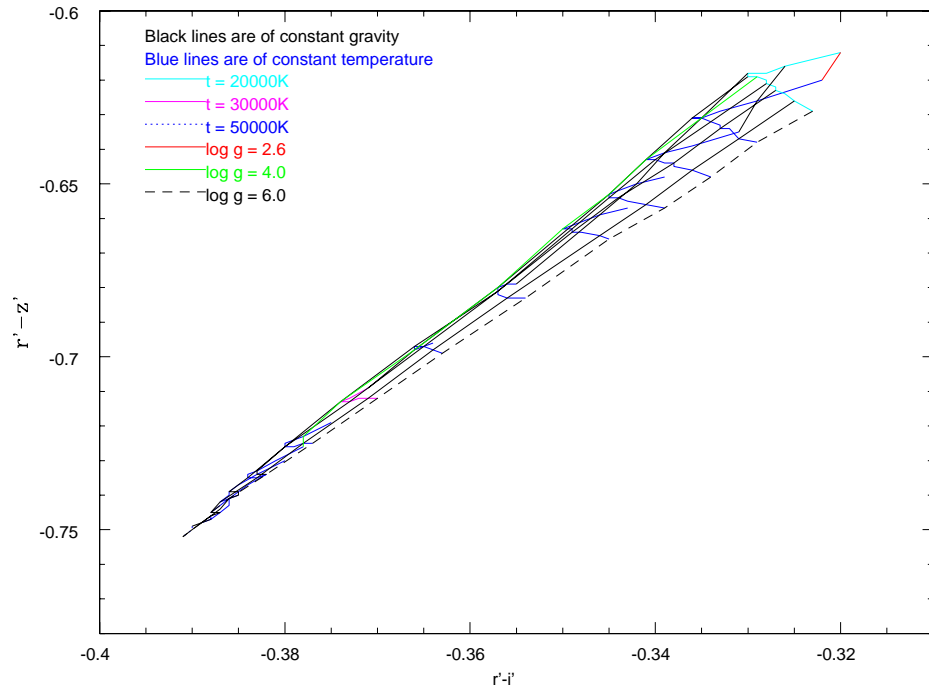Figure 4.11: CSPN model grid in a SDSS, $g' - r'/r' - i'$, colour-colour plot.

Figure 4.12: CSPN model grid in a SDSS, $r' - i'/i' - z'$, colour-colour plot.
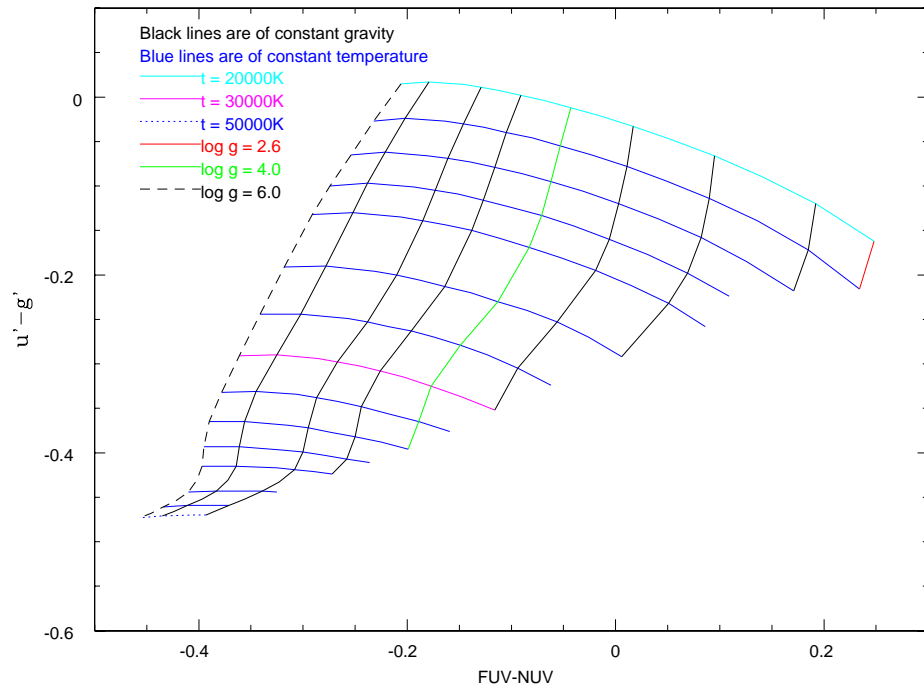
Figure 4.13: CSPN model grid in a GALEX-SDSS, $FUV-NUV/u' - g'$, colour-colour plot.
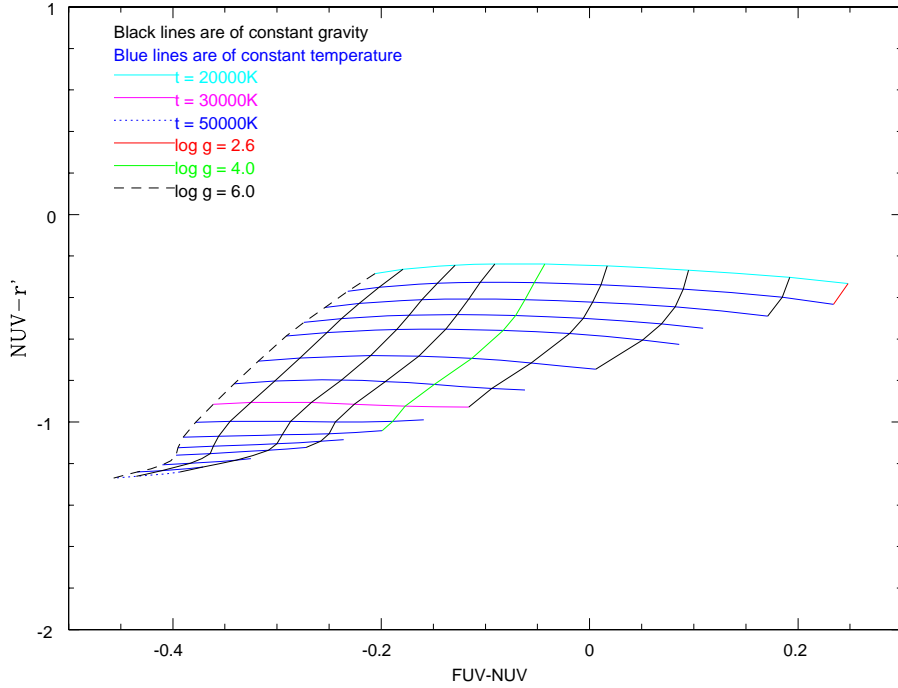
Figure 4.14: CSPN model grid in a GALEX-SDSS (similar to IPHAS), FUV$-r'$/FUV-NUV, colour-colour plot.

Table 4.11: SDSS/GALEX magnitudes of high Galactic latitude post-AGB stars

Name	T_{eff} [K]	$\log g$ [cm s^{-2}]	FUV	NUV	u'	g'	r'	i'	z'
PG1208+224	15303	2.39	15.84	15.44	15.165	14.793	15.068	15.345	15.465
PG1314+442	29499	3.87	14.15	14.36	14.879	14.994	15.319	15.499	15.605
PG1332+281	30965	4.25	14.15	14.53	14.949	15.177	15.686	16.015	16.308
PG1356+242	21394	3.33	14.62	14.93	14.869	14.870	15.242	15.527	15.735
PG2120+062	33218	4.22	–	–	14.062	14.212	14.464	14.619	14.733

colour is virtually reddening free (Bianchi et al., 2011). It is assumed that the interstellar extinction is concentrated in the Galactic disc and given the distance above the Galactic plane for each PNe, the total line of sight extinction is assumed. The de-reddened observed magnitudes are compared with synthetic magnitudes folded on top of ATLAS9 and TLUSTY generated SEDs for the given parameters. The offsets in the four SDSS colors of the five WDs are listed with the GALEX offsets (where applicable) in Table 4.12. The offsets found for the post-AGB stars are applied to the ATLAS9 and TLUSTY model grids. All points in the T_{eff}-$\log g$ space which lie above (smaller $\log g$) the $0.546 M_{\odot}$ track of Schönberner (1983)

Table 4.12: SDSS/GALEX colour offsets of high Galactic latitude post-AGB stars

Name	Δ (FUV$-$NUV)	$\Delta(u' - g')$	$\Delta(g' - r')$	$\Delta(r' - i')$	$\Delta(i' - z)$
PG1208+224	0.0073	0.184	0.048	-0.027	0.108
PG1314+442	-0.1325	0.122	0.148	0.157	0.218
PG1332+281	-0.2376	-0.060	-0.052	-0.001	0.021
PG1356+242	-0.4438	0.251	0.103	0.053	0.118
PG2120+062	–	0.056	0.188	0.159	0.190
Mean	-0.110	0.100	0.090	0.067	0.115
σ_{Mean}	0.163	0.103	0.086	0.077	0.059

shown in Fig. 4.2 are plotted in colour-colour space to define a region expected for post-AGBs. Figs. 4.15-4.18 show the selection region in each colour which is defined by a box surrounding the model grid and then expanded by 1σ of the offset (in Table 4.12) to include 68.2% of CSPNe. The equations which set the box limits and the limiting unreddened magnitudes are given below.

For $-0.476 < u' - g' < 0.952$ and $-0.555 < g' - r' < 0.043$

$$4.651(g' - r') + 2.106 > u' - g' > 4.651(g' - r') + 0.753 \qquad (4.15)$$

For $-0.555 < g' - r' < -0.076$ and $-0.390 < r' - i' < -0.067$

$$2.834(r' - i') + 0.550 > g' - r' > 2.834(r' - i') + 0.114 \qquad (4.16)$$

For $-0.390 < r' - i' < -0.067$ and $-0.418 < i' - z' < 0.094$

$$0.964(i' - z') - 0.158 > r' - i' > 0.964(i' - z') + 0.013 \qquad (4.17)$$

The UV colours are split into two equations to fit the grid. The complete limits are $-0.857 < FUV - NUV < 0.865$ and $-0.476 < u' - g' < 0.952$.
For $-0.476 < u' - g' < 0.403$

$$0.9843(u' - g') - 0.388 < FUV - NUV < 0.9843(u' - g') + 0.469 \qquad (4.18)$$

and for $0.403 < u' - g' < 0.952$

$$0.009 < FUV - NUV < 0.865 \tag{4.19}$$

All the post-AGBs from Saffer et al. (1997) lie within the selection regions but not necessarily on the model grid. This can be due to features within the observed object and the large scatter found for the objects in the filters. The calibration is applied as the post-AGB sample are low metallicity objects which are representative of the Galactic thick disc and halo populations. With the selection region confirmed a search in the SDSS photometric archive for CSPNe within the field of known PNe can be carried out.

Figure 4.15: Post-AGB model grid in a SDSS, $u' - g'/g' - r'$, colour-colour plot after correction. The bluest point is the lowest T_{eff} and $\log g$ WD model atmosphere in this study.

Figure 4.16: Post-AGB model grid in a SDSS, $g' - r'/r' - i'$, colour-colour plot after correction. The bluest point is the lowest T_{eff} and $\log g$ WD model atmosphere in this study.

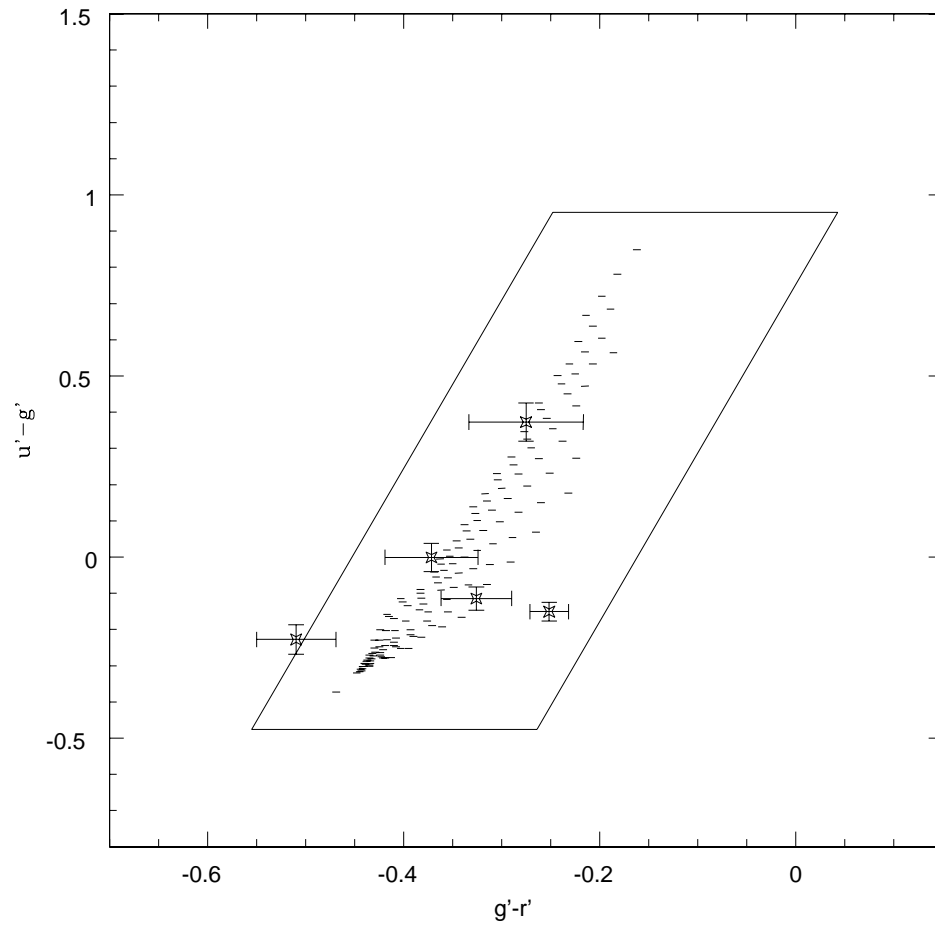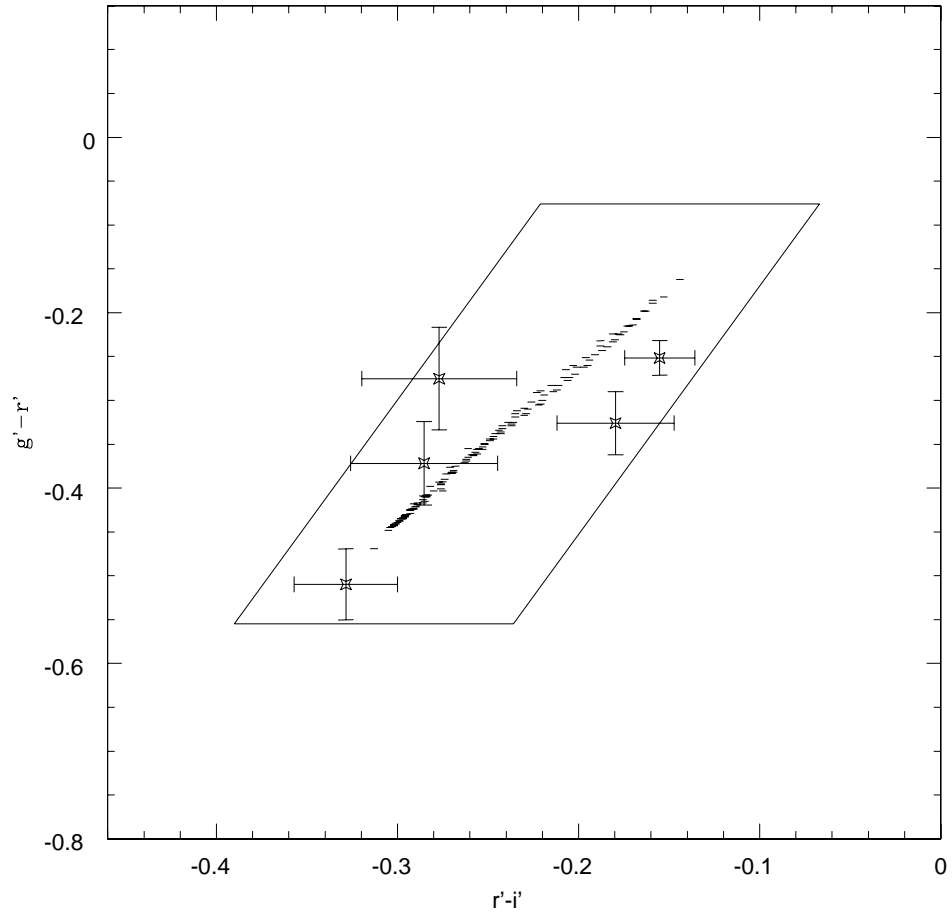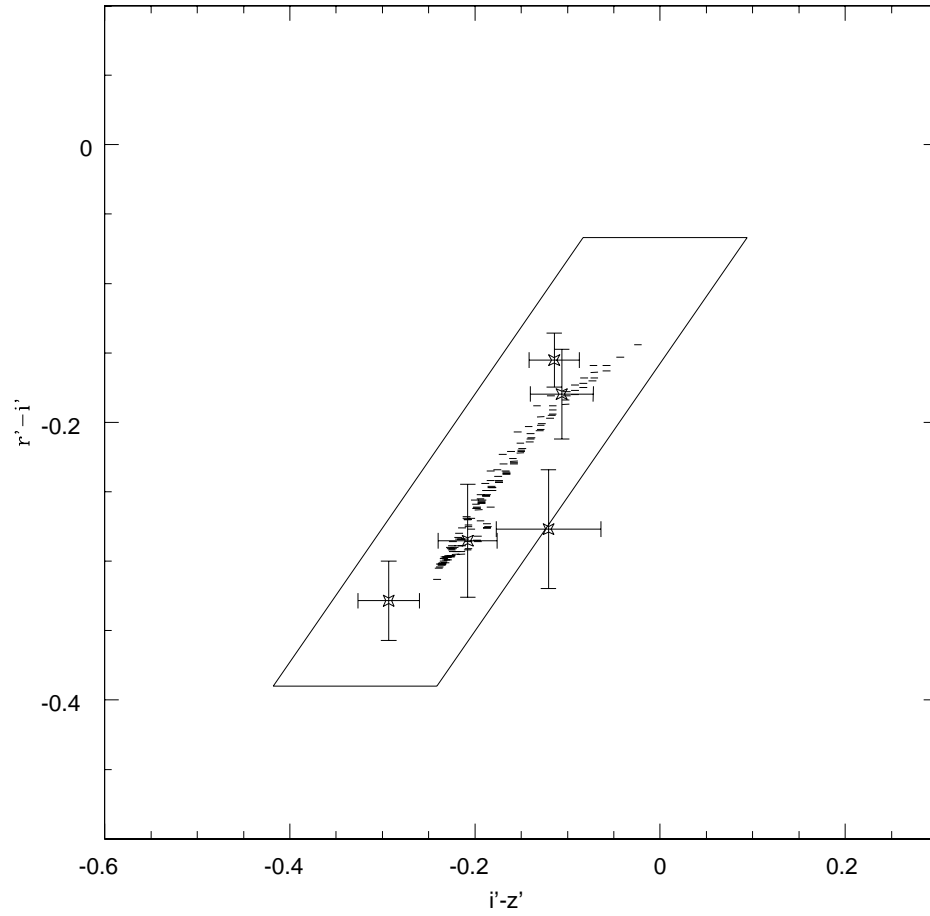Figure 4.17: Post-AGB model grid in a SDSS, $r' - i'/i' - z'$, colour-colour plot after correction. The bluest point is the lowest T_{eff} and $\log g$ WD model atmosphere in this study.
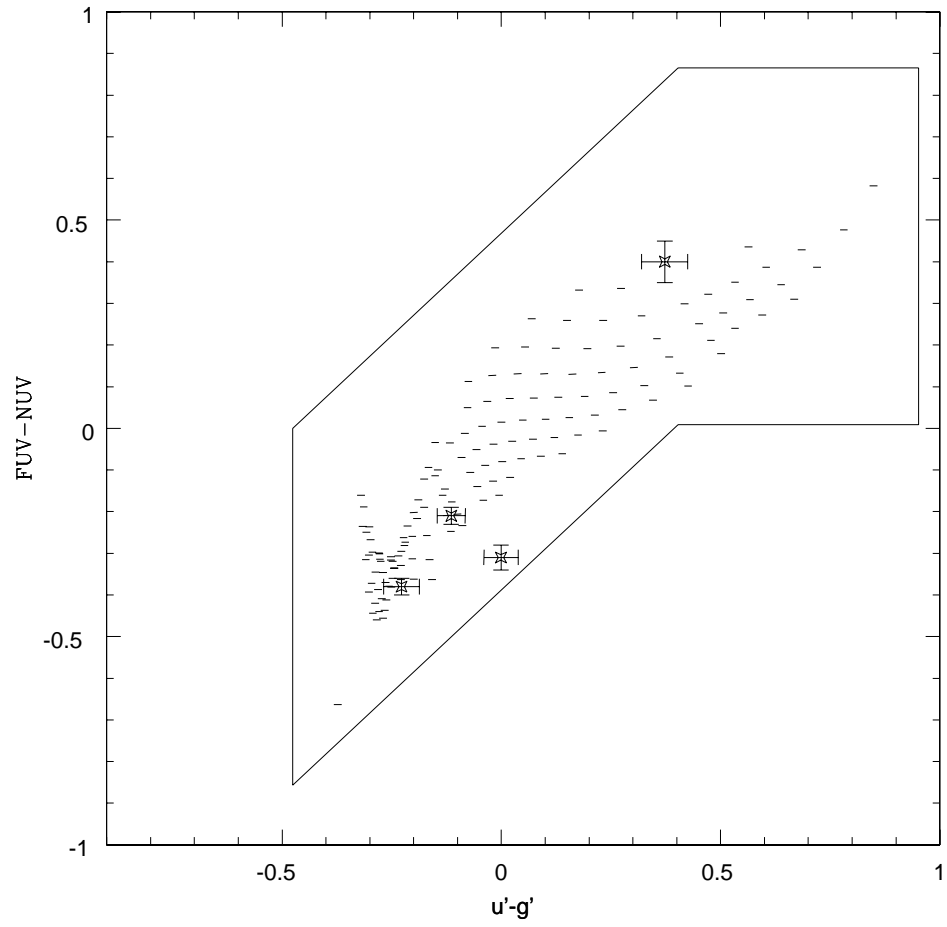
Figure 4.18: Post-AGB model grid in a GALEX-SDSS, FUV−NUV/$u' − g'$, colour-colour plot after correction. The bluest point is the lowest T_{eff} and $\log g$ WD model atmosphere in this study.

Chapter 5

Using Central Stars of PN to Improve PN Distance Estimates

Chapter 3 outlined the difficulties in estimating PN birthrates highlighting the major factor of uncertain distance estimates with a large variation of values found by different investigations. Previous studies have shown that these estimates are more accurate when the central star is used as opposed to using or assuming nebula properties (Mendez et al., 1988). The large number of recently discovered Galactic PNe has enabled complete samples out to greater distances which increase the volume of a distance limited sample. This is a result of deep observations of the Galactic thick disc and halo carried out by dedicated surveys like SDSS. Such samples are expected to be dominated by old PNe with low surface brightness (Frew & Parker, 2006) which may have previously gone undetected, as opposed to brightness limited samples which inherently contain only the brightest compact PNe. Accurate distances are required to construct a distance limited sample of old PNe and to determine a Galactic space density. The newly published catalogue of CSPNe (Weidmann & Gamen, 2011) highlights that only ∼13% of central stars are identified for known PNe, implying that distances estimated to the large majority of PNe are carried out using error-strewn statistical techniques like the Shklovksy method. If the unknown CSPNe are discovered then a distance estimate may

be made from photometric properties and follow-up spectroscopy can be carried out. Photometric colours derived from model atmospheres of the central star and the interstellar reddening give a limit of distances using observed magnitudes and can also be used in conjunction with one another to rule out otherwise feasible values. The methods require an understanding of the intrinsic properties of the central star, and the synthetic photometric model grids generated in Sect. 4 can be applied to deduce properties such as CSPNe reddening and absolute magnitudes.

5.1 Locating Central Stars of PNe in the ESO-Strasbourg Catalogue using SDSS

Evolved PNe are large and extended with faint central stars often not centrally located within the nebula (unlike their compact counterparts). Extreme cases like Sh 2-216 (Tweedy & Napiwotzki, 1992) and Sh 2-174 (Tweedy & Napiwotzki, 1994) show apparently displaced central stars due to the interaction of extended nebulae with the ISM. Therefore, it is important to have a reliable method that distinguishes CSPNe from other objects within the nebula's field. The ESO/Strasbourg catalogue of Galactic PNe (Acker et al., 1992) is a compilation of all known CSPNe (at the time of publication) and consists mainly of the catalogue of Galactic PNe (Perek & Kohoutek, 1967) and the catalogue of the central stars of true and possible planetary nebulae (Acker et al., 1982). The catalogue contains nebula parameters such as line intensities, angular diameters, expansion velocities along with other information from the literature such as previous distance estimates and details on the central star (where known). The central star compilation is supplemented and superseded by the study of Weidmann & Gamen (2011) which contains a detailed catalogue of CSPNe, many of which belong to nebulae from the aforementioned studies. Searching for PNe with angular diameters $\theta > 10''$ in the ESO/Strasbourg catalogue reveals a total of 41 PNe in the SDSS survey area, listed in Table 5.1. Column 1 denotes the PN's PG

name, columns 2-5 are the coordinates of the PN centre in equatorial and Galactic coordinates. Column 6 is the V magnitude of the central star (where known). Columns 7 and 8 denote if the CSPN is located in Acker et al. (1992) and Weidmann & Gamen (2011), respectively. Column 9 is the spectral type of the CSPN in Weidmann & Gamen (2011) if known, otherwise it is from Acker et al. (1992) or left blank. Of the 41 PNe, 26 of the central stars have spectral classifications with hgO(H) and PG1159 the most prominent. Wolf-Rayet, wels (weak emission line stars) and to a lesser degree non high gravity (hg) O type CSPNe, are unlikely to fulfill the photometric criteria of typical central stars as the colours will be affected by emission lines. Furthermore, nine of the CSPNe have magnitudes $m_{AB} < 14$ and are saturated in at least one filter, resulting in an incorrect colour. Eleven CSPNe are classified with spectral types that are expected to meet the photometric criteria and do not exceed the SDSS brightness limit. The colour regions of CSPNe in SDSS are taken from the post-AGB model grids of Sect. 4.3, with the added restriction of $T_{eff} > 20,000$K. The relatively small search radius means that significantly less contamination is expected than for a full sky search. Therefore, more generous criteria were applied by expanding the selection box by 3σ of the original calibration to increase the possibility of locating more CSPNe. A search to identify the 41 CSPNe was carried out within a $3'$ radius of the central coordinates of each PNe in the SDSS DR7 data archive. Fig. 5.1 shows all photometric sources in the field around the centre of PN G 047.0+42.4 with the colour criteria region highlighted with blue dashed lines. Although some contamination can be seen for each individual colour only the CSPN fills the criteria for each pair of colours. PN G 009.6+14.8 is a wels type central star and all stars within the nebula's field are shown in Fig. 5.2. As the central star was previously identified with accurate coordinates determined (Kerber et al., 2003), it is recovered from SDSS with colours of $u' - g' = 0.648$, $g' - r' - 0.388$, $r' - i' = -0.316$ and $i' - z' = 0.076$. The $u' - g'$ and $i' - z'$ are both out of the selection box likely due to emisson within those bands highlighting the issue of detecting emis-

Table 5.1: A List of PNe from the ESO/Strasbourg catalogue of Galactic PNe
Acker et al. (1992) observed in SDSS.

| Name PN G	RA [°]	Dec. [°]	l [°]	b [°]	Mag. V	CS ESO	CS WG11	Sp. Type
009.6+14.8	258.52	−12.91	9.66	14.81	16.58	Y	Y	wels
010.8+18.0	256.41	−10.14	10.90	18.06	14.70	Y	Y	B[e]
025.3+40.8	242.94	12.07	25.33	40.84	10.20	Y	Y	O7
043.1+37.7	251.12	23.80	43.11	37.76	11.70	Y	Y	O6
047.0+42.4	246.89	27.91	47.05	42.48	15.60	Y	Y	hgO(H)
048.7−01.5	291.61	13.33	48.76	−1.53	–	N	N	
050.1+03.3	287.88	16.86	50.20	3.31	11.50	Y	N	[WN8]
050.4+05.2	286.13	17.95	50.41	5.29	–	N	N	
051.0−04.5	295.51	13.84	51.05	−4.60	18.10	Y	N	
064.6+48.2	241.11	40.68	64.67	48.30	13.00	Y	Y	O9
066.7−28.2	324.22	12.79	66.78	−28.20	13.75	Y	Y	hybrid
068.8−00.0	301.18	31.46	68.86	−0.04	–	N	N	
069.2+03.8	297.50	33.76	69.21	3.81	–	N	N	
069.4−02.6	304.10	30.56	69.48	−2.62	–	N	Y	WD?
093.3−00.9	322.72	50.00	93.36	−0.99	–	N	N	
093.3−02.4	324.26	48.93	93.38	−2.45	19.11	Y	N	
093.4+05.4	315.14	54.54	93.41	5.49	12.80	Y	Y	O7
094.0+27.4	275.47	64.37	94.03	27.43	15.04	Y	Y	PG1159
095.2+07.8	314.11	57.43	95.26	7.80	–	N	N	
110.6−12.9	354.80	48.21	110.69	−12.94	20.70	Y	N	
111.0+11.6	334.89	70.93	111.09	11.64	15.50	N	Y	DA
125.9−47.0	14.99	15.74	125.94	−47.08	12.10	Y	Y	hgO(H)
129.2−02.0	25.66	60.16	129.26	−2.08	–	N	N	
130.2+01.3	29.40	63.32	130.28	1.40	15.40	Y	Y	[WO4]
130.9−10.5	25.58	51.58	130.93	−10.50	15.90	N	Y	PG1159
148.4+57.0	168.70	55.02	148.49	57.05	16.04	Y	Y	hgO(H)
149.4−09.2	51.81	45.41	149.50	−9.28	17.00	Y	Y	DAO
149.7−03.3	57.27	50.00	149.71	−3.40	16.57	Y	Y	PG1159
158.8+37.1	130.40	58.23	158.80	37.18	16.40	Y	N	
164.8+31.1	119.47	53.42	164.81	31.18	16.83	Y	Y	PG1159
201.9−04.6	93.64	7.57	201.96	−4.66	–	N	N	
204.0−08.5	91.20	3.94	204.02	−8.52	19.87	Y	N	
204.1+04.7	103.10	9.97	204.15	4.73	15.00	Y	Y	hgO(H)
208.5+33.2	131.72	17.88	208.56	33.29	14.30	Y	Y	[WC]/PG1159
211.4+18.4	118.80	9.55	211.47	18.46	17.60	Y	Y	hgO(H)
211.9+22.6	122.80	10.95	211.91	22.62	14.20	Y	Y	hgO(H)
219.1+31.2	133.55	8.90	219.13	31.29	15.51	Y	Y	hgO(H)
221.5+46.3	148.25	13.74	221.59	46.36	16.04	Y	Y	hgO(H)
229.6−02.7	108.15	−16.10	229.64	−2.73	–	N	N	
238.0+34.8	144.79	-2.81	238.02	34.86	15.54	Y	Y	O(H)
339.9+88.4	193.89	25.89	339.90	88.46	8.86	Y	Y	sdO+G5
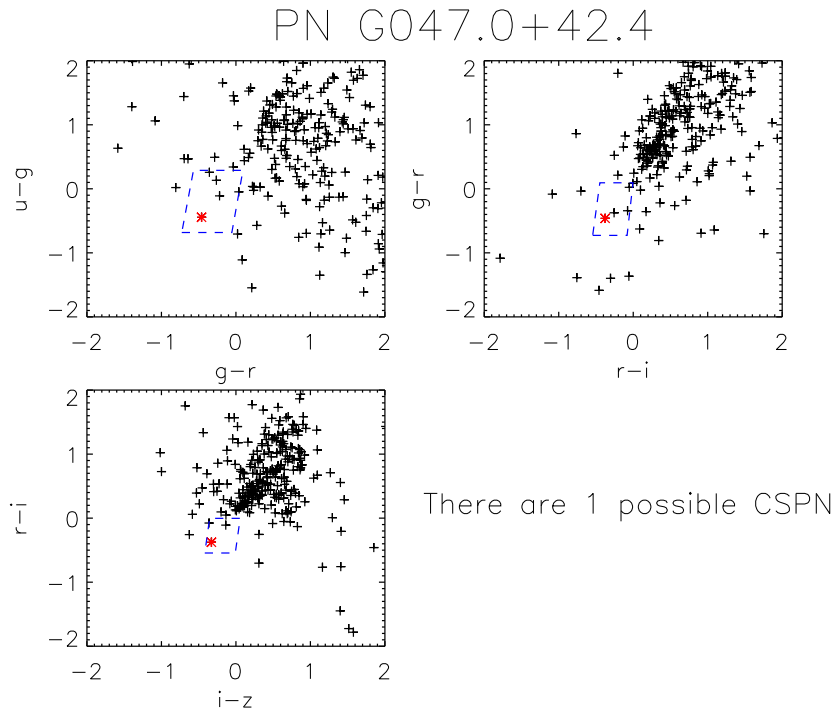
Figure 5.1: The stars in the field of the PN, PN G 047.0+42.4, in SDSS colour-color space. The central star is indicated by the asterisk. It is the only object inside the selection box for every colour.

sion line CSPNe. All of the hgO(H) and PG1159 CSPNe as well as a DA and a DAO CSPNe are successfully re-identified along with PN G 158.8+37.1 and PN G 110.6−12.9, a previously unknown central star. The remaining unknown objects have significantly smaller angular radii, indicating the bias of the method in favour of the more evolved CSPNe in extended nebulae. PN G 238.0+34.8 is an O(H) spectral type central star which does not meet the criteria set for $r'-i'/i'-z'$ colour space, however, it is the most prominent blue star in the field and is likely to have been de-selected due to an emission line in the i or z band, therefore, the r' band is still useful to determine a distance estimate. All of the colour-colour plots for the located central stars are shown in Appendix A and the SDSS right ascension and declination of the central star with the observed r' and i' magnitudes are listed in Table 5.2. Once the central star is identified, a distance estimate can be deduced using the star's magnitude with properties of the nebula from literature.
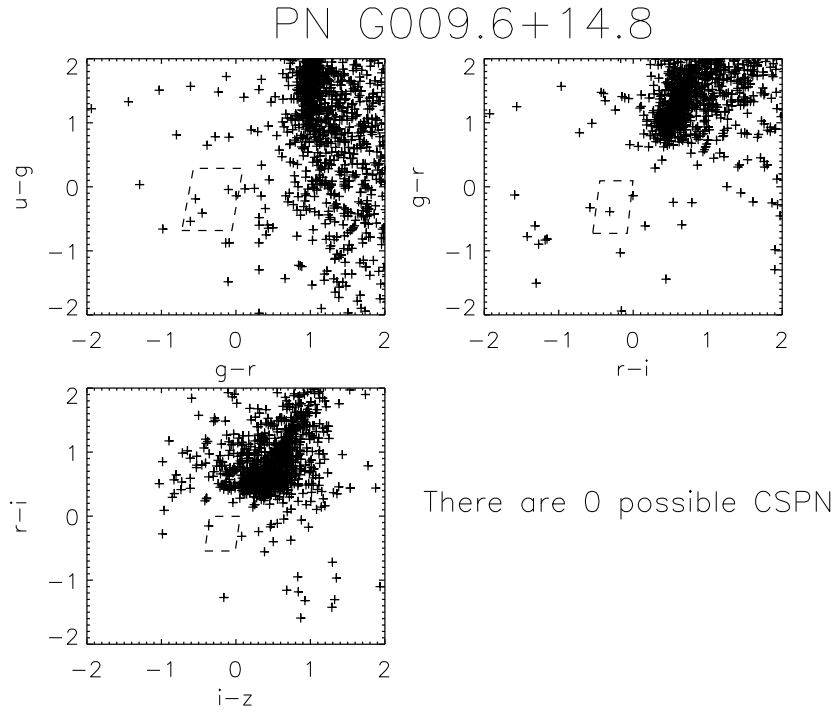
PN G009.6+14.8

There are 0 possible CSPN

Figure 5.2: The stars in the field of the PN, PN G 009.6+14.8, in colour-color space. The central star, of wels type, is not found within our colour selection criteria.

5.2 Distance Estimates from Evolutionary Tracks

The absolute magnitude of any astrophysical object can be determined using its observed magnitude and the distance modulus:

$$M = m - 5\log(d) + 5 - A \tag{5.1}$$

where M is the absolute magnitude, m is the apparent magnitude, d is the distance and A is a correction for interstellar extinction. Therefore for a known or hypothetical distance the absolute magnitude can be determined, neglecting extinction. Similarly, the kinematics of a nebula (the angular diameter, θ, and expansion velocity, $v_{\exp}$) are used with the distance to determine a nebula age as:

$$t_{\mathrm{kin}}\,[\mathrm{yrs}] = \frac{\theta[''](\pi/648000)\,d[\mathrm{pc}]}{v_{\exp}[\mathrm{km\,s^{-1}}] \times 3600 \times 24 \times 365} \tag{5.2}$$

Table 5.2: Parameters of PNe in SDSS. Columns 1 and 2 are the RA and Dec of the CSPNe in SDSS. Columns 4 and 5 display angular diameters and expansion velocities taken from Acker et al. (1992). Where the expansion velocity is unknown a value of 20kms^{-1} is assumed. The observed SDSS r' and i' magnitudes are in the 6th and 7th columns. The 8th column is the extinction, A_V from the Schlegel et al. (1998) maps.

| Name | RA | Dec. | Ang. Diam | $v_{\exp}$ [OIII] | r' | i' | A_V |
PN G	[°]	[°]	["]	[km s^{-1}]			
047.0+42.4	246.8905	27.9093	174.0	32.0	15.79	16.17	0.1886
094.0+27.4	275.4671	64.3648	114.0	22.5	15.26	15.70	0.1346
110.6−12.9	354.7952	48.2082	33.0	[20]	20.63	20.82	0.5655
111.0+11.6	334.8903	70.9342	530.0	5.0	15.64	15.95	2.1182
130.9−10.5	25.5820	51.5754	67.0	38.5	17.34	17.61	0.7543
148.4+57.0	168.6988	55.0190	170.0	29.0	16.02	16.41	0.0402
149.4−09.2	51.8142	45.4057	540.0	[20]	17.26	17.53	1.0197
149.7−03.3	57.2746	50.0041	780.0	5.0	16.62	16.90	4.0286
158.8+37.1	130.3982	58.2301	270.0	4.0	16.72	17.09	0.2713
164.8+31.1	119.4651	53.4214	380.0	22.0	17.35	17.71	0.1711
204.1+04.7	103.0965	9.9654	415.0	10.0	14.49	14.79	0.6655
211.4+18.4	118.7971	9.5526	94.0	[20]	18.13	18.52	0.0604
211.9+22.6	122.8032	10.9548	170.0	[20]	14.02	14.39	0.1337
219.1+31.2	133.5548	8.8980	970.0	10.0	15.75	16.10	0.2023
221.5+46.3	148.2457	13.7430	720.0	35.0	16.21	16.51	0.0975
238.0+34.8	144.7881	−2.8085	270.0	32.0	16.16	16.46	0.1054

Using post-AGB evolutionary tracks the absolute magnitude of the central star and the nebula age may be combined to deduce a distance assuming a CSPN mass. By definition, the kinematical age of a PN and its post-AGB central star are synonymous. However, an assumption has to be made as to when the nebula becomes detached from the progenitor AGB star and thus defining the zero-age of post-AGB stars is non-trivial. The post-AGB evolutionary tracks of Schönberner (1983) and Blöcker (1995) model the post-AGB evolution for CSPNe with masses ranging from $0.546 - 0.940 M_\odot$. Their definitions of the beginning of the post-AGB phase are different, however, the key assumption that the duration of the PN ejection process is short relative to the subsequent CSPN evolution is applied. Schönberner (1983) and displayed numerically in Blöcker (1995). A similarity is that both start the zero age when Reimers mass loss begins which is at $5,000$K for Schönberner (1983) and when the pulsational period drops below 50 days for
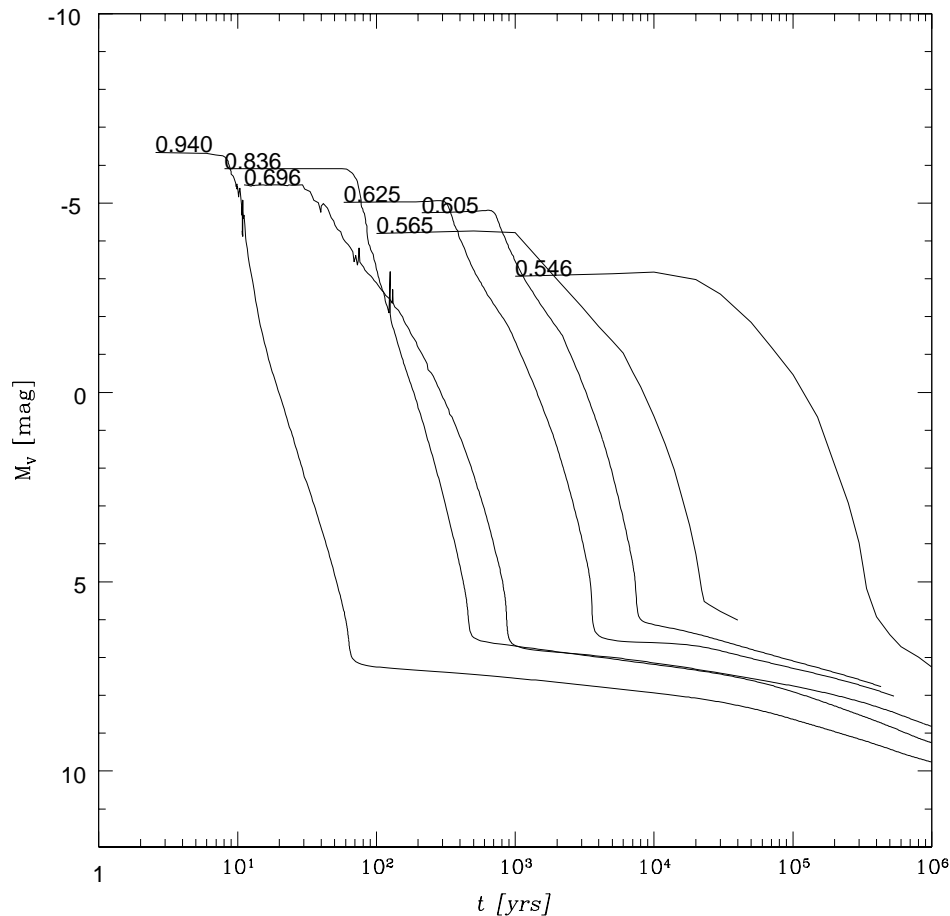
Figure 5.3: The post-AGB evolutionary tracks of Schönberner (1983) and Blöcker (1995) plotted with absolute magnitude against the post-AGB age, t, for the stated masses in $M_\odot$. The post-AGB age is defined in the text.

Blöcker (1995). The tracks are plotted in Fig. 5.3 and show high mass CSPNe evolving to higher magnitudes significantly faster than their low mass counterparts. Interstellar reddening can be significant for some PNe in the sample which are located at relatively low Galactic latitudes, therefore, its contribution must be determined. CSPNe with evolved and extended nebulae often do not exhibit emission lines in their spectra and the $r' - i'$ colour has a small range of expected values. For a given distance an absolute r' magnitude is derived using the observed magnitude and extinction, $A_{r'}$. Reddening is calculated using $E(r' - i')$ assuming an intrinsic $r' - i'$ value of -0.35 and is converted to extinction by $A_{r'} = 3.1978\, E(r' - i')$, explained in more detail in Sect. 5.3. Due to the high Galactic latitude of most SDSS PNe, the reddening maps of Schlegel et al. (1998)

are sufficient to determine extinction as all the interstellar dust along the line of sight is constrained to the Galactic plane. However, the maps are not accurate for the few SDSS PNe which lie near the plane and so are used as a comparison only. For most of the objects the extinction is small, with a reddening value ($E_{r'-i'}$) less than the intrinsic range of expected $r' - i'$, whereas the PNe with large reddening values are restricted to low Galactic latitudes and the Schlegel et al. (1998) maps are best ignored in these cases. Estimating distances using CSPN evolutionary tracks has not been used in the literature before. However, it is a robust method for extended nebulae which determines a range of distances rather than an exact value using photometry only. For any hypothetical distance, $M_{r'}$ and t_{kin} lie on a line, each point corresponding to a CSPN mass (Fig. 5.3). Mass distributions of CSPNe are narrow with most found within a narrow range between $M = 0.55 - 0.66 M_\odot$ in Galactic samples (Tylenda et al., 1991; Gesicki & Zijlstra, 2007), therefore, it is reasonable to assume this mass range for distance estimates. This will provide a reasonable estimate to select PNe for a distance limited sample. The method is least reliable for high mass CSPNe as the distance would be overestimated assuming a lower mass. However, the peak of the CSPNe mass distributions is prominent with a mean mass of $M = 0.60 M_\odot$ and a small scatter of $0.02 - 0.03 M_\odot$ (Tylenda et al., 1991; Gesicki & Zijlstra, 2007). Therefore, higher masses are rare with minimal impact on the statistics. Furthermore, the effect of the mass assumption is reduced for evolved CSPNe as all masses converge in a narrow range of peak absolute magnitude as can be seen in Fig. 5.3 (also discussed in Phillips 2005).

5.2.1   Distance Estimates for SDSS CSPNe

The 16 central stars located in the SDSS sample were used with their observed r' and i' magnitudes, angular diameters and expansion velocities of their PNe to estimate a distance range using the evolutionary tracks. The angular diameters and expansion velocities are taken from Acker et al. (1992) (where known), otherwise
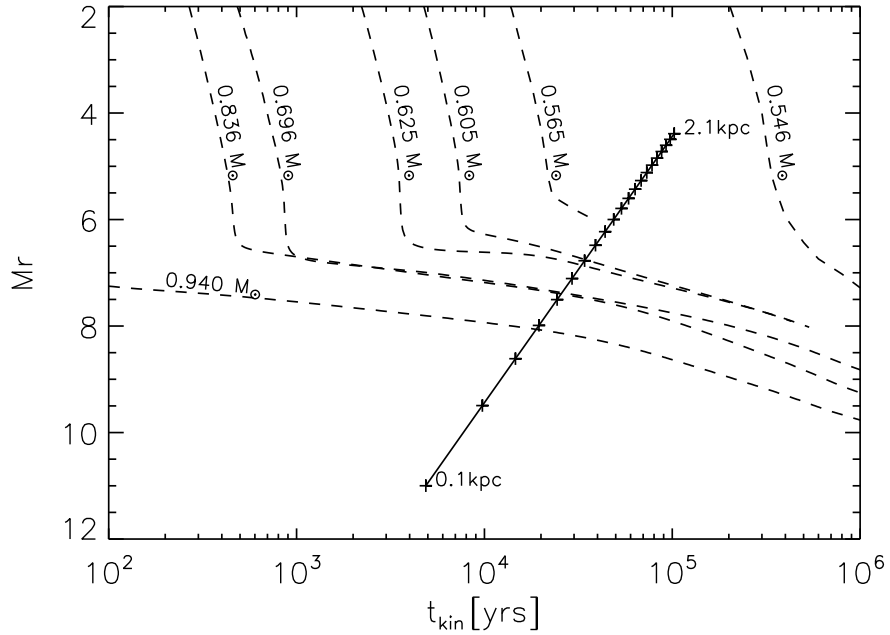
Figure 5.4: A M_r-t_{kin} plot with the evolutionary tracks of Schönberner (1983) and Blöcker (1995) for PN G 221.5+46.3. The plus symbols represent distance increments of 0.1kpc from $0.1-2.1$kpc.

a typical expansion velocity of $20\mathrm{km\,s^{-1}}$ is assumed. Distances are extracted from the $M_{r'}$-t_{kin} plot assuming a CSPN mass of $0.565 - 0.66M_\odot$ (PN G 221.5+46.3 is shown as an example in Fig. 5.4). The figures for the remaining 15 CSPNe are in Appendix B. Distances obtained from the literature are compared with the results in this work and are listed in Table. 5.3. All distances in column 3 are Shklovsky distances from Cahn et al. (1992). Other sources are quoted in columns 4 and 5 with the method and reference given in the footnotes. The results are mixed with some distances in fair agreement with previous estimates, however, there is a spread of $\sim$0.5kpc compared with other methods. Although some of the uncertainties for this work stems from the unknown CSPN mass, this is an improvement on the statistical methods used by Cahn et al. (1992) which have large systematic errors, underestimating the distances for extended PNe (Napiwotzki, 2001). The mass assumption applied here is reasonable for old PNe and the error in the CSPNe mass is expected to propagate to less than a 0.5kpc distance for extended PNe, thus putting them in agreement with most of the literature determinations.

Table 5.3: Distances to PN in SDSS. Column 2 is the distances from this work assuming a $0.6 M_\odot$ CSPN and column 3 is Shklovsky distances from Cahn et al. (1992), who use a modified Shklovsky method. Columns 4 and 5 list other distance methods and references.

Name PN G	Dist. This work [kpc]	Dist. Shklov. [kpc]	Dist. Other [kpc]	Dist. Other [kpc]
047.0+42.4	0.6−1.1	1.16	1.58[a]	0.53[b]
094.0+27.4	0.5−1.0	1.00	1.7[a]	
110.6−12.9	3.0−5.0+	4.18		
111.0+11.6	0.3−0.6		0.46[a]	0.3[d]
130.9−10.5	1.0−3.0	0.74	0.78[a]	
148.4+57.0	0.6−1.2	0.62	0.43[b]	
149.4−09.2	0.7−1.2		0.51[a]	1.5[b]
149.7−03.3	0.4−0.7		0.55[a]	0.54[b]
158.8+37.1	0.6−1.1	0.91	1.17[b]	
164.8+31.1	1.0−1.6	0.57	0.9[a]	
204.1+04.7	0.25−0.4	0.44		
211.4+18.4	1.8−3.0		2.2[c]	
211.9+22.6	0.25−0.6		0.5-0.7[a]	
219.1+31.2	0.4−0.7	0.23	0.57[d]	0.33[b]
221.5+46.3	0.5−0.9		0.525[a]	0.3[b]
238.0+34.8	0.6−1.0	0.75	1.26[a]	

[a] Spectroscopy (Pottasch, 1996)
[b] Various (Phillips, 2005)
[c] Shklovsky (Hartl & Weinberger, 1987)
[d] Parallax (Harris et al., 2007)

The distances can be further constrained using determined parameters of a CSPN from other techniques and studies to give the intrinsic properties of the star. PN G 111.0+11.6 and PN G 219.1+31.2 have parallax distances determined which are used to calculate absolute magnitudes of $M_V = 7.53$ and $M_V = 6.53$ from the distance modulus. Using these magnitudes in the $M_{r'}$-t_{kin} plot give masses of $0.60 M_\odot$ and $\sim 0.55 M_\odot$ and subsequently, distances of 0.4kpc and 0.8kpc. Both of these PNe as well as PN G 148.4+57.0 and PN G 164.8+31.1 have absolute magnitudes determined in Phillips (2005). They are calculated from distance measurements and so are only used as a reference here. Phillips (2005) determine absolute V magnitudes of 6.86, 7.91, 5.55 and 7.96, for PN G 111.0+11.6, PN G 148.4+57.0,

PN G 164.8+31.1 and PN G 219.1+31.2, giving distance estimates of 0.5-0.6 kpc, 0.4-0.5 kpc, >2 kpc and 0.3-0.4 kpc. PN G 164.8+31.1 has a distance larger than 2kpc for this magnitude which is in disagreement with all previous distance determinations, therefore is ignored. Three of the four CSPNe have distances from the literature absolute magnitudes which put them in agreement with other distance estimates. The check with the literature proves that with just photometry (magnitudes and images for angular diameters), reasonable distance estimates can be made and improved with follow-up analysis.

5.3 Distance Estimates from Extinction

Distance estimates obtained through reddening of the PN or the central star are carried out using 3D extinction maps outlined in Sect. 3.2.8. The methods of determining reddening vary from spectroscopic determination of PNe through the Balmer decrement method (the most common for PNe are the Hα/Hβ ratios, Phillips, 2006) and measuring the equivalent width of Na D lines (Napiwotzki & Schoenberner, 1991; Napiwotzki & Schönberner, 1995), to photometric methods making use of the small range of red optical colours of hot stars which are dominated by continuum features. Pottasch (1996) employs all of the above methods in his compilation of interstellar distances and uses $(B - V) = -0.38$ as the expected de-reddened colour for hot stars from Kaler & Feibelman (1985). The same method is carried out for IPHAS and SDSS $r' - i'$ colours mentioned in Weston et al. (2009), and is described in more detail here. A good distance estimate can only be obtained with a detailed 3D dust map. The maps of Schlegel et al. (1998) give only the integrated extinction and thus can not be used for this purpose. The work of Sale et al. (2009) utilises the dense stellar fields in IPHAS to determine high resolution extinction-distance relationships for the Galactic plane $|b| < 5°$. The extinction is determined from the colour excess of MS stars for a given region of sky to build an extinction map. This map can be exploited to determine a dis-

tance for the known extinction of an object. Weston et al. (2009) use this method for the IPHAS observation of PN G 126.6+01.3 and Giammanco et al. (2011) apply the maps to a larger dataset of IPHAS PNe and determine the reddening through a compilation of literature $H\alpha/H\beta$ ratios which is related to extinction by:

$$A_V = 2.15 \times 2.84 \times \log\frac{H\alpha/H\beta}{2.86} \tag{5.3}$$

Alternatively, all nebula ionising post-AGB stars have a narrow range of intrinsic $r' - i'$ colours ($r' - i' = -0.35 \pm 0.04$) and so an accurate estimate of $E(r' - i')$ can be determined using the observed colours. After converting reddening to an r' band extinction, $A_{r'}$, the distance can be extracted from the Sale et al. (2009) projection of Galactic dust. To demonstrate the capabilities of the 3D maps with a CSPN in the IPHAS field, the distance to PN G 126.6+01.3, also referred to as the Príncipes de Asturias (Mampaso et al., 2006) is carried out using the reddening methods. The r' and i' magnitudes are 18.12 ± 0.02 and 17.75 ± 0.02, respectively which leads to a photometric reddening of $E(r' - i') = 0.72$. Reddening is converted to extinction by $E(r' - i') = A_{r'} - A_{i'}$ with the relationships $A_{r'}/A_V = 0.858$ and $A_{i'}/A_V = 0.639$ (Fan, 1999), leaving $E(r' - i') = 0.219A_V$. The V band extinction is plotted against distance for the field around PN G 126.6+01.3 which has an extinction of $A_V = 2.82$ (Fig. 5.5). The distance for PN G 126.6+01.3 is between 0.5-1.5 kpc and depending on reddening and Galactic structure in the line of sight this method can yield well defined distances or a wide range of possible solutions. The wide spread of possible distances for PN G 126.6+01.3 emphasises that distance estimates by reddening are often more useful as confirmations rather than determinations. As a comparison, a distance is obtained using the evolutionary tracks and with the angular diameter and expansion velocity of $21''$ and $11\mathrm{km\,s}^1$, respectively from Mampaso et al. (2006) (Fig. 5.6). The distance to the PN depends on the assumed CSPN mass, and Mampaso et al. (2006) determine the nebula mass to be $0.05M_\odot$ and subsequently a low mass CSPN would be expected. For the post-AGB track of $M = 0.565M_\odot$ the PN
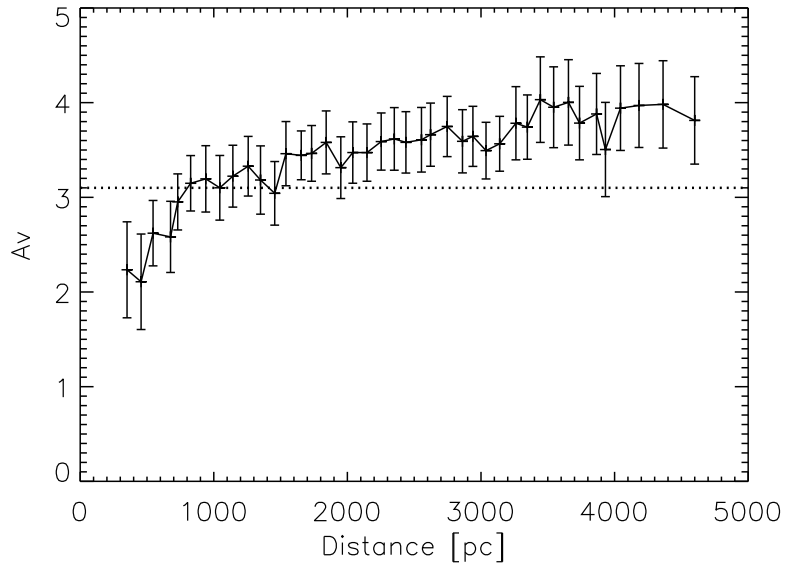
Figure 5.5: An extinction-distance plot of the field near the PN G 126.6+01.3 using the 3D extinction maps in IPHAS from Sale et al. (2009). The PN lies between 0.7 and 2 kpc away.

distance is 2.2kpc with a dynamical age $\sim 20,000$ years which is lower than the estimates of Mampaso et al. (2006). The central star of PN G 126.6+01.3 is likely to include emission from the nebula and this would have a significant impact on the $E(r' - i')$ determination as the r' magnitude will appear much brighter than if unaffected. This would have an even greater effect on the reddening distance and would explain the underestimate in the distance and extinction compared to Mampaso et al. (2006). Photometric reddening distance estimates are more accurate for more extended PNe than PN G 126.6+01.3 and will be a useful application for other IPHAS PNe with presently non-detected central stars.

5.4 Conclusion of CSPNe distances estimates using Photometry

The distance methods described here are a useful application when constructing a preliminary list of PNe in a distance limited sample to determine PNe birthrates. The methods provide a strong indicator as to whether newly discovered PNe in
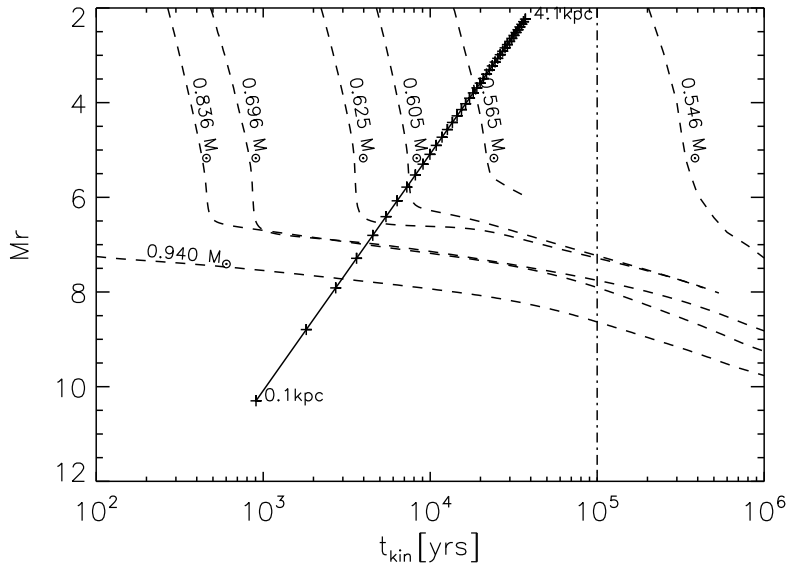
Figure 5.6: A kinematic age-absolute magnitude plot of PN G 126.6+01.3. The CSPN has a distance of $0.5-2.2$ kpc.

SDSS and IPHAS should be included within such a sample. At face value the method which suffers from large uncertainties for young PNe, especially those with massive CSPNe (see tracks in Fig 5.3). However, these will be very high surface brightness PNe and are easily identified with other methods or located at a large distance, in addition to being rare. If compiling a sample of PNe within $2\,\mathrm{kpc}$ based solely on photometry, then confidence can be placed in the distance estimates within an uncertainty of $0.5\,\mathrm{kpc}$ and so a CSPN estimated to be within $1.5\,\mathrm{kpc}$ and further than $2.5\,\mathrm{kpc}$ can be included or excluded, respectively. CSPNe with distances of $1.5\,\mathrm{kpc} < D < 2.5\,\mathrm{kpc}$ should be checked with another method and along with the $D < 1.5$ kpc PNe to further constrain the distance and subsequently the Galactic distribution. Using photometry to determine atmospheric parameters would be ideal for constraining absolute magnitudes (and distances). However, initial checks suggest that the scatter in the SDSS photometry and the fine model grid in colour-colour space would produce errors greater than the range of masses from the $M_{r'}$-t_{kin} plot.

Chapter 6

Post-AGB Stars and Central Stars of PNe in the Galactic Halo

Post-AGB stars are rare objects within the Milky Way, largely due to their short lifetimes. The post-AGB phase begins when the circumstellar envelope becomes detached from the star which rapidly evolves to a high temperature as the star contracts. Residual burning in the envelope and mass loss dictates how long the phase lasts until the star becomes a WD supported only by degeneracy pressure. Fast evolving stars become CSPNe as they ionise their ejected envelope while it is optically thick, and are likely to have a remnant mass of $M > 0.55 M_\odot$. Young post-AGB stars (which include all massive CSPNe) are difficult to observe in the UV and optical as they are enshrouded in their circumstellar envelope but are easily identified via their re-emitted radiation in IR surveys. This is particularly evident in higher mass stars, as they undergo significant mass loss and evolve rapidly during the post-AGB phase (Kaeufl et al., 1993). In this case it is not possible to observe the central star until the nebula is optically thin, at this point massive remnants will already be on the WD cooling track. However, extended PNe which reside in old populations like the Galactic halo evolve at a slower rate and the nebula disperses becoming optically thin to the radiation from the central star. For low mass post-AGB stars (of pop. II), the ejected nebula

becomes optically thin before ionisation temperatures are reached, and so never become CSPNe (Moehler, 2001). They experience relatively small mass loss on the AGB, and as a result little or no IR excess is expected as the stellar radiation is essentially unabsorbed. Therefore, all post-AGB stars below $0.55M_\odot$ are slow evolving, highly luminous sources which should be easily observable. However, there is a further cut off for which stars do not reach the tip of the AGB. The mass at which this cut off occurs is hard to define as the evolution is sensitive to envelope mass which is specified by AGB mass loss. Dorman et al. (1993) models show that a transition between post-AGB and post E-AGB type evolution occurs at $M \sim 0.52M_\odot$. Furthermore, the majority of their tracks show that stars fail to ascend the AGB with a core mass of $M < 0.5M_\odot$. This corresponds to an initial mass of $M \sim 0.74M_\odot$ (Catalán et al., 2008) which is lower than a typical globular cluster (GC) turn-off mass ($0.85M_\odot$, Jacoby et al., 1997), therefore, most GC and halo stars would be expected to evolve through the AGB.

An additional difficulty in locating and classifying post-AGB stars stems from objects which exhibit similar features in low or medium resolution spectra. HB, EHB, post-EHB and hot, massive MS stars lie in a similar region in T_{eff}-$\log g$ parameter space. In the case of post-AGB and MS stars of type O and B, only chemical abundances determined from high resolution spectra distinguish them from each other. However, not many hot MS stars are expected in the halo and if they are observed are likely to be "runaways" which are ejected from the Galactic plane at high velocities (up to $400\mathrm{km\,s^{-1}}$; Silva & Napiwotzki, 2011) and are easily identified by their kinematic properties. Therefore, post-AGB stars in the halo should be the dominant population in the blue region of colour-colour space in UV and optical photometry; however, very few are known. The PG survey has identified a few halo post-AGB candidates and SDSS has the potential to discover slowly evolving early-type post-AGB stars which will not become CSPNe.

6.1 Post-AGB Catalogues

The most complete post-AGB star catalogue compiled to date is the Torun catalogue (Szczerba et al., 2007) which contains a collection of post-AGB stars mainly selected due to their infra-red (IR) excess. The Torun catalogue contains 326 confirmed and 107 possible post-AGB stars, consisting mainly of young thin disc stars which will subsequently become CSPNe. The catalogue includes all of the IRAS objects from Suárez et al. (2006) which exhibit a selection bias towards more massive, young stars as they have dense ejected envelopes with strong thermal emission in the IR. The bias towards young and more massive stars transmits to Galactic regions with ongoing star formation (i.e. the disc). Figs. 2 & 3 from Szczerba et al. (2007) show Galactic positions akin to those populations. Finally, the Torun catalogue has a cut off of $T_{\text{eff}} < 25,000$K, at the nebula ionisation temperature. however, for reasons mentioned earlier one might expect to find lower mass stars with these temperatures without a nebula. The Torun catalogue contains a few high Galactic latitude post-AGB stars, and combined with a search through the literature, yields 32 well studied early-type post-AGB candidates not associated with a GC. These are listed in the first part of Table 6.1 with individual Galactic coordinates, magnitudes, spectral types and T_{eff} and $\log g$. The last two columns state if the star is a binary (if not confirmed then it is assumed not to be) and the object references. Many of the objects in Table 6.1 are results of systematic searches for high Galactic latitude sdBs/sdOs or studies of individual objects. McCausland et al. (1992) identified LS IV $-12.°111$, LB 3193, LB 3219 and LS IV $-4.°01$ as candidate halo post-AGB stars and carried out a high resolution spectroscopic follow-up. All four objects have B-type spectra with low metallicity and surface gravities and are noticeably depleted of C. McCausland et al. (1992) use these arguments as strong pointers to their post-AGB nature. Furthermore, LS IV $-12.°111$ was determined as starting to ionise its ejected envelope by Conlon et al. (1993a) and therefore, is a post-AGB about to become a CSPN. PHL 1580 and PHL 174 are used as comparison objects in McCausland et al. (1992)

and are candidates determined earlier by the same group (Conlon et al., 1991). Again the same conclusions are drawn from similar results with comparisons to CSPNe suggesting that these objects are post-AGB stars and therefore, potential CSPN progenitors. More recently discovered objects PG 1704 + 222 and PG 1323−086 (Moehler & Heber, 1998), HD 137569 (Giridhar & Arellano Ferro, 2005) and CPD−61°455 (Hambly et al., 1996; Rolleston et al., 1997) all have high resolution spectroscopy and have been confirmed as post-AGB objects by abundance comparisons with the previously mentioned objects. The five highest Galactic latitude stars from Gauba & Parthasarathy (2003) are IRAS 18371−3159, BD−18 4436, IRAS 17203−1534, Hen3−847 and CD−49 11554. They were identified as post-AGB candidates through their IRAS colours and atmospheric parameters, derived from low resolution optical and UV spectra, which enforces their classification. The list in Table 6.1 contains ten candidate post-AGB stars from the PG survey which are the faintest objects in the table suggesting that a deeper survey may discover more hot early type post-AGB stars which will not become PNe. There are fourteen known halo PNe (Otsuka et al., 2010), however, many are binaries and hence have undergone some level of interaction which can speed up the evolution from the AGB. Nine of these objects are summarised in Howard et al. (1997). Elemental abundance analyses suggest different groups of evolution within the small sample, thought to be caused by the third dredge up mass limit. The groups show a large scatter of properties from a halo population but are only resolved by high resolution spectroscopy.

GCs are dominated by pop. II stars like the Galactic halo and post-AGB stars are just as rare within GCs. Jacoby et al. (1997) note that few PNe (∼16) are expected in GCs based on the PNLF, however, their observations are a further order of magnitude below the number expected. Observational biases caused by non-detections of faint PNe may be an explanation, however, observations of a complete sub-sample (discussed later in the thesis) show few post-AGB stars which subsequently suggests even lower PN numbers. In the literature the number of

known post-AGB stars in GCs is smaller than non-associated halo objects. Well known objects such as Barnard 29 in M13 (Conlon et al., 1994; Thompson et al., 2007), ROB162 in NGC6397 (Heber & Kudritzki, 1986), ZNG-1 in M10 (Mooney et al., 2001), ZNG-1 in M15 (Mooney et al., 2004) and ROA 5701 in ω Centauri are all well studied GC post-AGB stars. High resolution spectroscopy gives detailed elemental abundances from which cluster membership can be confirmed and their evolutionary channel deduced. There are four known PNe in Galactic GCs, IRAS 18333−2357 in M 22, JaFu 1 in Palomar 6, JaFu 2 in NGC 6441 and K648 in M15. JaFu 1 and 2 are considered to be the product of merged binaries by Jacoby et al. (1997). IRAS 18333−2357 is a possible 'born-again' central star which encountered a late thermal pulse but may also be a merged binary product (Harrington & Paltoglou, 1993). K648 has been well studied and confirmed as a merged binary (Alves et al., 2000; Tajitsu & Otsuka, 2006; Mohamad-Yob et al., 2010). The small sample suggests that GC PNe are all binaries and standard single star evolutionary channels do not produce GC PNe.

6.1.1   Known Post-AGB stars in SDSS

Table 6.1 lists all the known early type post-AGB stars in the literature. In order to identify known post-AGB stars in SDSS a search for all of these objects in the SDSS DR7 photometric database is carried out. Unfortunately, very few of the stars are in the observed survey area and only eleven stars have counterparts within a 3′ search radius of their SIMBAD positions. The search region is selected in order to incorporate most of the nebula and to allow for poor astrometry from old photographic plates. HD 137569, BD+33 2642, PG1704+222 and HD 341617 along with six candidates from the Saffer et al. (1997) PG sample (discusssed in more detail later) are the only observed halo objects and the only GC post-AGB star is ZNG−1 in the cluster NGC 5272. Furthermore, SDSS is a deep survey with a saturation limit of $g' \approx 14$ and the four halo objects, ZNG−1 in NGC 5272 and one of the Saffer et al. (1997) sample are saturated in one or more photometric

bands. Only the five non-saturated post-AGB stars from the Saffer et al. (1997) follow up study of the PG survey remain.

Table 6.1: Hot known post-AGB stars in the halo and globular clusters.

Name	l	b	Mag.	Sp. Type[a]	T_{eff}	$\log g$	Binary	Refs.
	[°]	[°]	[V]		[K]	[cm s^{-2}]		
Halo								
IRAS 18371−3159	2.92	−11.82	11.9	B1	20,800	2.9	N	27,35
BD−18 4436	4.10	12.26	11.50	B5	17,100	3.40	N	27,35
IRAS 17203−1534	8.55	11.49	12.50	B1	19 000	2.5	N	27,35
LS IV −4°01	14.4	22.86	12.08	B7	11,000	2	N	1,35
BPS CS 29493−046	16.45	−50.43	15.8	B	20,000	3	N	23,35
HD 137569	21.87	51.93	7.91	B5	12,000	2	Y	7,35
LS IV −12°111	29.18	−21.26	11.32	Be	23,750	2.7	N	1,2,24,35
PHL 1580	31.33	−43.48	12.3	B1	24,000	3.6	N	3,35
PHL 174	33.16	−48.12	14.3	B2	18,000	2.7	N	3,35
PG 1704 + 222	43.06	32.36	12.74	B	21,000	3.2	N	4,5,29,35
HD 341617	50.67	19.79	11.4	B1	20,750	2.35	N	11,25,35

Continued on next page

Name	l	b	Mag.	Sp. Type[a]	T_{eff}	$\log g$	Binary	Refs.
	[°]	[°]	[V]		[K]	[cm s^{-2}]		
BD+33°2642	52.73	50.79	10.83	B2	20,200	2.9	Y	24,35
HD 172324	66.18	18.58	8.16	B9	11,000	2.5	N	11,35
BPS CS 22946−005	173.86	−82.41	14.5	B	20,000	2.7	N	23,35
CPD−61°455	269.97	−34.09	11.2	B0.5	24,500	3.7	Y	8,9,35
EC11507−2253	285.95	37.78	15.12	B5	15,500	2.6	N	28,35
LB 3193	297.28	−54.90	12.7	B5	13,000	2.2	N	1,26
LB 3219	299.02	−43.77	12.86	B2	21,250	2.8	N	1,35
Hen3−847	304.60	13.95	10.00	B5	–	–	N	27,35
PG 1323 − 086	317.11	53.11	14.6	B	16,000	2.5	N	4,23,35
LB 3116	331.56	−27.23	12.55	O	16,000	2.7	N	26,35
CD−49 11554	341.41	−9.04	10.74	B1	20,300	2.6	N	27,35
2MASS J17390218-4500388	345.58	−7.30	13.1	–	24,000	3.3	N	22,35
HD 177566	355.55	−20.42	10.17	B6	30,000	3.8	N	21,35
PG 1212+369	159.84	77.72	12.50	B2	29.248	4.04	N	29

Name	l	b	Mag.	Sp. Type[a]	T_{eff}	$\log g$	Binary	Refs.
	[°]	[°]	[V]		[K]	[cm s^{-2}]		
PG 1243+275	206.55	8.84	14.12	–	25,665	3.90	N	29
PG 2120+062	58.52	−29.42	14.40	O	33,218	4.22	N	29
PG 0832+676	147.75	35.01	14.15	O	26,407	3.82	N	29
PG 1208+244	239.56	79.59	14.90	O9.5	15,303	2.39	N	29
PG 1314+442	107.85	72.40	15.16	O	29,499	3.87	N	29
PG 1332+281	39.87	80.25	15.50	B	30,965	4.25	N	29
PG 1356+242	25.04	74.46	15.15	O	21,394	3.33	N	29
Globular Cluster								
360 in NGC 6723	0.02	−17.30	15.61	–	40,600	4.46	N	14,18
409 in NGC 6723	0.06	−17.27	14.64	–	20,600	3.34	N	14
ZNG-1 in M5	3.86	46.79	14.54	sdO	44,300	4.3	Y	12,35
ZNG-1 in M10	15.16	23.09	13.23	B:	27,000	3.6	N	10,20,35
ZNG-1 in NGC 6712	25.35	−4.33	13.00	–	11,000	2.1	N	10,35
ZNG-1 in NGC 5272	42.50	78.68	14.93	–	35,000	4.0	N	18,36,37

<div align="center">Continued on next page</div>

Name	l	b	Mag.	Sp. Type[a]	T_{eff}	$\log g$	Binary	Refs.
	[°]	[°]	[V]		[K]	[cm s^{-2}]		
Barnard 29 in M13	58.97	40.94	13.14	B2	20,000	3.0	N	14,15,16,35
ZNG-1 in M15	65.04	−27.29	14.80	–	28,000	3.7	N	10,35[b]
ROA 5342 in ω Centauri	308.45	15.40	15.89	–	–	–	N	18
ROA 342 in ω Centauri	308.91	15.07	12.41	–	5,445	1.57	N	17
V1 in ω Centauri	308.99	15.07	11.43	F6	5,570	0.82	N	6,17
ROA 24 in ω Centauri	309.07	15.18	10.79	F0	6,776	1.21	N	17
ROA 5701 in ω Centauri	309.24	15.05	13.16	–	23,000	3.3	N	14,16,35
PAGB-1 in NGC 5986	337.03	13.27	12.65	F?	–	–	N	19
PAGB-2 in NGC 5986	337.03	13.27	12.76	F?	–	–	N	19
ROB162 in NGC 6397	338.19	−11.94	13.23	sdOB	51,000	4.5	N	13,35[b]
NGC 6121−Y453	350.98	16.05	15.86	–	58,800	5.15	N	14

[a] Spectral types come from reference where stated otherwise taken from Simbad catalogue.

[b] Not a post-AGB star in Szczerba et al. (2007).

References for Table 6.1

(1) McCausland et al. (1992); (2) Conlon et al. (1993a); (3) Conlon et al. (1991); (4) Moehler & Heber (1998); (5) Conlon et al. (1993b); (6) Van Winckel (1997); (7) Giridhar & Arellano Ferro (2005); (8) Hambly et al. (1996); (9) Rolleston et al. (1997); (10) Mooney et al. (2004); (11) Arellano Ferro et al. (2001); (12) Dixon et al. (2004); (13) Heber & Kudritzki (1986); (14) Moehler et al. (1998); (15) Conlon et al. (1994); (16) Thompson et al. (2007); (17) Gonzalez & Wallerstein (1994); (18) Zsargó et al. (2003); (19) Alves et al. (2001); (20) Mooney et al. (2001); (21) Parthasarathy et al. (1992); (22) Giridhar et al. (2010); (23) Kendall et al. (1994); (24) Munn et al. (2004); (25) Kendall et al. (1997); (26) Napiwotzki et al. (1994); (27) Mooney et al. (2002); (28) Quin & Lamers (1992); (29) Kodaira et al. (1970); (30) Gauba & Parthasarathy (2003); (31) Waelkens et al. (1992); (32) Bakker et al. (1996); (33) Lynn et al. (2005); (34) Saffer et al. (1997); (35) Szczerba et al. (2007); (36) Strom & Strom (1970)

6.1.2   Post-AGB Stars in the Palomar Green Catalogue

The PG survey is a 10,714 square degree photographic survey of UV-excess objects at high galactic latitude (Green, 1976). 1874 objects from the original survey were selected for low resolution spectroscopic follow-up based upon the criteria $U - B < -0.46$ and given a spectral classification (Green et al., 1986). Due to the low resolution of the spectra the classifications were quite broad and some stars were classified HBB (blue horizontal branch), sd, sdB and sdBO, which were later found to be post-AGB stars, post-EAGB, HB, EHB, and pop. I and II MS stars from high resolution studies. Saffer et al. (1997) carried out an intermediate resolution follow-up of a collection of stars categorised as above and the resulting T_{eff}-$\log g$ diagram is shown in Fig. 6.1. The interesting objects for this study are the ten post-AGB candidates which are found near the Schönberner (1983) post-AGB tracks. However, also apparent from Fig. 6.1 are the post-EHBs evolutionary tracks and pop. I ZAMS, which overlap the hotter end of the post-AGB tracks. Therefore, to confidently classify the different populations, high resolution spectroscopy is required to determine the chemical composition. In an effort to contain a complete sample for their study and prioritise objects for follow-up observations, Saffer et al. (1997) selected three fields and a brightness limit $B_{\text{PG}} < 14.7$. Only three of the ten post-AGB candidates fulfill the crite-

ria, PG1212+369, PG1243+275 and PG2120+062. High resolution spectroscopy revealed that PG1212+369 has a close secondary component which it had probably interacted with, ruling it out as a standard post-AGB candidate (Hambly et al., 1997). PG1243+275 is metal-poor and its abundance makes it a strong post-AGB candidate. PG2120+062 was confirmed as a post-AGB star through its CNO depletion and further details are given in Lynn et al. (2004). Thus, only two post-AGB stars were observed within the 4200 square degree region of sky followed-up for the complete sample. The position of all the candidates in the T_{eff}-$\log g$ diagram (Fig. 6.1) suggests that they are low mass ($M < 0.55 M_\odot$). This is in agreement with observed mass distributions for similar WD populations (Pauli et al., 2006; Liebert et al., 2005). The two post-AGB stars within the complete sample of three regions of the Galaxy give a reference for the number expected per square degree within a halo. These can be used to compare with synthetic models and extrapolated to the number expected within the whole observing area of SDSS, which is five magnitudes deeper.

6.2   The Population Synthesis Model

Population synthesis models predict the number density of a given population using well studied features and characteristics of the Milky Way. This is done by empirical and theoretical models of the Galactic structure, evolution and star formation. Synthetic maps of the different populations of the Galaxy can be compared to determine a difference between observed and predicted numbers of stars for each phase of evolution. A Monte-Carlo simulation of the post-AGB and WD population was presented by Napiwotzki (2009) which produces a synthetic map of the Galaxy for each type of object. The simulation uses the Galactic model structure of Robin et al. (2003) to randomly assign locations of a large number of stars based on observed densities. Depending on population membership, each star is given a metallicity, an initial mass and kinematical properties. The
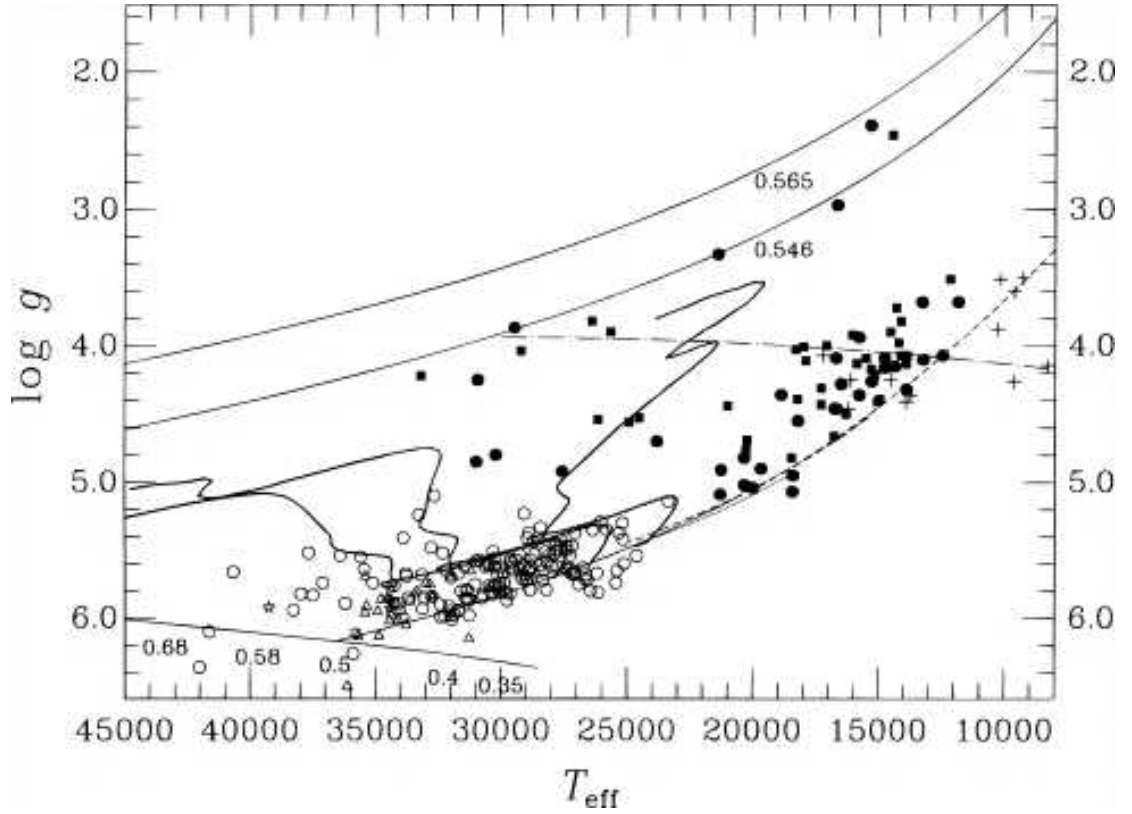
Figure 6.1: The T_{eff}-$\log g$ diagram of the followed up PG regions, Fig. 5 in Saffer et al. (1997). The solid symbols are halo B-type star candidates and the squares are the complete sample (details in this and their paper). The evolutionary tracks listed from low to high gravity are the post-AGB tracks of Schönberner (1983) for the stated masses (solid lines). The dash-dot line (around $\log g{=}4.0$) is the pop. I ZAMS, the various dashed, dotted and undulating curves are HB and post-HB tracks with the solid He ZAMS at the bottom (near $\log g{=}6.0$).

metallicity distribution within each population is defined by Gaussians fitted to the observed data. The thin disc has an age, τ, dependent metallicity relation determined by Fuhrmann (2004):

$$[\mathrm{Fe/H}] = +0.021 - 0.014\tau \tag{6.1}$$

$$\sigma_{[\mathrm{Fe/H}]} = 0.14 + 0.011\tau \tag{6.2}$$

where $\tau = 0$ at the present age. The thick disc is modelled by a Gaussian as per Fuhrmann (2008) with a mean $[\mathrm{Fe/H}] = -0.58$ and scatter $\sigma_{[\mathrm{Fe/H}]} = 0.22$ with an extended tail at low metallicities by Napiwotzki (priv. comm). The Gaussian is

spliced with an exponential function, modelling the tail to:

$$
[\text{Fe/H}] = \begin{cases} e^{-\frac{1}{2}\left(\frac{[\text{Fe/H}] - \overline{[\text{Fe/H}]}}{\sigma}\right)^2} & \text{for } [\text{Fe/H}] > [\text{Fe/H}]_{\text{lim}} \\ k e^{k[\text{Fe/H}]} & \text{for } [\text{Fe/H}] < [\text{Fe/H}]_{\text{lim}} \end{cases}
$$

where $k = 2.6$ is the best fit value and $[\text{Fe/H}]_{\text{lim}} = -0.9$. Finally the halo metallicity distribution is modelled on fits of GCs, with a bimodal fit. The higher metallicity peak is placed similarly to the thick disc. The lower peak is dominant and much broader with $[\text{Fe/H}] = -1.61$ and $\sigma_{[\text{Fe/H}]} = 0.36$.

The Salpeter (1955) IMF is used universally over the Galaxy and is a good representation for the stars likely to reach the post-AGB phase. Number densities of the three populations (thin disc, thick disc and halo) are calibrated with the local population based on the WDs in SPY (Napiwotzki et al., 2003; Pauli et al., 2006). The evolution of each individual star up to the post-AGB phase is determined from the Padova evolutionary tracks (Girardi et al., 2000 and refs. therein). The tracks give a metallicity range of Z=0.0001–0.1 corresponding to a $[\text{Fe/H}]$ of -2.3 to 0.95. This fully covers the range from observed populations which are reproduced in the simulation. All stars which are not old enough to have evolved to the tip of the AGB are discarded. The evolution of the remaining stars is followed through the post-AGB phase and the WD cooling sequence. Post-AGB tracks computed by different groups result in significantly different evoloutionary speeds. Moreover, small variations of the remnant mass can translate into large differences in timescales. Therefore, the simulations are performed using various mass and metallicity post-AGB tracks of Schönberner (1983), Vassiliadis & Wood (1993), Vassiliadis & Wood (1994), Blöcker (1995) and Weiss & Ferguson (2009) to compute T_{eff} and $\log g$ for each object. The post-AGB tracks are described in more detail in Sec. 6.2.1. The final recovered post-AGB populations are normalised with the WDs to the local WD number density of Holberg et al. (2008) which contains a complete sample of WDs within $D < 13$kpc.

6.2.1 Post-AGB Evolutionary tracks

Post-AGB evolutionary tracks have been developed from the basic model of a degenerate core and H burning shell of Paczyński (1971). With core processes of a star defining its luminosity, which remains constant for post-AGB stars, the T_{eff} increase stems from H and He shell burning. The timescale of a post-AGB star to traverse the top of the H-R diagram is related to the stellar burning rate ($\dot{M}_c$) and the envelope mass (M_e) simply by $\Delta t = M_e/\dot{M}_c$. However, transition times are very short for high mass stars due to fast burning processes and with remnant masses observed to be much lower than the AGB mass, a significant mass-loss phase through thermal pulses is required. The thermal pulse phase is notoriously difficult to model and the four sets of post-AGB evolutionary tracks we use vary significantly resulting in different evolutionary speeds. Schönberner (1983) presented the first post-AGB evolution model which included mass loss on the AGB and used the mass loss formula based on the RGB of Reimers (1975). The mass-loss due to a radiative driven wind is empirically related to the parameters of the star by:

$$\dot{M}_R = 4 \times 10^{-13} \frac{L/L_\odot \; M/M_\odot}{R/R_\odot} \tag{6.3}$$

With the luminosity at a constant and the mass relatively unchanged, the mass loss increases as the star contracts. Increased mass loss removes the envelope at a faster rate, thus speeding up evolution time as well. Vassiliadis & Wood (1994) derive a post-AGB mass loss formula based on a best fit of AGB stars in the Magellanic Clouds of:

$$\log \frac{\dot{M}}{\dot{M}_{\text{lim}}} = -3.92 + 0.67 T_{\text{eff}} \tag{6.4}$$

where,

$$\dot{M}_{\text{lim}} = \frac{L}{c v_\infty} \tag{6.5}$$

where c is the speed of light and v_∞ is the expansion velocity of the nebula. Blöcker (1995) used a Reimers mass loss rate on the AGB and then a Mira-like

mass loss to replicate an increase in mass loss expected:

$$\dot{M} = 4.83 \times 10^{-9} M_{\mathrm{ZAMS}}^{-2.1} L^{2.7} \dot{M}_R \tag{6.6}$$

$\dot{M}_R$ is the Reimers rate defined in Eq. 6.3. Which is applied again as the thermal pulse rate reduces until $\sim 20,000$K where the temperature increases the contribution of radiation driven winds from resonant lines with $\dot{M}_{\mathrm{CPN}} = 1.29 \times 10^{-15} L^{1.86}$. Weiss & Ferguson (2009) use similar models as Schönberner (1983) and Blöcker (1995) from the beginning of the post-AGB phase using the Mira relation until the period of Mira pulsations are less than 400 days apart and then apply a linear relation down to the Reimers equation before the increase in temperature and the contribution of resonant lines produce radiative driven winds. The main differences occur on the AGB with radiation-dust interactions and a choice between a theoretical or empirical mass loss depending on the C/O ratio. The resulting post-AGB numbers differ greatly from one track to another and there is a general trend with mass and metallicity as well. The models of Vassiliadis & Wood (1994) leave the AGB earlier and so undergo less mass loss resulting in a significantly larger number of post-AGB stars. However, the other three tracks are in general agreement with each other while the Weiss & Ferguson (2009) models produce a consistent set of results for low metallicities.

The population synthesis model determines the age of a number of post-AGB stars. As post-AGB evolution is so uncertain, all of the aforementioned tracks are applied and post-AGB parameters are determined by interpolating within each model grid. The expected magnitudes of the stars depend on the mass, metallicity, envelope mass and the modelled post-AGB mass loss, which defines the evolutionary speed. The masses range from 0.524–0.943$M_\odot$ and metallicities Z=0.0005 to 0.04 (equivalent to [Fe/H]=−1.6 to 0.3). All post-AGB tracks used for our analysis see the star leave the AGB as H-burners. He-burners evolve at a slower rate and thus would produce an even greater number of observable stars. The higher

mass post-AGB stars evolve at a faster rate to hotter temperatures and so will spend less time on the top of the H-R diagram prior to the WD cooling track, which results in less post-AGB stars at a given time.

6.2.2 What do the Population Synthesis Models Predict?

The synthetic populations take into consideration interstellar extinction and a brightness limit can be set to determine a magnitude limited sample. Figs. 6.2-6.4 show a synthetic post-AGB population of the Galaxy using the $M = 0.546M_\odot$ evolutionary tracks of Schönberner (1983) with brightness limits of $V = 12$, $V = 16$ and $V = 20$, respectively. The predicted numbers for the $M = 0.546M_\odot$ track with these brightness limits applied are listed in Table 6.2. The simulation implies that the majority of Galactic post-AGB stars are detected for a limiting magnitude of $V = 20$ which is double the predicted number of the PG survey which has a limit of $V = 14.7$. The post-AGB evolution for a $M = 0.546M_\odot$ is too slow to ionise the ejected nebula before it is dispersed (Schönberner, 1983). Therefore, the simulation suggests there are no PNe outside of the thin disc, which is in agreement with the observed halo population to date (mentioned earlier) which suggests that all known halo PNe are the product of interacting binary systems. According to the simulations, post-AGB stars (with and without PNe) are predicted to be distributed across the Galaxy with the calculated ratios of 2:1:2 for thin disc : thick disc : halo populations. For a typical post-AGB mass in the Galactic halo ($M = 0.55M_\odot$) thousands of hot post-AGB stars ($T_{\mathrm{eff}} > 10,000$K) without PNe are expected to be observed, but only $\sim$30 are known (see Table 6.1). Similarly to the Galactic PNe sample, known post-AGB stars in the halo are only $\sim$1% of the number expected. In order to quantify the populations to compare with literature, the birthrate is a more universal parameter. The post-AGB birthrate is simply the number of stars reaching the tip of the AGB per year and to determine an average, birthrates are calculated by binning the post-AGBs in 5,000 year increments. The average number for each bin gives the total for a

Table 6.2: A summary of observable post-AGBs for varying magnitude limits within the Galaxy predicted by simulations.

V_{lim}	N_{thin}	N_{thick}	N_{halo}	N_{total}
12	1442	1416	1225	4083
14.7	4312	6669	10,990	21,971
16	5499	9040	16,632	31,171
20	7572	11,012	20,303	38,887
All	7780	11,611	20,441	39,832

given population with the standard deviation providing an estimate of statistical fluctuations. Birthrates of 0.29 ± 0.03, 0.17 ± 0.02 and 0.41 ± 0.05 post-AGBs per year are determined for the thin disc, thick disc and halo respectively. This produces a Galactic post-AGB birthrate of $0.87 \pm 0.10 \text{yr}^{-1}$.

6.2.3 Synthetic Population Estimates from other Methods

Synthetic population estimates of post-AGB stars have been determined by other methods within the literature. Moe & De Marco (2006) use a population synthesis model to determine the contribution of binaries towards PNe. An offshoot from their results is an estimate of post-AGB birthrates for each component of the Milky Way. They estimate the stellar density by using an approximation of the population mass. For the halo they randomly distribute stars around the halo with weighting using the Robin et al. (2003) Galactic distribution. A mass is assigned using a Chabrier (2003) IMF until the total mass is reached. The stellar lifetimes are determined using the same Padova group (Girardi et al., 2000 and refs. therein) evolutionary tracks as used here. The SFH for the halo and thick disc are both in the form of one long lasting burst. Each burst is estimated to be 4-5 Gyrs, with mean ages of 11.5 and 10 Gyrs for halo and thick disc respectively. Further details including metallicity distributions are given in Moe & De Marco (2006). They produce birthrates of 1.3 ± 0.4, 0.09 ± 0.02 and 0.14 ± 0.04 post-AGBs yr^{-1} for the thin and thick discs and halo respectively. Assuming a 20 kpc radius spheroid the halo post-AGB birthrate per unit volume can be shown as 4.18×10^{-6} $\text{kpc}^{-3} \text{yr}^{-1}$. de Boer (1987) make an estimate of the number of Galactic halo post-
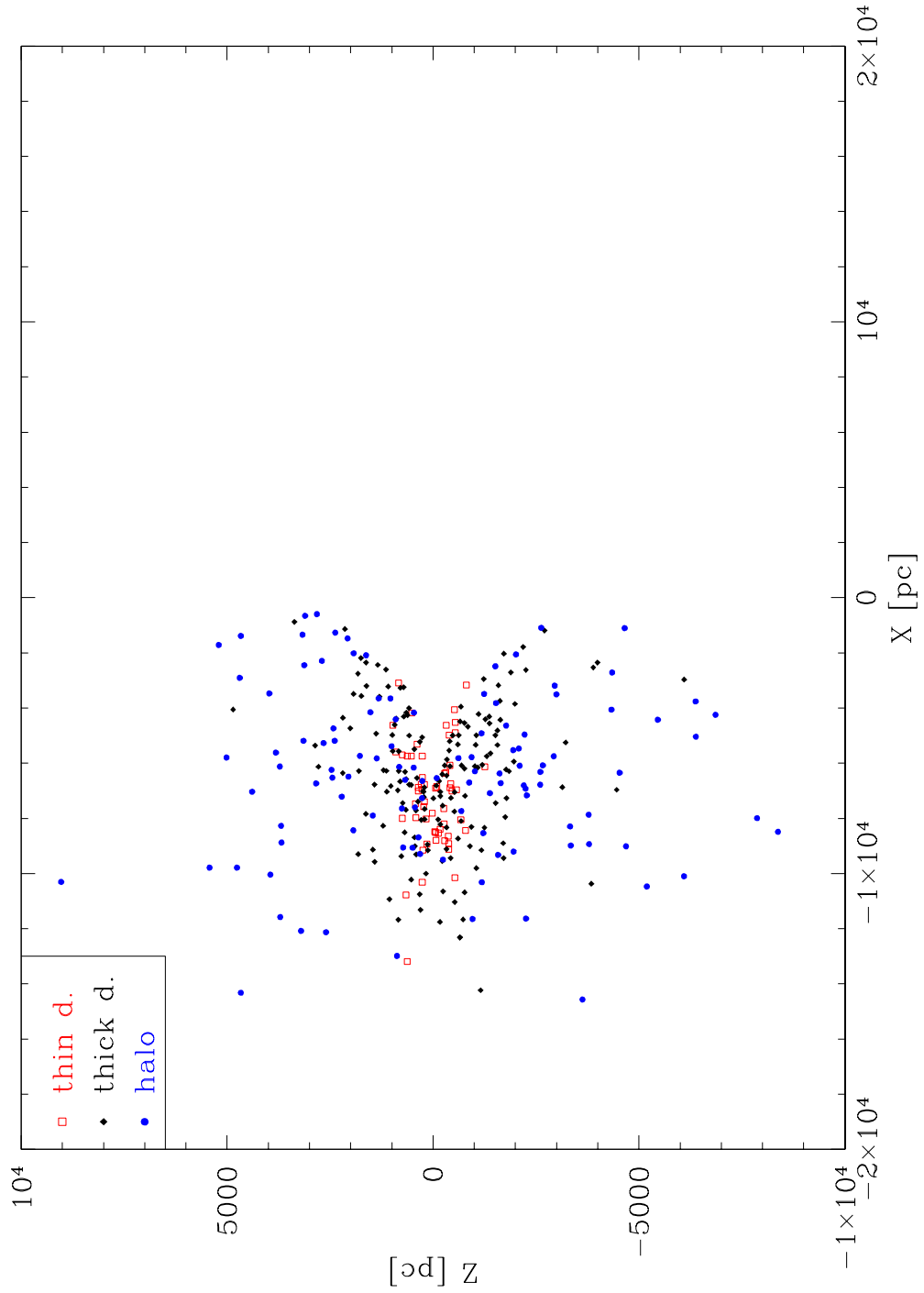
Figure 6.2: A synthetic map of the post-AGB population by Napiwotzki (2009) complete to a brightness limit of $V = 12$. Blue spots are halo objects, black diamonds are thick disc and red squares, thin disc.

111
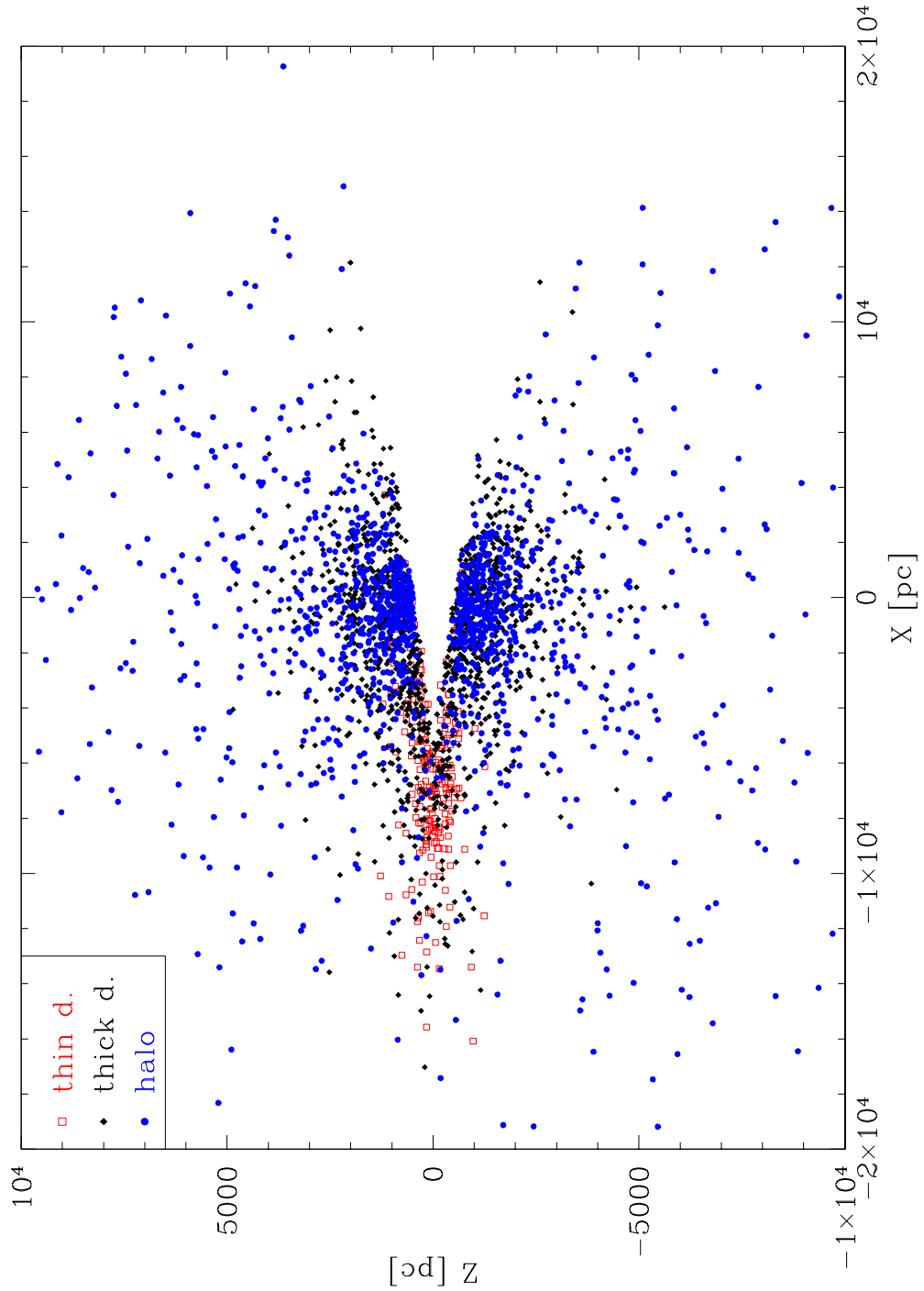
Figure 6.3: A synthetic map of the post-AGB population by Napiwotzki (2009) complete to a brightness limit of $V = 16$. Blue spots are halo objects, black diamonds are thick disc and red squares, thin disc.
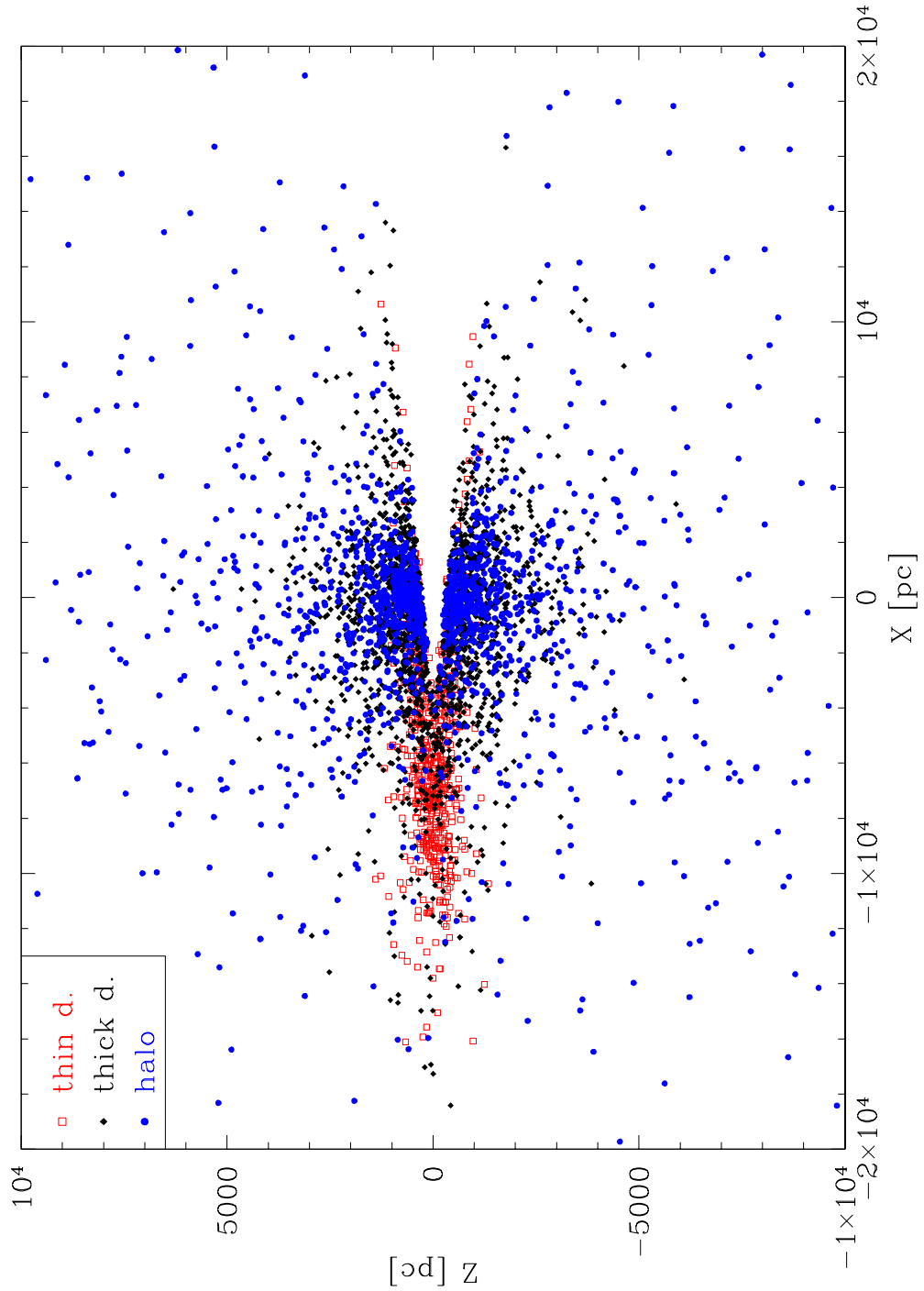
Figure 6.4: A synthetic map of the post-AGB population by Napiwotzki (2009) complete to a brightness limit of $V = 20$. Blue spots are halo objects, black diamonds are thick disc and red squares, thin disc.

AGB stars using star counts and observed UV bright stars in GCs. Their sample consisted of 36 GCs containing 50 UV bright stars, a third of which are post-AGB stars. Approximating an average GC mass they determine that there is one UV bright star per $3 \times 10^5 M_\odot$ for GCs. Applying some further assumptions based on distribution and GC and halo mass, they predict 10,000 post-AGB stars in the Galactic halo population. Assuming a post-AGB lifetime of 30,000 years the total number translates to a post-AGB halo birthrate of 0.33 post-AGB yr^{-1} Again assuming a 20kpc spheroid the total number translates to a post-AGB halo birthrate per unit volume of 8.95×10^{-5} post-AGBs $\mathrm{kpc}^{-3}\mathrm{yr}^{-1}$. These two synthetic estimates agree relatively well with our estimates but the thin disc to halo ratio for Moe & De Marco (2006) is markedly different to this study. With the thin disc containing no post-AGB objects due to fast evolution, the thin disc difference may be overlooked but the halo estimate, if three times greater, could be significant. However, the mass of the spheroid is not well known and given as Moe & De Marco (2006) estimated a value of $2 \times 10^9 M_\odot$ from a range of 0.3-3.0 $\times 10^9 M_\odot$, their estimate contains a significantly larger error than quoted putting it in agreement with our halo population. Observational WD birthrates are fairly well determined. The latest estimate of $1 \pm 0.25 \times 10^{-12}\,\mathrm{pc}^{-3}\,\mathrm{yr}^{-1}$ by Liebert et al. (2005) is of the local population and is of the same order of magnitude as our total sample, but the authors do not distinguish the individual Galactic components. The synthetic population determined here is in general agreement with the discussed theoretical and observational birthrate determinations (see Table 6.3) and thus our comparison to the observations is validated. To determine the number of synthetic post-AGB stars that are observable, the post-AGB stars evolved through evolutionary tracks and the determined absolute magnitudes are compared to the limitations of a survey.

Table 6.3: A summary of post-AGB birthrate estimates for the various populations.

Study	χ_{thin} [yr^{-1}]	χ_{thick} [yr^{-1}]	χ_{halo} [yr^{-1}]	χ_{total}
Moe & De Marco (2006)	1.3 ± 0.4	0.09 ± 0.02	0.14 ± 0.04	1.54 ± 0.56
de Boer (1987)	–	–	0.33	–
This study	0.29 ± 0.03	0.17 ± 0.02	0.41 ± 0.05	0.87 ± 0.10

6.3   PG – Synthetic Vs. Observed

The total synthetic Galactic population of post-AGB stars suggests that the known population is a small fraction of what is expected, this number can be quantified using a complete magnitude limited sample. The Saffer et al. (1997) PG sub-sample contained three complete regions of the Galactic halo up to a brightness limit of $B_{\text{PG}} < 14.7$. A simulated population of post-AGB stars in the Saffer et al. (1997) regions was extracted by selecting the stars from the same three fields applying the same brightness limit and the positional limitations of $21^{\text{h}} < \text{R.A.} < 1^{\text{h}}$, $0^{\text{o}} < \text{Dec.} < 20^{\text{o}}$ for field one, $8.5^{\text{h}} < \text{R.A.} < 10.5^{\text{h}}$, $-10^{\text{o}} < \text{Dec.} < 50^{\text{o}}$ for field two and the final field $b > 70^{\text{o}}$. A temperature criteria of 14,000–34,000K was defined with the low end estimate corresponding to the to the PG $U - B$ cutoff criteria and the considerable photometric uncertainty from the photographic plates, and the high end by the hottest post-AGB candidate found in their sample. These criteria are conservative and can be interpreted as a lower limit on the number of stars which should be observed in that survey. The resulting synthetic post-AGB numbers differ greatly from one track to another. Figs. 6.5 and 6.6 show a simulated post-AGB population, within the brightness and positional criteria set out, applying the $M = 0.546 M_{\odot}$ evolutionary track of Schönberner (1983). Similar plots are produced for each post-AGB evolutionary track and are summarised in Table 6.4. The masses stated in the first and second columns are of the final post-AGB/WD objects and the initial zero-age MS (ZAMS) in their respective papers. The metallicities are the initial compositions of the stars on the MS. The numbers for each population and the total
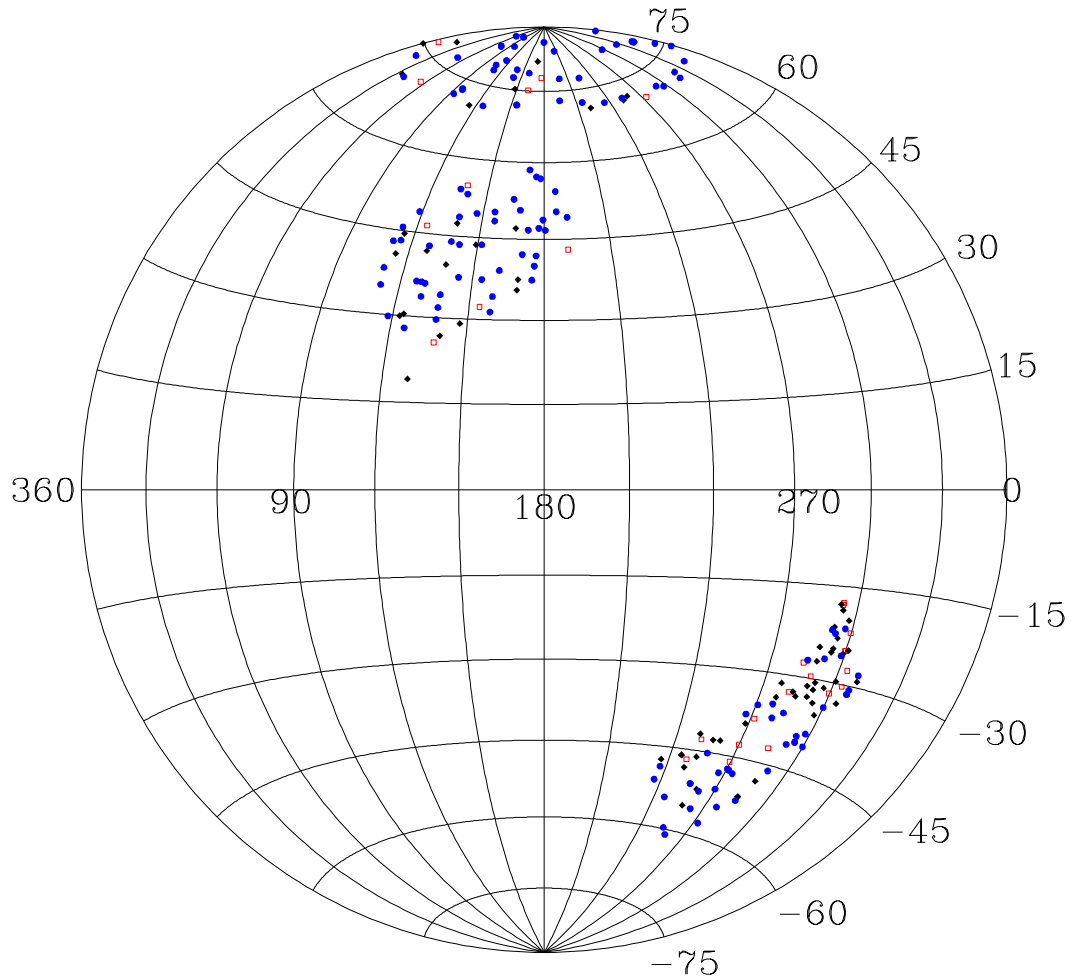
Figure 6.5: An Aitoff-Hammer projection of the post-AGB population from the three selected complete regions of the PG survey in Galactic coordinates. This example is for a $0.546 M_\odot$ assumed post-AGB mass. The red, square, open symbols represent thin disc post-AGBs, the black, filled, diamonds the thick disc and the blue filled circles the halo.

are given for the Galaxy with the reference for each model is stated in the final column. The errors are determined using the 20 times over-populated original Monte-Carlo simulation. 5% of the whole sample is randomly selected, which is the scale factor for the normalisation based on the local WD density. The population is re-sampled 10,000 times and the mean and standard deviation represent the average total and error respectively. The same trend is observed for all four evolutionary tracks used which find a sharp increase in the number expected for low masses. The tracks of Vassiliadis & Wood (1993) produce significantly higher
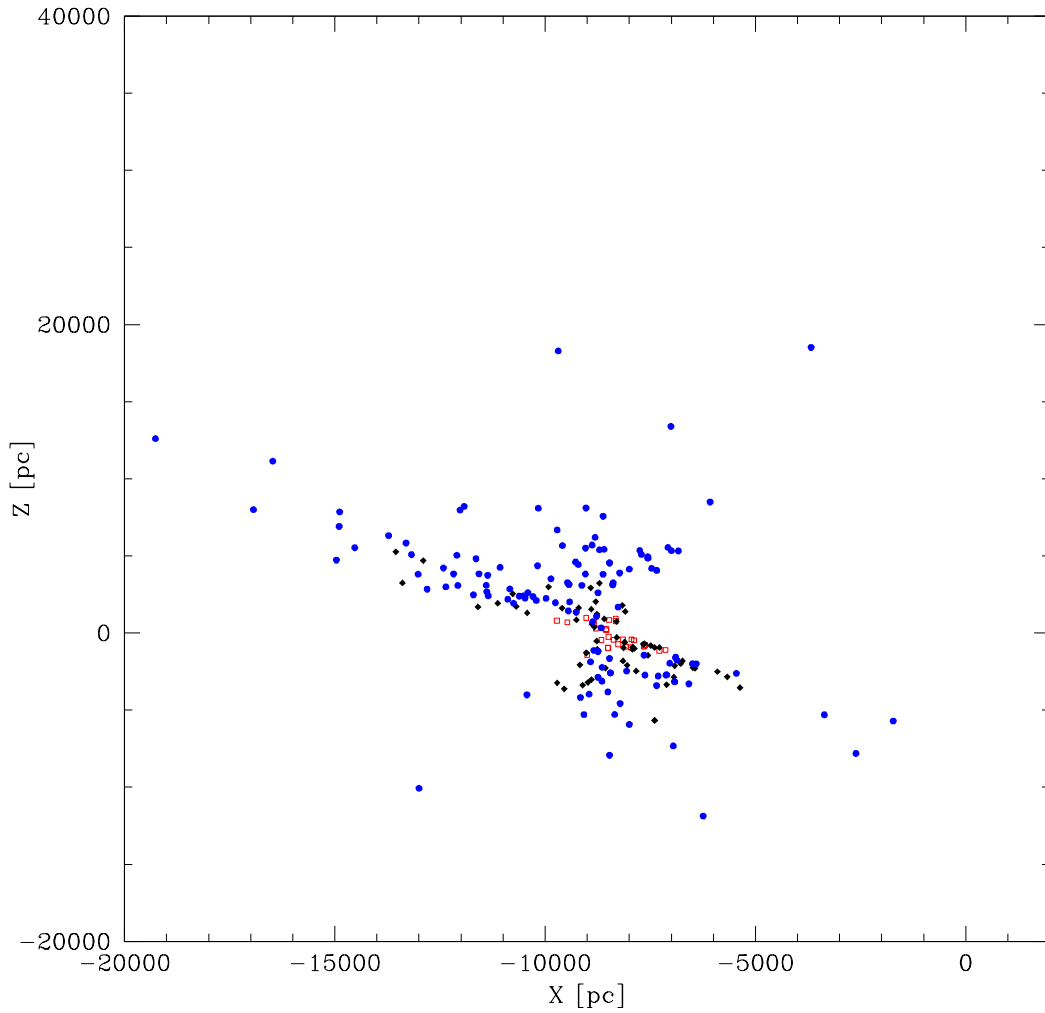
Figure 6.6: A Galactic vector projection of the post-AGB population shown in Fig. 6.5. The post-AGB mass and symbols are the same as Fig. 6.5. Note the Galactic centre is at vector [X,Z]=(0,0) and the objects converge to the Sun's position in the Galaxy at approximately [X,Z]=(8500,0).

post-AGB masses, however their initial masses, where similar to the other three studies, produce a similar number of post-AGB stars, suggesting that the evolutionary speed is in agreement but a lower mass loss is applied on the AGB with the envelope mass not affected. The low mass, low metallicity tracks should represent the predicted halo population well, however, the tracks predict high numbers of post-AGB stars, two to ten times greater than the observed number. The high mass tracks are in agreement with the low number of post-AGB stars observed but this is due to their fast evolution into central stars as they ionise their ejected

envelopes. This is unrealistic as high remnant masses are not observed in the sample of known halo post-AGB stars (Saffer et al., 1997) and the number of known halo PNe is even smaller (possibly none if binaries are ruled out).

6.4 How do Globular Clusters fit in?

It has long been observed that GCs produce very few PNe and in fact mean WD mass determinations imply low mass remnants ($M \approx 0.50 \pm 0.02 M_\odot$; Alves et al., 2000) with the GC mean turn off mass of $0.85 M_\odot$ (Jacoby et al., 1997). A comprehensive review of hot stars in GCs was carried out by Moehler (2001) and includes all UV bright objects from several studies. A back of the envelope estimate of the number of post-AGB stars expected for GCs can be determined using the number of stars leaving the MS, N_{PMS}, estimated from simple stellar populations. Renzini & Buzzoni (1986) pointed out that the ratio of N_{PMS} to luminosity is almost constant for populations of intermediate to old age and Eq. 8 in Buzzoni (1989) gives:

$$N_{\mathrm{PMS}} = 1.7 \pm 0.4 \times 10^{-11} [L_\odot^{-1} \, \mathrm{yr}^{-1}] \, L_*[L_\odot] \, t_{\mathrm{PMS}}[\mathrm{yrs}] \tag{6.7}$$

This predicts the number leaving the MS for the total luminosity of a population, L_*, and the evolutionary timescale, t_{PMS}. The total luminosity of all GCs within the Galaxy is determined as $2.4 \times 10^7 \, L_\odot$ based on integrating the GC luminosity function (Jacoby et al., 1997). Assuming all GC stars evolve through the post-AGB phase with $M = 0.546 M_\odot$, using the Schönberner (1983) track, it takes 170,000 years to evolve from $T_{\mathrm{eff}} = 10,000\mathrm{K}$ to $T_{\mathrm{eff}} = 60,000\mathrm{K}$. In that timescale 69 ± 16 post-AGB stars are predicted to be observed in GCs. Moehler (2001) and Table 6.1 show that less than 20 have been observed to date, implying that less than a third of GC stars are evolving through the post-AGB phase. GCs contribute approximately a third (halo+GC combined) of the observed halo post-AGB population with less than 10% of the halo mass (Schaerer & Charbonnel,

2011). GCs are not explicitly modelled in the synthetic populations but if included, would add considerably to numbers of halo post-AGB stars yet still leave a serious deficit. However, even GCs themselves are consistent with our findings for the halo population in that the minority of stars are evolving through the post-AGB phase.

6.5 Halo Post-AGB and CSPNe Population Conclusion

Surveys and studies of the Galactic halo have detected very few post-AGB stars and even less PNe. Predicted numbers are heavily dependent on the post-AGB track used, however, the old population of the Galactic halo implies that post-AGB stars (and possible CSPNe) are expected to be of low mass. The synthetic Galactic model shows that the lower the mass of the central star (and progenitor) the slower the evolution and so the more likely the star is to sit within the post-AGB region of parameter space. This increases the number of expected post-AGBs with lower masses and this is displayed in Fig. 16 of Weiss & Ferguson (2009). In the same figure, a small metallicity effect can be seen and both effects can be seen within the sample here, however, the difference in predicted post-AGB numbers is fairly small at sub-solar metallicities. The contrast between the numbers expected and observed is significant with many less post-AGB stars observed than are predicted. If these stars do not exist then it could be possible that only very few thick disc/halo stars evolve through the post-AGB channel, which is generally the assumed standard path. The PG sub-sample is only a fraction of the halo population and could prove to be an anomaly. To confirm the findings a systematic search for post-AGB candidates in SDSS is executed in Sect. 7.

Table 6.4: Simulated post-AGB population for various models in the region of the Saffer et al. (1997) complete sample

Post-AGB Mass $[M_\odot]$	MS Mass $[M_\odot]$	MS Metallicity $[Z]$	N^o thin disc	N^o thick disc	N^o halo	Total	Ref.
0.538	1.0	0.0005	0 ± 1	3 ± 2	58 ± 7	61 ± 8	WF09
0.551	1.2	0.0005	0 ± 0	1 ± 1	37 ± 6	38 ± 6	WF09
0.579	1.6	0.0005	0 ± 0	0 ± 1	14 ± 4	15 ± 4	WF09
0.565	1.8	0.0005	0 ± 0	0 ± 1	12 ± 3	12 ± 3	WF09
0.600	2.0	0.0005	0 ± 0	0 ± 0	6 ± 2	6 ± 2	WF09
0.623	1.0	0.001	0 ± 1	3 ± 2	64 ± 8	67 ± 8	VW93
0.663	1.5	0.001	0 ± 0	0 ± 1	14 ± 4	15 ± 4	VW93
0.593	1.0	0.004	1 ± 1	6 ± 2	139 ± 12	146 ± 12	VW93
0.533	1.2	0.004	0 ± 1	3 ± 2	58 ± 7	61 ± 8	WF09
0.536	1.5	0.004	0 ± 0	1 ± 1	31 ± 5	32 ± 6	WF09
0.640	1.5	0.004	0 ± 0	1 ± 1	37 ± 6	38 ± 6	VW93
0.537	1.6	0.004	0 ± 0	1 ± 1	21 ± 5	22 ± 5	WF09

Post-AGB Mass $[M_\odot]$	MS Mass $[M_\odot]$	MS Metallicity $[Z]$	N^o thin disc	N^o thick disc	N^o halo	Total	Ref.
0.493	1.8	0.004	0 ± 0	2 ± 1	63 ± 8	65 ± 8	WF09
0.529	2.0	0.004	0 ± 0	2 ± 1	38 ± 6	40 ± 6	WF09
0.672	2.0	0.004	0 ± 0	2 ± 1	42 ± 6	43 ± 7	VW93
0.692	2.5	0.004	0 ± 0	0 ± 0	2 ± 1	2 ± 1	VW93
0.855	3.5	0.004	0 ± 0	0 ± 0	1 ± 1	1 ± 1	VW93
0.943	5.0	0.004	0 ± 0	0 ± 0	0 ± 1	0 ± 1	VW93
0.532	1.0	0.008	0 ± 1	3 ± 2	49 ± 7	52 ± 7	WF09
0.530	1.2	0.008	0 ± 0	2 ± 1	46 ± 7	48 ± 7	WF09
0.620	1.5	0.008	0 ± 0	0 ± 1	11 ± 3	12 ± 3	VW93
0.538	1.6	0.008	0 ± 0	1 ± 1	19 ± 4	20 ± 4	WF09
0.527	1.8	0.008	0 ± 0	0 ± 1	16 ± 4	17 ± 4	WF09
0.528	2.0	0.008	0 ± 0	0 ± 0	0 ± 1	0 ± 1	WF09
0.668	2.0	0.008	1 ± 1	1 ± 1	12 ± 3	13 ± 4	VW93
0.797	3.5	0.008	0 ± 0	0 ± 0	2 ± 1	2 ± 1	VW93

<div align="center">Continued on next page</div>

Post-AGB Mass $[M_\odot]$	MS Mass $[M_\odot]$	MS Metallicity [Z]	N^o thin disc	N^o thick disc	N^o halo	Total	Ref.
0.912	5.0	0.008	0 ± 0	0 ± 0	0 ± 1	0 ± 1	VW93
0.569	1.0	0.016	1 ± 1	7 ± 3	182 ± 13	191 ± 14	VW93
0.597	1.5	0.016	0 ± 0	2 ± 2	50 ± 7	52 ± 7	VW93
0.633	2.0	0.016	0 ± 0	0 ± 1	17 ± 4	17 ± 4	VW93
0.677	2.5	0.016	0 ± 0	0 ± 0	9 ± 3	9 ± 3	VW93
0.754	3.5	0.016	0 ± 0	0 ± 0	3 ± 2	3 ± 2	VW93
0.900	5.0	0.016	0 ± 0	0 ± 0	0 ± 1	0 ± 1	VW93
0.508	1.0	0.02	0 ± 1	3 ± 2	60 ± 8	64 ± 8	WF09
0.524	1.2	0.02	0 ± 0	3 ± 2	54 ± 7	57 ± 7	WF09
0.539	1.5	0.02	0 ± 0	1 ± 1	26 ± 5	26 ± 5	WF09
0.541	1.6	0.02	0 ± 0	1 ± 1	21 ± 4	22 ± 5	WF09
0.525	1.8	0.02	1 ± 1	12 ± 3	237 ± 15	250 ± 15	WF09
0.543	2.0	0.02	0 ± 0	0 ± 1	11 ± 3	11 ± 3	WF09
0.546	0.8	0.021	8 ± 3	50 ± 7	397 ± 19	455 ± 21	DS83

<div align="center">Continued on next page</div>

Post-AGB Mass [$M_\odot$]	MS Mass [$M_\odot$]	MS Metallicity [Z]	N^o thin disc	N^o thick disc	N^o halo	Total	Ref.
0.524	1.0	0.021	8 ± 3	54 ± 7	443 ± 21	505 ± 22	TB95
0.565	1.0	0.021	1 ± 1	3 ± 2	37 ± 6	40 ± 6	DS83
0.605	3.0	0.021	0 ± 0	2 ± 1	14 ± 4	16 ± 4	TB95
0.625	3.0	0.021	0 ± 0	0 ± 1	6 ± 2	6 ± 3	TB95
0.696	4.0	0.021	0 ± 0	0 ± 0	1 ± 1	1 ± 1	TB95
0.836	5.0	0.021	0 ± 0	0 ± 0	1 ± 1	1 ± 1	TB95
0.940	7.0	0.021	0 ± 0	0 ± 0	0 ± 0	0 ± 0	TB95
0.512	1.0	0.04	2 ± 1	9 ± 3	219 ± 14	229 ± 15	WF09
0.523	1.2	0.04	1 ± 1	6 ± 2	107 ± 10	113 ± 10	WF09
0.533	1.5	0.04	0 ± 1	4 ± 2	72 ± 8	76 ± 9	WF09
0.536	1.6	0.04	0 ± 0	1 ± 1	21 ± 5	22 ± 5	WF09
0.537	1.8	0.04	0 ± 0	1 ± 1	23 ± 5	24 ± 5	WF09
0.552	2.0	0.04	0 ± 0	0 ± 1	15 ± 4	15 ± 4	WF09
0.534	1.0	0.0005^α	0 ± 1	3 ± 2	64 ± 8	68 ± 8	WF09

Continued on next page

| Post-AGB Mass | MS Mass | MS Metallicity | N^o thin disc | N^o thick disc | N^o halo | Total | Ref. |
[$M_\odot$]	[$M_\odot$]	[Z]					
0.546	1.2	0.0005^α	0 ± 0	2 ± 1	47 ± 7	50 ± 7	WF09
0.567	1.5	0.0005^α	0 ± 0	1 ± 1	23 ± 5	24 ± 5	WF09
0.558	1.6	0.0005^α	0 ± 0	0 ± 1	16 ± 4	17 ± 4	WF09
0.561	1.8	0.0005^α	0 ± 0	0 ± 1	16 ± 4	16 ± 4	WF09
0.599	2.0	0.0005^α	0 ± 0	0 ± 0	8 ± 3	8 ± 3	WF09
0.531	1.0	0.004^α	0 ± 1	3 ± 2	61 ± 8	64 ± 8	WF09
0.539	1.2	0.004^α	0 ± 0	2 ± 2	47 ± 7	49 ± 7	WF09
0.544	1.5	0.004^α	0 ± 0	1 ± 1	27 ± 5	28 ± 5	WF09
0.520	1.6	0.004^α	0 ± 0	1 ± 1	25 ± 5	25 ± 5	WF09
0.528	1.8	0.004^α	0 ± 0	3 ± 2	55 ± 7	58 ± 7	WF09
0.516	2.0	0.004^α	0 ± 0	0 ± 1	13 ± 4	13 ± 4	WF09
0.525	1.0	0.008^α	0 ± 0	1 ± 1	17 ± 4	18 ± 4	WF09
0.532	1.2	0.008^α	0 ± 0	3 ± 2	57 ± 7	60 ± 8	WF09
0.538	1.5	0.008^α	0 ± 0	0 ± 0	5 ± 2	5 ± 2	WF09

<div align="center">Continued on next page</div>

Post-AGB Mass [$M_\odot$]	MS Mass [$M_\odot$]	MS Metallicity [Z]	N^o thin disc	N^o thick disc	N^o halo	Total	Ref.
0.537	1.6	0.008^α	0 ± 0	0 ± 0	2 ± 1	2 ± 1	WF09
0.523	1.8	0.008^α	0 ± 0	1 ± 1	28 ± 5	29 ± 5	WF09
0.498	2.0	0.008^α	0 ± 0	0 ± 0	0 ± 1	0 ± 1	WF09
0.509	1.0	0.02^α	1 ± 1	4 ± 2	88 ± 9	93 ± 9	WF09
0.520	1.2	0.02^α	0 ± 0	1 ± 1	26 ± 5	27 ± 5	WF09
0.538	1.5	0.02^α	0 ± 0	1 ± 1	24 ± 5	24 ± 5	WF09
0.545	1.6	0.02^α	0 ± 0	0 ± 1	16 ± 4	17 ± 4	WF09
0.541	1.8	0.02^α	0 ± 0	0 ± 1	14 ± 4	15 ± 4	WF09
0.537	2.0	0.02^α	0 ± 0	0 ± 0	9 ± 3	10 ± 3	WF09
0.513	1.0	0.04^α	1 ± 1	8 ± 3	191 ± 13	200 ± 14	WF09
0.522	1.2	0.04^α	1 ± 1	5 ± 2	107 ± 10	113 ± 11	WF09
0.537	1.5	0.04^α	0 ± 1	3 ± 2	58 ± 7	61 ± 8	WF09
0.535	1.6	0.04^α	0 ± 0	0 ± 1	18 ± 4	19 ± 4	WF09
0.538	1.8	0.04^α	0 ± 1	3 ± 2	62 ± 8	65 ± 8	WF09

Post-AGB Mass	MS Mass	MS Metallicity	N^o thin disc	N^o thick disc	N^o halo	Total	Ref.
[$M_\odot$]	[$M_\odot$]	[Z]					
0.552	2.0	0.04$^\alpha$	0 ± 0	0 ± 1	8 ± 3	9 ± 3	WF09
Observed	–	–	0	0	2(?)	2	–

References:- TB95 – Blöcker (1995); DS83 – Schönberner (1983); VW93 – Vassiliadis & Wood (1993); WF09 – Weiss & Ferguson (2009)
α denotes an alpha-enhanced initial composition for the models of Weiss & Ferguson (2009).

Chapter 7

Extending the Search for Galactic Halo post-AGB Stars to SDSS

The seventh public data release (DR7) of SDSS contains completeted observations of the field surrounding the northern Galactic pole (NGP) (Abazajian et al., 2009) containing 11,663 square degrees of imaging (Figs. 7.1 and 7.2). Photometry of 357 million objects are included in the $u'g'r'i'z'$ photometric bands to depths of 22.0, 22.2, 22.2, 21.3 and 20.5, respectively. Included within DR7 is the Sloan Extension for Galactic Understanding and Exploration (SEGUE) which is a project dedicated to studying the kinematics and populations of the Galaxy, in particular the halo (Yanny et al., 2009). SEGUE selects candidates for spectroscopic follow-up using a photometric criteria set out in Table 5 of Yanny et al. (2009). Combined with the spectra from the original legacy survey, an extensive spectroscopic database of over 1.6 million objects with a minimum brightness of $r' < 19.1$ has been archived. The spectra cover a wavelength range of $3800-9200\,\text{Å}$ with a resolution of $R \equiv \lambda/\Delta\lambda = 1800 - 2200$. Approximately 25% of spectra are classified as stellar objects and any post-AGB candidates fall into the target category of WD/sdO/sdB, where sdO and sdB are subdwarfs of O and B type, respectively. The SDSS DR4 WD catalogue contains over 16,000 WD spectra and almost 1,000 spectra of sds (Kleinman et al., 2007). The DR7 release doubles the
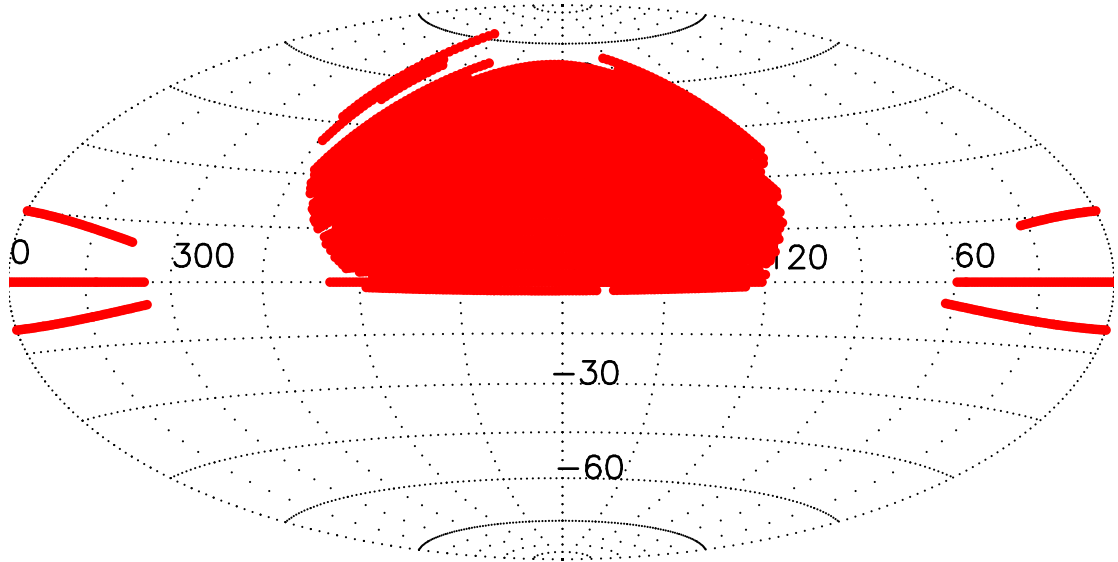
Figure 7.1: The Observed areas of SDSS in Equatorial coordinates. The image is from the SDSS website.
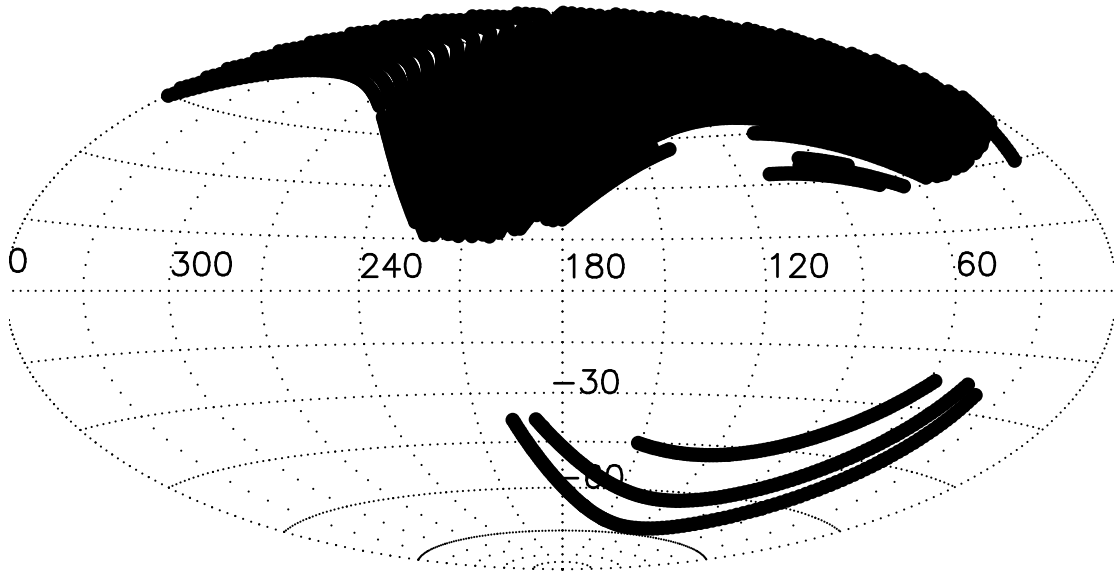
Figure 7.2: The Observed areas of SDSS in Galactic coordinates. The image is from the SDSS website.

number of observed candidate WDs (Kleinman, 2010) and the same is expected for hot sds, increasing the possibility of observed post-AGB spectra within DR7. Spectroscopy identifies post-AGB candidates with more certainty than photometry as atmospheric parameters are more accurately determined. However, the limited number of fibres in the SDSS spectrograph and the selection criteria for these objects within SDSS mean that possible post-AGB stars may be overlooked. Therefore, we carried out a post-AGB search for the vast amount of SDSS spectra as well as a preliminary photometric search which identifies plausible candidates which would require spectroscopic follow-up to be classified as post-AGB stars.

7.1   SDSS Spectroscopic Search

The large number of SDSS spectra available meant that a photometric pre-selection had to be applied to search for post-AGB stars to save on memory space and cut down on CPU time when fitting profiles. The photometric colour criteria are deduced from the SEDs of the model grids applied in Sect. 4 with a generous allowance for reddening and emission lines. Applying photometric criteria removes all red objects with cuts at $u'-g' < 1.5$, $g'-r' < 0.1$, $r'-i' < 0.1$ and $i'-z' < 0.2$. To test the photometric cuts, the ten candidate post-AGB stars spectroscopically observed in the PG survey were cross-matched with the SDSS databases. None of the ten candidate post-AGB stars have been observed spectroscopically in SDSS. However, eight of the objects are in the SDSS photometric database and all but one (due to saturation) of these fulfill the photometric criteria used to initially identify spectroscopic candidates. Therefore, none or few objects will be discarded by the photometric cut. This results in some QSOs, Seyferts and other emission line galaxies being incorporated in the sample with expected stellar contaminants such as WDs, MS and HB stars. The spectra of objects with blue photometric colours, are downloaded from the central database which have been reduced by the automated pipeline. The spectra are observed with two spectrographs, blue

(3800-6510 Å) and red (5800-9200 Å) in the optical each containing 320 fibres. The total exposure time for each observation is 45 minutes, split into three exposures to remove the effect of cosmic rays. Flat fields are taken with observations of standard stars before and after each exposure to calibrate the spectra before co-adding and merging the three exposures and two spectrographs together. The database contains a .fit file for each spectra titled, spSpec-$mjd-$plate-$fiber.fit, where $mjd is the observation date, $plate, the plate number and $fiber is the fibre used for the individual object. The .fit file contains the flux and wavelength calibrated spectra, sky subtracted spectra with error and mask arrays. The calibrated spectra is extracted and converted to an ascii file to perform a fit to the Balmer lines and determine atmospheric parameters. Balmer lines are used to determine stellar parameters as the wings are sensitive to $\log g$ and the line core depth to T_{eff}. Additionally, other features can be used to determine and confirm stellar type, (i.e. He I lines 4471 Å and 5876 Å are prominent absorption lines in post-AGB stars).

7.2 Deriving Atmospheric Parameters from Spectroscopy

Applying the photometric cut leaves $\sim 21,000$ remaining candidate post-AGB spectra from the SDSS spectroscopic database. Atmospheric parameters of H-rich stars may be determined from low or medium resolution spectroscopy by fitting Balmer lines. Model spectra are fitted to the observed spectra using the FITSB2 program (Napiwotzki et al., 2004) which minimizes the reduced χ^2 by applying a simplex algorithm based on the AMOEBA routine (Press et al., 1992). The routine is stable and highly likely to find a solution, however, it can settle at local minima. This is particularly likely for hot and cool WD solutions, therefore for every spectrum four fits are carried out. A cool WD solution with starting $T_{\mathrm{eff}} < 12,000$ K and a hot WD solution with $T_{\mathrm{eff}} > 12,000$ K are fitted. This is due

Table 7.1: The Range of atmospheric Parameters for each model grid.

Grid	T_{eff} [K]	$\log g$ $[\text{cm s}^{-2}]$	$T_{\text{eff}}^{\text{start}}$ [K]	$\log \text{g}^{\text{start}}$ $[\text{cm s}^{-2}]$
ATLAS9	$8{,}000 - 50{,}000$	$2.00 - 6.50^{\text{a}}$	$20{,}000$	4.00
TLUSTY	$27{,}500 - 55{,}000$	$3.00 - 4.75^{\text{a}}$	$20{,}000$	4.00
Cool WD	$10{,}000 - 100{,}000$	$7.00 - 9.00$	$10{,}000$	8.00
Hot WD	$10{,}000 - 100{,}000$	$7.00 - 9.00$	$20{,}000$	8.00

[a] The ATLAS9 and TLUSTY grids do not converge to solutions for some high T_{eff} and low $\log g$ values within this range.

to a peak of occupation numbers in the $n = 2$ level at $T_{\text{eff}} \sim 12{,}000$K as given by the Saha-Boltzmann equation. This meant that the normalised spectrum appears similar for temperatures above and below this value. The third and fourth runs are done with grids of ATLAS9 and TLUSTY model spectra. The parameter range for the model grids are listed in Table 7.1 together with the starting temperature and gravity for each solution. The sampling of the three sets of model spectra vary but are all higher than the observed spectra. Subsequently the spectra are convolved with a Gaussian to the same resolution as the observed spectra. Linear interpolation is carried out to compute spectra for points between the grid. The observed and model spectra are normalised by a linear fit to the region selected for line fitting. Initial T_{eff} and $\log g$ are set for the first fit as well as a step size and are optimised using the AMOEBA routine by minimising the χ^2. The standard deviation over the fitted region of the observed spectrum, σ, is determined using a smoothed parabola for a given pixel size. This is better than a direct determination of the model and observed spectra for an initial fit as it will decrease the statistical weight of emission lines from extragalactic objects (e.g QSOs and emission line galaxies). Thus for every target four solutions are computed from the three different grids, with the hot and cold solutions from the WD grid. The best fitting solution is defined as the fit that lies on the given model grid with the lowest reduced χ^2.

Figs. 7.4 - 7.8 show a best Balmer line fit solution for five spectra using the AT-LAS9 or TLUSTY grid, as stated in Table 7.2. Formal errors may be determined

for the parameters but it is time intensive and are not useful for initial fits. Bergeron et al. (1992) used repeated observations of objects and find 1σ errors of 10% of T_{eff} and 0.2dex $\log g$ and so this is assumed for all fits. An initial fit to the first six Balmer lines for all spectra is carried out and the objects with very poor fits (reduced $\chi^2 > 5.0$) are discarded. Quasars and ther extragalactic objects give poor fits due to broad emission lines and often fall into this category. The remaining candidates are visually inspected to confirm the fit is reasonable. In addition to the derived atmospheric parameters and fitted lines, a visual inspection of the whole spectrum was used to discard some spectra.

7.3 Post-AGB Candidates from the Spectroscopic Analysis

After fitting all $\sim 21{,}000$ spectra with three model grids, the spectra are divided into categories based on the final determined atmospheric parameters. Objects are classified as WDs if they lie within the model grid and have the smallest reduced χ^2 of the four fits. These objects are discarded along with the extragalactic objects leaving just the objects with best fits on the ATLAS9 and TLUSTY model grids. The confirmed model atmosphere parameters of the remaining objects were plotted with evolutionary tracks in T_{eff}-$\log g$ space to determine likely post-AGB candidates (Fig. 7.3). 52 objects have atmospheric parameters which lie near to the $M = 0.546 M_{\odot}$ post-AGB track of Schönberner (1983). These objects are selected by two sets of criteria, for the cool region ($T_{\text{eff}} < 20{,}000$K) by $\log g < 3.05\,\text{cm}\,\text{s}^{-2}$ and the hotter candidates ($T_{\text{eff}} > 20{,}000$K) have been selected by $\log g < 5.0\,\text{cm}\,\text{s}^{-2}$. Candidates are listed in Table 7.2 with the Balmer line fits shown in Appendix C. 14 of the objects (found in the upper right hand corner of Fig. 7.3) are cool and show deeper Hϵ cores than expected for the models with deep absorption lines on the blue wing of the same region. These features are strong due to the presence of Ca II H and K absorption lines at $\lambda = 3968.5\,\text{Å}$

(which blends with Hϵ, $\lambda = 3970.0$ Å) and $\lambda = 3933.7$ Å. The strength of these lines are compatible with late F type stars but H and K lines are also associated with BHB stars. The G band feature of varying strengths is found in the wing of Hδ, indicating a cool star. The Balmer line and continuum fits yield consistent values of T_{eff} which are too hot for F-stars but the $\log g$ is too low for a HB star with that T_{eff}. Therefore, these stars are likely composite stars and are ruled out as candidate post-AGB stars. The five strongest post-AGB candidates are spSpec-51993-0542-122 (Fig. 7.4), spSpec-52029-0538-603 (Fig. 7.5), spSpec-51660-0291-485 (Fig. 7.6), spSpec-52583-0890-099 (Fig. 7.7) and spSpec-53741-2315-018 (Fig. 7.8). All of these objects lie on or above the $M = 0.546 M_\odot$ track of Schönberner (1983). Four of the objects were identified as sds by Eisenstein et al. (2006) (in this instance it means they have a lower $\log g$ than WDs) whereas spSpec-53741-2315-018 has no entry in SIMBAD. spSpec-51660-0291-485 is the least convincing of the five candidates on inspection of the fit, as the observed spectrum is noisy. It has a second spectrum within the database which is equally inconclusive. Continuum fits reveal that spSpec-51660-0291-485 has a much lower T_{eff} than the Balmer fit with $T_{\text{eff}} = 17,903$K, however, the parameters are still consistent with the evolutionary tracks of post-AGB stars. The remaining four objects have continuum fits in agreement with T_{eff} determined from the Balmer fit. All five candidates require high resolution spectroscopy to confirm their post-AGB classification through abundance analysis. The remaining 33 objects are split into two categories. The objects with $\log g$ close to $5.0 \, \text{cm s}^{-2}$ are likely to be low gravity sds belonging to the large group with $24,000$K $< T_{\text{eff}} < 50,000$K. These are evolved He core burning stars with a thin H envelope. The remaining objects are possible post-EHB stars which have left the HB and are traversing across the H-R diagram towards the WD cooling track.

Only five stars remain with parameters making them plausible candidate post-AGB stars. This is at odds with estimates of post-AGB numbers in the halo. However, possible biases in the selection of SDSS targets for follow-up include ob-

ject saturation and non unique photometric parameters. Post-AGB stars are low priority objects for follow-up observations, being grouped with the more numerous hot sds and WDs. Some known post-AGB objects from the Torun catalogue (Szczerba et al., 2007) fall within the SDSS survey area but were not included in the spectroscopic database. This is likely to be due to one of the selection biases mentioned above. To determine if this is the case, a search for potential post-AGB candidates is carried out in the SDSS photometric database. The identified objects would be good candidates for spectroscopic follow-up and classifying these candidates may identify post-AGB stars or show a genuine lack of post-AGB stars within the halo population.
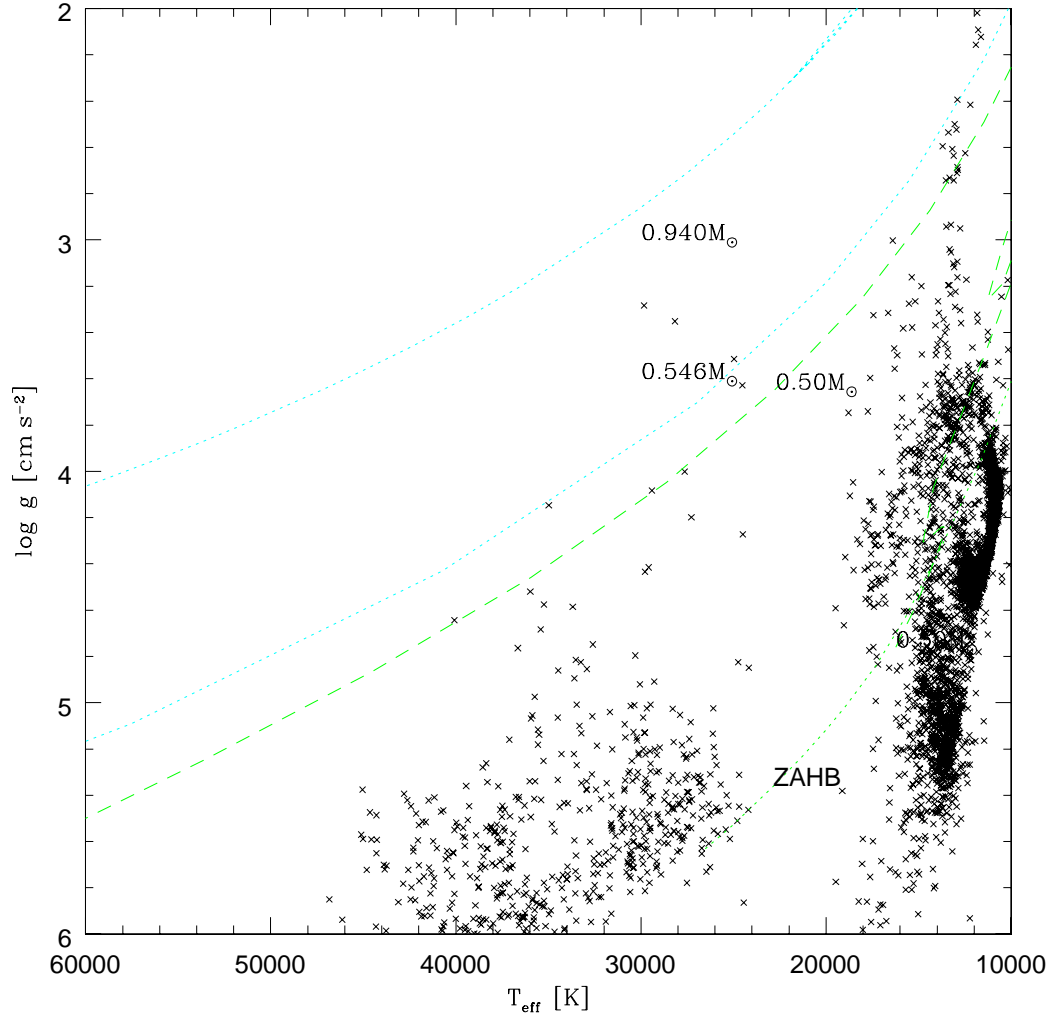
Figure 7.3: SDSS spectroscopic atmospheric parameters in T_{eff}-$\log g$ space of blue objects. The post-AGB evolutionary tracks of $M = 0.546 M_{\odot}$ (Schönberner, 1983) and $M = 0.940 M_{\odot}$ (Blöcker, 1995) are shown (cyan, dotted lines) with a $M = 0.50 M_{\odot}$ post-EAGB track of Dorman et al. (1993) (green, long dashed lines) and the zero age horizontal branch for a range of masses (green, short dashed lines).
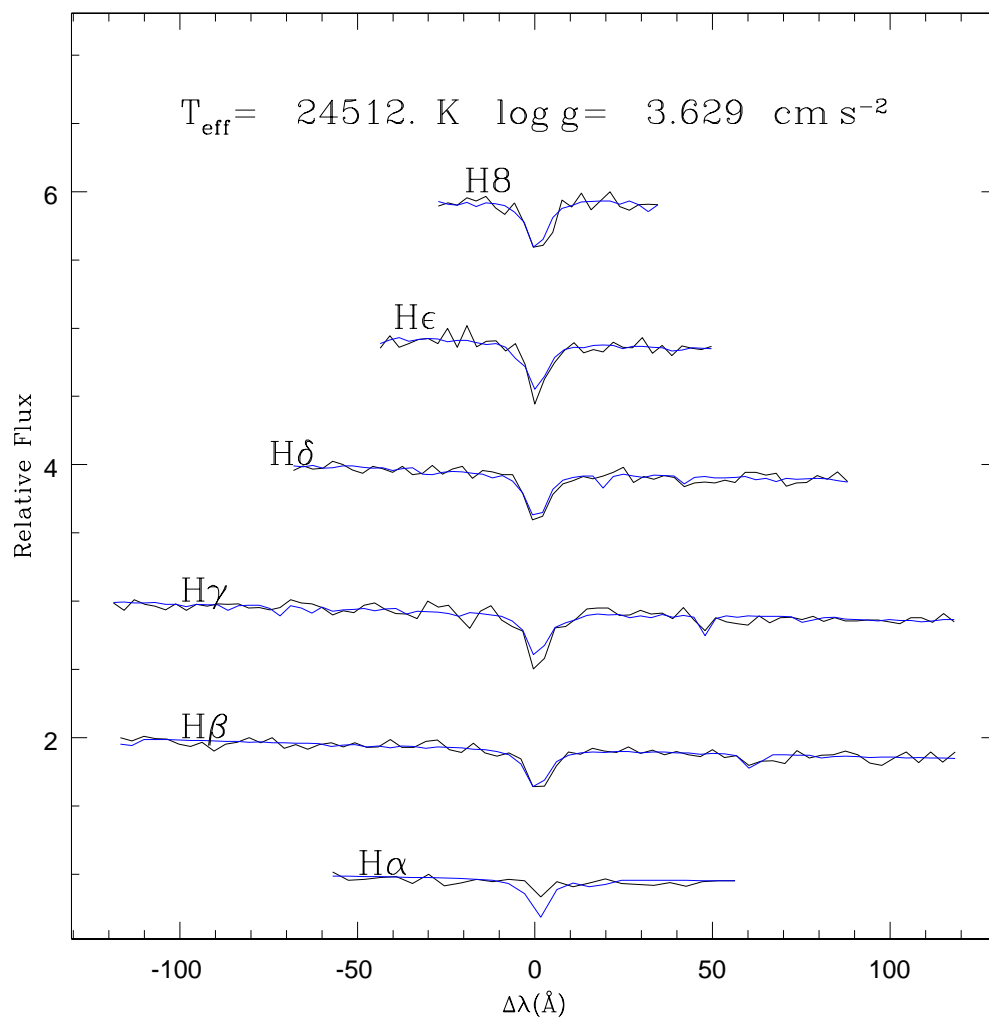
Figure 7.4: The best Balmer line fit of spSpec-51993-0542-122. The observed spectrum is in black and the smooth, synthetic ATLAS9 model is in blue.
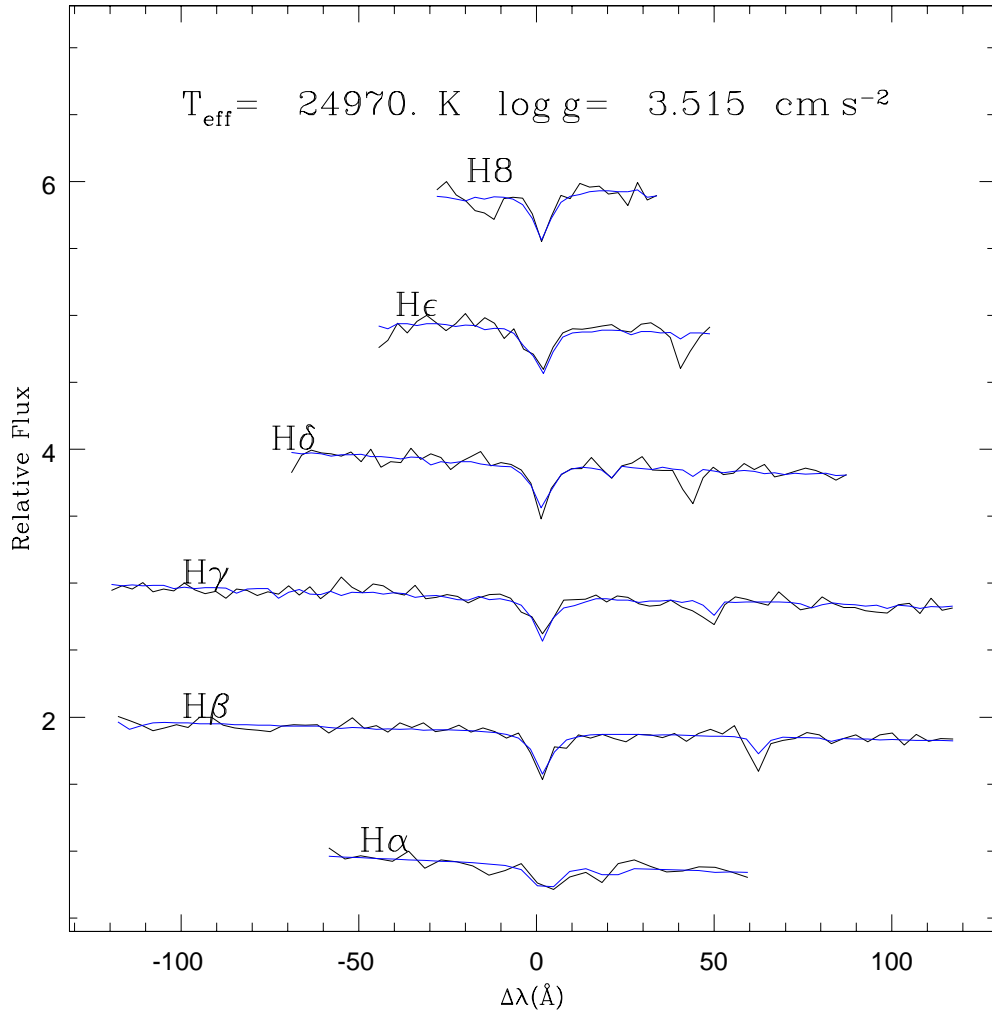
Figure 7.5: The best Balmer line fit of spSpec-52029-0538-603. The observed spectrum is in black and the smooth, synthetic ATLAS9 model is in blue.
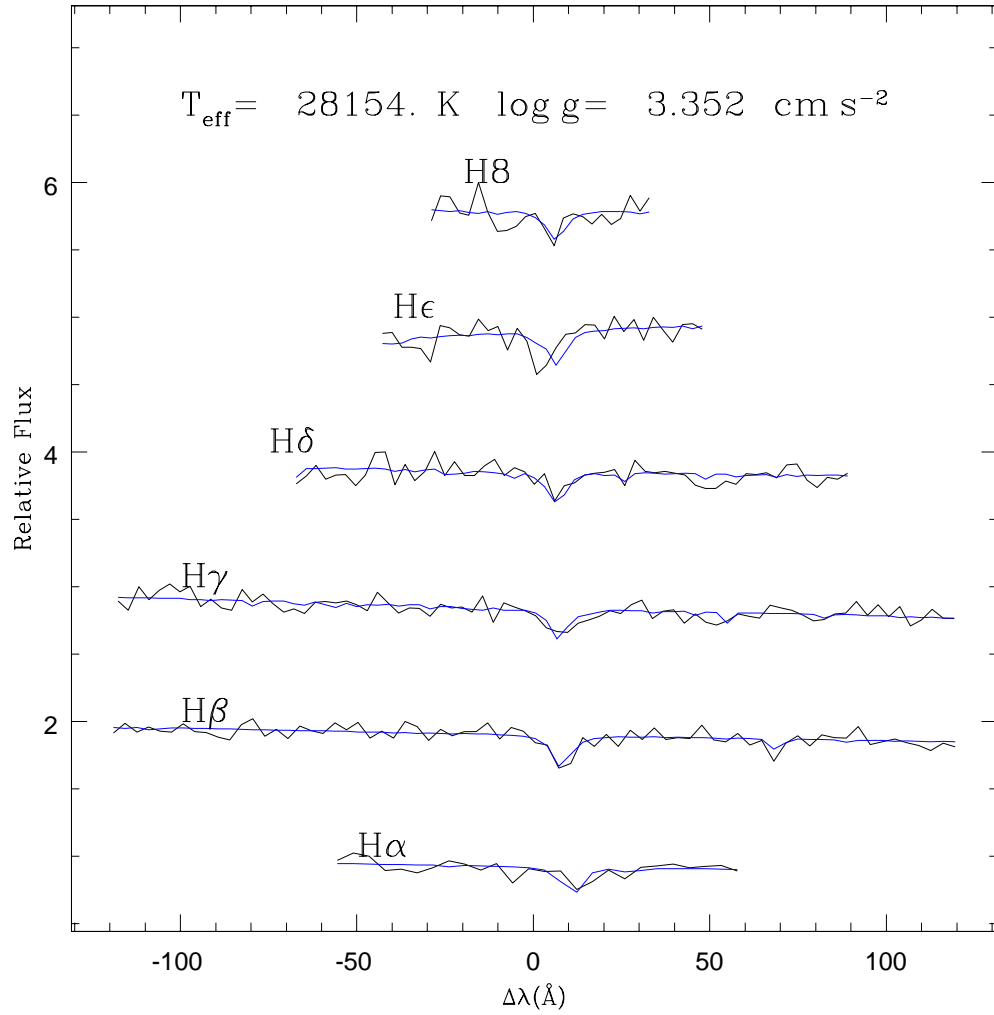
Figure 7.6: The best Balmer line fit of spSpec-51660-0291-485. The observed spectrum is in black and the smooth, synthetic TLUSTY model is in blue.
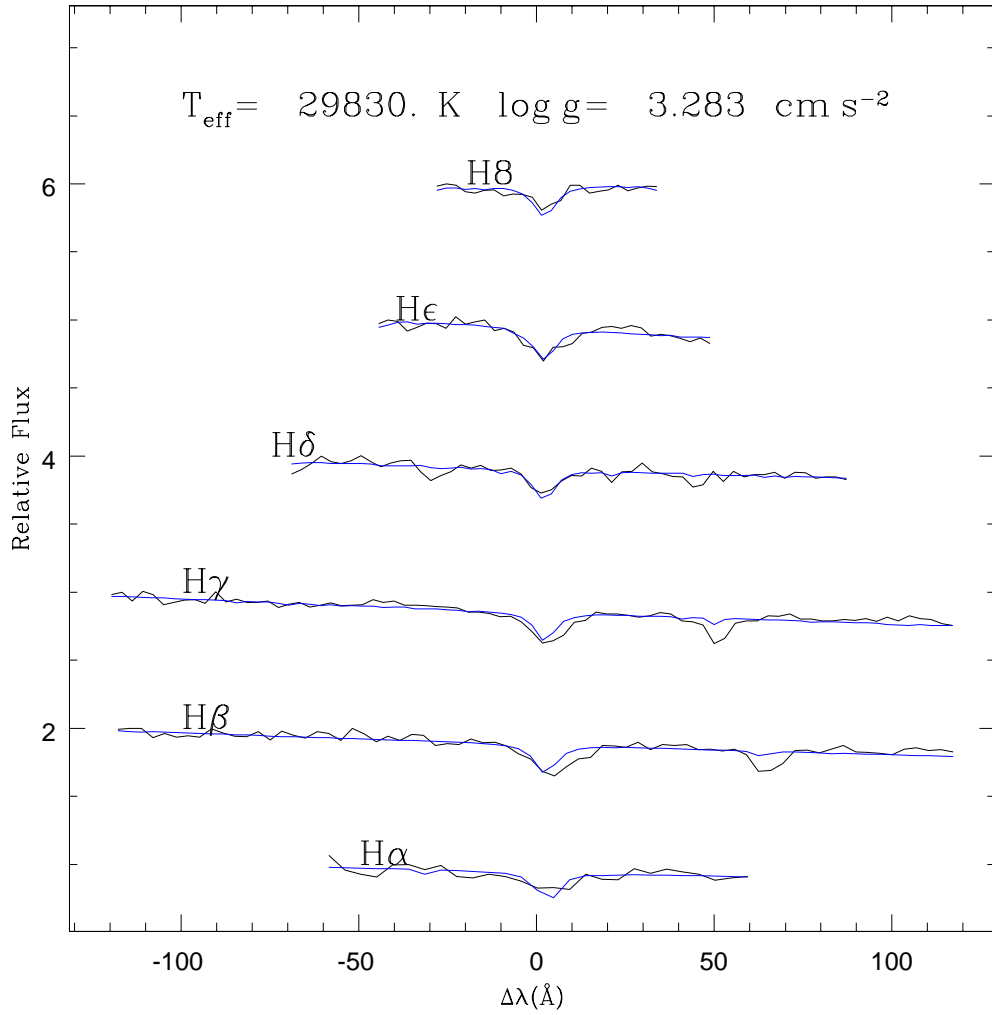
Figure 7.7: The best Balmer line fit of spSpec-52583-0890-099. The observed spectrum is in black and the smooth, synthetic TLUSTY model is in blue.
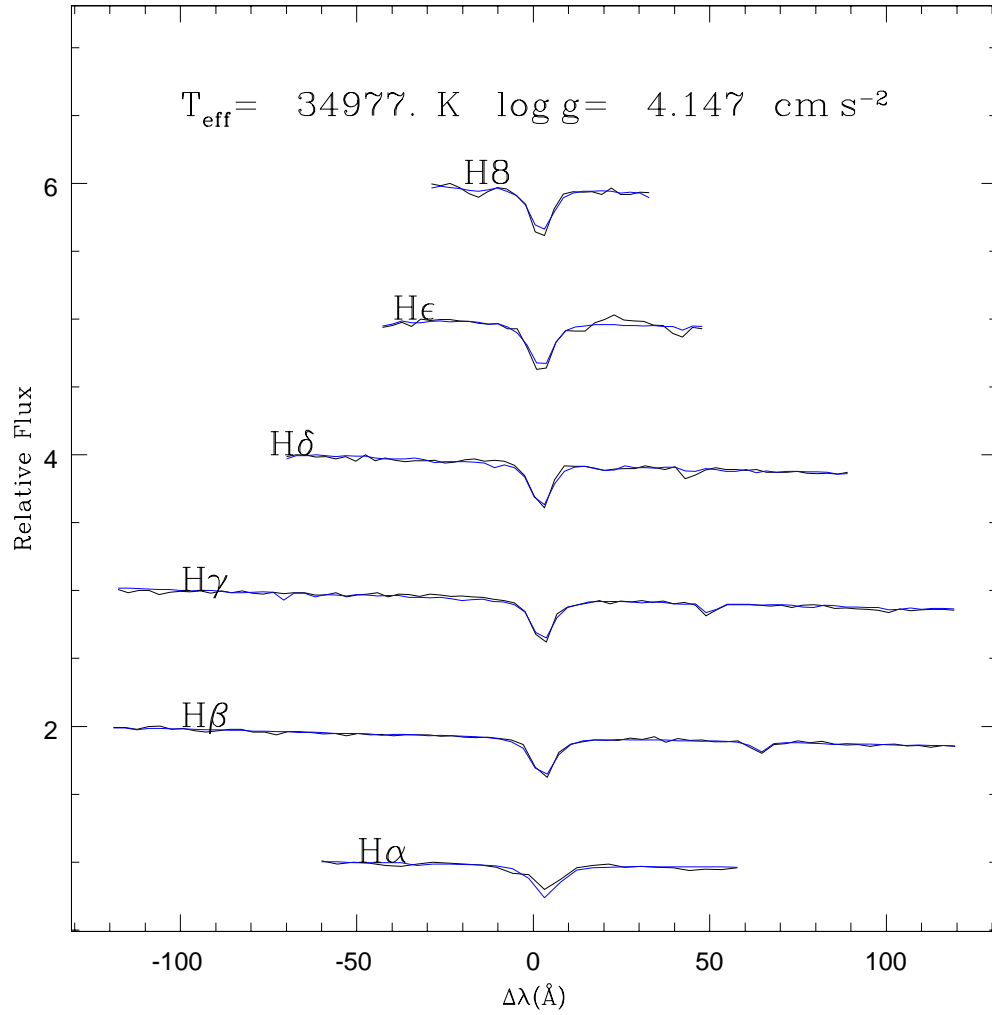
Figure 7.8: The best Balmer line fit of spSpec-53741-2315-018. The observed spectrum is in black and the smooth, synthetic TLUSTY model is in blue.

Table 7.2: A summary of SDSS spectra which lie near the $M = 0.546 M_\odot$ post-AGB evolutionary track with atmospheric parameters.

SDSS Spectrum spSpec-	RA [°]	Dec. [°]	Model Grid	T_{eff} [K]	$\log g$ [cm s^{-2}]	red. χ^2
54498-2882-466	162.8454	64.0617	ATLAS9	11832.	2.019	0.3049
53556-1799-625	202.8602	7.4763	ATLAS9	11781.	2.092	0.4137
53848-2437-371	137.2599	17.9429	ATLAS9	11628.	2.123	0.3206
54582-2526-459	242.0019	10.5858	ATLAS9	11911.	2.157	0.3198
54495-2647-246	187.8978	21.4924	ATLAS9	12895.	2.394	0.2884
53727-2290-241	139.4562	20.8000	ATLAS9	12212.	2.416	0.2960
54484-2656-583	183.0788	25.6059	ATLAS9	13048.	2.499	0.3032
52764-1056-232	242.8177	36.8166	ATLAS9	12963.	2.524	0.3270
54506-2760-551	216.6800	17.6447	ATLAS9	13392.	2.536	0.4348
52468-1053-428	235.5650	42.0992	ATLAS9	13703.	2.595	0.4906
53084-1368-611	179.5839	44.6995	ATLAS9	13186.	2.607	0.2866
51914-0488-409	154.1039	65.4144	ATLAS9	12480.	2.625	0.3315
53794-2217-261	170.8011	28.7945	ATLAS9	13099.	2.636	0.3092
53472-1694-285	190.4583	11.7067	ATLAS9	12897.	2.686	0.2837
52825-1178-435	326.1226	−7.4878	ATLAS9	12873.	2.697	0.3113
52294-0831-050	136.1340	42.0589	ATLAS9	12921.	2.711	0.2642
53815-2430-462	132.7400	13.4041	ATLAS9	13320.	2.732	0.3031
53737-2004-088	183.3688	31.4047	ATLAS9	13111.	2.742	0.2838
54583-2861-521	172.5697	−6.4829	ATLAS9	13519.	2.743	0.3749
54207-2596-342	182.4072	18.1475	ATLAS9	13242.	2.934	0.3954
53321-1910-636	346.0314	−8.9409	ATLAS9	13496.	2.943	0.0484
54612-2175-356	240.0159	5.7288	ATLAS9	12750.	2.950	0.2154
52381-0510-381	168.2947	2.8523	ATLAS9	16400.	3.003	0.2367
53534-1852-016	243.5611	22.1557	ATLAS9	24174.	4.849	0.9072

SDSS Spectrum spSpec-	RA [°]	Dec. [°]	Model Grid	T_{eff} [K]	$\log g$ [cm s^{-2}]	red. χ^2
54554-2776-176	221.1405	18.3730	ATLAS9	24496.	4.273	0.8164
51993-0542-122	115.9498	33.6948	ATLAS9	24512.	3.629	0.4561
53318-1868-029	117.0791	48.3521	ATLAS9	24745.	4.825	0.8534
52029-0538-603	224.5730	2.4685	ATLAS9	24970.	3.515	0.4928
52295-0525-423	197.6461	2.5577	ATLAS9	27275.	4.199	0.5684
53471-2002-285	198.9213	28.1489	ATLAS9	27628.	4.001	0.7915
51660-0291-485	190.9433	0.4264	TLUSTY	28154.	3.352	0.7939
52176-0636-605	314.6484	-5.2662	ATLAS9	29277.	4.908	0.3344
54624-2189-620	243.2294	5.1978	ATLAS9	29409.	4.083	0.6203
53498-1771-097	195.1725	13.8680	ATLAS9	29579.	4.415	0.4603
53799-2222-536	176.8255	30.5281	ATLAS9	29780.	4.434	0.4421
52583-0890-099	118.2082	30.9931	TLUSTY	29830.	3.283	0.7691
53172-1399-446	228.1455	39.4047	ATLAS9	30055.	4.920	0.2800
54180-2121-499	210.6368	32.2562	ATLAS9	30305.	4.796	0.3273
52674-1209-165	130.2453	32.0810	TLUSTY	32589.	4.748	0.3875
53464-1674-010	220.4305	46.1140	ATLAS9	32930.	4.854	0.8753
52370-0330-020	179.2254	-3.4195	ATLAS9	33240.	4.825	0.9177
53917-2547-172	217.7598	58.1935	ATLAS9	33512.	4.815	0.8707
54589-2532-451	246.7165	9.0583	ATLAS9	33598.	4.894	0.9004
54140-2558-445	185.9845	0.8587	TLUSTY	33683.	4.586	0.3278
53786-2211-610	167.0898	29.6136	ATLAS9	34473.	4.861	0.8814
53741-2315-018	128.8029	23.5479	TLUSTY	34977.	4.147	0.8573
52023-0586-629	220.1773	4.5451	TLUSTY	35230.	4.575	0.4586
52782-1333-409	235.4177	45.6075	TLUSTY	35425.	4.684	0.3529
52316-0598-241	177.4177	63.6598	ATLAS9	35744.	4.974	0.8012
53033-1310-060	174.2902	56.2447	TLUSTY	35975.	4.519	0.3669

Continued on next page

SDSS Spectrum	RA	Dec.	Model	T_{eff}	$\log g$	red. χ^2
spSpec-	[°]	[°]	Grid	[K]	$[\text{cm}\,\text{s}^{-2}]$	
51690-0341-435	199.8842	−1.6920	TLUSTY	36649.	4.764	0.4478
52079-0604-245	203.9651	62.6860	TLUSTY	40069.	4.643	0.2741

7.4 Photometric Search of Regions of the SDSS Survey

The spectroscopic search identified five candidate post-AGB stars, however, with only a fraction of photometric objects in SDSS having spectral observations, a photometric search may identify post-AGB candidates targets which were overlooked. Using the photometric grids described in Sect. 4, a number of potential candidates can be identified for follow-up spectroscopy. Initially, all photometric sources are downloaded from the SDSS database with the same colour criteria set for selecting objects in the spectroscopic database. This criteria selects all of the blue photometric objects in SDSS which cover the observation region shown in Fig. 7.2. The broad selection criteria means that many contaminants remain. To determine a magnitude limited complete sample, three selection regions were defined, two of the regions within the Saffer et al. (1997) sample are fully observed and so were used again as a comparison to SDSS ($8.5^{\text{h}} <$ R.A. $< 10.5^{\text{h}}$, $-10^{\text{o}} <$ decl. $< 50^{\text{o}}$ for region one and $b > 70°$ for region two), with a third region ($0° < l < 150°$, $50° < b < 70°$) added to remove any anomalies from the previous sample (Fig. 7.9). Removing the temperature restrictions from the PG sample, increasing the magnitude limit and with the new observation region within SDSS, the expected number of stars from the synthetic populations is three to four times greater with SDSS than the limits set in Saffer et al. (1997), with most of the additional post-AGB stars expected in the halo. Applying a magnitude limit of

$g' < 20$, the colour-colour plots for each region are very densely populated leaving thousands of objects satisfying the criteria for post-AGB stars. Contaminating objects include hot WDs, BHB stars, sds as well as a contribution from QSOs and emission line galaxies. Applying a brightness limit of $g' < 16$ greatly reduces the contribution of WDs, QSOs and emission line galaxies, with the loss of only $\sim 10\%$ of post-AGB stars based on synthetic populations. The small fraction lost is due to the high luminosity of post-AGB stars and at $g' = 16$ the outer regions of the Galaxy are already encountered. This is shown for a $M = 0.546 M_\odot$ post-AGB star track, which at $T_{\text{eff}} = 20,000$K gives $M_{g'} \sim -1.2$. Applying the distance modulus and neglecting reddening gives a distance of $D \sim 27.5$kpc for $g' = 16$. Therefore, post-AGBs numbers barely increase applying a fainter limited magnitude. Colour-colour plots of the $g' < 16$ sample of each of the three regions are presented in Figs. 7.10, 7.11 and 7.12. Each of the three plots show similar features and in total 1106 sources are identified as post-AGB candidates (combined $u' - g/g' - r'$ diagram shown in Fig. 7.13). Also plotted are the evolutionary tracks of post-AGB stars (blue), WDs (green) and HB/post-EHB (cyan). The grids are indistinguishable at high temperatures due to diminishing sensitivity of optical colours. Despite the brightness limit a significant number of WDs are likely to be included in the sample (due to the conservative selection region). The colours of HB/EHB and post-AGB stars are so similar that it is difficult to distinguish between these. Indeed, some of the 1106 sources are known objects within the Eisenstein et al. (2006) SDSS spectroscopic sample of WDs and sds. Quantifying the number of contaminants within the selection is difficult and obtaining low resolution spectroscopy would rule out most non post-AGB objects. The number of expected post-AGB stars in the halo from synthetic models varies with different tracks, however, the average predicted numbers are three to four times larger than are predicted for the smaller PG regions (shown in Table 6.4). The predicted number of post-AGB stars in the three SDSS regions for the $M = 0.546 M_\odot$ Schönberner (1983) track is shown in Table 7.3. The $M = 0.546 M_\odot$ predicts one
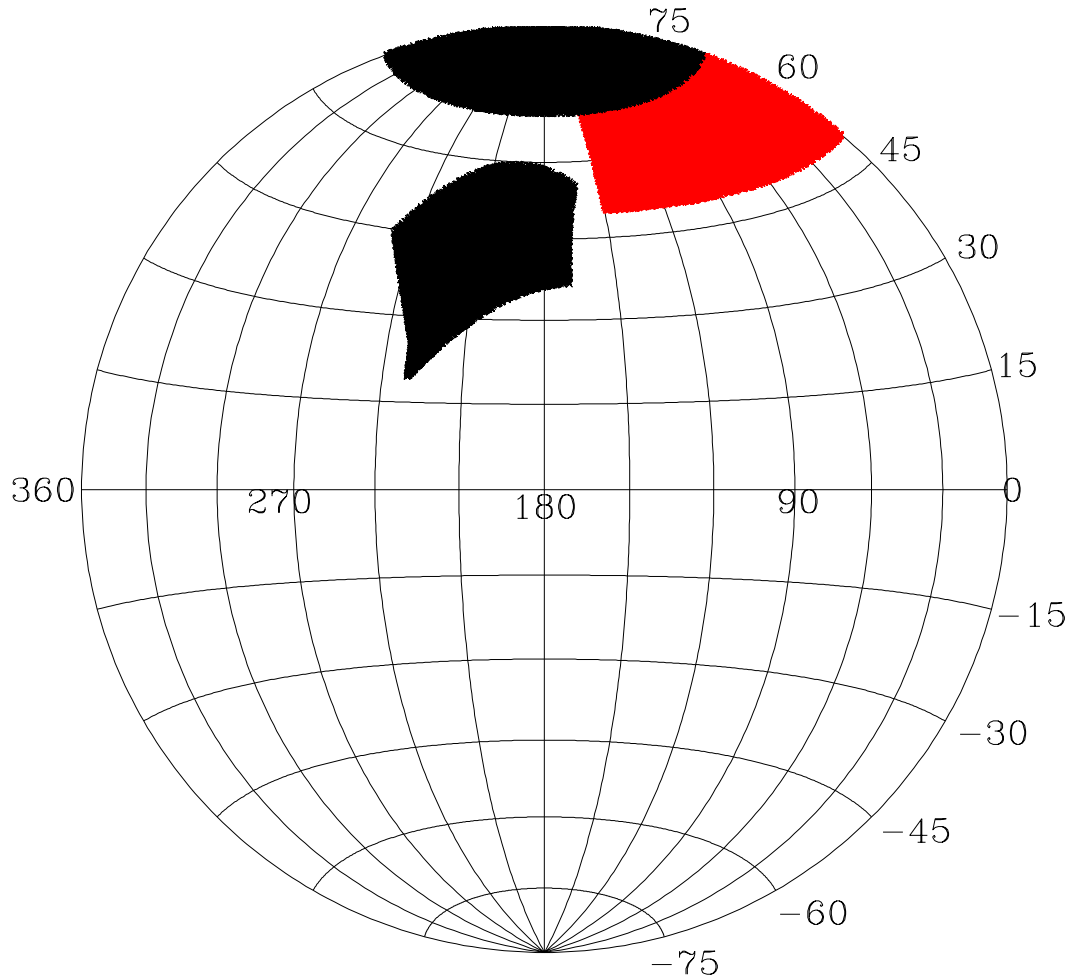
Figure 7.9: The complete regions selected within SDSS shown in Galactic co-ordinates. The black regions are the two identical regions in Saffer et al. (1997) while the red region is an area with no previous complete sample.

of the highest number of post-AGB stars, however, other low mass tracks predict a minimum number of ~150 halo post-AGB stars. Therefore, if 10% of the candidates are confirmed as post-AGB stars then the missing population may be reconciled. This would increase the number of halo post-AGB stars five-fold. The Saffer et al. (1997) sample found 10 post-AGB candidates from a sample of 298 low resolution spectra which had already removed WD contamination. Their sample, shows a 5% chance of identifying post-AGB stars from HB stars and sds and so a smaller fraction should be assumed from the SDSS candidate sample. 25 of the 1106 objects from the SDSS sample have spectra in the SDSS archive

Table 7.3: The predicted and observed number of post-AGB stars in the three regions in SDSS.

	N_{thin}	N_{thick}	N_{halo}	N_{total}	V_{lim}
Predicted	10 ± 3	80 ± 9	1457 ± 37	1546 ± 39	16
Predicted	10 ± 3	79 ± 9	1687 ± 40	1776 ± 41	20
Observed	–	–	–	8	–

The predicted numbers are for the $M = 0.546 M_\odot$ evolutionary track of Schönberner (1983).

and atmospheric parameters determined from the Balmer fitting carried out for the spectroscopic sample. 10 (40%) of the candidates are WDs, 9 (36%) have T_{eff} and $\log g$ placing them below the post-AGB tracks in T_{eff}-$\log g$ space where sds are expected and 6 (24%) have low T_{eff} and a $\log g$ consistent with a HB nature. From this small sample, 1 in 26 is the best possible ratio meaning less than 4% of the photometric sample are likely to be confirmed as post-AGB stars. This result would agree with the implications of the PG and SDSS spectroscopic sample, that only a small fraction of halo objects evolve through the post-AGB channel. However, systematic spectroscopic follow-up is important to either confirm the low number of halo post-AGB stars found in the spectroscopic samples or increase the number known halo post-AGB stars by up to five times.

7.5 SDSS post-AGB Galactic Halo Search Conclusion

The observed PG subsample of Saffer et al. (1997) implies that there are very few post-AGB stars in the halo and the ones that exist have low masses ($M < 0.55 M_\odot$). These masses are in good agreement with halo WD mass distributions based on the studies of several GCs (Alves et al., 2000). However, the synthetic Galactic model shows that the lower the mass of the central star (and progenitor) the slower the evolution, and so the higher the number of stars falling into the PG selection criteria. This is displayed in Fig. 16 of Weiss & Ferguson (2009) and in
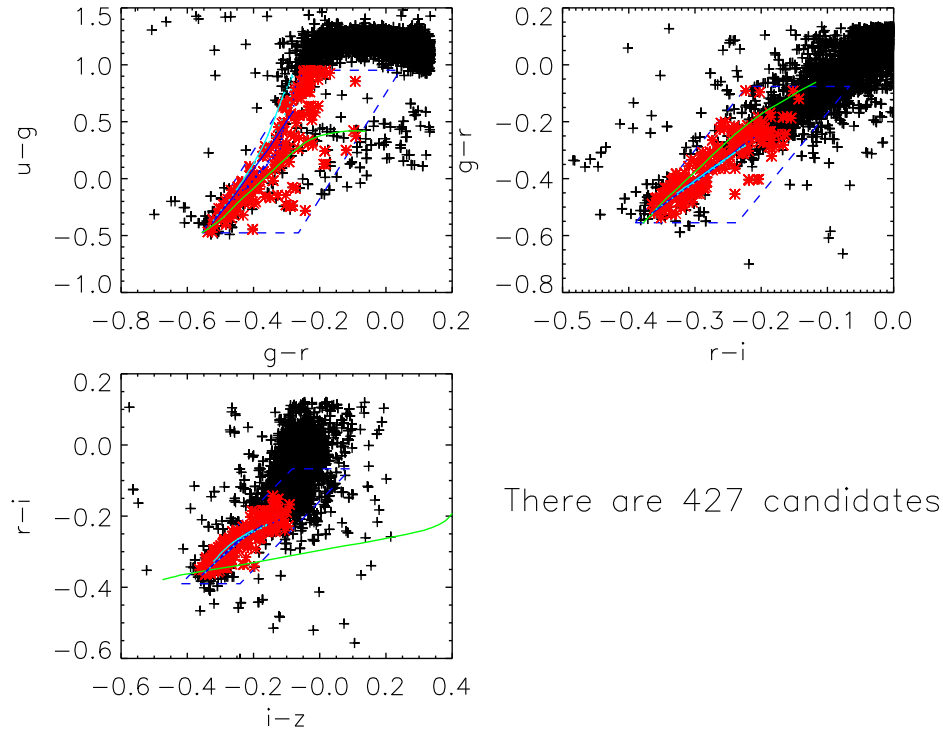
Figure 7.10: The candidate post-AGB stars in the region $8.5^{\mathrm{h}} <$ R.A. $< 10.5^{\mathrm{h}}$, $-10^{\circ} <$ decl. $< 50^{\circ}$ of Saffer et al. (1997). The black points are ruled out sources and the red stars are post-AGB candidate objects. The blue lines are the synthetic colours for post-AGB tracks with $M = 0.546 M_{\odot}$ (full) and $M = 0.940 M_{\odot}$ (dotted), respectively. The green line is a WD track with a range of T_{eff} and fixed $\log g$=8.0. The cyan lines represent a post-EAGB evolutionary track with $M = 0.50 M_{\odot}$ (dotted) and the ZAHB for a range of masses (solid).

Fig. 5.3 here. This increases the number of expected post-AGB stars with lower masses. As demonstrated in Table 6.4, a small metallicity effect can be seen in the predicted numbers but this is fairly small at sub-solar metallicities. The study of SDSS, described in this chapter, shows that the spectroscopic results are in agreement with the PG sample showing a small number of halo post-AGB stars, and has identified five new candidates. High resolution spectroscopy is needed to confirm the classification of these objects. The initial SDSS photometric search gives an inconclusive result, but based on the low confirmation rate of post-AGB stars from other photometric and low resolution spectroscopic studies, is likely to confirm the findings from the PG and and SDSS spectroscopic surveys. The results suggest that as the observational fields are complete, the evolutionary paths or
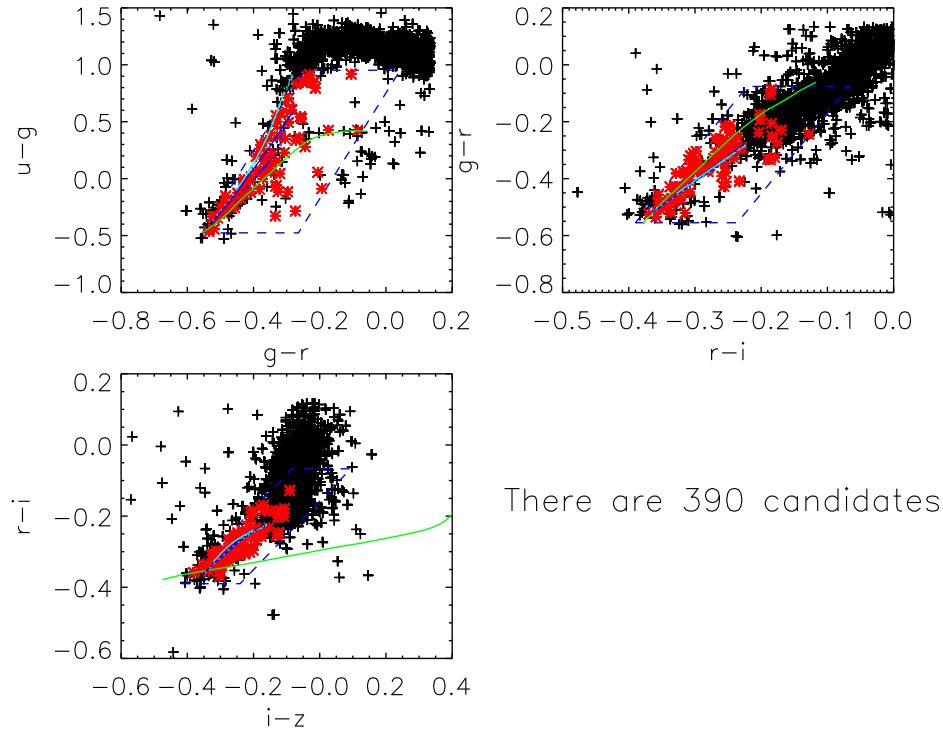
Figure 7.11: The candidate post-AGB stars in the region $b > 70$ of Saffer et al. (1997). The black points are ruled out sources and the red stars are post-AGB candidate objects and the tracks are the same as Fig. 7.10.

timescales for the majority of halo stars differ from the theory. Increasing the central star evolutionary speed across the H-R diagram would bring the observed and theoretical population numbers into agreement, however, this would lead to a higher number of PNe. Even fewer PNe are known in the halo than post-AGB stars ruling out this possibility. If there is a missing quantity of post-AGB stars in the halo then comparisons can be made to M32 where a dearth is also observed (Brown et al., 2008). As M32 is an elliptical galaxy it will contain old stars like the Milky Way halo, which are predicted by evolutionary theory to contain post-AGB stars. As an alternative, many more stars of these populations could evolve through the EHB channel than is currently believed. This would reduce the number of post-AGB stars predicted and would also be consistent with the HB/post-AGB ratio observed in the Saffer et al. (1997) sample. The implications for such a result are far reaching. On a Galactic scale, the majority of stars may be
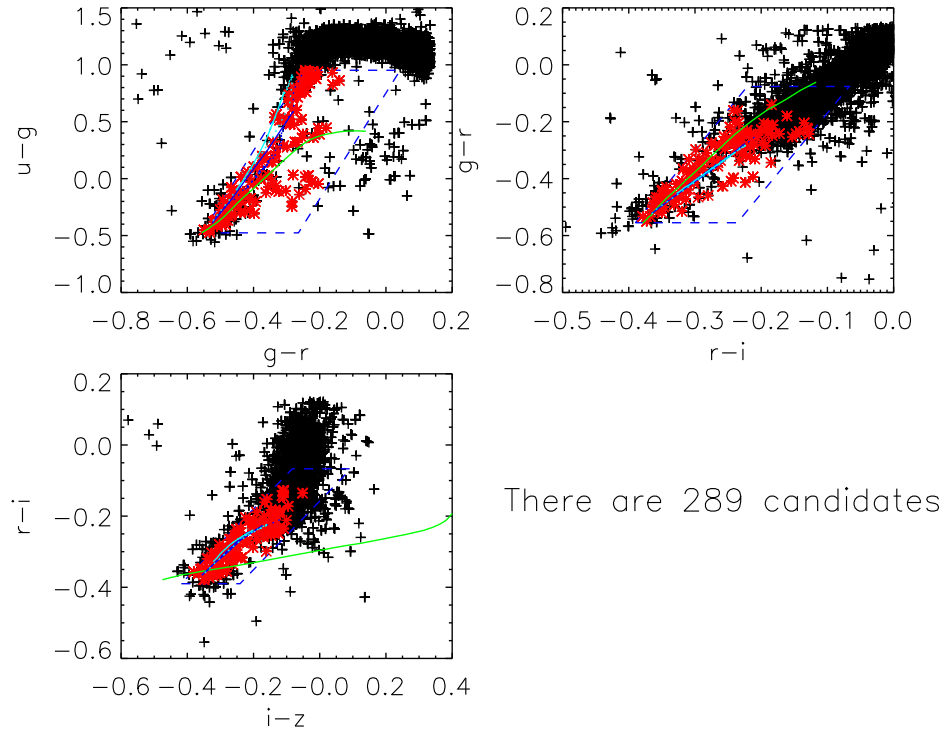
Figure 7.12: The candidate post-AGB stars in the region $0° < l < 150°$, $50° < b < 70°$. The black points are ruled out sources and the red stars are post-AGB candidate objects and the tracks are the same as Fig. 7.10.

failing to evolve through the post-AGB phase, evolving through the post-EAGB or EHB phases instead. The likely reasons being to greater mass loss in earlier phases of evolution. This would effect the chemical enrichment of the Galaxy and subsequent evolution. In extragalactic terms the UV upturn in elliptical galaxies (Yi & Yoon, 2004) uses the ratio of UV to optical flux to determine distances to elliptical galaxies. Post-AGB stars are thought to contribute between 10-30% of UV flux assuming a post-AGB dominant scenario (as opposed to post-EAGB and EHB). If found to be less than expected this is likely to underestimate redshifts (Brown et al., 2008).
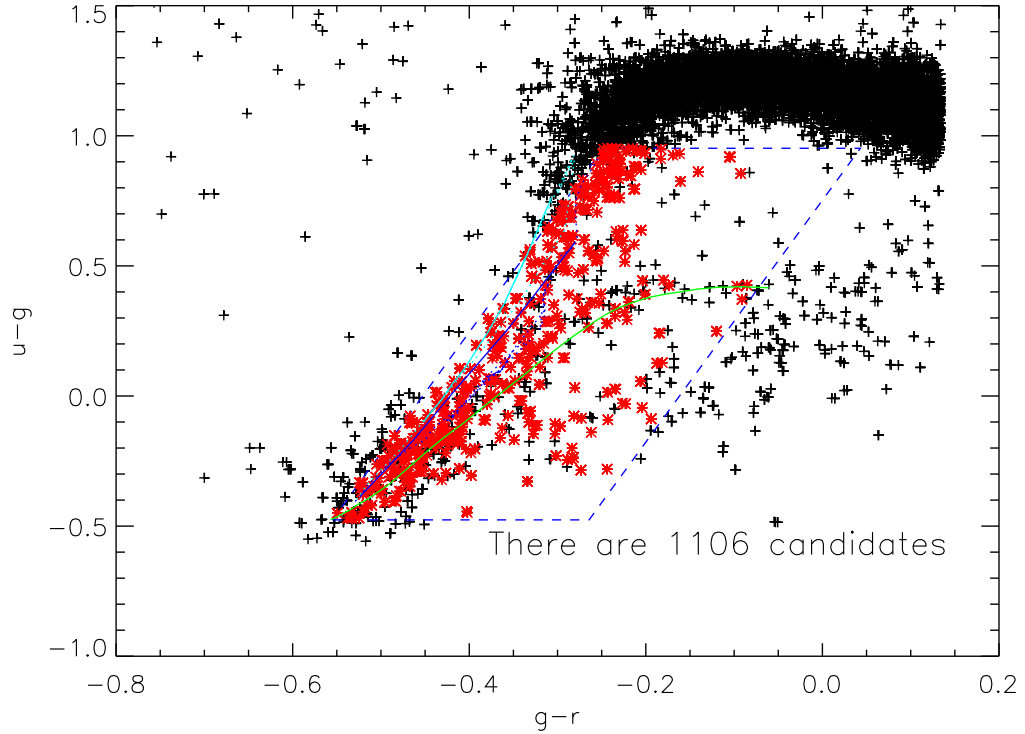
Figure 7.13: The candidate post-AGB stars in all three SDSS regions for $u' - g'/g' - r'$ colour space. The black points are ruled out sources and the red stars are post-AGB candidate objects. The blue lines are the synthetic colours for post-AGB tracks with $M = 0.546 M_\odot$ (full) and $M = 0.940 M_\odot$ (dotted), respectively. The green line is a WD track with a range of $T_{\rm eff}$ and fixed $\log g$=8.0. The cyan lines represent a post-EAGB evolutionary track with $M = 0.50 M_\odot$ (dotted) and the ZAHB for a range of masses (solid).

Chapter 8

Summary

The discovery of ∼1500 PNe from new surveys such as IPHAS and MASH has doubled the number of known PNe with the majority of the new objects found in the Galactic plane. A bias towards compact PNe is evident and with extended nebulae expected to dominate a distance limited sample, locating the hidden population is essential for improving PNe birthrate estimates. Furthermore, previous compilations of the local PN sample have underestimated the distances to extended PNe which has an effect on the PN birthrate. A first order estimate of the distance is needed to select candidate PNe for a complete sample, particularly for extended PNe. This is done by locating the luminous central stars of extended PNe and post-AGB objects which never become CSPNe.

In order to locate CSPNe, photometric criteria were determined based on SEDs produced from a grid of model atmospheres covering the parameter range of CSPNe. Synthetic photometry of post-AGB stars, CSPNe and WDs were produced with model atmospheres including LTE and non-LTE assumptions for SDSS, IPHAS and GALEX observations. They were applied to each survey to locate post-AGB stars and CSPNe. The CSPNe have been used to determine a range of distance estimates to PNe in SDSS by using post-AGB evolutionary tracks in conjunction with the kinematical age of the nebula. The distance estimate is most accurate for old and extended PNe which are most likely to be

underestimated using statistical methods. The same method has been applied to IPHAS PNe along with more accurate reddening distance estimates. Both methods and all three surveys allow for a significantly increased volume limited sample of PNe, however, also increasing the likeliness of containing faint extended PNe, which may be more easily identified by their luminous central stars.

A systematic search for hot Galactic halo post-AGB stars was carried out applying synthetic photometry to SDSS observations. A specific halo post-AGB search has never been attempted before , with the currently known objects mainly identified as UV and/or optically bright stars at high Galactic latitudes. The new generation of telescopes and surveys available like SDSS provides a deep and broad range of photometry and spectroscopy of Galactic objects out to the far reaches of the Galaxy for luminous objects such as post-AGB stars. The lack of halo post-AGB stars observed in the PG survey and within the literature as a whole is at odds with the number predicted through models. To identify candidate post-AGB stars at high Galactic latitudes, Balmer line fitting was carried out on all spectra in SDSS DR7 with blue photometric colours. The $\sim 21,000$ spectra fitted were dominated by WDs, HB stars, sds and extragalactic objects such as QSOs and emission line galaxies. Five candidate post-AGB stars were identified from the SDSS spectra with a higher resolution spectroscopic follow-up required in order to confirm their classification. If confirmed, they would add considerably to the known halo post-AGB population. However, the result would still be a small fraction of the number predicted from models and so a complete photometric region is required to confirm this low observed number is not an anomaly based on a bias in the criteria set out for spectroscopic follow-up within SDSS.

The photometric post-AGB search is comprised of three complete spacial regions with a magnitude limit of $g' = 16$. The photometric criteria for post-AGB stars is broad and many contaminants fall within the same region in colour-colour space. A qualitative analysis of 1100 objects which fulfill the photometric criteria for post-AGB stars can be applied to determine the fraction which are likely to be

true post-AGB stars. The low post-AGB confirmation rate in a low resolution spectroscopic sample of similar appearing objects (such as sds and HB stars) is likely to be further reduced for the SDSS photometric search (containing WDs and extragalactic contaminants also) resulting in a less than 5% (55 candidates) chance of confirmation. Thus, this work agrees with the PG and SDSS spectroscopic result of a lack of post-AGB stars which is truly observed in the Galactic halo.

High resolution spectroscopic follow-up of the 1100 candidate objects is needed to confirm the findings but taken at face value, this work implies that the minority of halo stars evolve through the post-AGB channel. As an alternative, many more stars of these populations could evolve through the EHB instead. This would reduce the number of post-AGB stars predicted and would also be consistent with the HB/post-AGB ratio observed in previous studies of the halo and in old elliptical galaxies like M32. This result is significant for stellar evolutionary models, evolution of old galactic populations and models of ellipical galaxies which rely on the contribution of post-AGB stars towards the UV flux.

Bibliography

Abazajian, K. N., Adelman-McCarthy, J. K., Agüeros, M. A., Allam, S. S., Allende Prieto, C., An, D., Anderson, K. S. J., Anderson, S. F., Annis, J., Bahcall, N. A., & et al. (2009). The Seventh Data Release of the Sloan Digital Sky Survey. *ApJS*, 182, 543–558.

Acker, A., Fresneau, A., Pottasch, S. R., & Jasniewicz, G. (1998). A sample of planetary nebulae observed by HIPPARCOS. *A&A*, 337, 253–260.

Acker, A., Gleizes, F., Chopinet, M., Marcout, J., Ochsenbein, F., & Roques, J. M. (1982). Catalogue of the central stars of true and possible planetary nebulae. *Publ. Spéc. Cent. Données Stellaires, No. 3, 4+246 pp.*, 3.

Acker, A., Marcout, J., Ochsenbein, F., Stenholm, B., & Tylenda, R. (1992). *Strasbourg – ESO catalogue of galactic planetary nebulae.* Garching: European Southern Observatory, 1992.

Alves, D. R., Bond, H. E., & Livio, M. (2000). Hubble Space Telescope Observations of the Planetary Nebula K648 in the Globular Cluster M15. *AJ*, 120, 2044–2053.

Alves, D. R., Bond, H. E., & Onken, C. (2001). CCD Photometry of the Globular Cluster NGC 5986 and Its Post-Asymptotic Giant Branch and RR Lyrae Stars. *AJ*, 121, 318–326.

Arellano Ferro, A., Giridhar, S., & Mathias, P. (2001). Atmospheric abundances in post-AGB candidates of intermediate temperature. *A&A*, 368, 250–266.

Bakker, E. J., van der Wolf, F. L. A., Lamers, H. J. G. L. M., Gulliver, A. F., Ferlet, R., & Vidal-Madjar, A. (1996). The optical spectrum of HR 4049 (includes a line identification from 3650 to 10850A). *A&A*, 306, 924–+.

Balick, B. & Frank, A. (2002). Shapes and Shaping of Planetary Nebulae. *ARA&A*, 40, 439–486.

Barlow, M. J. (1987). The determination of the masses of Magellanic Cloud planetary nebulae using forbidden O II doublet ratio electron densities. *MNRAS*, 227, 161–183.

Benedict, G. F., McArthur, B. E., Fredrick, L. W., Harrison, T. E., Skrutskie, M. F., Slesnick, C. L., Rhee, J., Patterson, R. J., Nelan, E., Jefferys, W. H., van Altena, W., Montemayor, T., Shelus, P. J., Franz, O. G., Wasserman, L. H., Hemenway, P. D., Duncombe, R. L., Story, D., Whipple, A. L., & Bradley, A. J. (2003). Astrometry with The Hubble Space Telescope: A Parallax of the Central Star of the Planetary Nebula NGC 6853. *AJ*, 126, 2549–2556.

Benedict, G. F., McArthur, B. E., Napiwotzki, R., Harrison, T. E., Harris, H. C., Nelan, E., Bond, H. E., Patterson, R. J., & Ciardullo, R. (2009). Astrometry with the Hubble Space Telescope: Trigonometric Parallaxes of Planetary Nebula Nuclei NGC 6853, NGC 7293, Abell 31, and DeHt 5. *AJ*, 138, 1969–1984.

Bergeron, P., Saffer, R. A., & Liebert, J. (1992). A spectroscopic determination of the mass distribution of DA white dwarfs. *ApJ*, 394, 228–247.

Bianchi, L., Efremova, B., Herald, J., Girardi, L., Zabot, A., Marigo, P., & Martin, C. (2011). Catalogues of hot white dwarfs in the Milky Way from GALEX's ultraviolet sky surveys: constraining stellar evolution. *MNRAS*, 411, 2770–2791.

Blackman, E. G., Frank, A., Markiel, J. A., Thomas, J. H., & Van Horn, H. M. (2001). Dynamos in asymptotic-giant-branch stars as the origin of magnetic fields shaping planetary nebulae. *Nature*, 409, 485–487.

Blöcker, T. (1995). Stellar evolution of low- and intermediate-mass stars. II. Post-AGB evolution. *A&A*, 299, 755.

Boffi, F. R. & Stanghellini, L. (1994). Filling factors and ionized masses in planetary nebulae. *A&A*, 284, 248–258.

Bohlin, R. C. (2007). HST Stellar Standards with 1% Accuracy in Absolute Flux. In C. Sterken (Ed.), *The Future of Photometric, Spectrophotometric and Polarimetric Standardization*, volume 364 of *Astronomical Society of the Pacific Conference Series* (pp. 315).

Bond, H. E. (2000). Binarity of Central Stars of Planetary Nebulae. In J. H. Kastner, N. Soker, & S. Rappaport (Ed.), *Asymmetrical Planetary Nebulae II: From Origins to Microstructures*, volume 199 of *Astronomical Society of the Pacific Conference Series* (pp. 115–+).

Brown, T. M., Smith, E., Ferguson, H. C., Sweigart, A. V., Kimble, R. A., & Bowers, C. W. (2008). The Dearth of UV-Bright Stars in M32: Implications for Stellar Evolution Theory. *ApJ*, 682, 319–335.

Busso, M., Gallino, R., & Wasserburg, G. J. (1999). Nucleosynthesis in Asymptotic Giant Branch Stars: Relevance for Galactic Enrichment and Solar System Formation. *ARA&A*, 37, 239–309.

Buzzoni, A. (1989). Evolutionary population synthesis in stellar systems. I - A global approach. *ApJS*, 71, 817–869.

Buzzoni, A., Arnaboldi, M., & Corradi, R. L. M. (2006). Planetary nebulae as tracers of galaxy stellar populations. *MNRAS*, 368, 877–894.

Cahn, J. H., Kaler, J. B., & Stanghellini, L. (1992). A catalogue of absolute fluxes and distances of planetary nebulae. *A&AS*, 94, 399.

Catalán, S., Isern, J., García-Berro, E., & Ribas, I. (2008). The initial-final mass relationship of white dwarfs revisited: effect on the luminosity function and mass distribution. *MNRAS*, 387, 1693–1706.

Chabrier, G. (2003). Galactic Stellar and Substellar Initial Mass Function. *PASP*, 115, 763–795.

Ciardullo, R., Bond, H. E., Sipior, M. S., Fullton, L. K., Zhang, C.-Y., & Schaefer, K. G. (1999). A HUBBLE SPACE TELESCOPE Survey for Resolved Companions of Planetary Nebula Nuclei. *AJ*, 118, 488–508.

Ciardullo, R., Jacoby, G. H., Ford, H. C., & Neill, J. D. (1989). Planetary nebulae as standard candles. II - The calibration in M31 and its companions. *ApJ*, 339, 53–69.

Conlon, E. S., Dufton, P. L., & Keenan, F. P. (1994). Abundance analysis of the hot post-AGB star Barnard 29. *A&A*, 290, 897–905.

Conlon, E. S., Dufton, P. L., Keenan, F. P., & McCausland, R. J. H. (1991). Two early-type post-AGB stars at high galactic latitudes. *MNRAS*, 248, 820–826.

Conlon, E. S., Dufton, P. L., McCausland, R. J. H., & Keenan, F. P. (1993a). LSIV -12 deg 111 - A candidate halo proto-planetary nebula. *ApJ*, 408, 593–599.

Conlon, E. S., Theissen, A., & Moehler, S. (1993b). The nature of two blue stars in the galactic halo. *A&A*, 269, L1–L4.

Daub, C. T. (1982). A statistical survey of local planetary nebulae. *ApJ*, 260, 612–624.

de Boer, K. S. (1987). Observations of UV-bright stars in galactic globular clusters. In A. G. D. Philip, D. S. Hayes, & J. W. Liebert (Ed.), *IAU Colloq. 95: Second Conference on Faint Blue Stars* (pp. 95–104).

de Marco, O. (2009). The Origin and Shaping of Planetary Nebulae: Putting the Binary Hypothesis to the Test. *PASP*, 121, 316–342.

De Marco, O., Bond, H. E., Harmer, D., & Fleming, A. J. (2004). Indications of a Large Fraction of Spectroscopic Binaries among Nuclei of Planetary Nebulae. *ApJ*, 602, L93–L96.

De Marco, O. & Moe, M. (2005). Common Envelope Evolution through Planetary Nebula Eyes. In R. Szczerba, G. Stasińska, & S. K. Gorny (Eds.), *Planetary Nebulae as Astronomical Tools*, volume 804 of *American Institute of Physics Conference Series* (pp. 169).

Dixon, W. V. D., Brown, T. M., & Landsman, W. B. (2004). The Rapidly Rotating, Hydrogen-deficient, Hot Post-Asymptotic Giant Branch Star ZNG 1 in the Globular Cluster M5. *ApJ*, 600, L43–L46.

Dorman, B. (1992). Oxygen-enhanced models for globular cluster stars. III - Horizontal-branch sequences. *ApJS*, 81, 221–250.

Dorman, B., Rood, R. T., & O'Connell, R. W. (1993). Ultraviolet Radiation from Evolved Stellar Populations. I. Models. *ApJ*, 419, 596–+.

Drew, J. E., Greimel, R., Irwin, M. J., et al. (2005). The INT Photometric Hα Survey of the Northern Galactic Plane (IPHAS). *MNRAS*, 362, 753.

Drilling, J. S. (1985). LSS 2018 - A double-lined spectroscopic binary central star with an extremely large reflection effect. *ApJ*, 294, L107–L111.

Drilling, J. S. & Schönberner, D. (1985). On the progenitors of white dwarfs. *A&A*, 146, L23.

Eisenstein, D. J., Liebert, J., Harris, H. C., Kleinman, S. J., Nitta, A., Silvestri, N., Anderson, S. A., Barentine, J. C., Brewington, H. J., Brinkmann, J., Harvanek, M., Krzesiński, J., Neilsen, Jr., E. H., Long, D., Schneider, D. P., & Snedden, S. A. (2006). A Catalog of Spectroscopically Confirmed White Dwarfs from the Sloan Digital Sky Survey Data Release 4. *ApJS*, 167, 40–58.

Fan, X. (1999). Simulation of Stellar Objects in SDSS Color Space. *AJ*, 117, 2528–2551.

Finley, D. S., Koester, D., & Basri, G. (1997). The Temperature Scale and Mass Distribution of Hot DA White Dwarfs. *ApJ*, 488, 375.

Fitzgerald, M. P. (1968). The Distribution of Interstellar Reddening Material. *AJ*, 73, 983–+.

Fontaine, G., Brassard, P., & Bergeron, P. (2001). The Potential of White Dwarf Cosmochronology. *PASP*, 113, 409–435.

Frew, D. J. & Parker, Q. A. (2006). Towards a New Distance Scale and Luminosity Function for Nearby Planetary Nebulae. In M. J. Barlow & R. H. Méndez (Ed.), *Planetary Nebulae in our Galaxy and Beyond*, volume 234 of *IAU Symposium* (pp. 49–54).

Fuhrmann, K. (2004). Nearby stars of the Galactic disk and halo. III. *Astronomische Nachrichten*, 325, 3–80.

Fuhrmann, K. (2008). Nearby stars of the Galactic disc and halo - IV. *MNRAS*, 384, 173–224.

Gauba, G. & Parthasarathy, M. (2003). UV(IUE) spectra of hot post-AGB candidates. *A&A*, 407, 1007–1020.

Gesicki, K. & Zijlstra, A. A. (2007). White dwarf masses derived from planetary nebula modelling. *A&A*, 467, L29–L32.

Giammanco, C., Sale, S. E., Corradi, R. L. M., Barlow, M. J., Viironen, K., Sabin, L., Santander-García, M., Frew, D. J., Greimel, R., Miszalski, B., Phillipps, S., Zijlstra, A. A., Mampaso, A., Drew, J. E., Parker, Q. A., & Napiwotzki, R. (2011). IPHAS extinction distances to planetary nebulae. *A&A*, 525, A58+.

Girardi, L., Bressan, A., Bertelli, G., & Chiosi, C. (2000). Evolutionary tracks and isochrones for low- and intermediate-mass stars: From 0.15 to 7 M_{sun}, and from Z=0.0004 to 0.03. *A&AS*, 141, 371–383.

Giridhar, S. & Arellano Ferro, A. (2005). Chemical composition of evolved stars of high galactic latitude. *A&A*, 443, 297–308.

Giridhar, S., Molina, R., Ferro, A. A., & Selvakumar, G. (2010). Chemical composition of A-F type post-AGB candidates. *MNRAS*, 406, 290–306.

Gonzalez, G. & Wallerstein, G. (1994). Study of the UV-bright stars in omega Cen, 2: Abundances and evidence for evolutionary mixing. *AJ*, 108, 1325–1349.

González-Solares, E. A., Walton, N. A., Greimel, R., et al. (2008). Initial data release from the INT Photometric Hα Survey of the Northern Galactic Plane (IPHAS). *MNRAS*, 388, 89.

Green, R. F. (1976). A discovery program for bright quasars - Preliminary results. *PASP*, 88, 665–668.

Green, R. F., Schmidt, M., & Liebert, J. (1986). The Palomar-Green catalog of ultraviolet-excess stellar objects. *ApJS*, 61, 305–352.

Groot, P. J., Verbeek, K., Greimel, R., Irwin, M., González-Solares, E., Gänsicke, B. T., de Groot, E., Drew, J., Augusteijn, T., Aungwerojwit, A., Barlow, M., Barros, S., van den Besselaar, E. J. M., Casares, J., Corradi, R., Corral-Santana, J. M., Deacon, N., van Ham, W., Hu, H., Heber, U., Jonker, P. G., King, R., Knigge, C., Mampaso, A., Marsh, T. R., Morales-Rueda, L., Napiwotzki, R., Naylor, T., Nelemans, G., Oosting, T., Pyrzas, S., Pretorius, M., Rodríguez-Gil, P., Roelofs, G. H. A., Sale, S., Schellart, P., Steeghs, D., Szyszka, C., Unruh, Y., Walton, N. A., Weston, S., Witham, A., Woudt, P., & Zijlstra, A. (2009). The UV-Excess survey of the northern Galactic plane. *MNRAS*, 399, 323–339.

Habing, H. J. & Olofsson, H., Eds. (2003). *Asymptotic giant branch stars.*

Hajian, A. R., Terzian, Y., & Bignell, C. (1993). Planetary nebulae expansion distances. *AJ*, 106, 1965–1972.

Hajian, A. R., Terzian, Y., & Bignell, C. (1995). Planetary Nebulae Expansion Distances. II. NGC 6572, NGC6210, NGC 3242, and NGC 2392. *AJ*, 109, 2600–+.

Hambly, N. C., Dufton, P. L., Keenan, F. P., & Lumsden, S. L. (1996). On the nature of the high-latitude B-type star CPD-61 deg455. *MNRAS*, 278, 811–820.

Hambly, N. C., Rolleston, W. R. J., Keenan, F. P., Dufton, P. L., & Saffer, R. A. (1997). Early-Type Stars in the Galactic Halo from the Palomar-Green Survey. I. A Sample of Evolved, Low-Mass Stars. *ApJS*, 111, 419–+.

Harrington, J. P. & Paltoglou, G. (1993). The spectrum of the central star of the planetary nebula in M22. *ApJ*, 411, L103–L106.

Harris, H. C., Dahn, C. C., Canzian, B., et al. (2007). Trigonometric Parallaxes of Central Stars of Planetary Nebulae. *AJ*, 133, 631.

Hartl, H. & Weinberger, R. (1987). Planetary nebulae of low surface brightness - Gleanings from the 'POSS'. *A&AS*, 69, 519.

Heber, U. (1986). The atmosphere of subluminous B stars. II - Analysis of 10 helium poor subdwarfs and the birthrate of sdB stars. *A&A*, 155, 33.

Heber, U. & Kudritzki, R. P. (1986). NLTE-analysis of the sdO star ROB 162 in the globular cluster NGC 6397. *A&A*, 169, 244–250.

Herwig, F. (2005). Evolution of Asymptotic Giant Branch Stars. *ARA&A*, 43, 435–479.

Holberg, J. B. & Bergeron, P. (2006). Calibration of Synthetic Photometry Using DA White Dwarfs. *AJ*, 132, 1221.

Holberg, J. B., Sion, E. M., Oswalt, T., McCook, G. P., Foran, S., & Subasavage, J. P. (2008). A New Look at the Local White Dwarf Population. *AJ*, 135, 1225–1238.

Howard, J. W., Henry, R. B. C., & McCartney, S. (1997). A detailed abundance analysis of nine halo planetary nebulae. *MNRAS*, 284, 465–476.

Hubeny, I. & Lanz, T. (1995). Non-LTE line-blanketed model atmospheres of hot stars. 1: Hybrid complete linearization/accelerated lambda iteration method. *ApJ*, 439, 875–904.

IRSA (2011). Galactic dust reddening and extinction.

Ishida, K. & Weinberger, R. (1987). Two senile nearby planetary nebulae and the local PN population. *A&A*, 178, 227.

Jacoby, G. H. (1980). The luminosity function for planetary nebulae and the number of planetary nebulae in local group galaxies. *ApJS*, 42, 1.

Jacoby, G. H., Morse, J. A., Fullton, L. K., Kwitter, K. B., & Henry, R. B. C. (1997). Planetary Nebulae in the Globular Cluster PAL 6 and NGC 6441. *AJ*, 114, 2611–+.

Kaeufl, H. U., Renzini, A., & Stanghellini, L. (1993). Search for ionized cores in proto-planetary nebulae, and the asymptotic giant branch to planetary nebula transition. *ApJ*, 410, 251–259.

Kaler, J. B. & Feibelman, W. A. (1985). Ultraviolet spectra of the central stars of large planetary nebulae. *ApJ*, 297, 724–750.

Kendall, T. R., Brown, P. J. F., Conlon, E. S., Dufton, P. L., & Keenan, F. P. (1994). Optical observations of the hot post-asymptotic giant branch star, HD 177566. *A&A*, 291, 851–855.

Kendall, T. R., Dufton, P. L., Keenan, F. P., Beers, T. C., & Hambly, N. C. (1997). Abundance analyses of a sample of five faint blue stars in the galactic halo. *A&A*, 317, 82–89.

Kerber, F., Mignani, R. P., Guglielmetti, F., & Wicenec, A. (2003). Galactic Planetary Nebulae and their central stars. I. An accurate and homogeneous set of coordinates. *A&A*, 408, 1029–1035.

Kleinman, S. J. (2010). The SDSS DR7 White Dwarf Catalog. In K. Werner & T. Rauch (Ed.), *American Institute of Physics Conference Series*, volume 1273 of *American Institute of Physics Conference Series* (pp. 156–159).

Kleinman, S. J., Eisenstein, D. J., Liebert, J., & Harris, H. C. (2007). The SDSS DR4 White Dwarf Catalog. In R. Napiwotzki & M. R. Burleigh (Ed.), *15th European Workshop on White Dwarfs*, volume 372 of *Astronomical Society of the Pacific Conference Series* (pp. 121–+).

Kodaira, K., Greenstein, J. L., & Oke, J. B. (1970). The Unusual Composition of +39°4926. *ApJ*, 159, 485–+.

Koester, D., Napiwotzki, R., Christlieb, N., et al. (2001). High-resolution UVES/VLT spectra of white dwarfs observed for the ESO SN Ia progenitor survey (SPY). I. *A&A*, 378, 556.

Kudritzki, R. P. (1976). Non-LTE model atmospheres of subluminous O-stars. *A&A*, 52, 11–21.

Kurucz, R. L. (1991). New Opacity Calculations. In *NATO ASIC Proc. 341: Stellar Atmospheres – Beyond Classical Models* (pp. 441).

Kwok, S. (2000). *The Origin and Evolution of Planetary Nebulae.*

Kwok, S., Purton, C. R., & Fitzgerald, P. M. (1978). On the origin of planetary nebulae. *ApJ*, 219, L125–L127.

Lanz, T. & Hubeny, I. (2003). A Grid of Non-LTE Line-blanketed Model Atmospheres of O-Type Stars. *ApJS*, 146, 417–441.

Lemke, M. (1997). Extended VCS Stark broadening tables for hydrogen – Lyman to Brackett series. *A&AS*, 122, 285–292.

Liebert, J., Bergeron, P., & Holberg, J. B. (2005). The Formation Rate and Mass and Luminosity Functions of DA White Dwarfs from the Palomar Green Survey. *ApJS*, 156, 47.

Liller, M. H. & Liller, W. (1968). Observed Angular Motions in Planetary Nebulae. In D. E. Osterbrock & C. R. O'dell (Ed.), *Planetary Nebulae*, volume 34 of *IAU Symposium* (pp. 38–+).

Liller, M. H., Welther, B. L., & Liller, W. (1966). Angular Expansions of Planetary Nebulae. *ApJ*, 144, 280–+.

Lucke, P. B. (1978). The distribution of color excesses and interstellar reddening material in the solar neighborhood. *A&A*, 64, 367–377.

Lynn, B. B., Keenan, F. P., Dufton, P. L., Rolleston, W. R. J., Smoker, J. V., Ryans, R. S. I., Kilkenny, D., O'Donoghue, D., Hambly, N., & McGillivray, H. T. (2005). High-resolution spectroscopic observations of post-asymptotic giant branch candidates from the Edinburgh-Cape Survey. *MNRAS*, 363, 911–917.

Lynn, B. B., Keenan, F. P., Dufton, P. L., Saffer, R. A., Rolleston, W. R. J., & Smoker, J. V. (2004). Early-type stars in the Galactic halo from the Palomar-Green survey-III. Completion of a magnitude range limited sample. *MNRAS*, 349, 821–832.

Maciel, W. J. & Pottasch, S. R. (1980). Distances of planetary nebulae. *A&A*, 88, 1–7.

Mampaso, A., Corradi, R. L. M., Viironen, K., Leisy, P., Greimel, R., Drew, J. E., Barlow, M. J., Frew, D. J., Irwin, J., Morris, R. A. H., Parker, Q. A., Phillipps, S., Rodríguez-Flores, E. R., & Zijlstra, A. A. (2006). The "Príncipes de Asturias" nebula: a new quadrupolar planetary nebula from the IPHAS survey. *A&A*, 458, 203–212.

Marigo, P., Girardi, L., Weiss, A., Groenewegen, M. A. T., & Chiosi, C. (2004). Evolution of planetary nebulae. II. Population effects on the bright cut-off of the PNLF. *A&A*, 423, 995–1015.

Marten, H. & Schoenberner, D. (1991). On the dynamical evolution of planetary nebulae. *A&A*, 248, 590–598.

Maxted, P. f. L., Heber, U., Marsh, T. R., & North, R. C. (2001). The binary fraction of extreme horizontal branch stars. *MNRAS*, 326, 1391–1402.

McCausland, R. J. H., Conlon, E. S., Dufton, P. L., & Keenan, F. P. (1992). Hot post-asymptotic giant branch stars at high galactic latitudes. *ApJ*, 394, 298–304.

McCook, G. P. & Sion, E. M. (1999). A Catalog of Spectroscopically Identified White Dwarfs. *ApJS*, 121, 1–130.

Méndez, R. H. (1989). Binary and intrinsic variability in central stars of PN. In S. Torres-Peimbert (Ed.), *Planetary Nebulae*, volume 131 of *IAU Symposium* (pp. 261–272).

Mendez, R. H. (1991). Photospheric Abundances in Central Stars of Planeteray Nebulae, and Evolutionary Implications. In G. Michaud & A. V. Tutukov (Ed.), *Evolution of Stars: the Photospheric Abundance Connection*, volume 145 of *IAU Symposium* (pp. 375–+).

Mendez, R. H., Kudritzki, R. P., Herrero, A., Husfeld, D., & Groth, H. G. (1988).

High resolution spectroscopy of central stars of planetary nebulae. I - Basic atmospheric parameters and their interpretation. *A&A*, 190, 113–136.

Milne, D. K. (1982). On the radio distance scale for planetary nebulae. *MNRAS*, 200, 51P–54P.

Milne, D. K. & Aller, L. H. (1975). Radio observations at 5 GHz of southern planetary nebulae. *A&A*, 38, 183–196.

Minkowski, R. (1965). Planetary Nebulae. In A. Blaauw & M. Schmidt (Ed.), *Galactic Structure* (pp. 321–+).

Miszalski, B., Parker, Q. A., Acker, A., Birkby, J. L., Frew, D. J., & Kovacevic, A. (2008). MASH-II: more planetary nebulae from the AAO/UKST Hα survey. *MNRAS*, 384, 525–534.

Moe, M. & De Marco, O. (2006). Do Most Planetary Nebulae Derive from Binaries? I. Population Synthesis Model of the Galactic Planetary Nebula Population Produced by Single Stars and Binaries. *ApJ*, 650, 916.

Moehler, S. (2001). Hot Stars in Globular Clusters: A Spectroscopist's View. *PASP*, 113, 1162–1177.

Moehler, S. & Heber, U. (1998). PG 1323-086 and PG 1704+222 - two post-AGB stars at high galactic latitudes. *A&A*, 335, 985–990.

Moehler, S., Landsman, W., & Napiwotzki, R. (1998). Hot UV bright stars in globular clusters. *A&A*, 335, 510–516.

Mohamad-Yob, S. J., Ziegler, M., Rauch, T., & Werner, K. (2010). (F)UV Spectroscopy of K648: Abundance Determination of Trace Elements. In K. Werner & T. Rauch (Ed.), *American Institute of Physics Conference Series*, volume 1273 of *American Institute of Physics Conference Series* (pp. 239–242).

Mooney, C. J., Rolleston, W. R. J., Keenan, F. P., Dufton, P. L., Pollacco, D. L., & Magee, H. R. (2001). A detailed abundance analysis of the hot post-AGB star ZNG-1 in M10. *MNRAS*, 326, 1101–1109.

Mooney, C. J., Rolleston, W. R. J., Keenan, F. P., Dufton, P. L., Smoker, J. V., Ryans, R. S. I., & Aller, L. H. (2002). High-resolution Keck I spectroscopy of Galactic halo post-asymptotic giant branch stars. *MNRAS*, 337, 851–860.

Mooney, C. J., Rolleston, W. R. J., Keenan, F. P., Dufton, P. L., Smoker, J. V., Ryans, R. S. I., Aller, L. H., & Trundle, C. (2004). High-resolution spectroscopy of globular cluster post-Asymptotic Giant Branch stars. *A&A*, 419, 1123–1132.

Morrissey, P., Conrow, T., Barlow, T. A., et al. (2007). The Calibration and Data Products of GALEX. *ApJS*, 173, 682.

Munn, K. E., Dufton, P. L., Smartt, S. J., & Hambly, N. C. (2004). A chemical analysis of five hot stars towards the Galactic centre. *A&A*, 419, 713–723.

Napiwotzki, R. (1997). LTE or NLTE for the analysis of hot white dwarf and subdwarf B stars? *A&A*, 322, 256–265.

Napiwotzki, R. (1999). Spectroscopic investigation of old planetaries. IV. Model atmosphere analysis. *A&A*, 350, 101–119.

Napiwotzki, R. (2001). Spectroscopic investigation of old planetaries. V. Distance scales. *A&A*, 367, 973.

Napiwotzki, R. (2009). The galactic population of white dwarfs. *Journal of Physics Conference Series*, 172(1), 012004–+.

Napiwotzki, R., Christlieb, N., Drechsel, H., Hagen, H., Heber, U., Homeier, D., Karl, C., Koester, D., Leibundgut, B., Marsh, T. R., Moehler, S., Nelemans, G., Pauli, E., Reimers, D., Renzini, A., & Yungelson, L. (2003). SPY - the ESO Supernovae type Ia Progenitor survey. *The Messenger*, 112, 25–30.

Napiwotzki, R., Edelmann, H., Heber, U., Karl, C., Drechsel, H., Pauli, E.-M., & Christlieb, N. (2001). Binaries discovered by the SPY project. I. HE 1047-0436: A subdwarf B + white dwarf syste. *A&A*, 378, L17.

Napiwotzki, R., Heber, U., & Koeppen, J. (1994). Analysis of BD+33 deg 2642: A newly detected planetary nebula in the galactic halo and its central star. *A&A*, 292, 239–248.

Napiwotzki, R. & Schoenberner, D. (1991). Spectroscopic investigation of old planetaries. II - Detection of a 'hybrid' central star. *A&A*, 249, L16–L18.

Napiwotzki, R. & Schönberner, D. (1995). Spectroscopic investigation of old planetaries. III. Spectral types, magnitudes, and distances. *A&A*, 301, 545–+.

Napiwotzki, R., Yungelson, L., Nelemans, G., Marsh, T. R., Leibundgut, B., Renzini, R., Homeier, D., Koester, D., Moehler, S., Christlieb, N., Reimers, D., Drechsel, H., Heber, U., Karl, C., & Pauli, E. (2004). Double degenerates and progenitors of supernovae type Ia. In R. W. Hilditch, H. Hensberge, & K. Pavlovski (Ed.), *Spectroscopically and Spatially Resolving the Components of the Close Binary Stars*, volume 318 of *Astronomical Society of the Pacific Conference Series* (pp. 402–410).

O'Connell, R. W. (1999). Far-Ultraviolet Radiation from Elliptical Galaxies. *ARA&A*, 37, 603–648.

Oke, J. B. & Gunn, J. E. (1983). Secondary standard stars for absolute spectrophotometry. *ApJ*, 266, 713–717.

Osterbrock, D. E. (1974). *Astrophysics of gaseous nebulae.*

Otsuka, M., Tajitsu, A., Hyung, S., & Izumiura, H. (2010). The Origin and Evolution of the Halo PN BoBn 1: From a Viewpoint of Chemical Abundances Based on Multiwavelength Spectra. *ApJ*, 723, 658–683.

Paczyński, B. (1971). Evolution of Single Stars. VI. Model Nuclei of Planetary Nebulae. *Acta Astronomica*, 21, 417–+.

Parker, Q. A., Acker, A., Frew, D. J., et al. (2006). The Macquarie/AAO/Strasbourg Hα Planetary Nebula Catalogue: MASH. *MNRAS*, 373, 79.

Parthasarathy, M., Garcia Lario, P., & Pottasch, S. R. (1992). The chemical composition of the high velocity POST AGB star HD 56126(F5I). *A&A*, 264, 159–168.

Pauldrach, A., Puls, J., Kudritzki, R. P., Mendez, R. H., & Heap, S. R. (1988). Radiation-driven winds of hot stars. V - Wind models for central stars of planetary nebulae. *A&A*, 207, 123–131.

Pauli, E., Napiwotzki, R., Heber, U., Altmann, M., & Odenkirchen, M. (2006). 3D kinematics of white dwarfs from the SPY project. II. *A&A*, 447, 173–184.

Perek, L. & Kohoutek, L. (1967). *Catalogue of galactic planetary nebulae.*

Phillips, J. P. (2002). The Distances of Planetary Nebulae: A Scale Based upon Nearby Sources. *ApJS*, 139, 199.

Phillips, J. P. (2005). The distances of highly evolved planetary nebulae. *MNRAS*, 357, 619.

Phillips, J. P. (2006). Searching for Balmer Self-Absorption in Planetary Nebulae. *Rev. Mexicana Astron. Astrofis.*, 42, 291–297.

Pottasch, S. R. (1980). Masses of planetary nebulae. *A&A*, 89, 336–341.

Pottasch, S. R. (1996). Local space density and formation rate of planetary nebulae. *A&A*, 307, 561.

Pottasch, S. R. & Zijlstra, A. A. (1992). Shklovsky distances to galactic bulge planetary nebulae. *A&A*, 256, 251–254.

Press, W. H., Teukolsky, S. A., Vetterling, W. T., & Flannery, B. P. (1992). *Numerical recipes in FORTRAN. The art of scientific computing.*

Quin, D. A. & Lamers, H. J. G. L. M. (1992). UV observations of LB 3193 and LB 3116 - Two hot post-AGB objects in the galactic halo? *A&A*, 260, 261–267.

Reimers, C., Dorfi, E. A., & Höfner, S. (2000). Shaping of elliptical planetary nebulae. The influence of dust-driven winds of AGB stars. *A&A*, 354, 573–578.

Reimers, D. (1975). Circumstellar absorption lines and mass loss from red giants. *Memoires of the Societe Royale des Sciences de Liege*, 8, 369–382.

Renzini, A. & Buzzoni, A. (1986). Global properties of stellar populations and the spectral evolution of galaxies. In C. Chiosi & A. Renzini (Ed.), *Spectral Evolution of Galaxies*, volume 122 of *Astrophysics and Space Science Library* (pp. 195–231).

Robin, A. C., Reylé, C., Derrière, S., & Picaud, S. (2003). A synthetic view on structure and evolution of the Milky Way. *A&A*, 409, 523–540.

Rolleston, W. R. J., Hambly, N. C., Dufton, P. L., Keenan, F. P., Little, J. E., Kilkenny, D., O'Donoghue, D., Koen, C., & Stobie, R. S. (1997). High-resolution spectroscopic observations of B-type stars from the Edinburgh-Cape survey. *MNRAS*, 290, 422–430.

Sabin, L., Zijlstra, A. A., Wareing, C., Corradi, R. L. M., Mampaso, A., Viironen, K., Wright, N. J., & Parker, Q. A. (2010). New Candidate Planetary Nebulae in the IPHAS Survey: the Case of Planetary Nebulae with ISM interaction. *PASA*, 27, 166–173.

Saffer, R. A., Bergeron, P., Koester, D., & Liebert, J. (1994). Atmospheric parameters of field subdwarf B stars. *ApJ*, 432, 351.

Saffer, R. A., Keenan, F. P., Hambly, N. C., Dufton, P. L., & Liebert, J. (1997).

A Large-Scale Spectroscopic Survey of Early-Type Stars at High Galactic Latitudes. *ApJ*, 491, 172–+.

Sahai, R., Morris, M. R., & Villar, G. G. (2011). Young Planetary Nebulae: Hubble Space Telescope Imaging and a New Morphological Classification System. *AJ*, 141, 134–+.

Sale, S. E., Drew, J. E., Unruh, Y. C., Irwin, M. J., Knigge, C., Phillipps, S., Zijlstra, A. A., Gänsicke, B. T., Greimel, R., Groot, P. J., Mampaso, A., Morris, R. A. H., Napiwotzki, R., Steeghs, D., & Walton, N. A. (2009). High spatial resolution Galactic 3D extinction mapping with IPHAS. *MNRAS*, 392, 497–513.

Salpeter, E. E. (1955). The Luminosity Function and Stellar Evolution. *ApJ*, 121, 161.

Schaerer, D. & Charbonnel, C. (2011). A new perspective on globular clusters, their initial mass function and their contribution to the stellar halo and the cosmic reionization. *MNRAS*, 413, 2297–2304.

Schlegel, D. J., Finkbeiner, D. P., & Davis, M. (1998). Maps of Dust Infrared Emission for Use in Estimation of Reddening and Cosmic Microwave Background Radiation Foregrounds. *ApJ*, 500, 525.

Schönberner, D. (1983). Late stages of stellar evolution. II – Mass loss and the transition of asymptotic giant branch stars into hot remnants. *ApJ*, 272, 708.

Shklovsky, I. (1956). . *Astr. Zh.*, 33, 315.

Silva, M. D. V. & Napiwotzki, R. (2011). Ejection velocities of high Galactic latitude runaway stars. *MNRAS*, 411, 2596–2614.

Soker, N. (1997). Properties That Cannot Be Explained by the Progenitors of Planetary Nebulae. *ApJS*, 112, 487–+.

Stanghellini, L. & Kaler, J. B. (1989). Electron densities in planetary nebulae. *ApJ*, 343, 811–827.

Stanghellini, L., Villaver, E., Manchado, A., & Guerrero, M. A. (2002). The Correlations between Planetary Nebula Morphology and Central Star Evolution: Analysis of the Northern Galactic Sample. *ApJ*, 576, 285–293.

Stasińska, G., Tylenda, R., Acker, A., & Stenholm, B. (1991). An extensive study of planetary nebulae in the Galactic bulge. II - Statistical properties of the nebular envelopes. *A&A*, 247, 173–182.

Strom, S. E. & Strom, K. M. (1970). An Analysis of the Bright O Star in the Globular Cluster M3. *ApJ*, 159, 195–+.

Suárez, O., García-Lario, P., Manchado, A., Manteiga, M., Ulla, A., & Pottasch, S. R. (2006). A spectroscopic atlas of post-AGB stars and planetary nebulae selected from the IRAS point source catalogue. *A&A*, 458, 173–180.

Szczerba, R., Siódmiak, N., Stasińska, G., & Borkowski, J. (2007). An evolutionary catalogue of galactic post-AGB and related objects. *A&A*, 469, 799.

Tajitsu, A. & Otsuka, M. (2006). High Dispersion Spectroscopy of the PN K 648 in the Globular Cluster M 15. In M. J. Barlow & R. H. Méndez (Ed.), *Planetary Nebulae in our Galaxy and Beyond*, volume 234 of *IAU Symposium* (pp. 523–524).

Thompson, H. M. A., Keenan, F. P., Dufton, P. L., Ryans, R. S. I., Smoker, J. V., Lambert, D. L., & Zijlstra, A. A. (2007). Iron abundances of B-type post-asymptotic giant branch stars in globular clusters: Barnard29 in M13 and ROA5701 in ωCen. *MNRAS*, 378, 1619–1632.

Trams, N. R., Waters, L. B. F. M., Waelkens, C., Lamers, H. J. G. L. M., & van der Veen, W. E. C. J. (1989). The effect of mass loss on the evolution of low-mass post-AGB stars. *A&A*, 218, L1–L4.

Tremblay, P.-E. & Bergeron, P. (2008). The Ratio of Helium- to Hydrogen-

Atmosphere White Dwarfs: Direct Evidence for Convective Mixing. *ApJ*, 672, 1144–1152.

Tweedy, R. W. & Napiwotzki, R. (1992). The central star of S 216. *MNRAS*, 259, 315–322.

Tweedy, R. W. & Napiwotzki, R. (1994). The planetary nebula abandoned by its central star. *AJ*, 108, 978–983.

Tylenda, R., Stasińska, G., Acker, A., & Stenholm, B. (1991). An extensive study of planetary nebulae in the Galactic bulge. III - The observed central star mass distribution. *A&A*, 246, 221–230.

van Loon, J. T., Cioni, M.-R. L., Zijlstra, A. A., & Loup, C. (2005). An empirical formula for the mass-loss rates of dust-enshrouded red supergiants and oxygen-rich Asymptotic Giant Branch stars. *A&A*, 438, 273–289.

Van Winckel, H. (1997). Chemical composition of optically bright post-AGB stars. *A&A*, 319, 561–577.

van Winckel, H. (2003). Post-Agb Stars. *ARA&A*, 41, 391–427.

Vassiliadis, E. & Wood, P. R. (1993). Evolution of low- and intermediate-mass stars to the end of the asymptotic giant branch with mass loss. *ApJ*, 413, 641–657.

Vassiliadis, E. & Wood, P. R. (1994). Post-asymptotic giant branch evolution of low- to intermediate-mass stars. *ApJS*, 92, 125–144.

Viironen, K., Mampaso, A., Corradi, R. L. M., Rodríguez, M., Greimel, R., Sabin, L., Sale, S. E., Unruh, Y., Delgado-Inglada, G., Drew, J. E., Giammanco, C., Groot, P., Parker, Q. A., Sokoloski, J., & Zijlstra, A. (2009). New young planetary nebulae in IPHAS. *A&A*, 502, 113–129.

Viironen, K., Sabin, L., Rodríguez-Flores, E. R., Mampaso, A., Corradi, R. L. M., & Greimel, R. (2006). New Planetary Nebulae found by the IPHAS Survey. In M. J. Barlow & R. H. Méndez (Eds.), *Planetary Nebulae in our Galaxy and Beyond*, volume 234 of *IAU Symposium* (pp. 533).

Wachter, A., Schröder, K.-P., Winters, J. M., Arndt, T. U., & Sedlmayr, E. (2002). An improved mass-loss description for dust-driven superwinds and tip-AGB evolution models. *A&A*, 384, 452–459.

Waelkens, C., Van Winckel, H., Trams, N. R., & Waters, L. B. F. M. (1992). High-resolution spectroscopy of the central star of the Red-Rectangle nebula. *A&A*, 256, L15–L18.

Weidemann, V. (1977). On the distance scale of planetary nebulae and white dwarf birth rates. *A&A*, 61, L27–L30.

Weidmann, W. A. & Gamen, R. (2011). Central stars of planetary nebulae: New spectral classifications and catalogue. *A&A*, 526, A6+.

Weiss, A. & Ferguson, J. W. (2009). New asymptotic giant branch models for a range of metallicities. *A&A*, 508, 1343–1358.

Weston, S., Napiwotzki, R., & Sale, S. (2009). Central stars of Planetary Nebulae in SDSS and IPHAS. *Journal of Physics Conference Series*, 172(1), 012033–+.

Yanny, B., Rockosi, C., Newberg, H. J., Knapp, G. R., Adelman-McCarthy, J. K., Alcorn, B., Allam, S., Allende Prieto, C., An, D., Anderson, K. S. J., Anderson, S., Bailer-Jones, C. A. L., Bastian, S., Beers, T. C., Bell, E., Belokurov, V., Bizyaev, D., Blythe, N., Bochanski, J. J., Boroski, W. N., Brinchmann, J., Brinkmann, J., Brewington, H., Carey, L., Cudworth, K. M., Evans, M., Evans, N. W., Gates, E., Gänsicke, B. T., Gillespie, B., Gilmore, G., Nebot Gomez-Moran, A., Grebel, E. K., Greenwell, J., Gunn, J. E., Jordan, C., Jordan, W., Harding, P., Harris, H., Hendry, J. S., Holder, D., Ivans, I. I., Ivezič, Ž., Jester,

S., Johnson, J. A., Kent, S. M., Kleinman, S., Kniazev, A., Krzesinski, J., Kron, R., Kuropatkin, N., Lebedeva, S., Lee, Y. S., French Leger, R., Lépine, S., Levine, S., Lin, H., Long, D. C., Loomis, C., Lupton, R., Malanushenko, O., Malanushenko, V., Margon, B., Martinez-Delgado, D., McGehee, P., Monet, D., Morrison, H. L., Munn, J. A., Neilsen, Jr., E. H., Nitta, A., Norris, J. E., Oravetz, D., Owen, R., Padmanabhan, N., Pan, K., Peterson, R. S., Pier, J. R., Platson, J., Re Fiorentin, P., Richards, G. T., Rix, H.-W., Schlegel, D. J., Schneider, D. P., Schreiber, M. R., Schwope, A., Sibley, V., Simmons, A., Snedden, S. A., Allyn Smith, J., Stark, L., Stauffer, F., Steinmetz, M., Stoughton, C., SubbaRao, M., Szalay, A., Szkody, P., Thakar, A. R., Thirupathi, S., Tucker, D., Uomoto, A., Vanden Berk, D., Vidrih, S., Wadadekar, Y., Watters, S., Wilhelm, R., Wyse, R. F. G., Yarger, J., & Zucker, D. (2009). SEGUE: A Spectroscopic Survey of 240,000 Stars with g = 14-20. *AJ*, 137, 4377–4399.

Yi, S. K. & Yoon, S.-J. (2004). UV Upturn in Elliptical Galaxies: Theory. *Ap&SS*, 291, 205–213.

York, D. G., Adelman, J., Anderson, Jr., J. E., et al. (2000). The Sloan Digital Sky Survey: Technical Summary. *AJ*, 120, 1579.

Zanstra, H. (1927). An Application of the Quantum Theory to the Luminosity of Diffuse Nebulae. *ApJ*, 65, 50–+.

Zijlstra, A. A. & Pottasch, S. R. (1991). On the scale height of planetary nebulae. *A&A*, 243, 478–482.

Zsargó, J., Sembach, K. R., Howk, J. C., & Savage, B. D. (2003). Highly Ionized Gas in the Galactic Halo: A FUSE Survey of O VI Absorption toward 22 Halo Stars. *ApJ*, 586, 1019–1049.

Appendix A

CSPNe in SDSS from the ESO/Strasbourg Galactic Catalogue of Planetary Nebulae
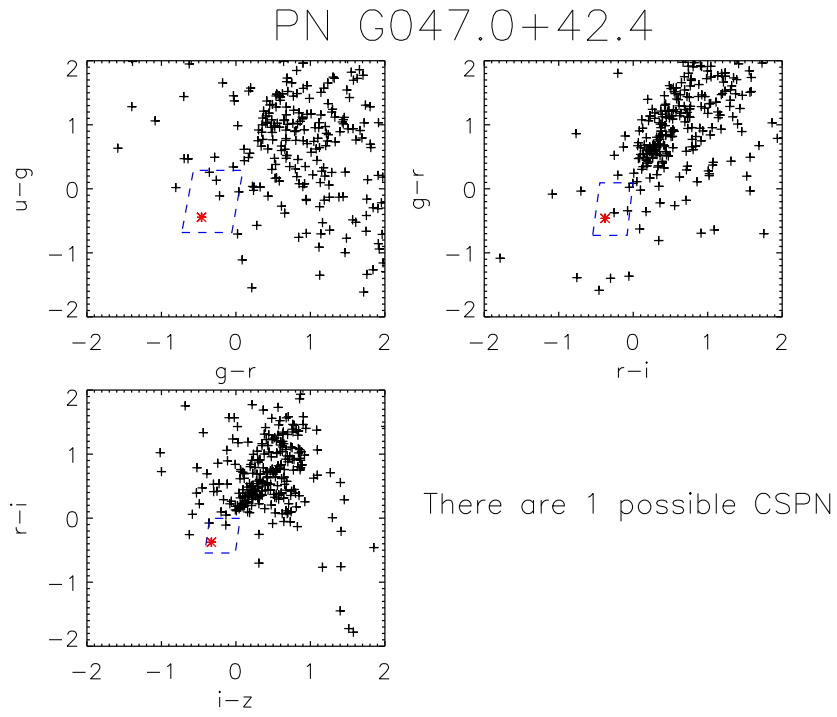
Figure A.1: The stars in the field of the PN, PN G 047.0+42.4, in colour-color space. The central star is found within our colour selection criteria
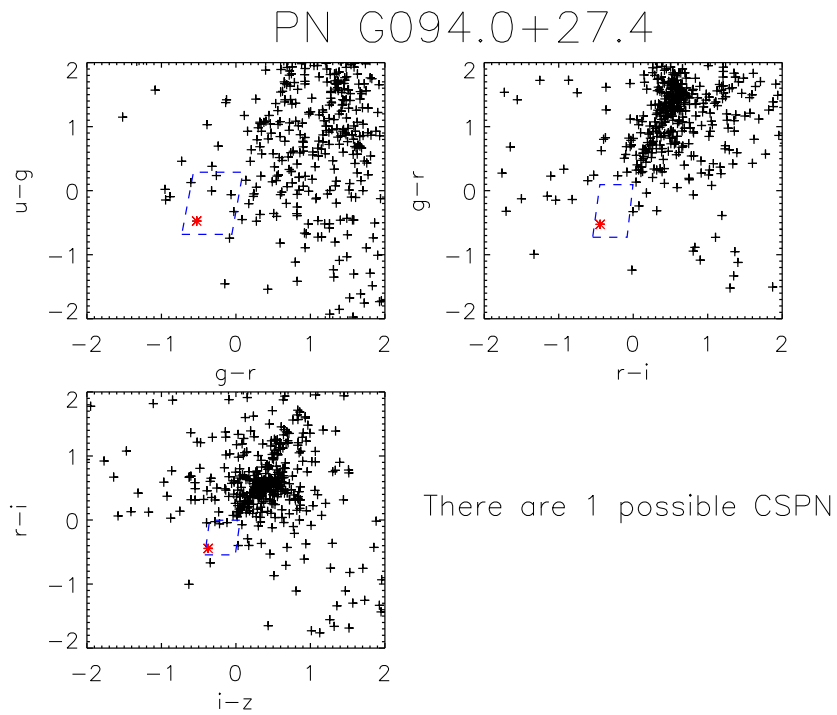
Figure A.2: The stars in the field of the PN, PN G 094.0+27.4, in colour-color space. The central star is found within our colour selection criteria
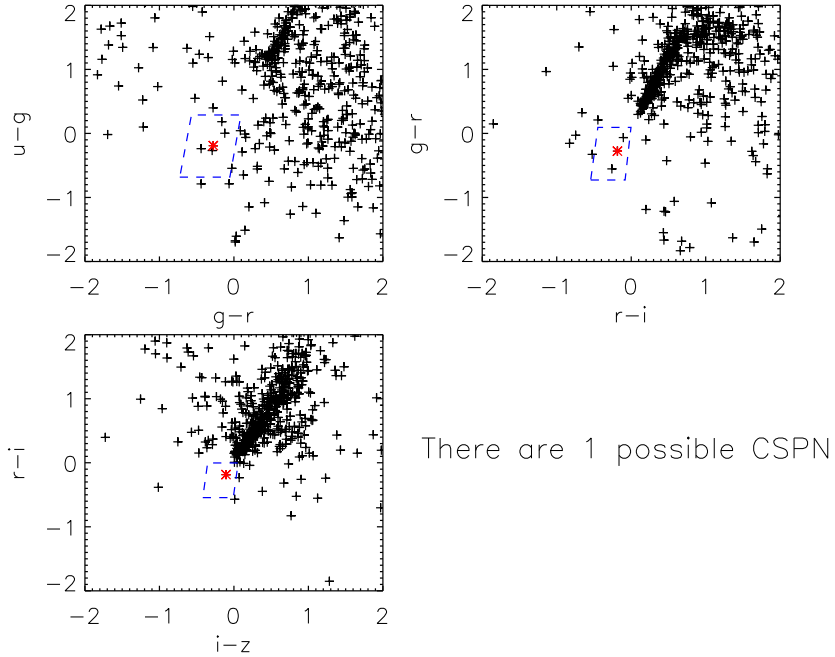
Figure A.3: The stars in the field of the PN, PN G 110.6−12.9, in colour-color space. The central star is found within our colour selection criteria
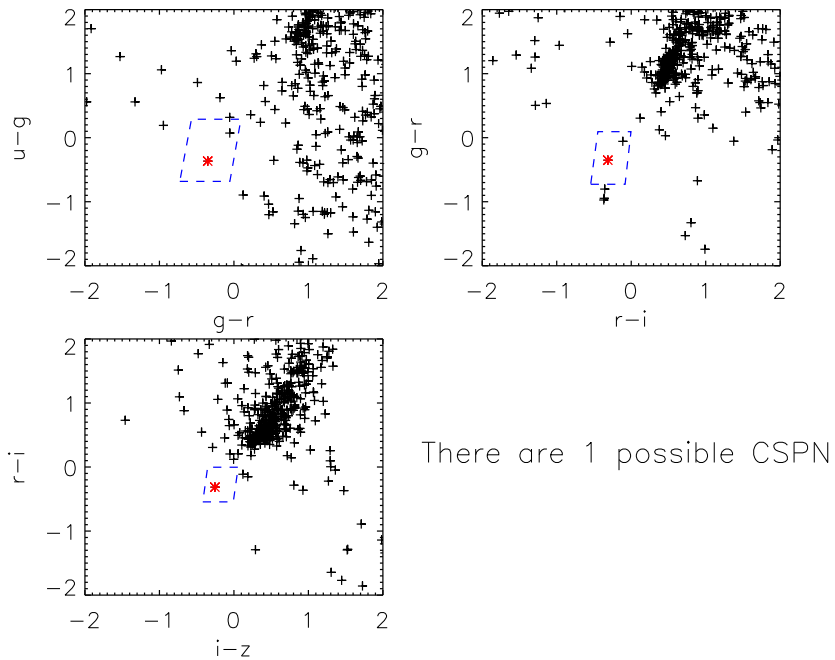
Figure A.4: The stars in the field of the PN, PN G 111.0+11.6, in colour-color space. The central star is found within our colour selection criteria
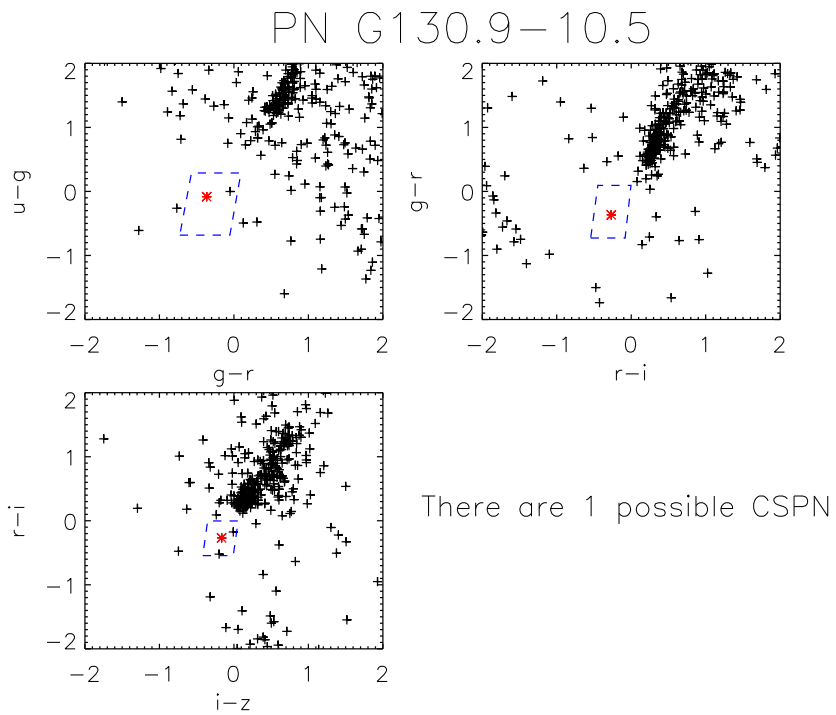
Figure A.5: The stars in the field of the PN, PN G 130.9−10.5, in colour-color space. The central star is found within our colour selection criteria
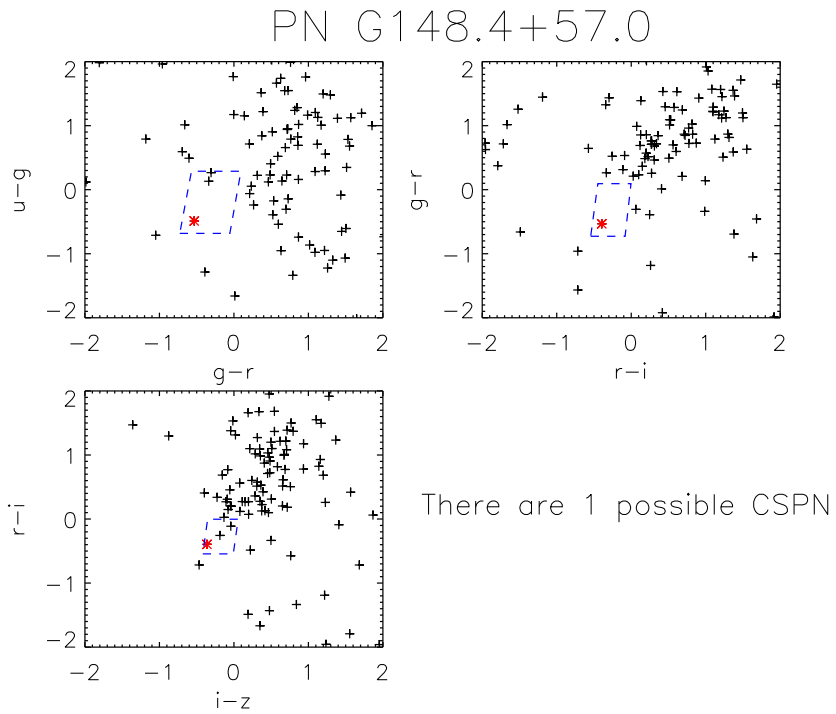
Figure A.6: The stars in the field of the PN, PN G 148.4+57.0, in colour-color space. The central star is found within our colour selection criteria
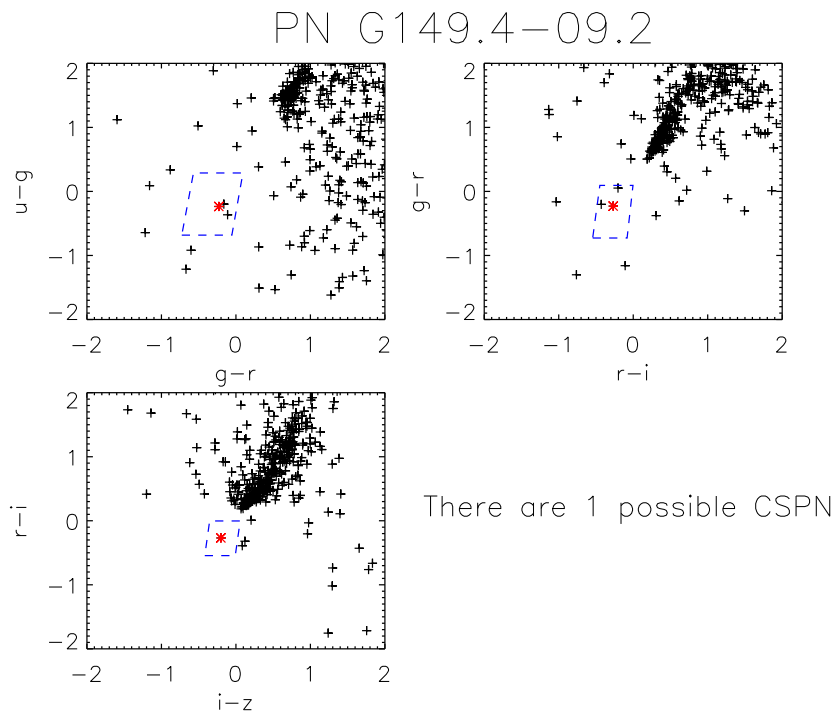
Figure A.7: The stars in the field of the PN, PN G 149.4−09.2, in colour-color space. The central star is found within our colour selection criteria
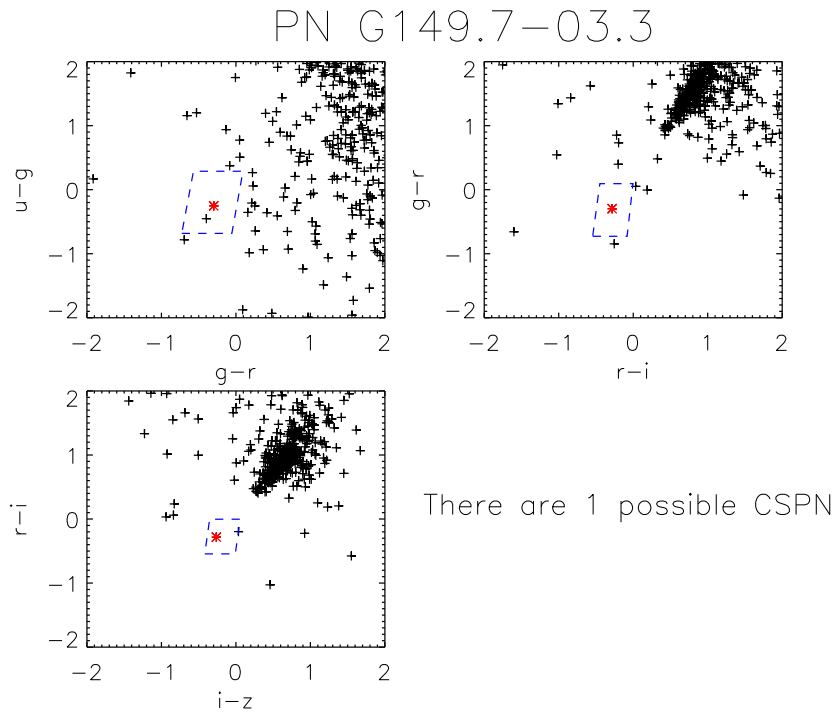
Figure A.8: The stars in the field of the PN, PN G 149.7−03.3, in colour-color space. The central star is found within our colour selection criteria
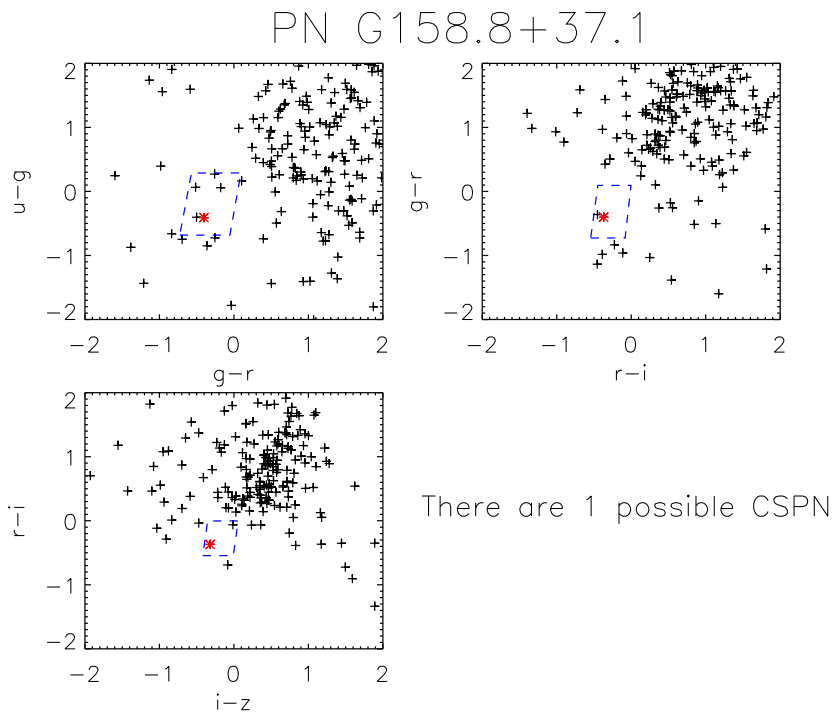
Figure A.9: The stars in the field of the PN, PN G 158.8+37.1, in colour-color space. The central star is found within our colour selection criteria
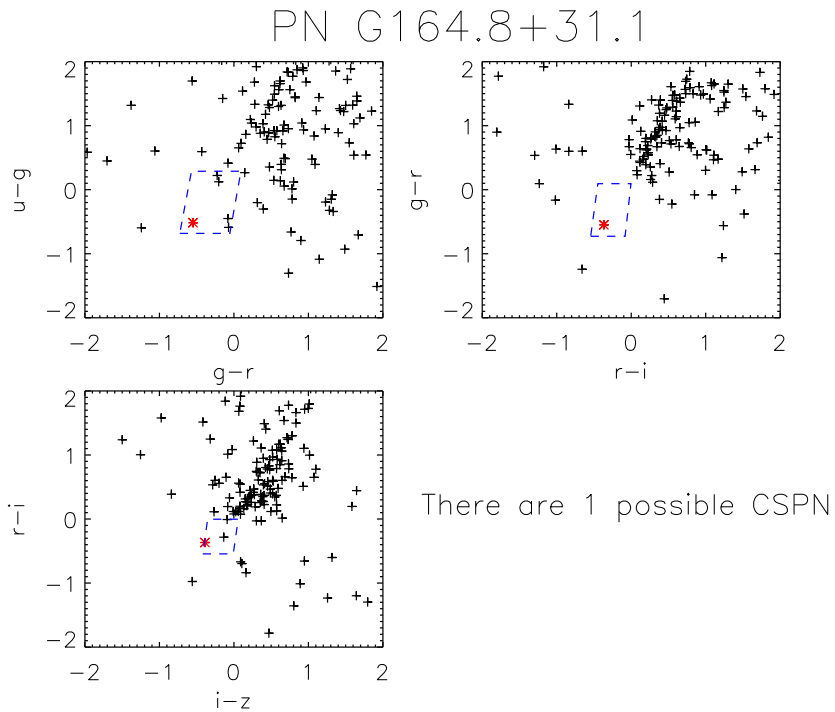
Figure A.10: The stars in the field of the PN, PN G 164.8+31.1, in colour-color space. The central star is found within our colour selection criteria
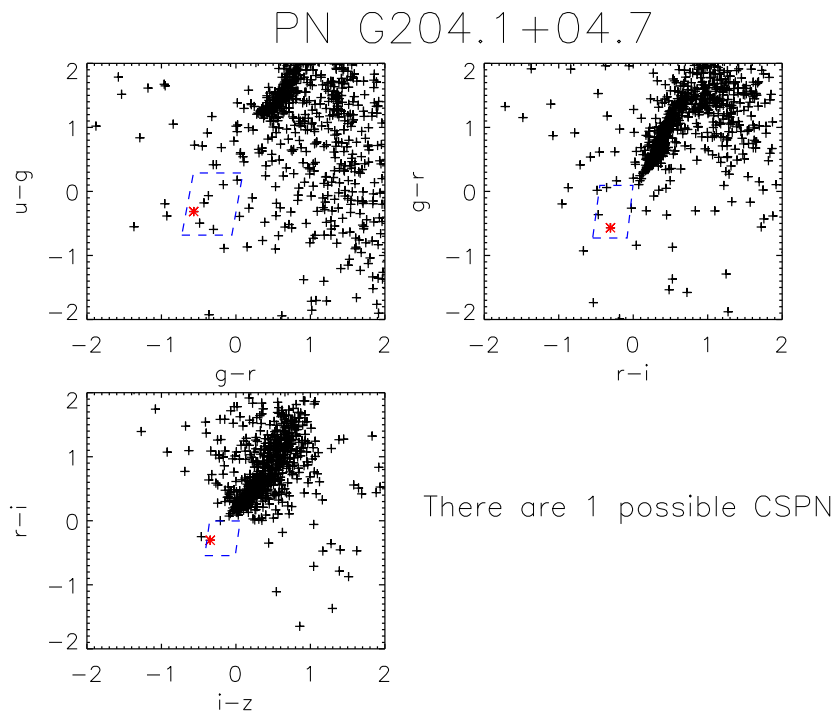
Figure A.11: The stars in the field of the PN, PN G 204.1+04.7, in colour-color space. The central star is found within our colour selection criteria
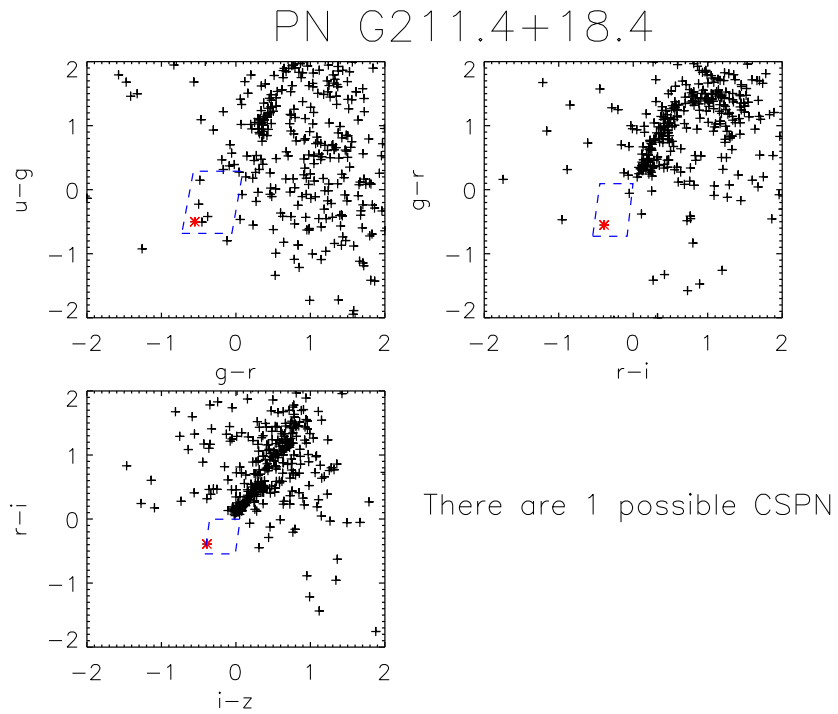
Figure A.12: The stars in the field of the PN, PN G 211.4+18.4, in colour-color space. The central star is found within our colour selection criteria
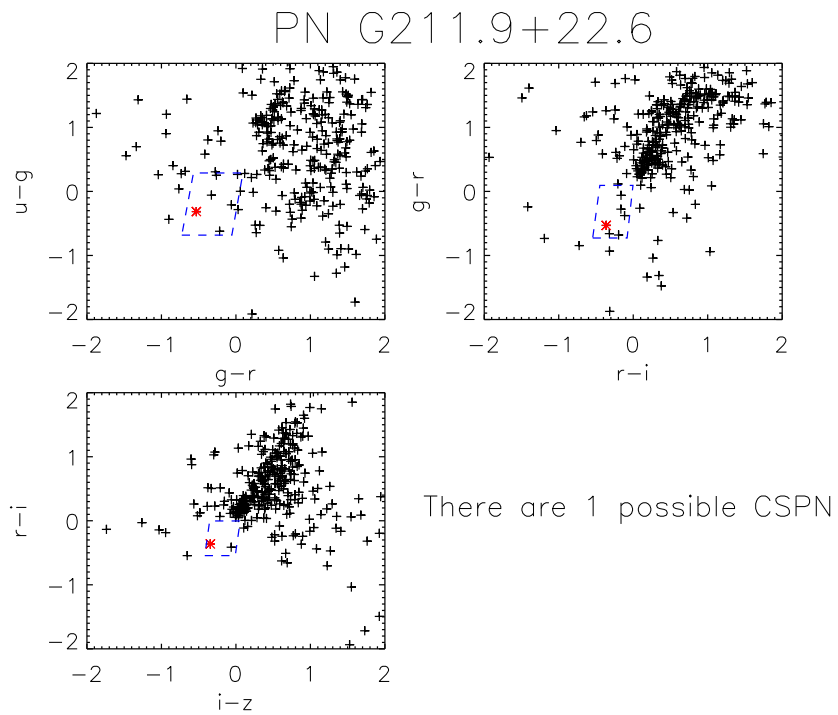
Figure A.13: The stars in the field of the PN, PN G 211.9+22.6, in colour-color space. The central star is found within our colour selection criteria
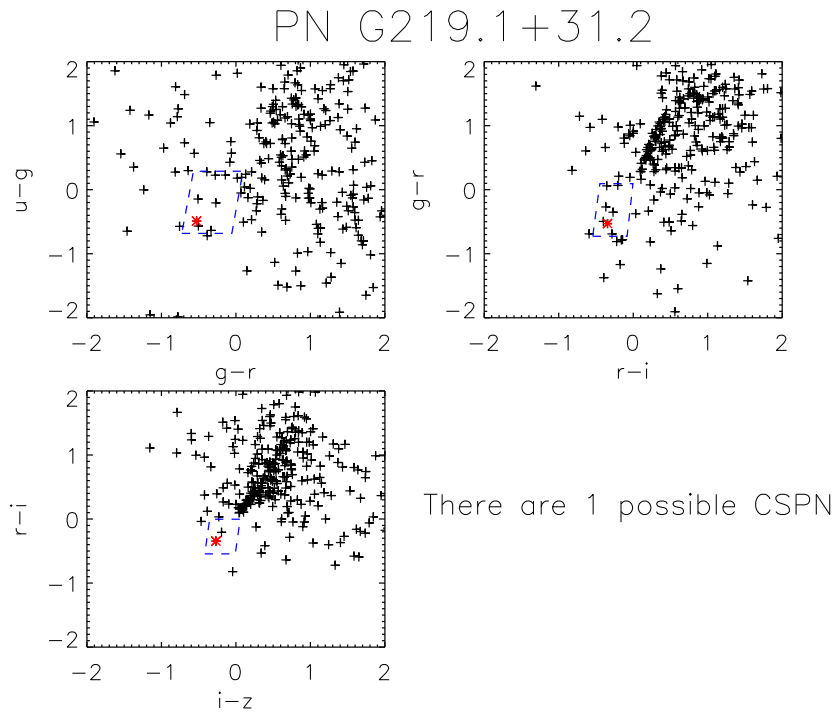
Figure A.14: The stars in the field of the PN, PN G 219.1+31.2, in colour-color space. The central star is found within our colour selection criteria

PN G221.5+46.3

There are 1 possible CSPN
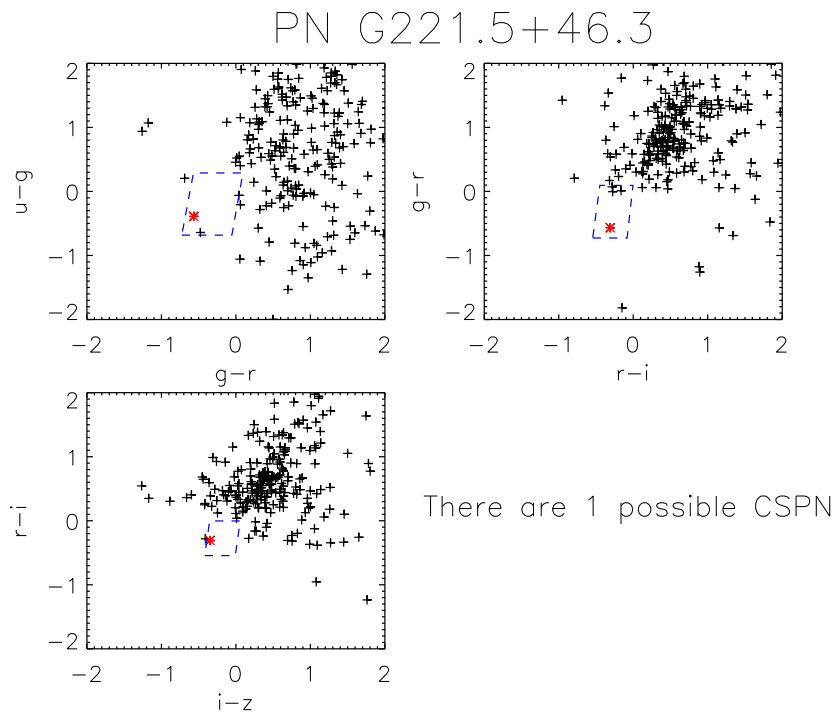
Figure A.15: The stars in the field of the PN, PN G 221.5+46.3, in colour-color space. The central star is found within our colour selection criteria

PN G238.0+34.8

There are 1 possible CSPN
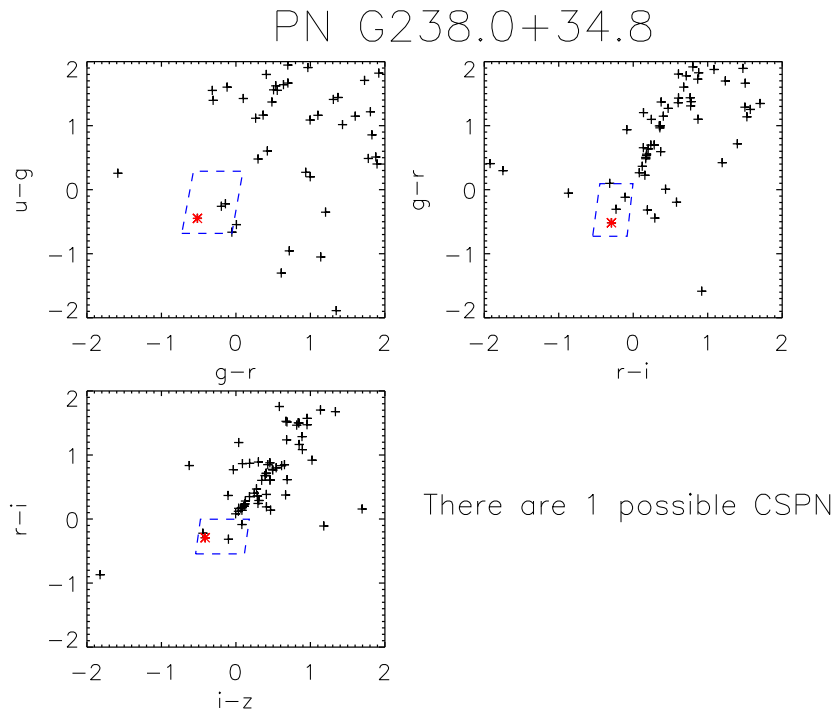
Figure A.16: The stars in the field of the PN, PN G 238.0+34.8, in colour-color space. The central star is found within our colour selection criteria

Appendix B

Evolutionary Track Distance Estimates of CSPNe in SDSS from the ESO/Strasbourg Galactic Catalogue of Planetary Nebulae
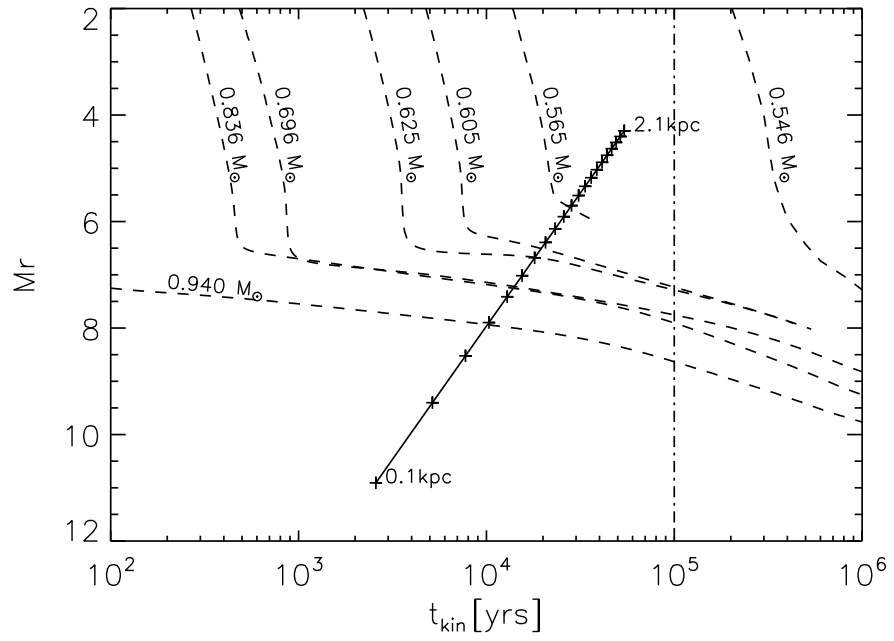
Figure B.1: The stars in the field of the PN, PN G 047.0+42.4, in colour-color space. The central star is found within our colour selection criteria
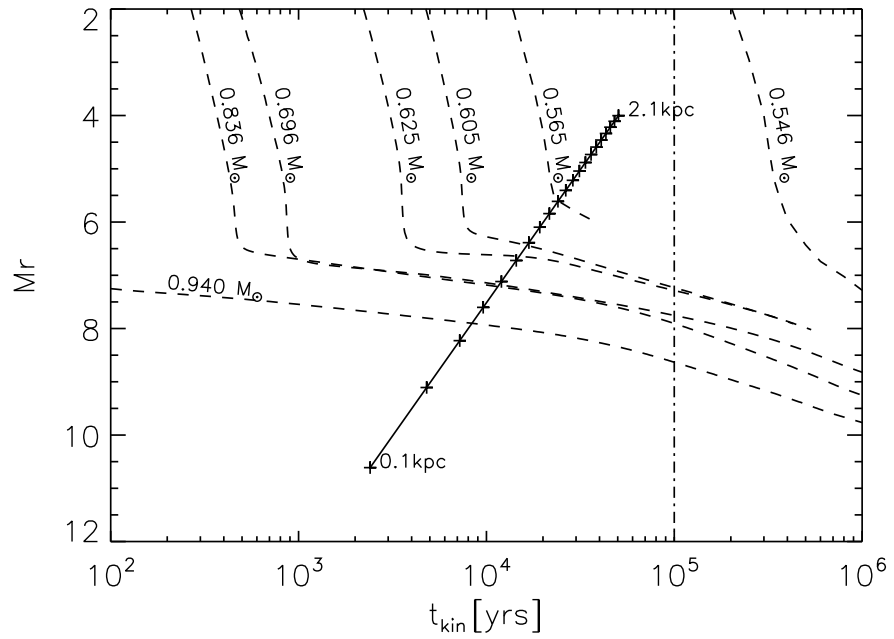
Figure B.2: The stars in the field of the PN, PN G 094.0+27.4, in colour-color space. The central star is found within our colour selection criteria
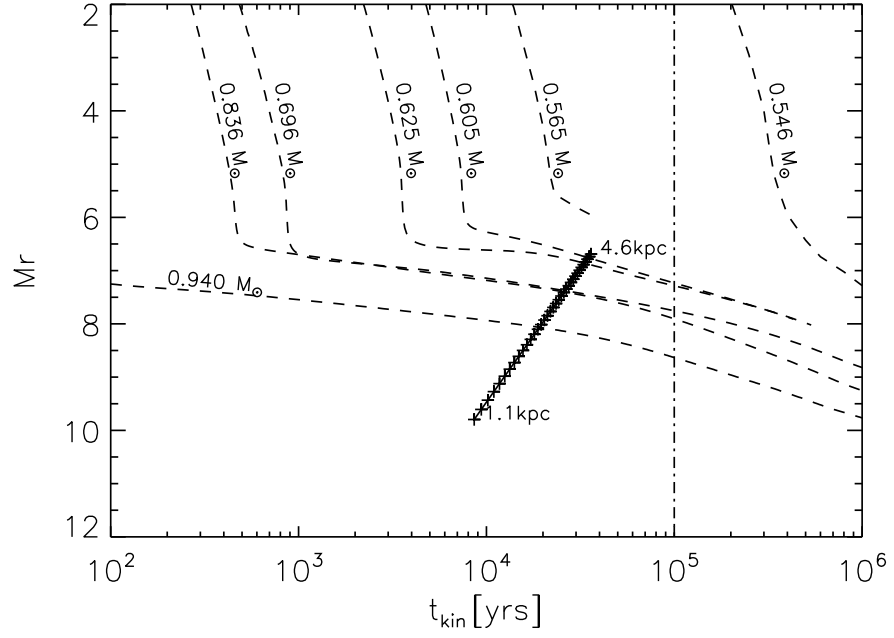
Figure B.3: The stars in the field of the PN, PN G 110.6−12.9, in colour-color space. The central star is found within our colour selection criteria
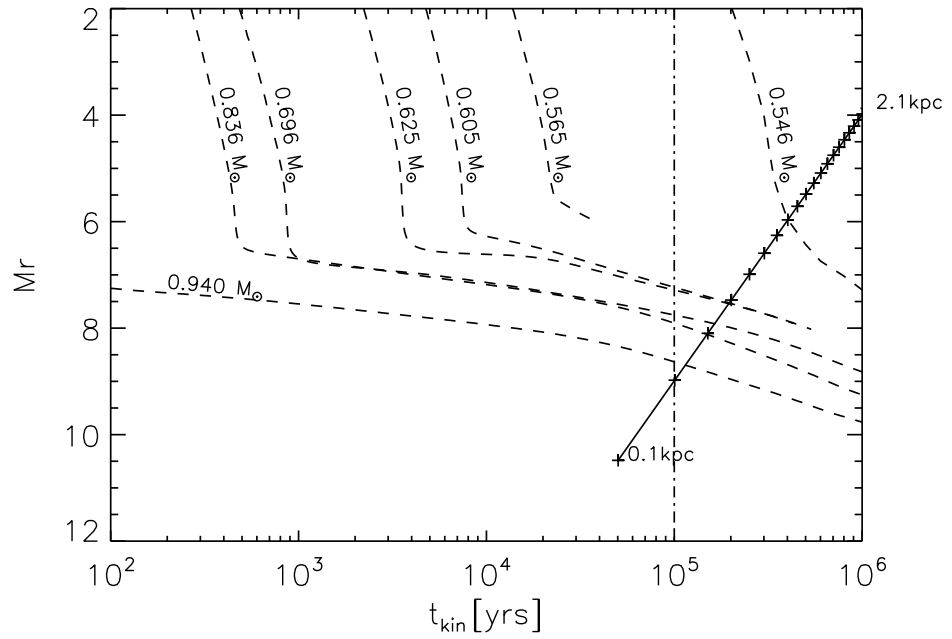
Figure B.4: The stars in the field of the PN, PN G 111.0+11.6, in colour-color space. The central star is found within our colour selection criteria
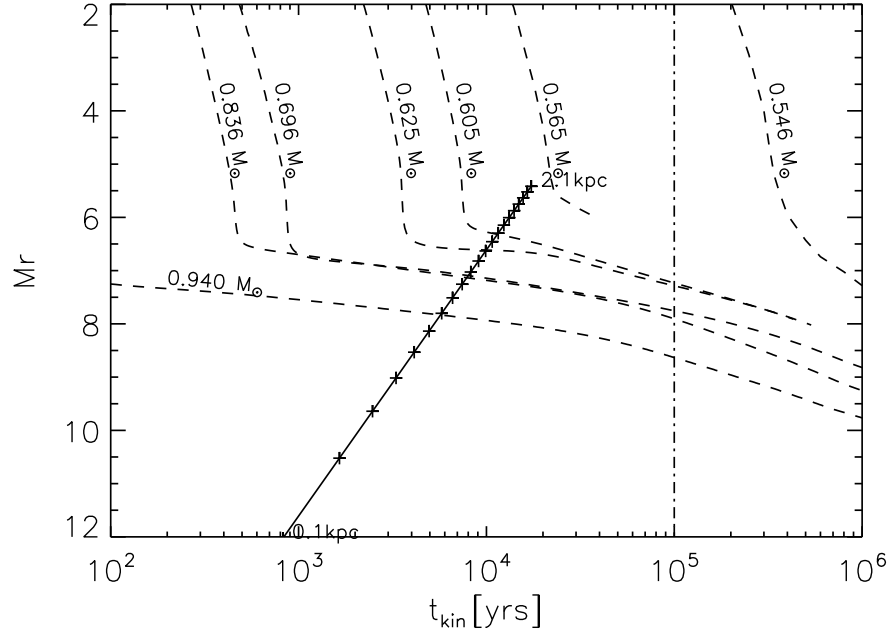
Figure B.5: The stars in the field of the PN, PN G 130.9−10.5, in colour-color space. The central star is found within our colour selection criteria
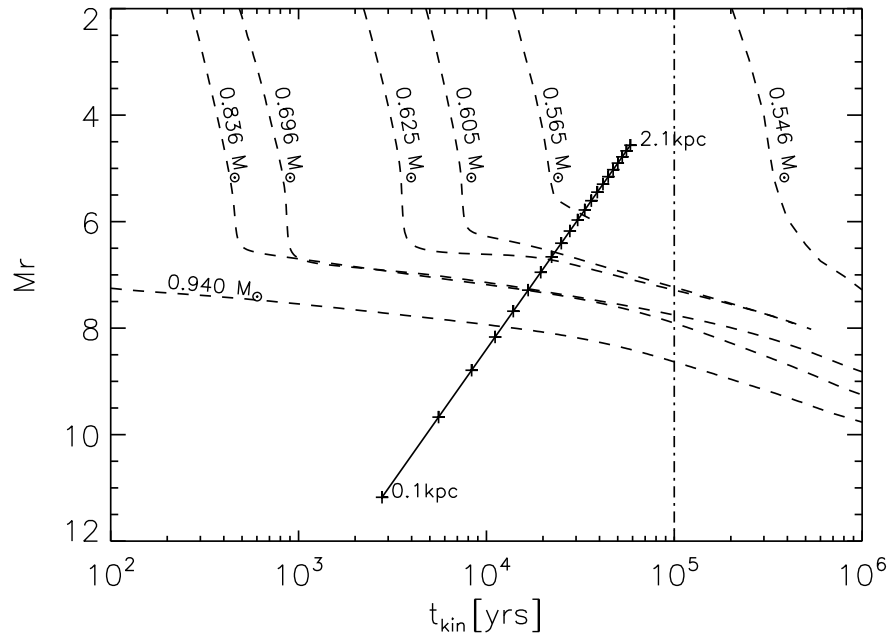
Figure B.6: The stars in the field of the PN, PN G 148.4+57.0, in colour-color space. The central star is found within our colour selection criteria
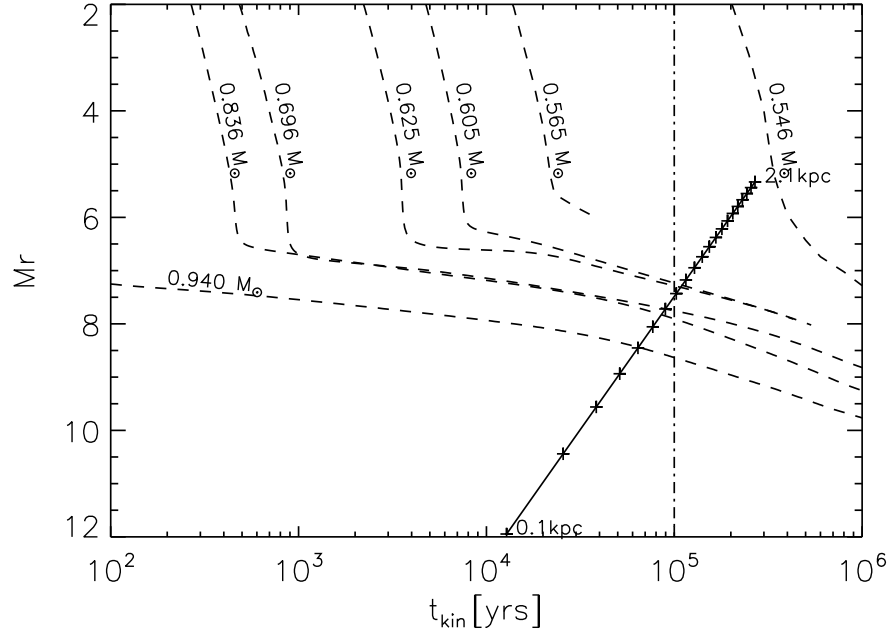
Figure B.7: The stars in the field of the PN, PN G 149.4−09.2, in colour-color space. The central star is found within our colour selection criteria
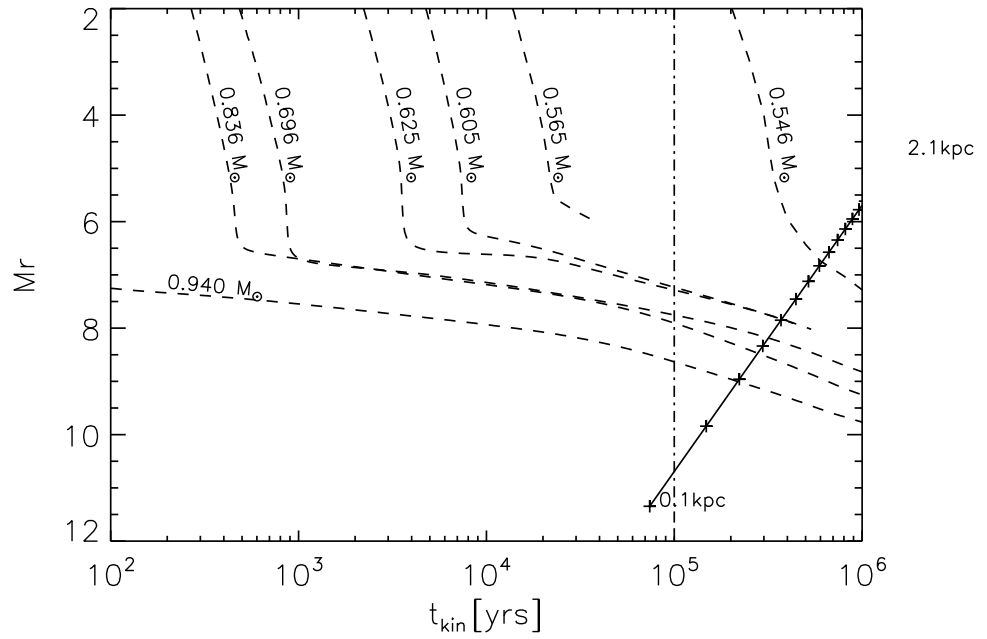
Figure B.8: The stars in the field of the PN, PN G 149.7−03.3, in colour-color space. The central star is found within our colour selection criteria
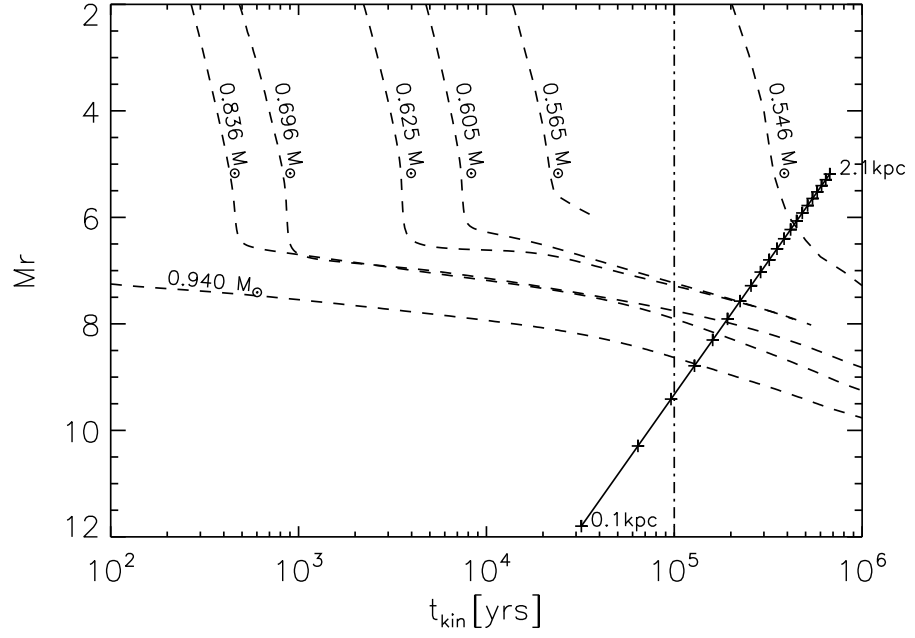
Figure B.9: The stars in the field of the PN, PN G 158.8+37.1, in colour-color space. The central star is found within our colour selection criteria
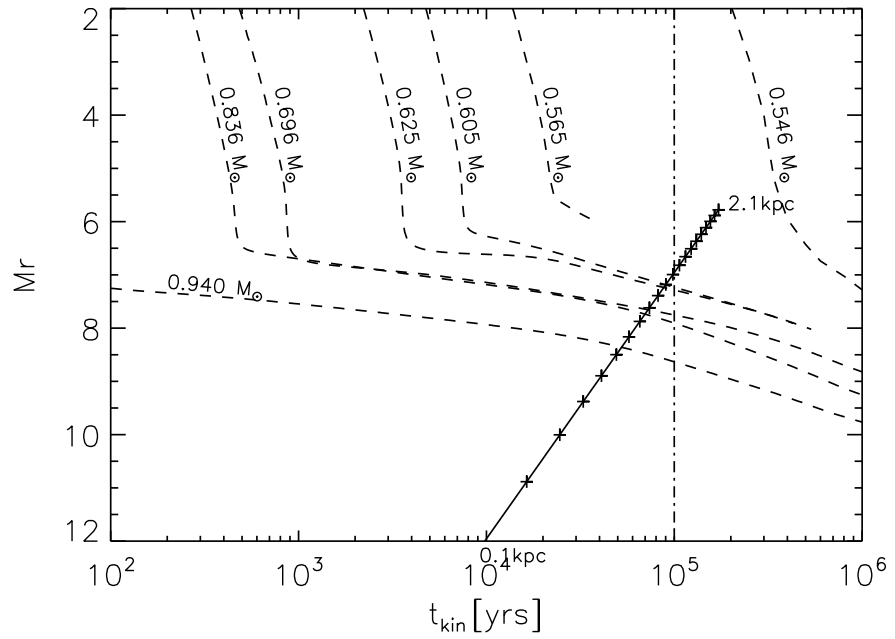
Figure B.10: The stars in the field of the PN, PN G 164.8+31.1, in colour-color space. The central star is found within our colour selection criteria
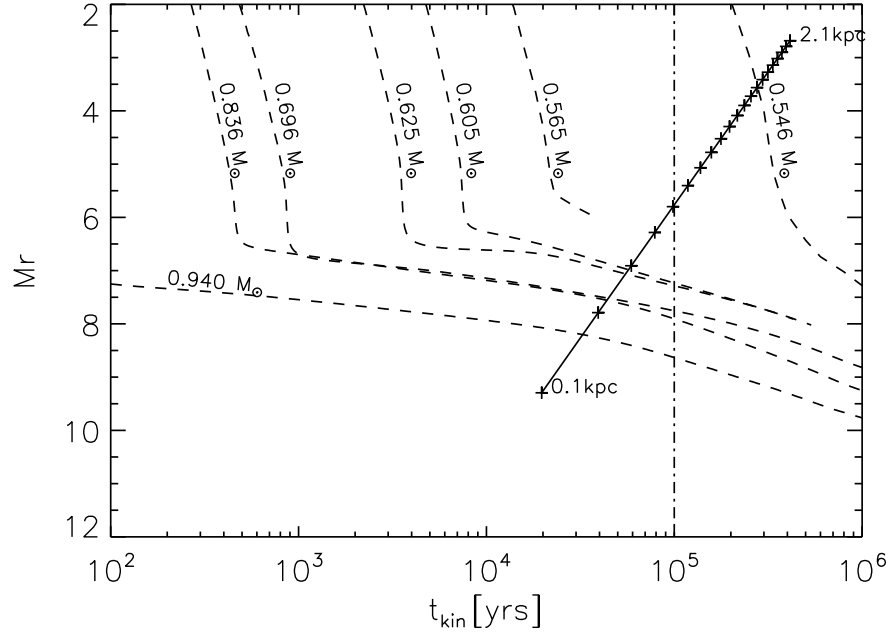
Figure B.11: The stars in the field of the PN, PN G 204.1+04.7, in colour-color space. The central star is found within our colour selection criteria
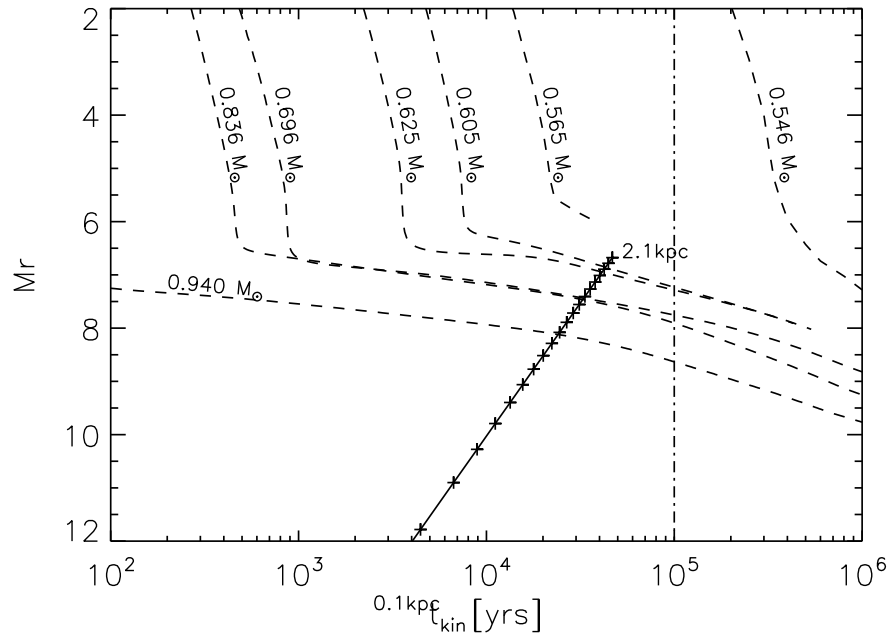
Figure B.12: The stars in the field of the PN, PN G 211.4+18.4, in colour-color space. The central star is found within our colour selection criteria
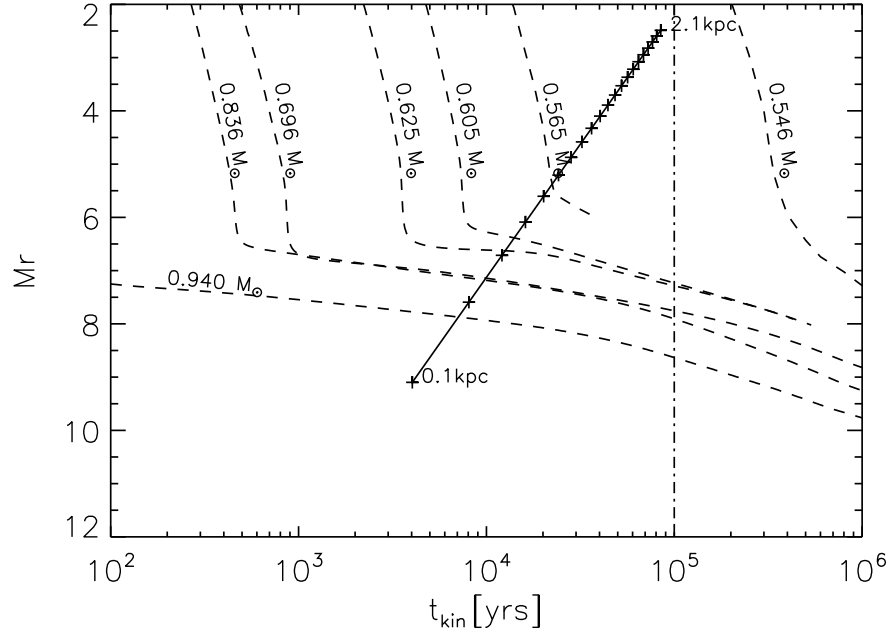
Figure B.13: The stars in the field of the PN, PN G 211.9+22.6, in colour-color space. The central star is found within our colour selection criteria
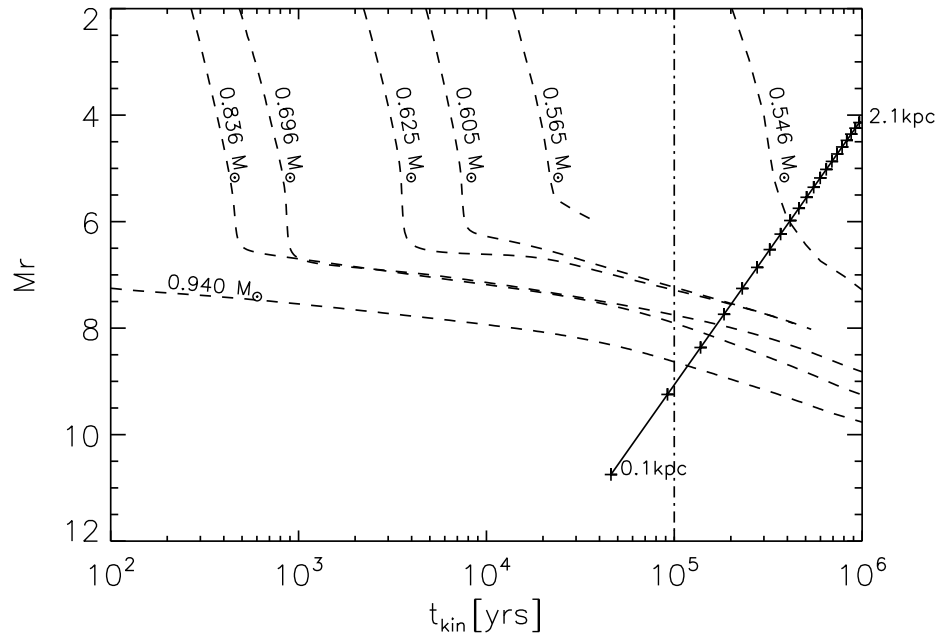
Figure B.14: The stars in the field of the PN, PN G 219.1+31.2, in colour-color space. The central star is found within our colour selection criteria
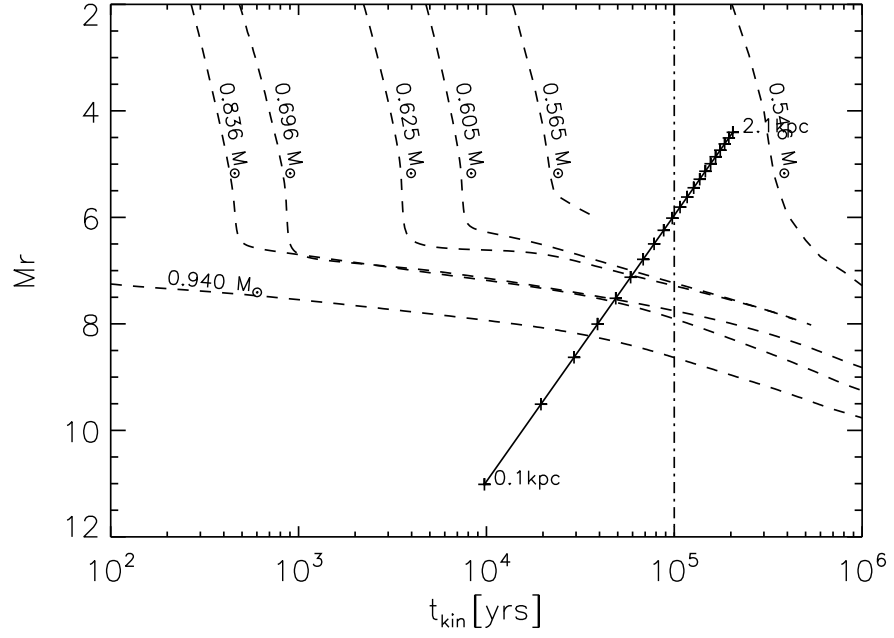
Figure B.15: The stars in the field of the PN, PN G 221.5+46.3, in colour-color space. The central star is found within our colour selection criteria
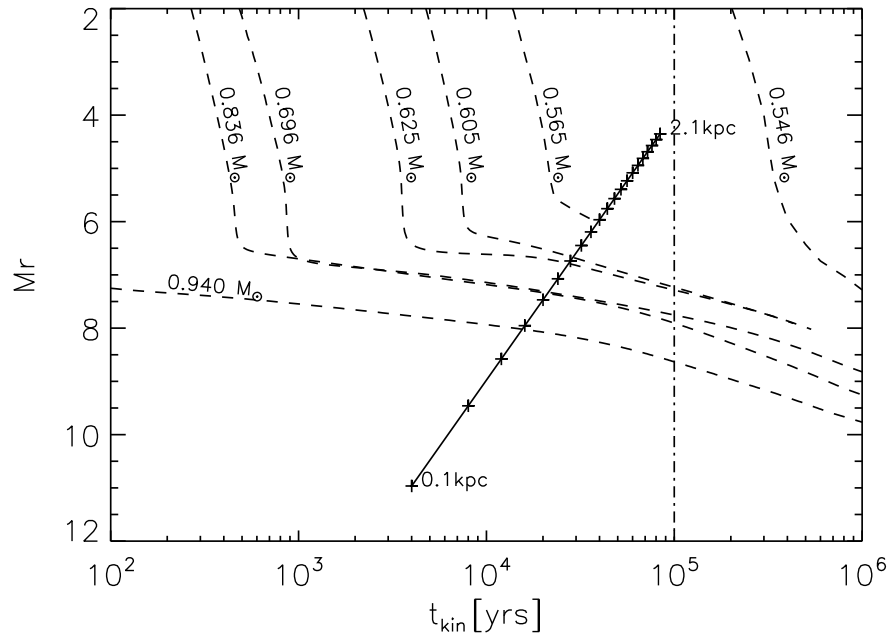
Figure B.16: The stars in the field of the PN, PN G 238.0+34.8, in colour-color space. The central star is found within our colour selection criteria

Appendix C

Balmer Line Fitting Candidate post-AGB Spectra from SDSS
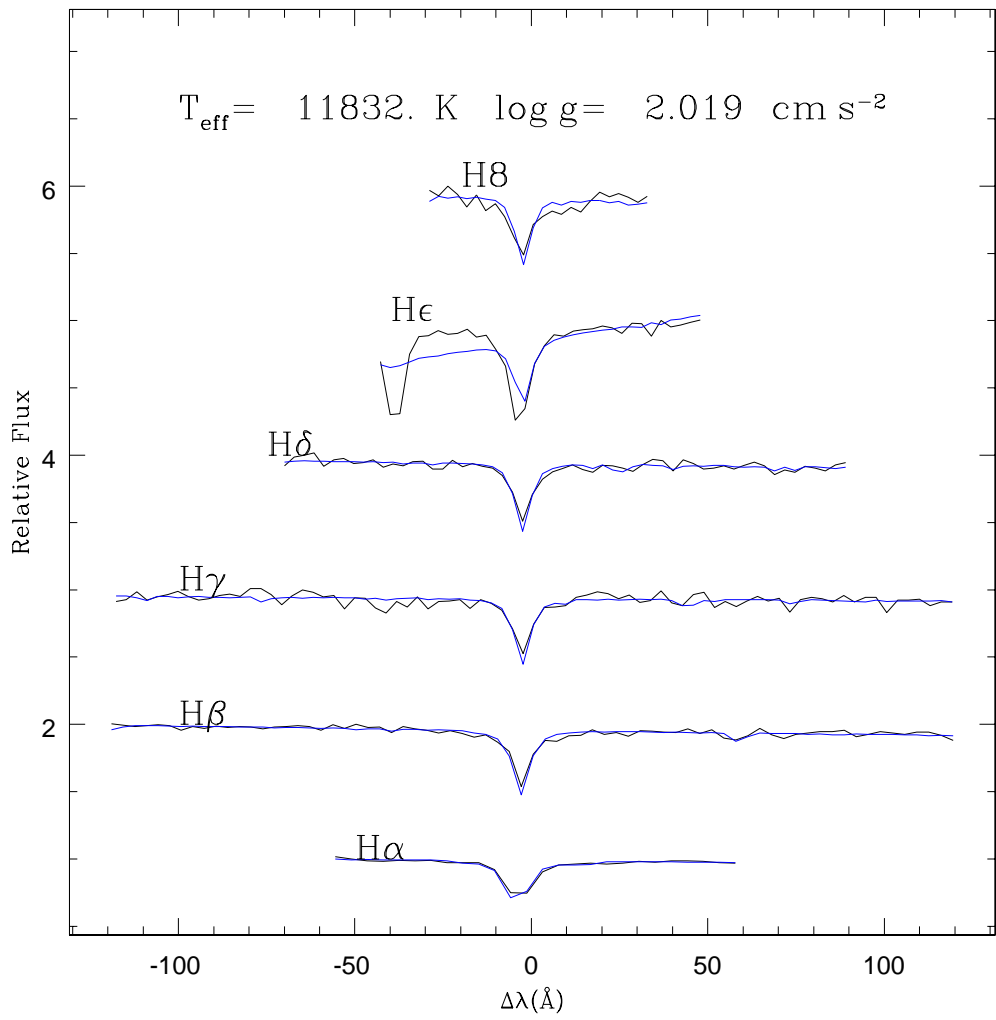
Figure C.1: The best Balmer Line fit of spSpec-54498-2882-466.
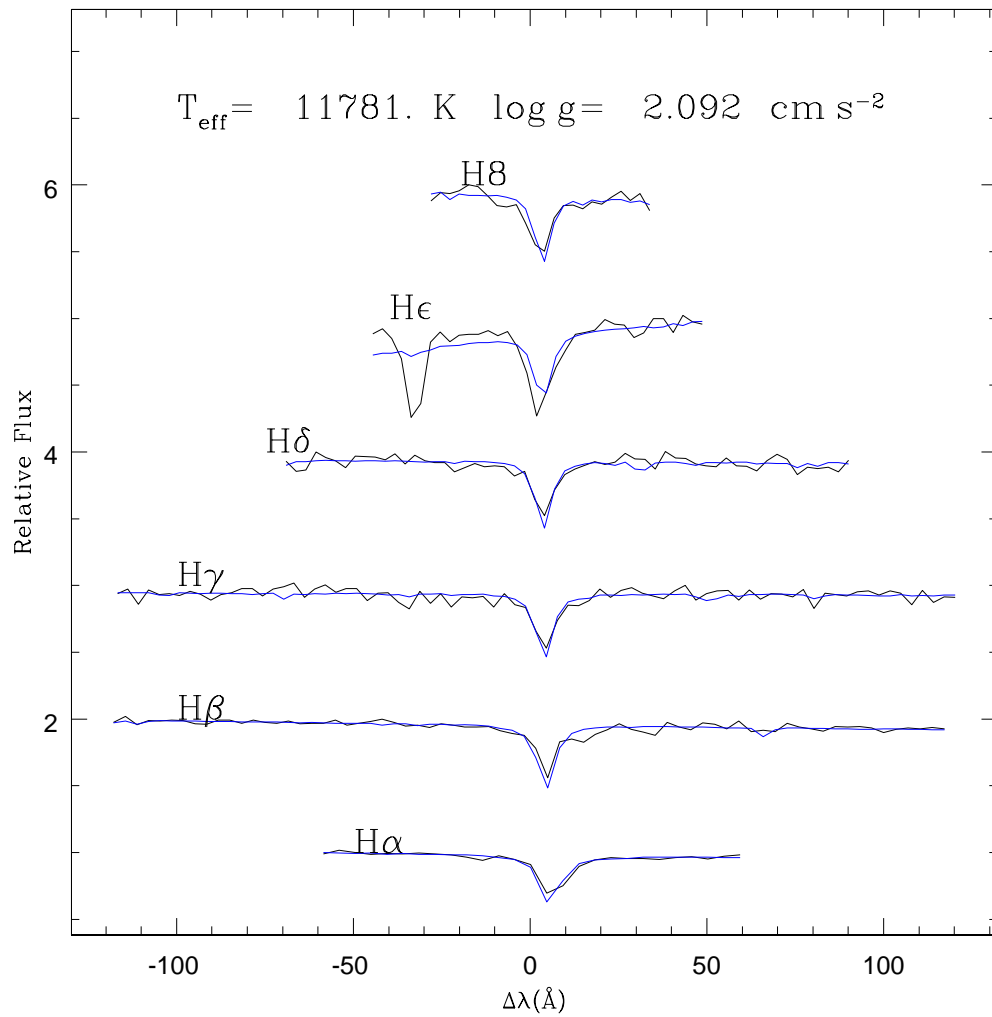
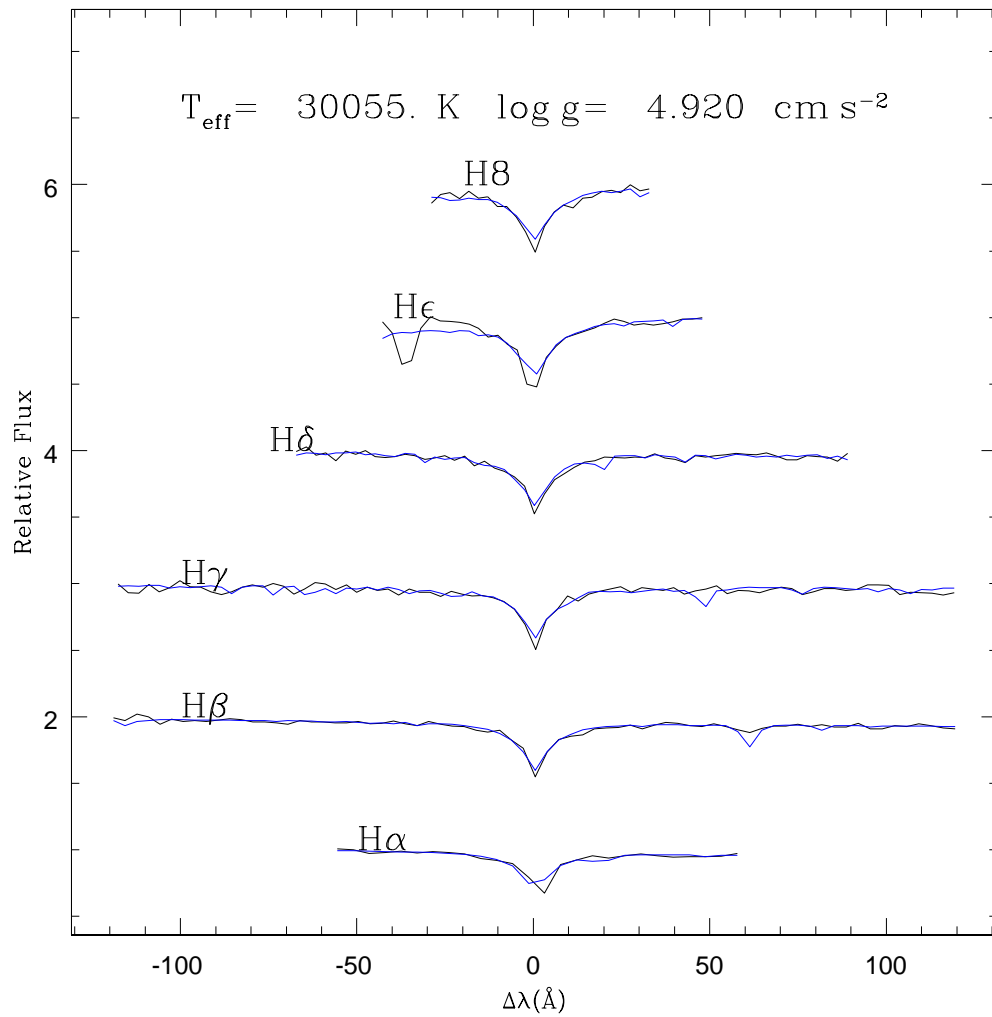Figure C.2: The best Balmer Line fit of spSpec-53556-1799-625.
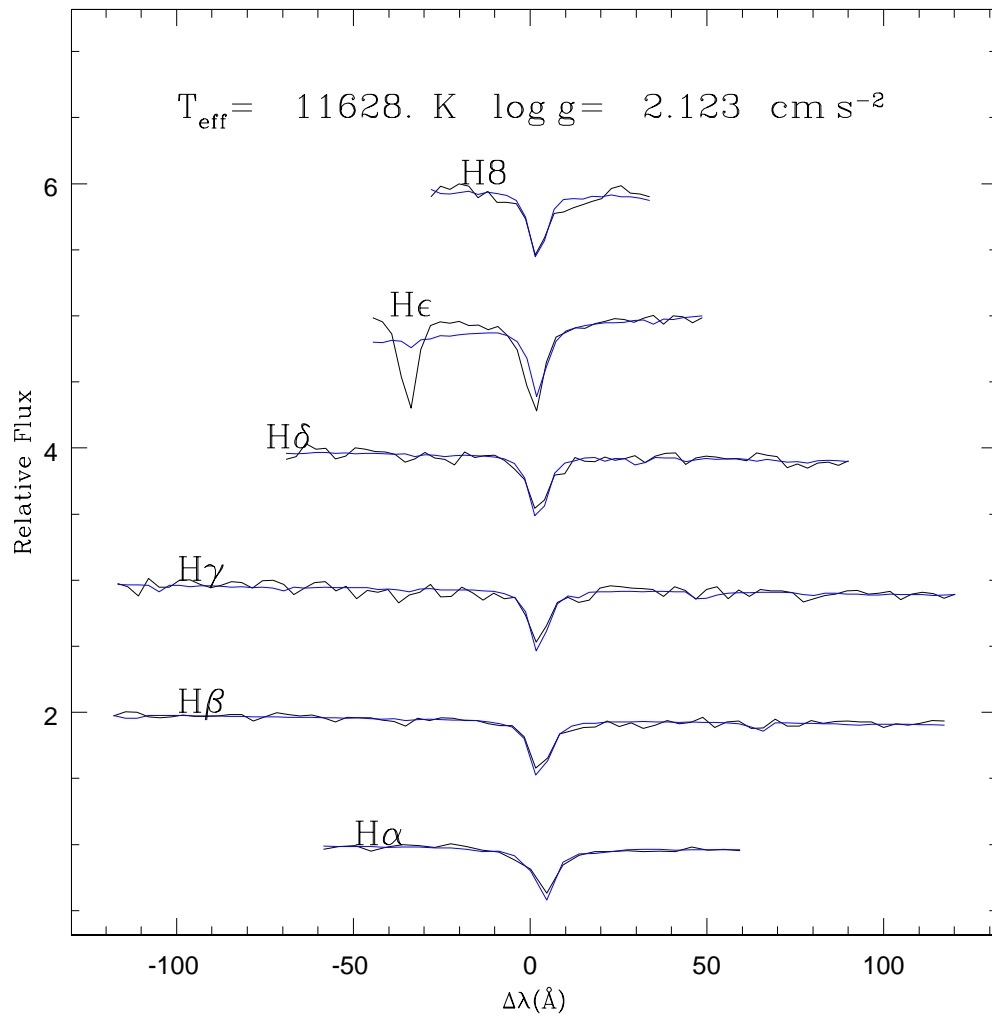
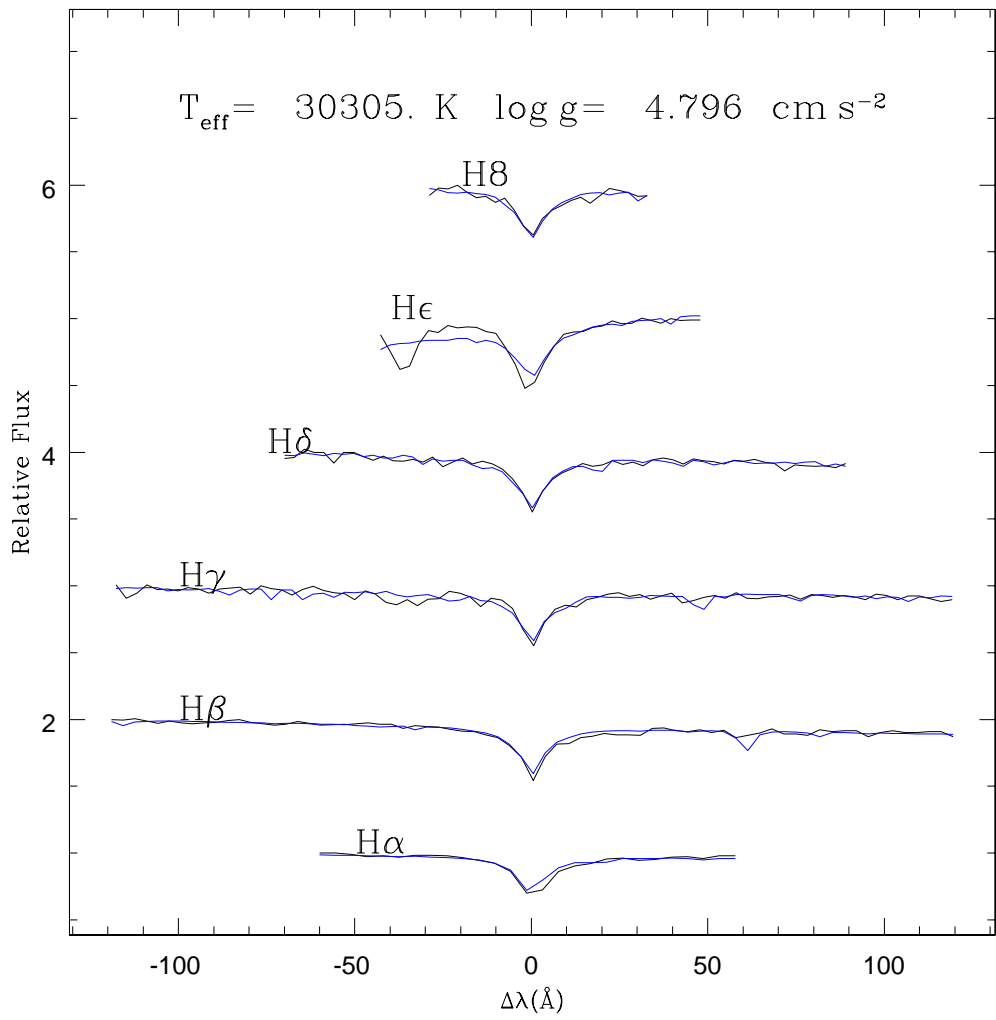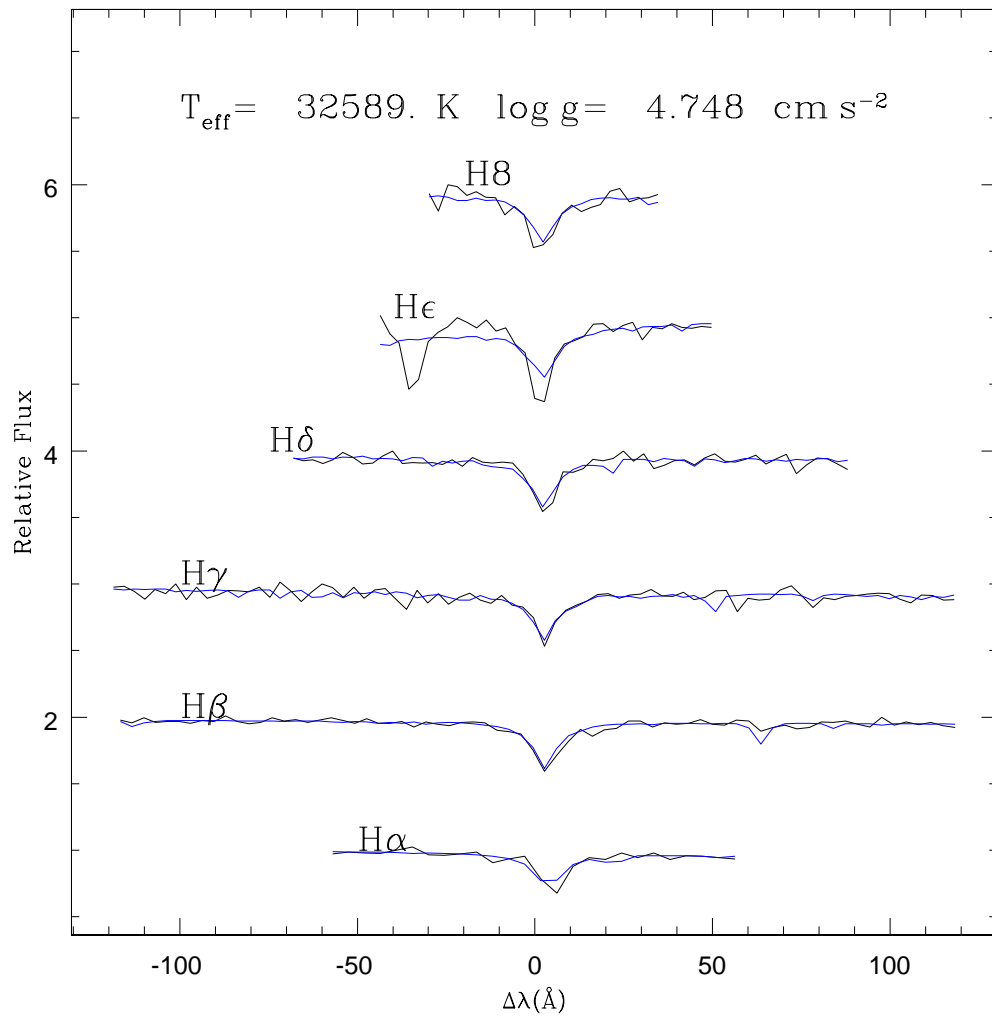Figure C.3: The best Balmer Line fit of spSpec-53848-2437-371.
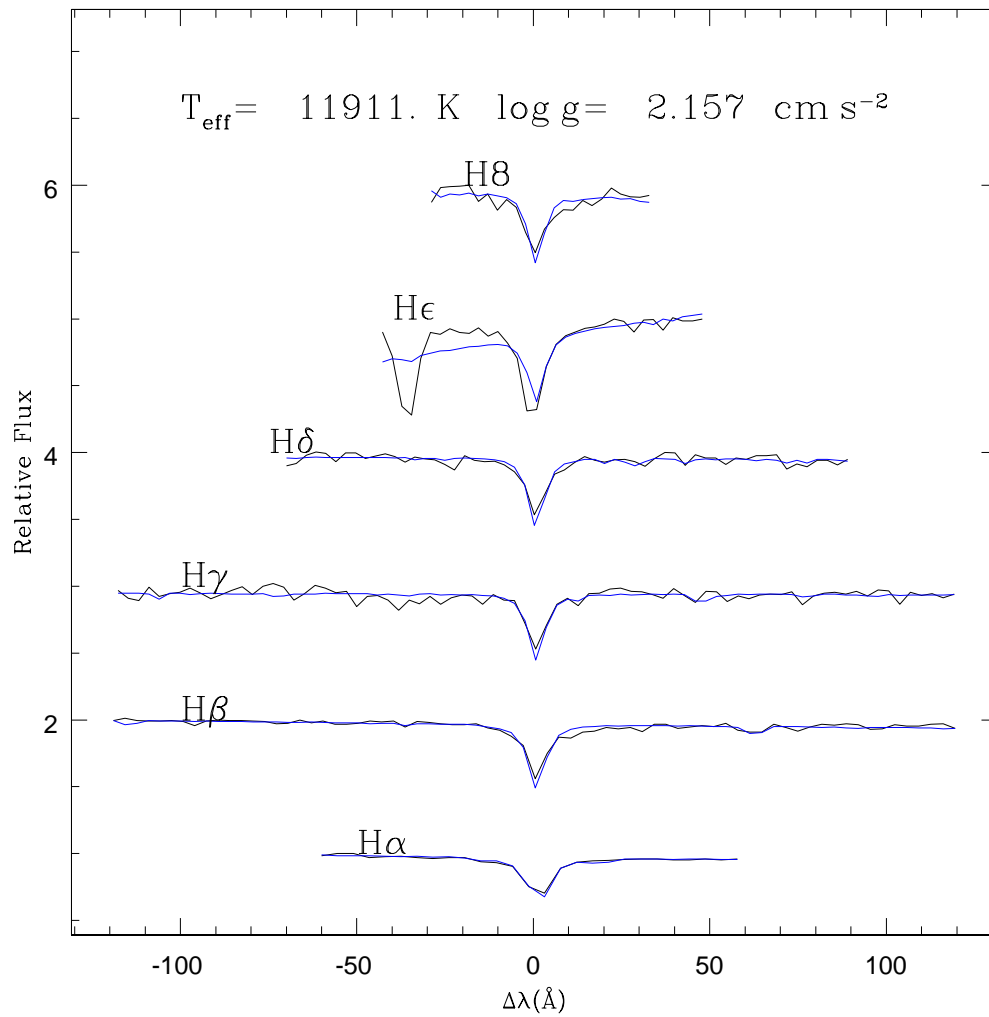
Figure C.4: The best Balmer Line fit of spSpec-54582-2526-459.
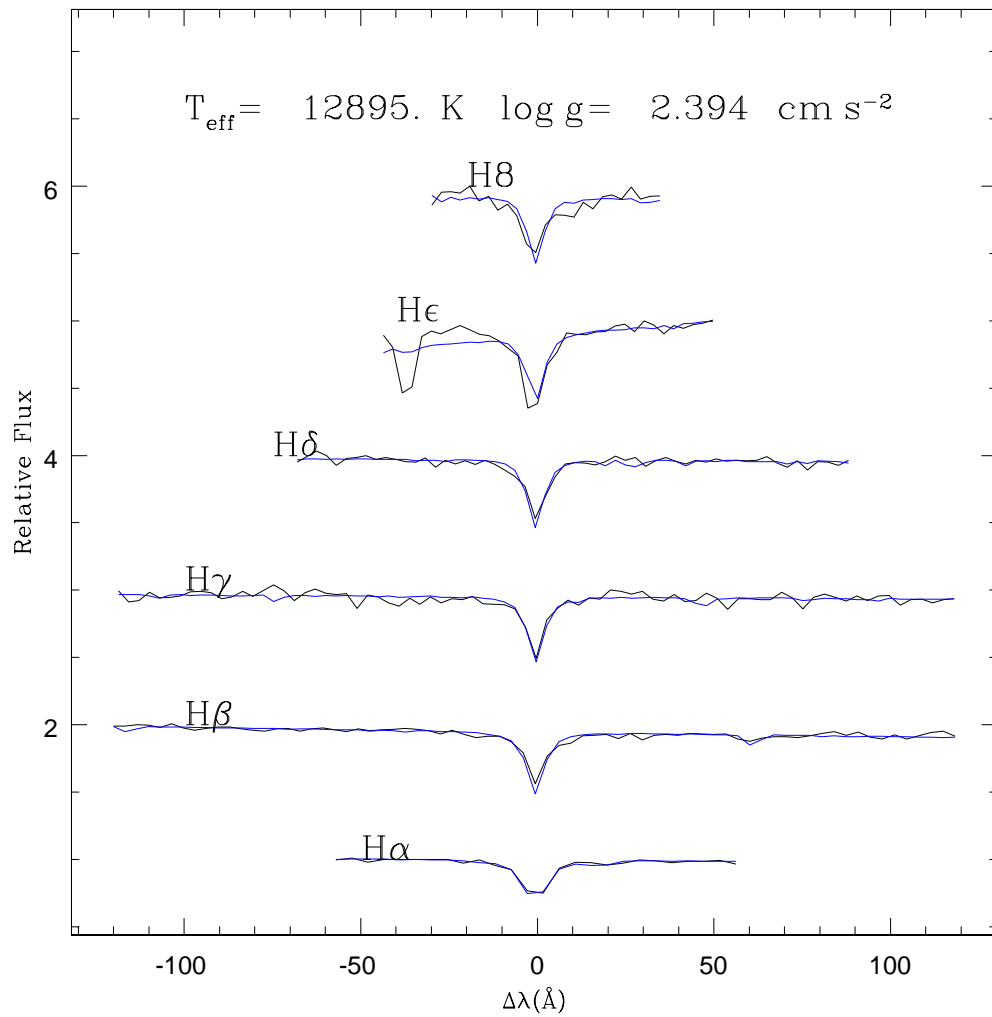
Figure C.5: The best Balmer Line fit of spSpec-54495-2647-246.
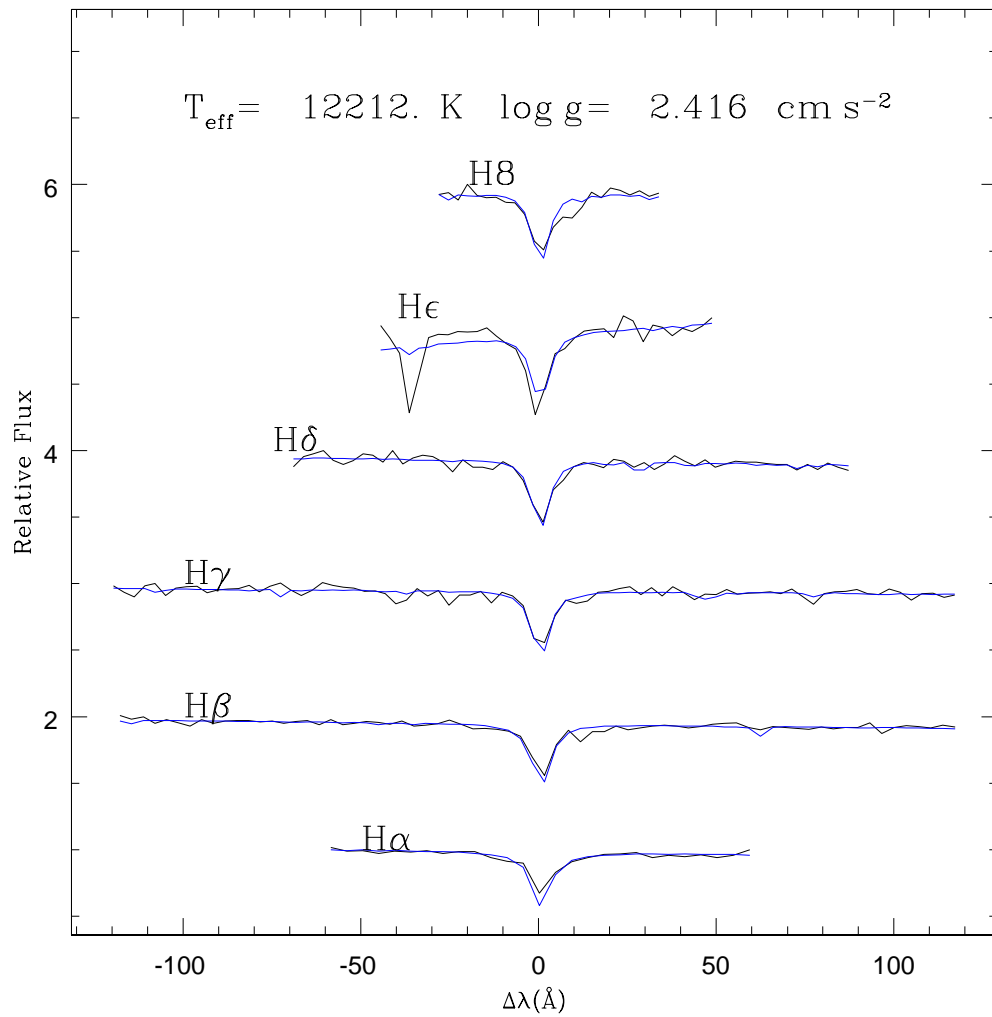
Figure C.6: The best Balmer Line fit of spSpec-53727-2290-241.
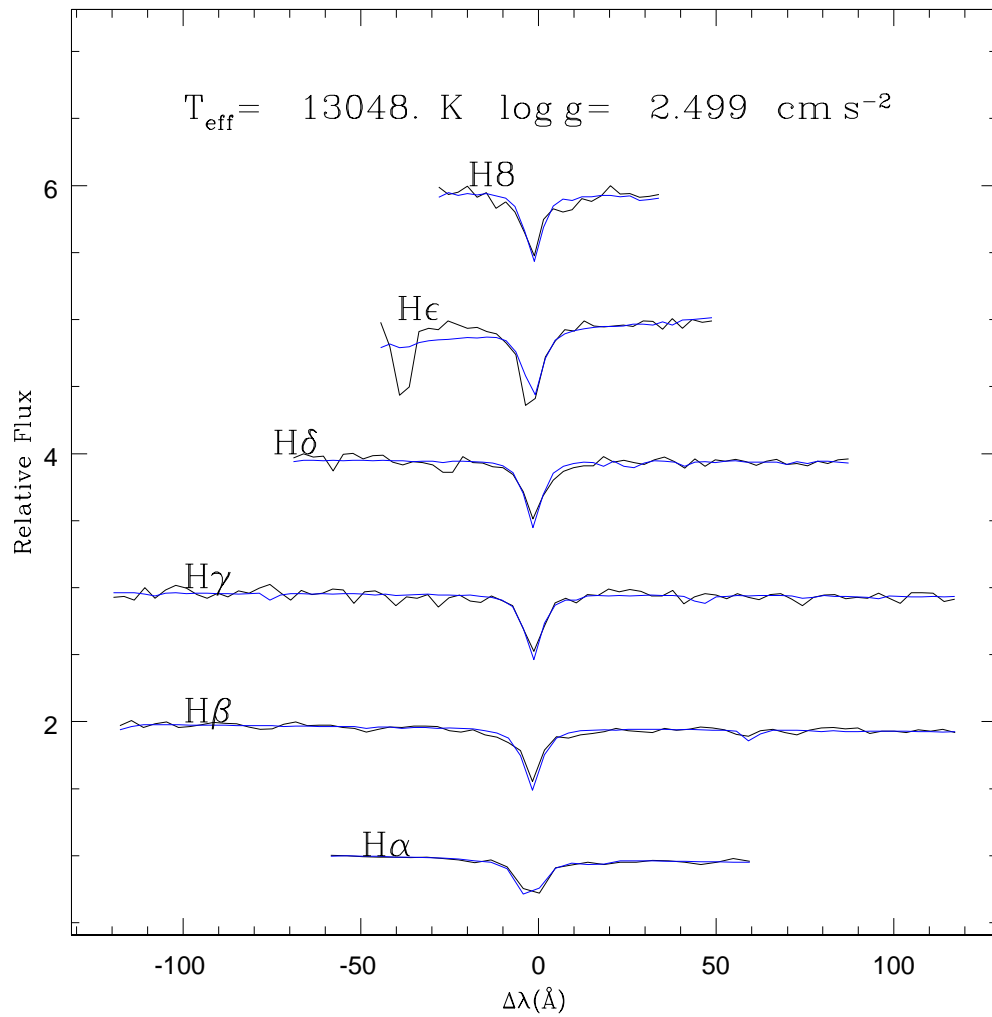
Figure C.7: The best Balmer Line fit of spSpec-54484-2656-583.
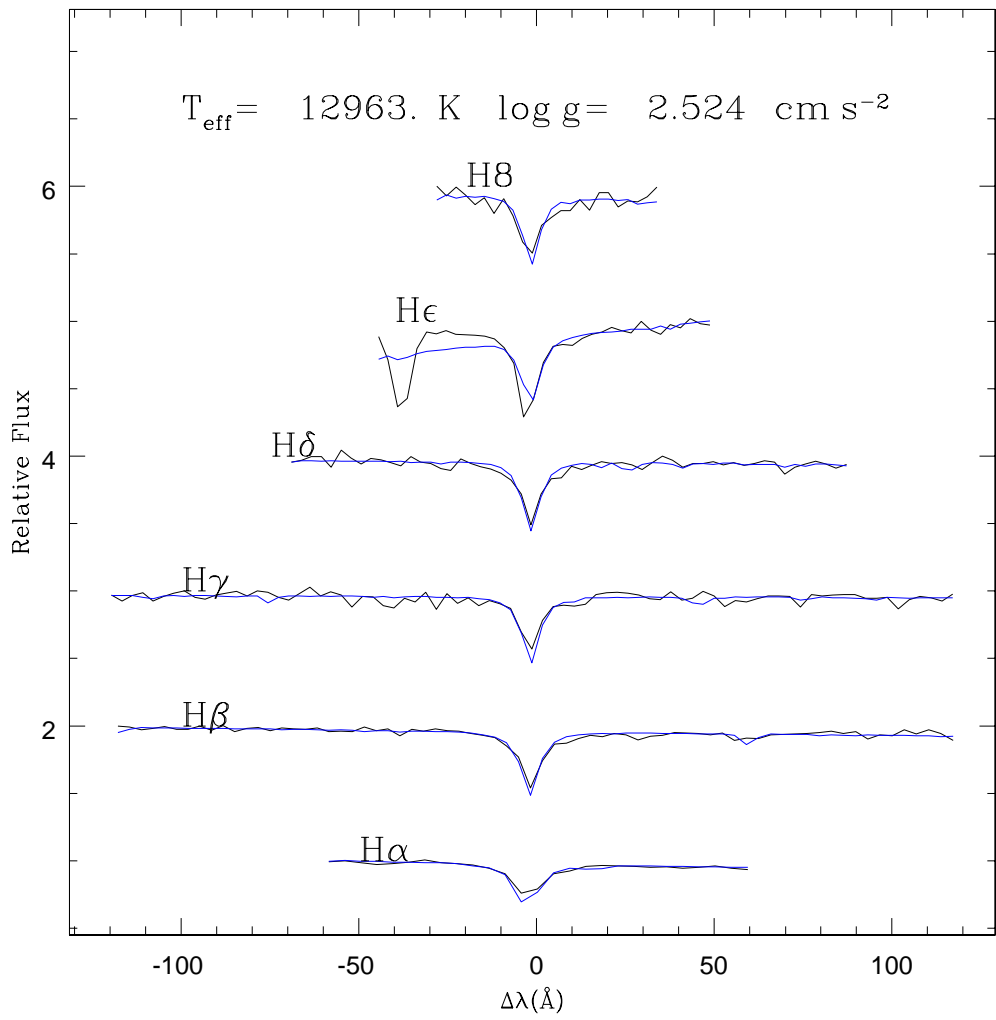
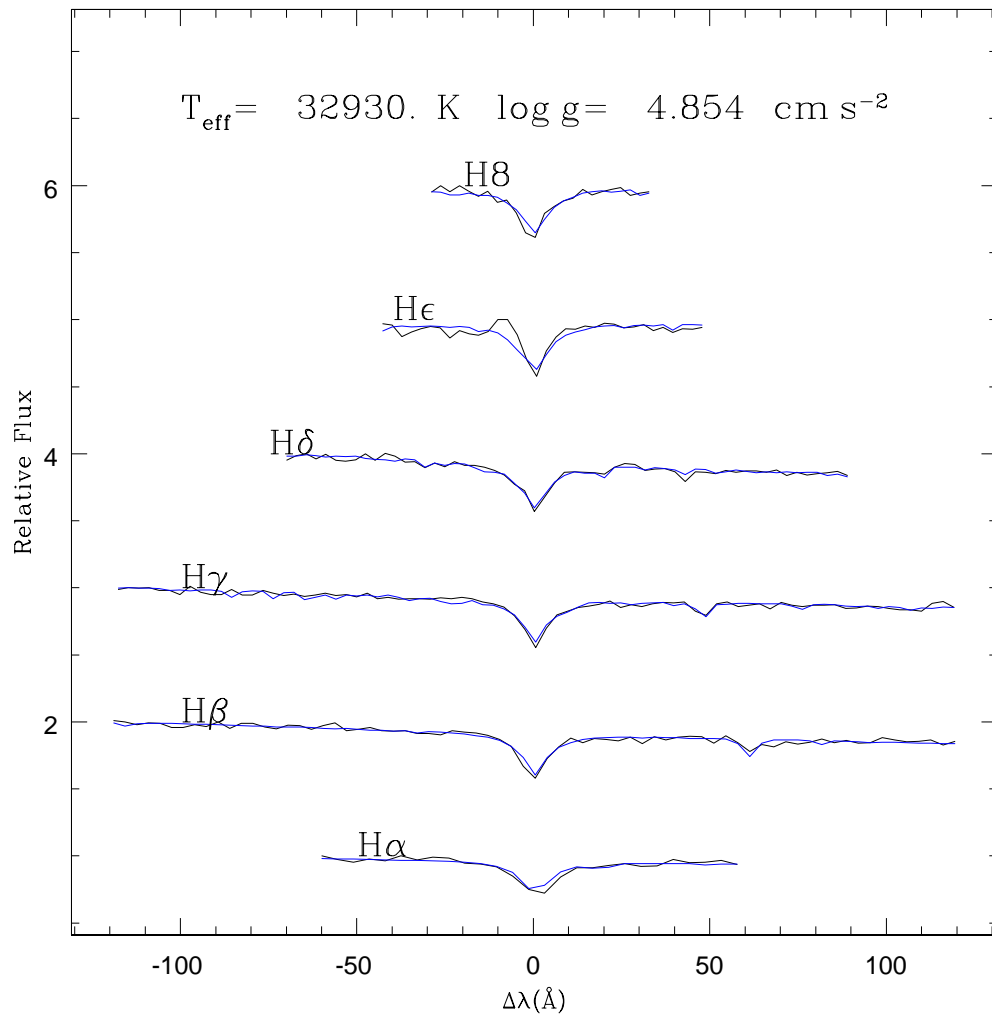Figure C.8: The best Balmer Line fit of spSpec-52764-1056-232.
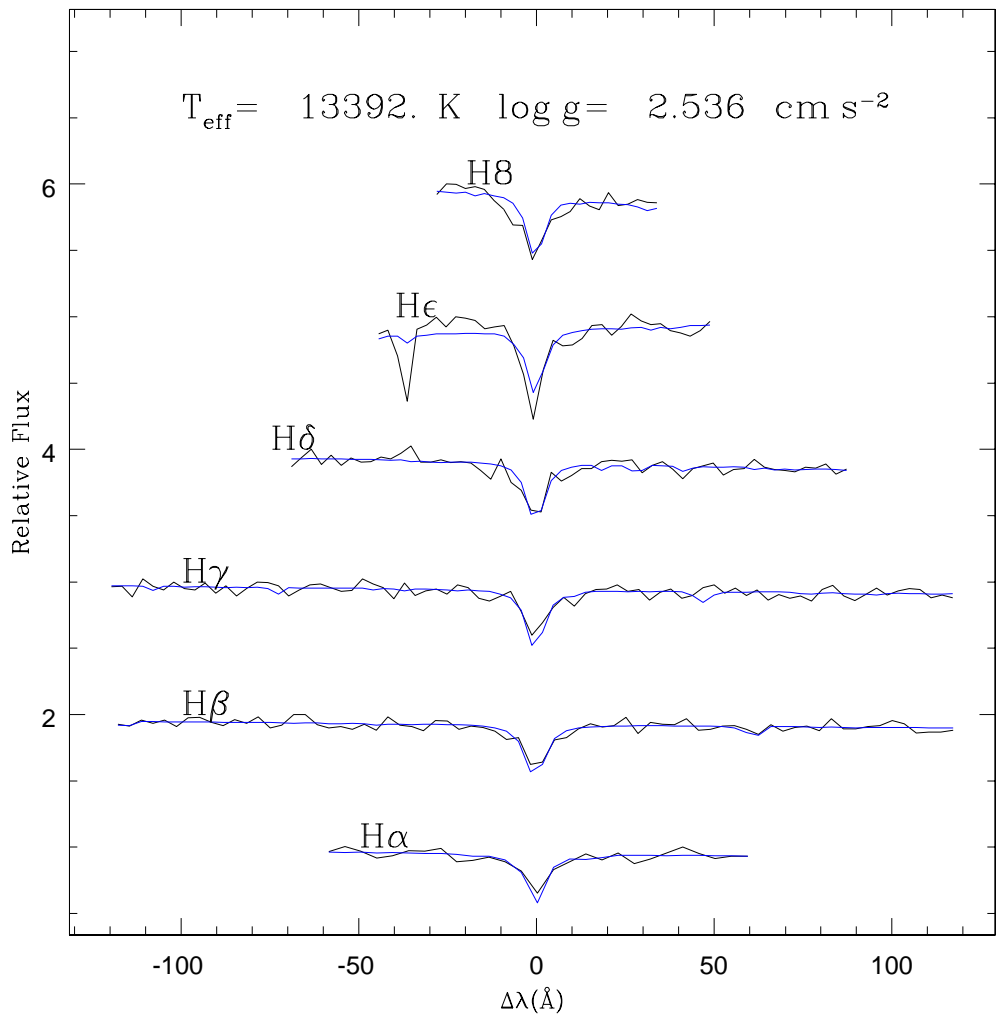
Figure C.9: The best Balmer Line fit of spSpec-54506-2760-551.
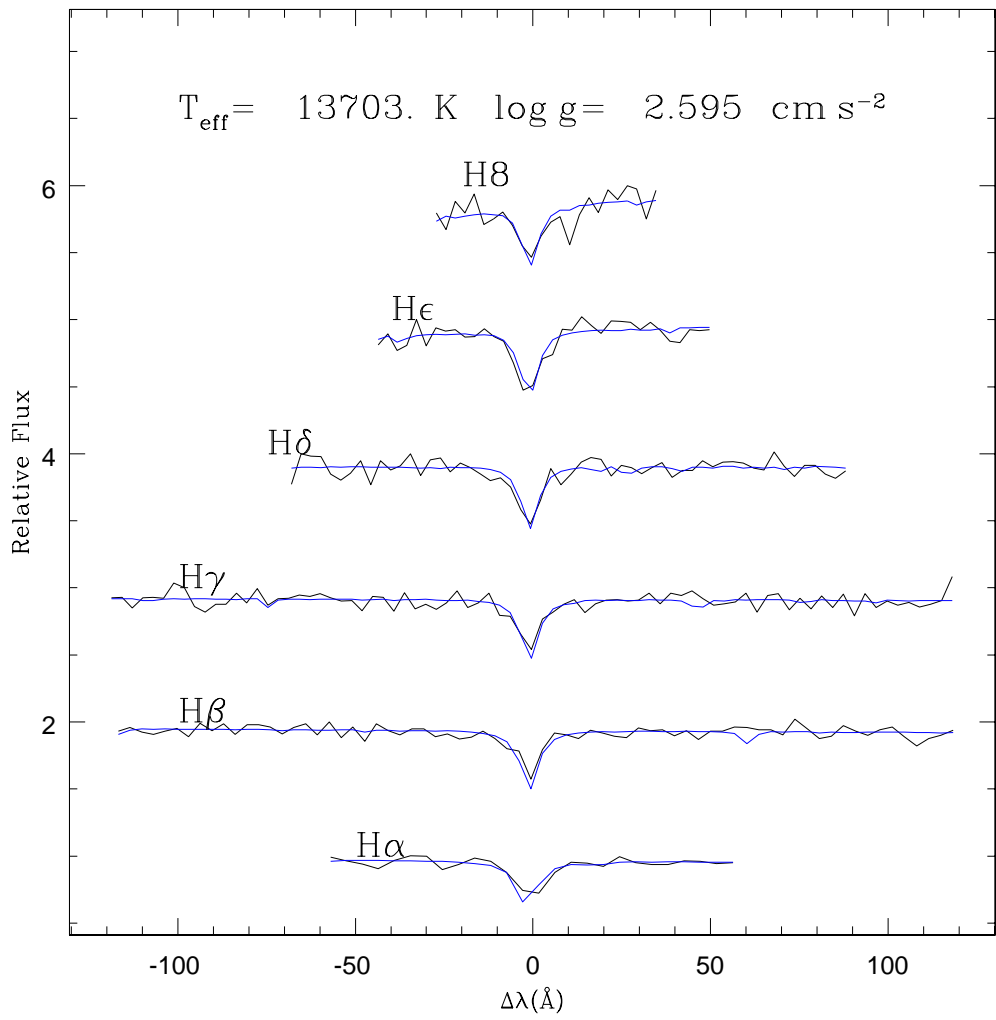
Figure C.10: The best Balmer Line fit of spSpec-52468-1053-428.
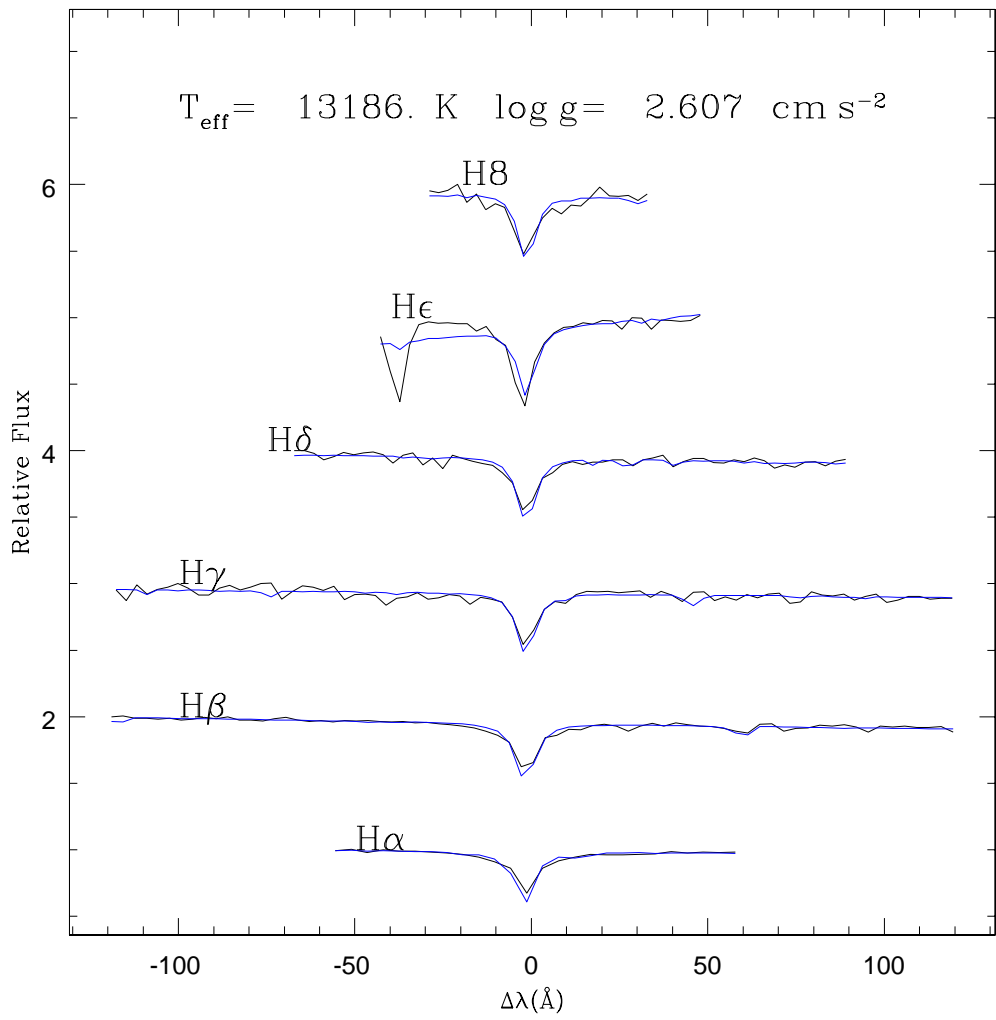
Figure C.11: The best Balmer Line fit of spSpec-53084-1368-611.
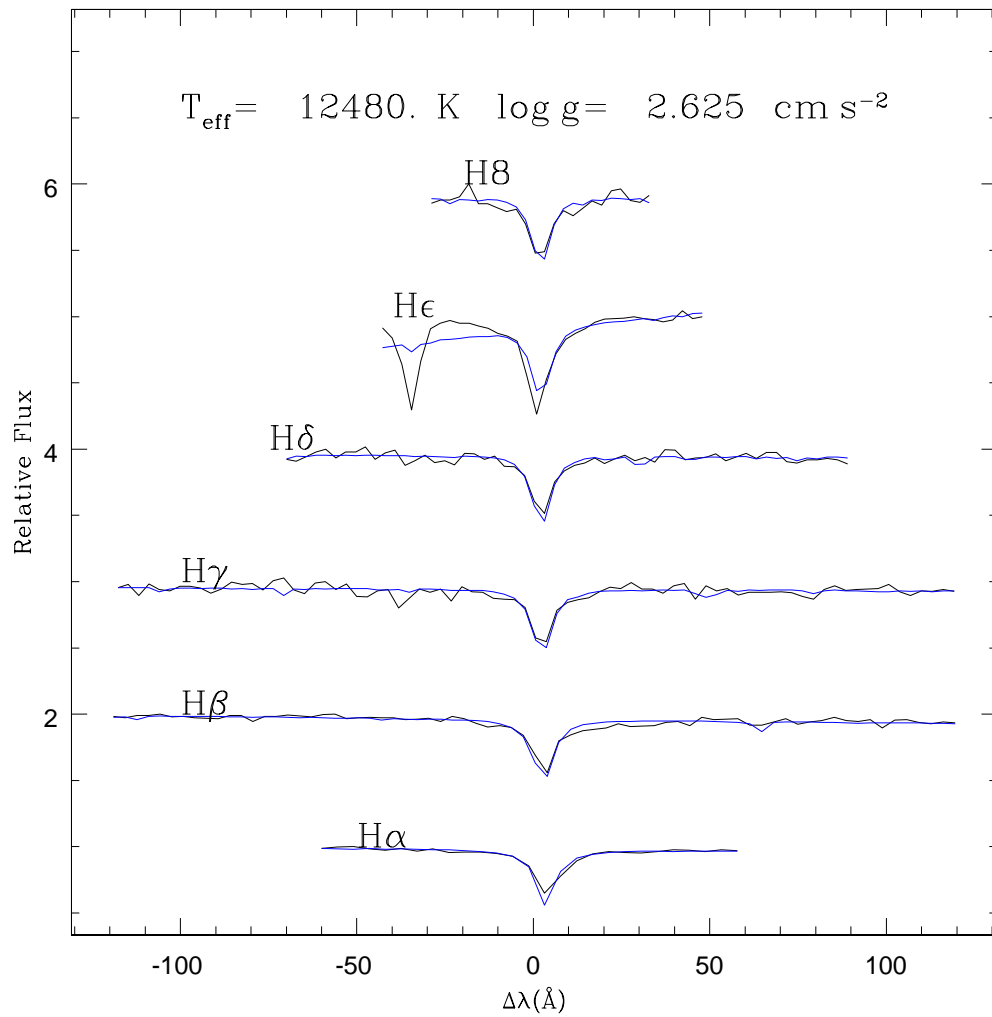
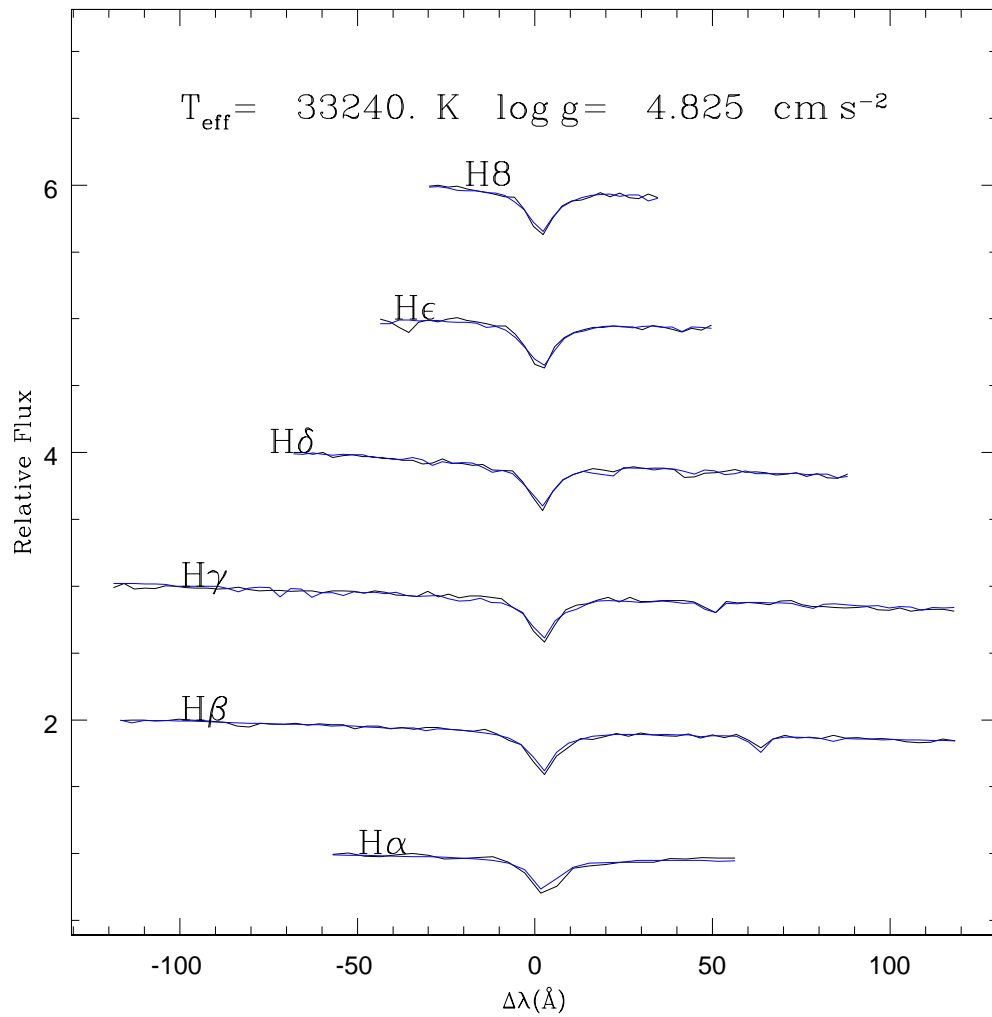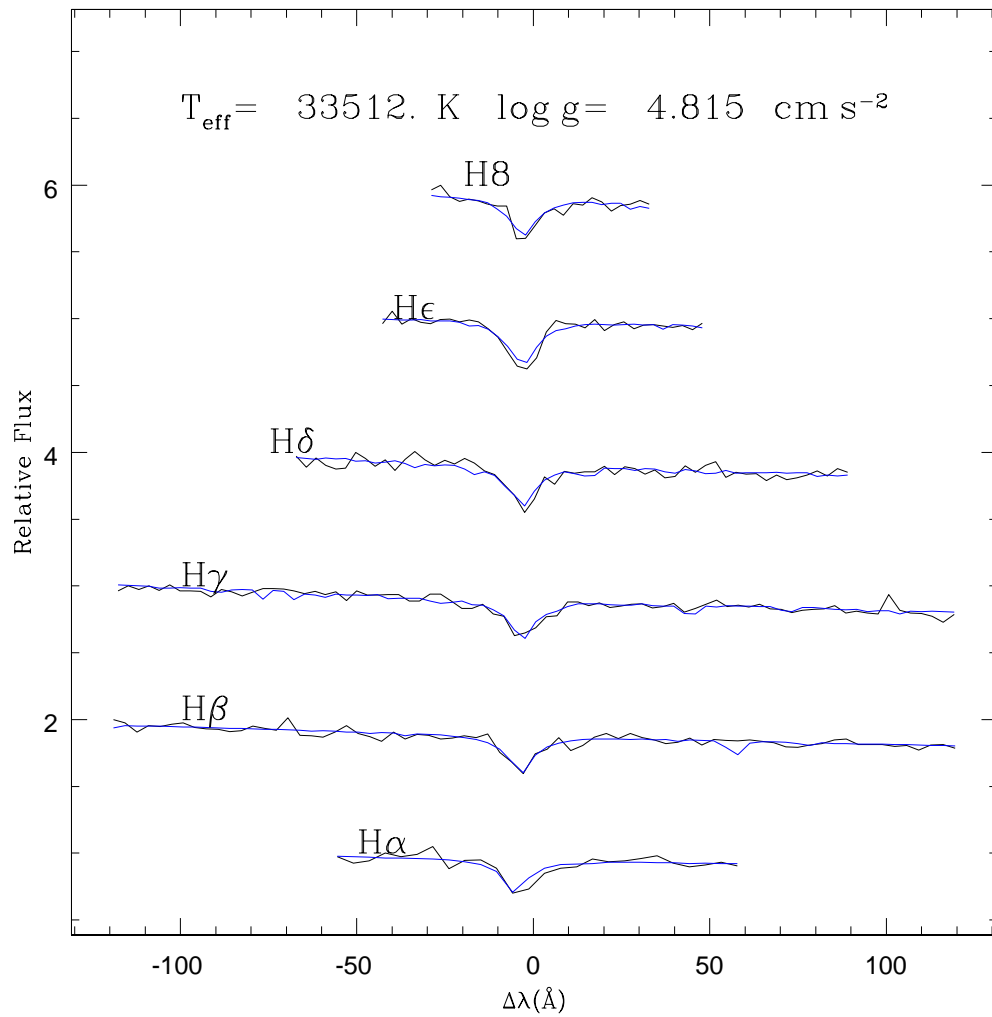Figure C.12: The best Balmer Line fit of spSpec-51914-0488.909.
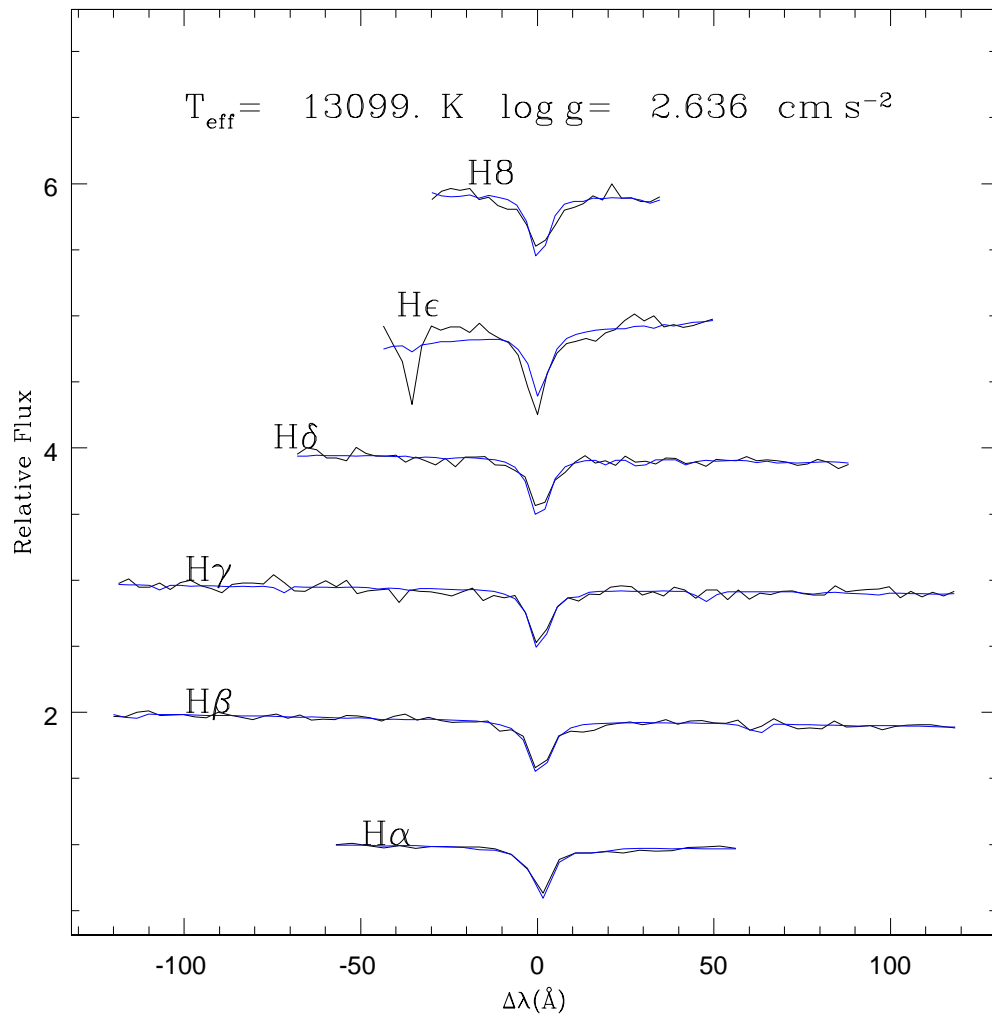
Figure C.13: The best Balmer Line fit of spSpec-53794-2217-261.
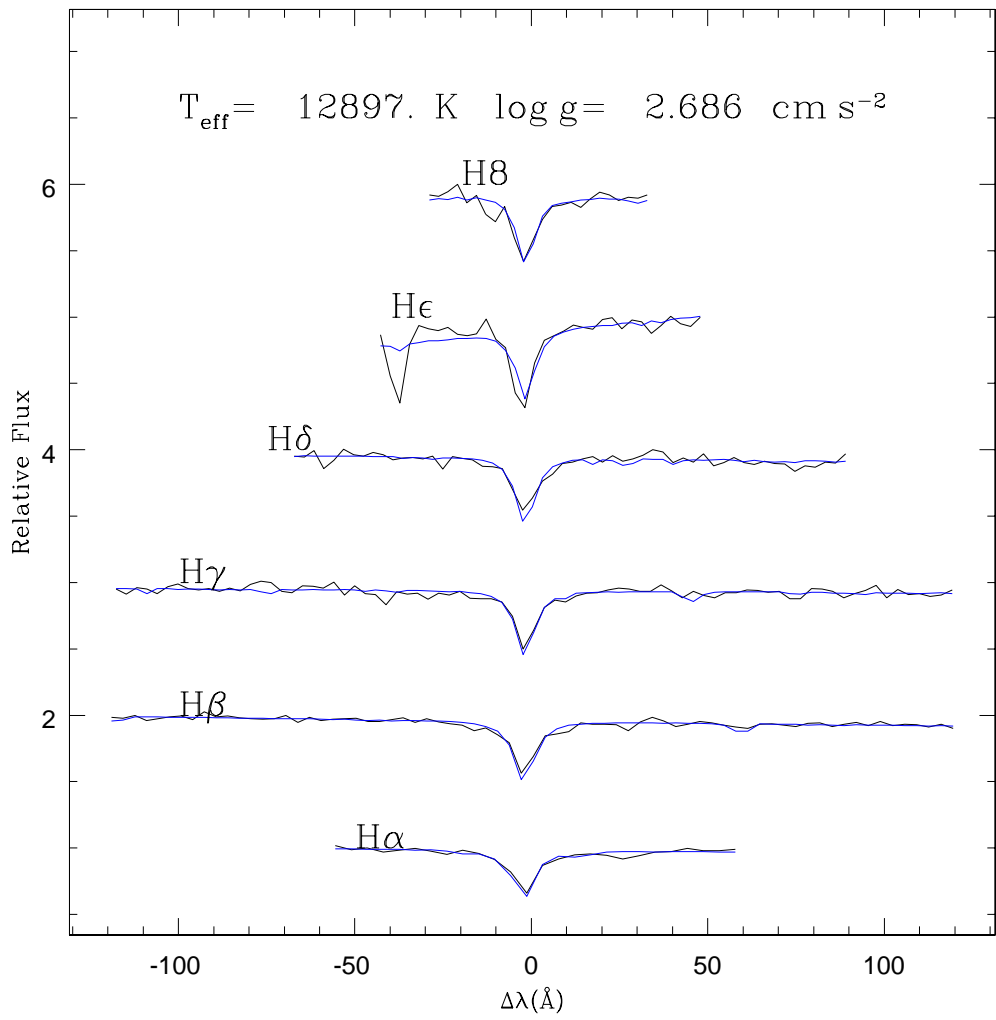
Figure C.14: The best Balmer Line fit of spSpec-53472-1694-285.
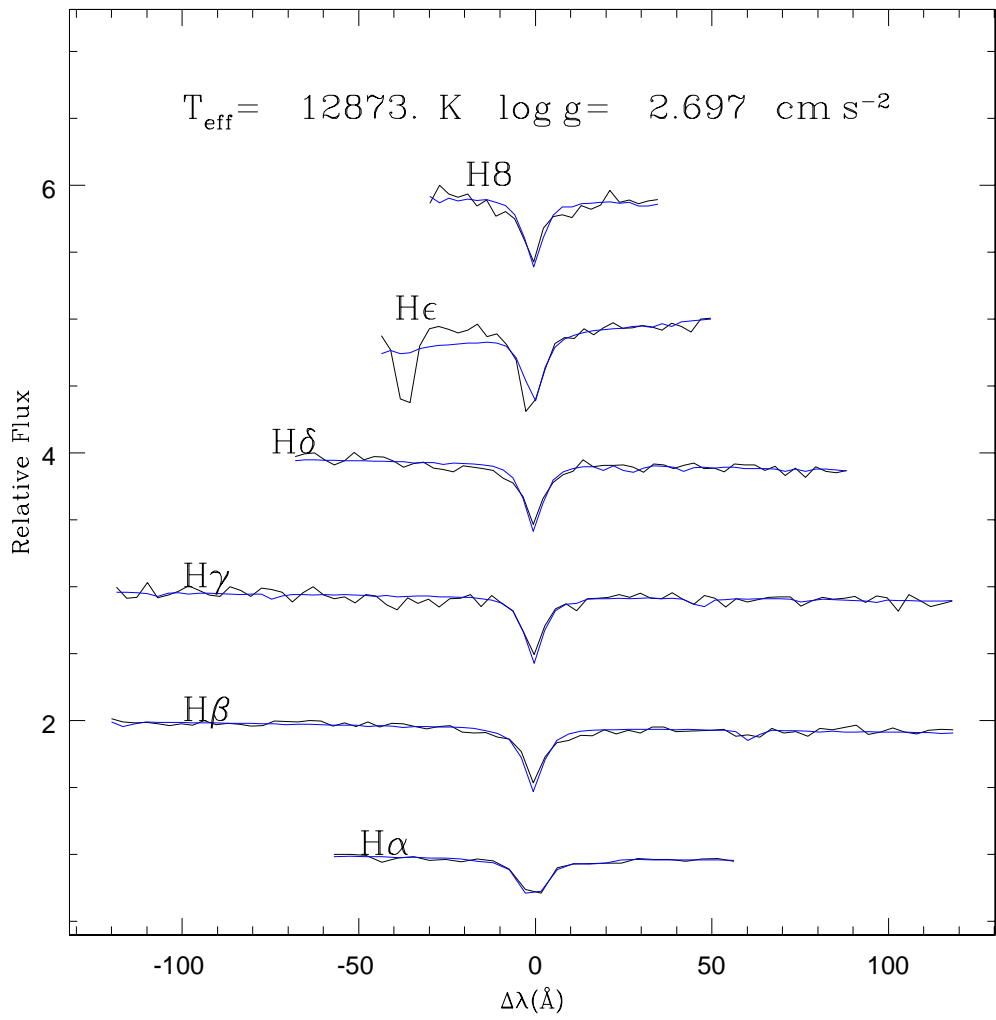
Figure C.15: The best Balmer Line fit of spSpec-52825-1178-435.
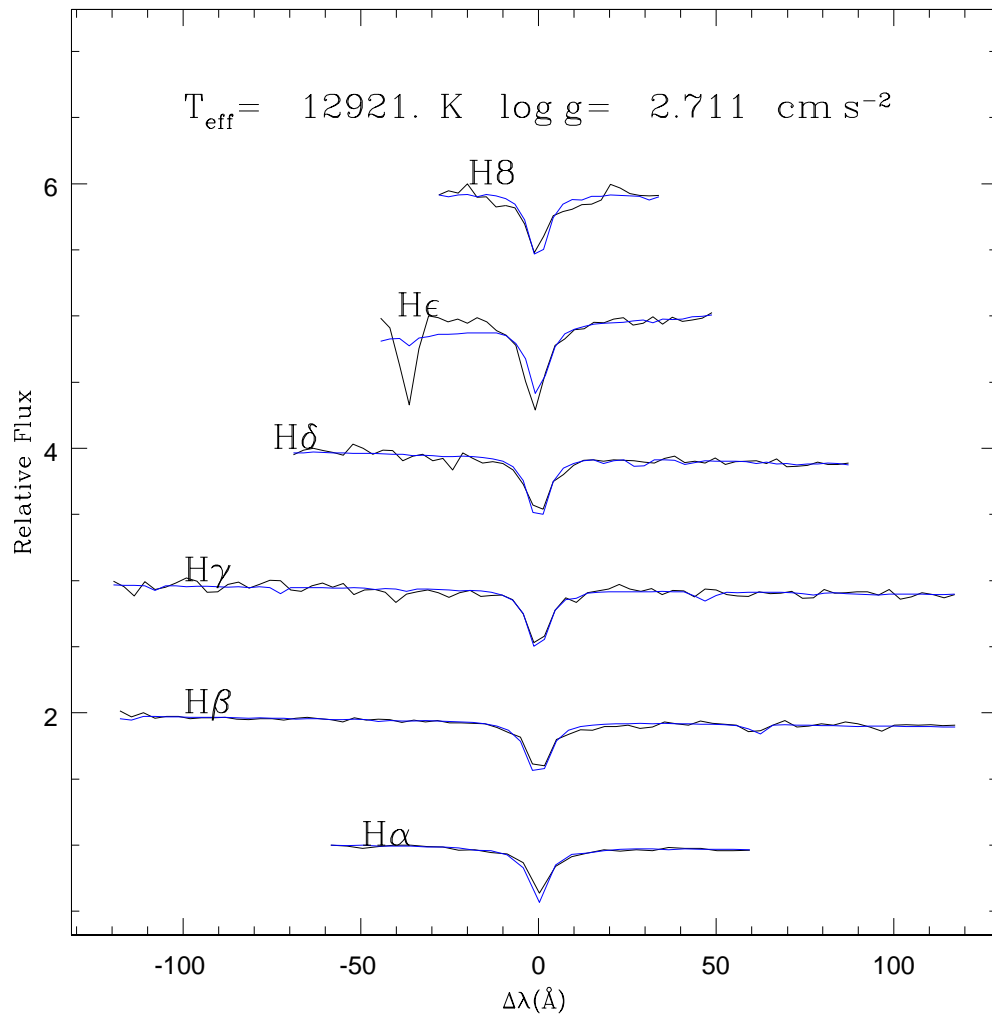
Figure C.16: The best Balmer Line fit of spSpec-52294-0831-050.
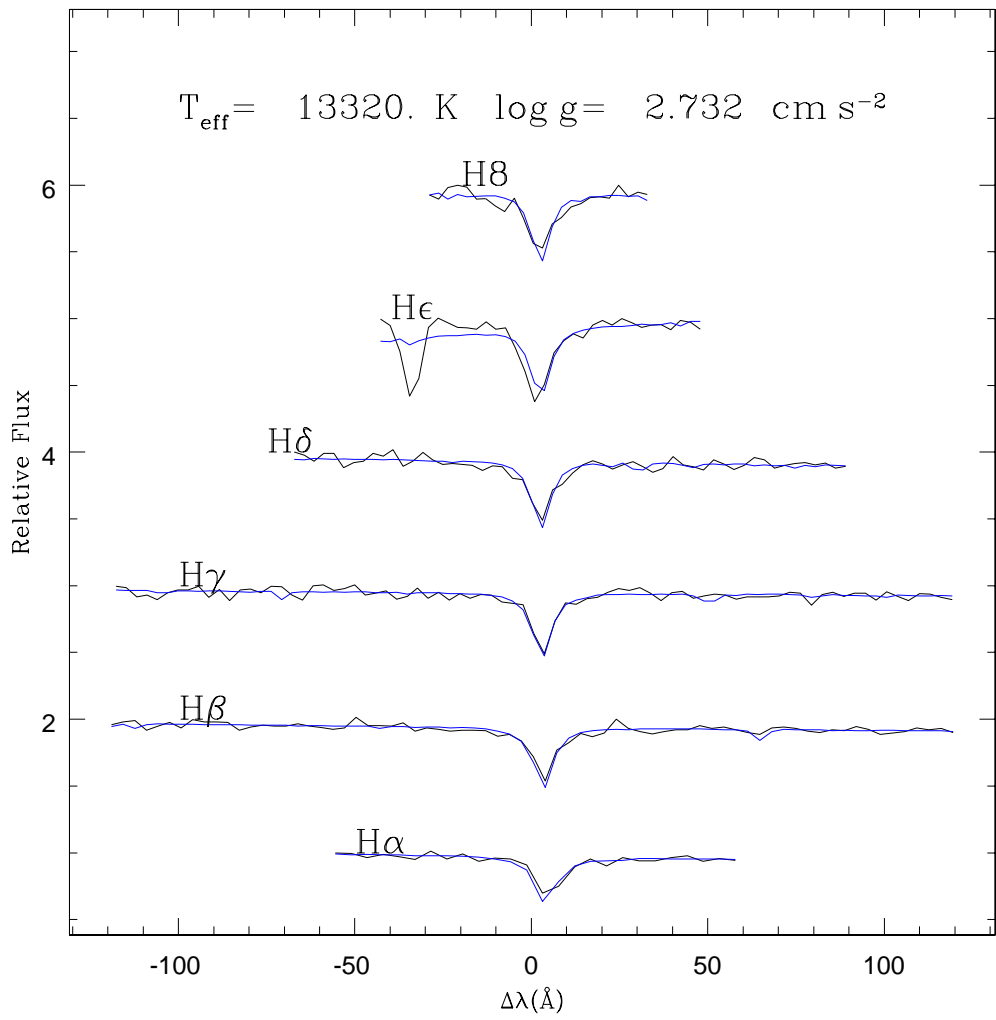
Figure C.17: The best Balmer Line fit of spSpec-53815-2430-462.
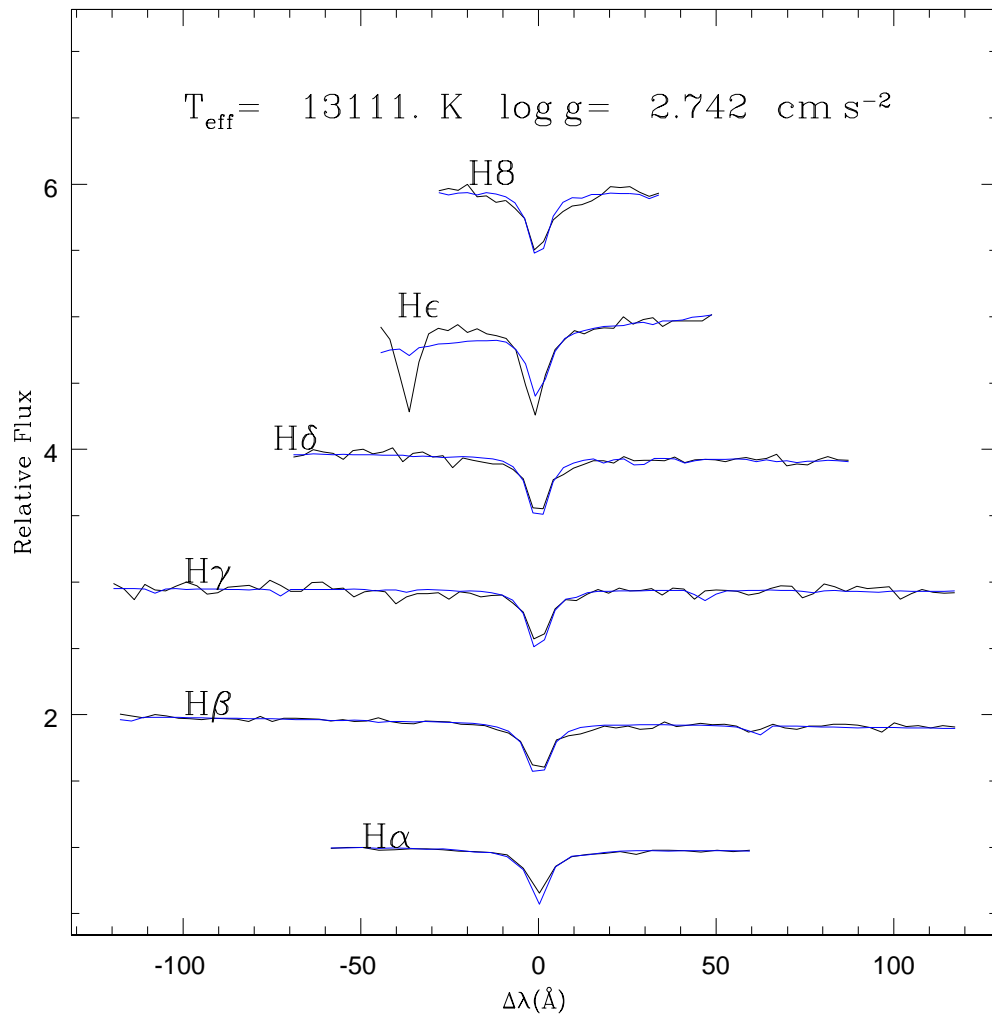
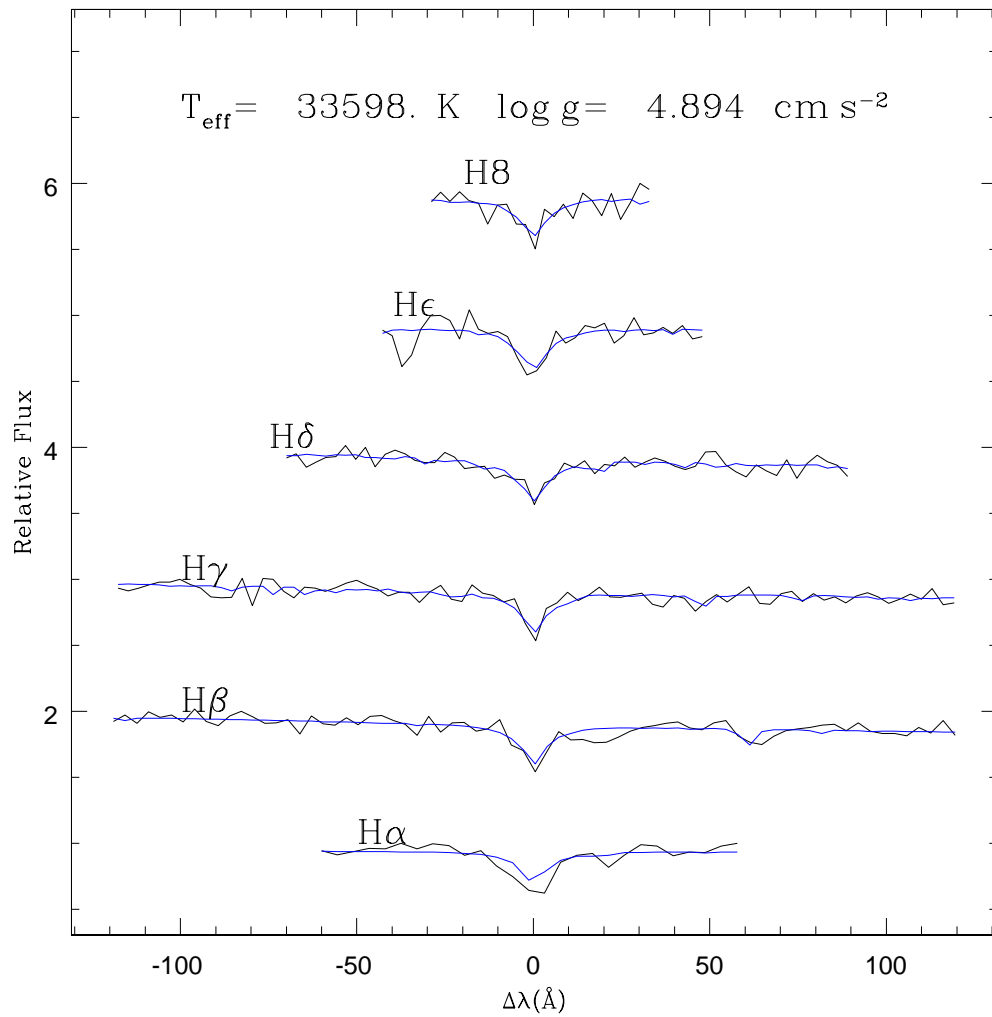Figure C.18: The best Balmer Line fit of spSpec-53737-2004-088.
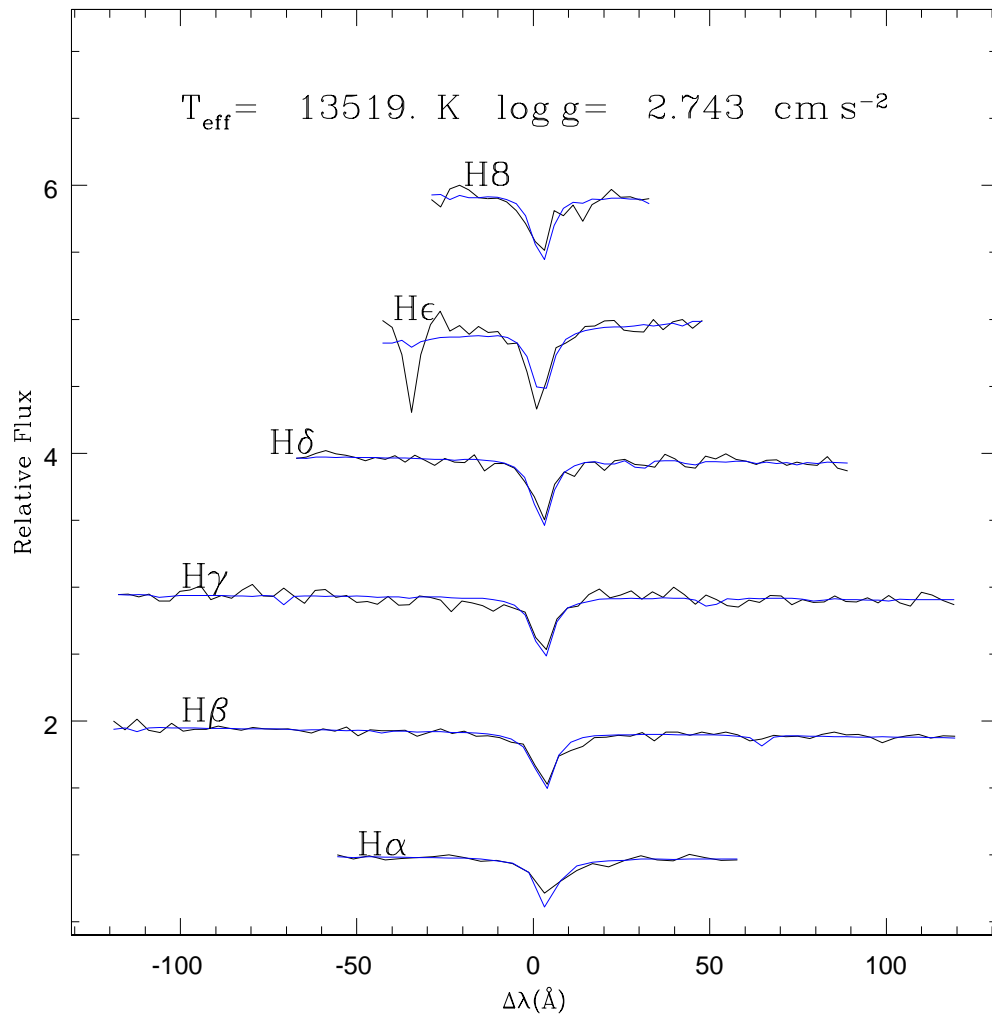
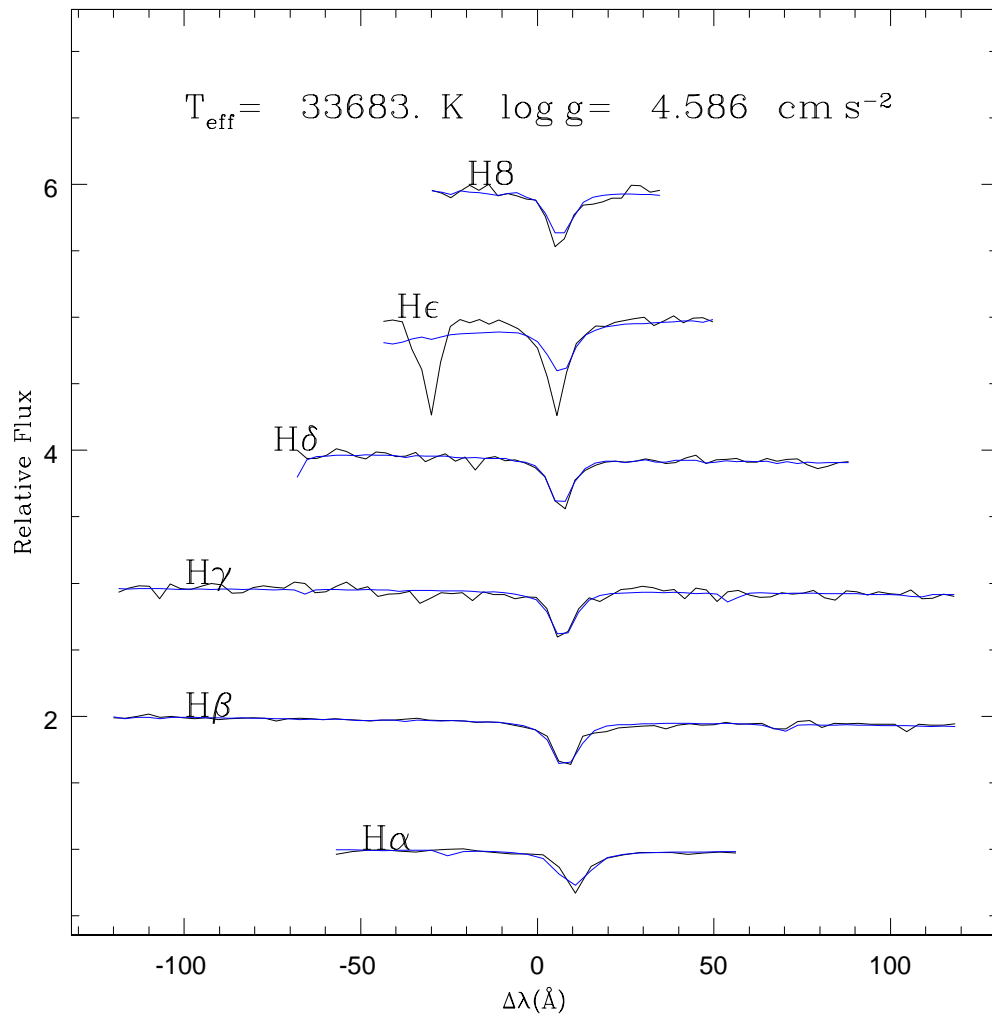Figure C.19: The best Balmer Line fit of spSpec-54583-2861-521.
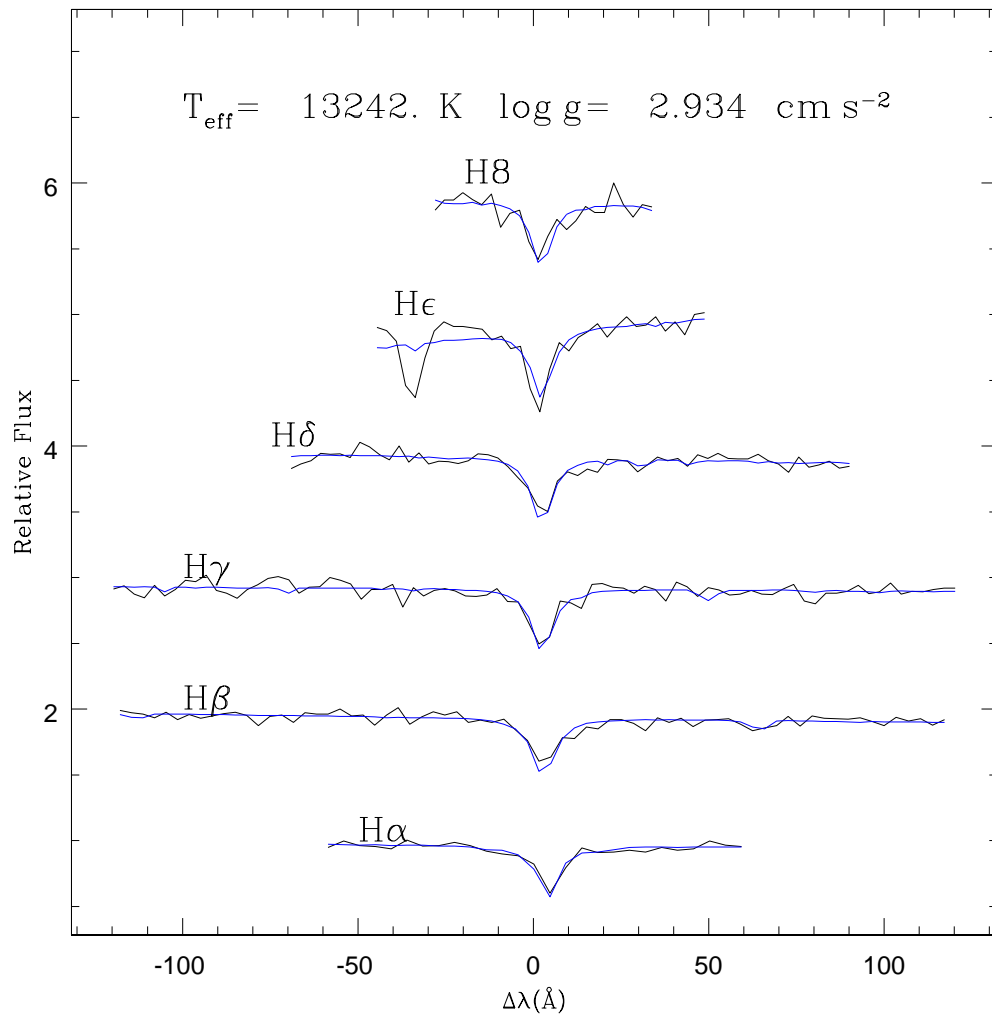
Figure C.20: The best Balmer Line fit of spSpec-54207-2596-342.
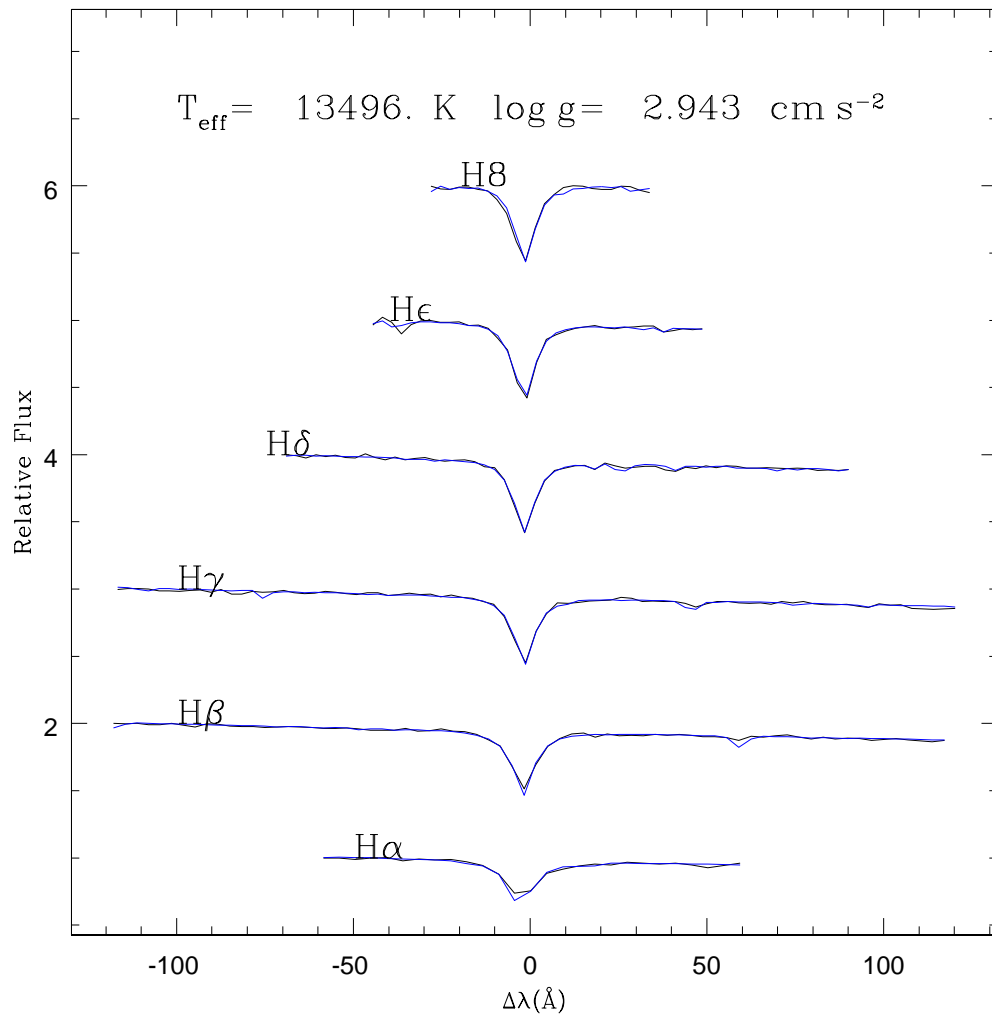
Figure C.21: The best Balmer Line fit of spSpec-53321-1910-636.
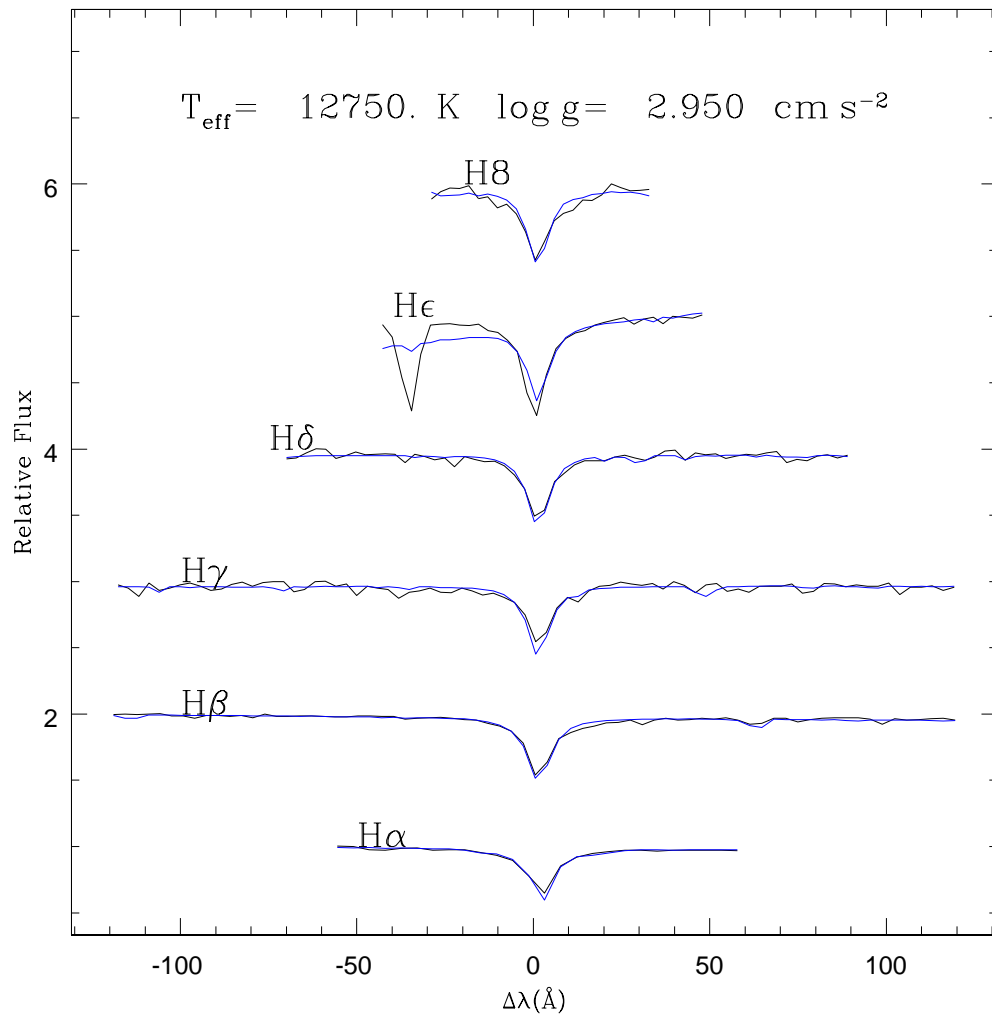
Figure C.22: The best Balmer Line fit of spSpec-54612-2175-356.
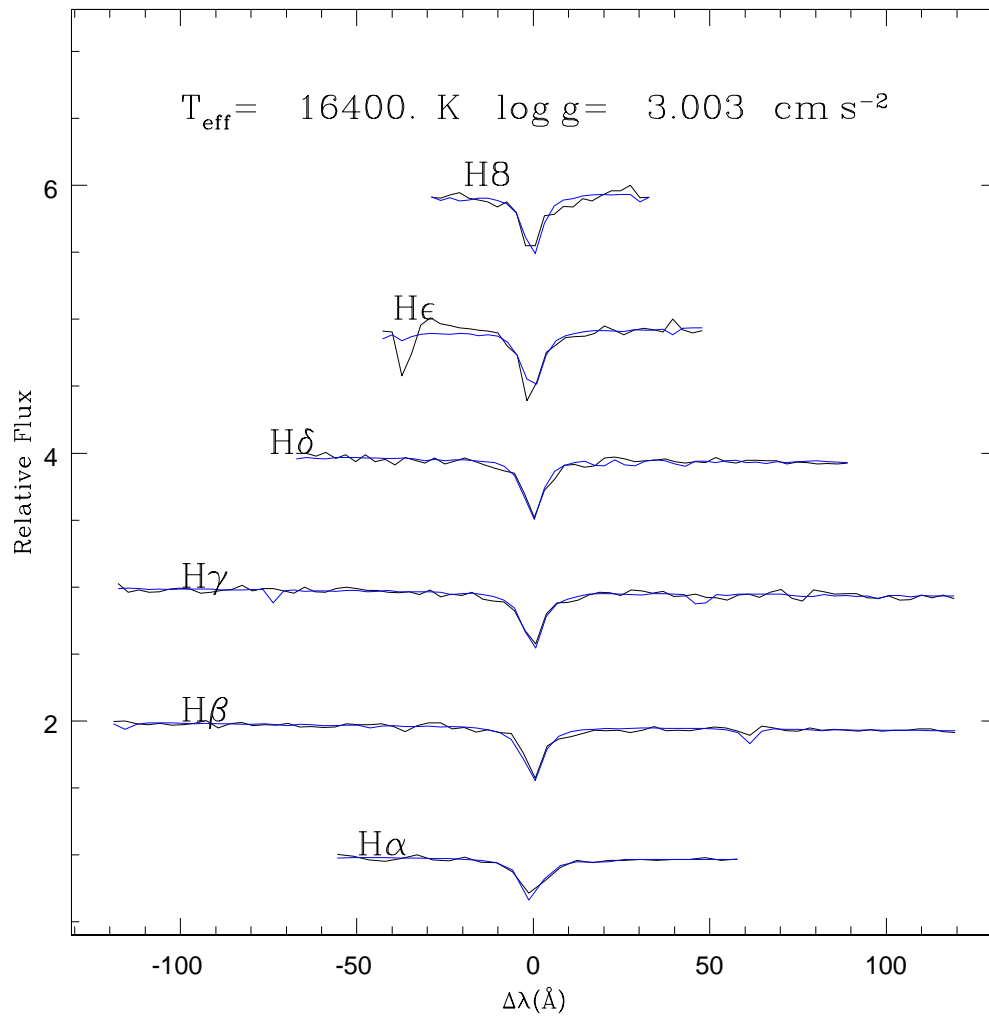
Figure C.23: The best Balmer Line fit of spSpec-52381-0510-381.
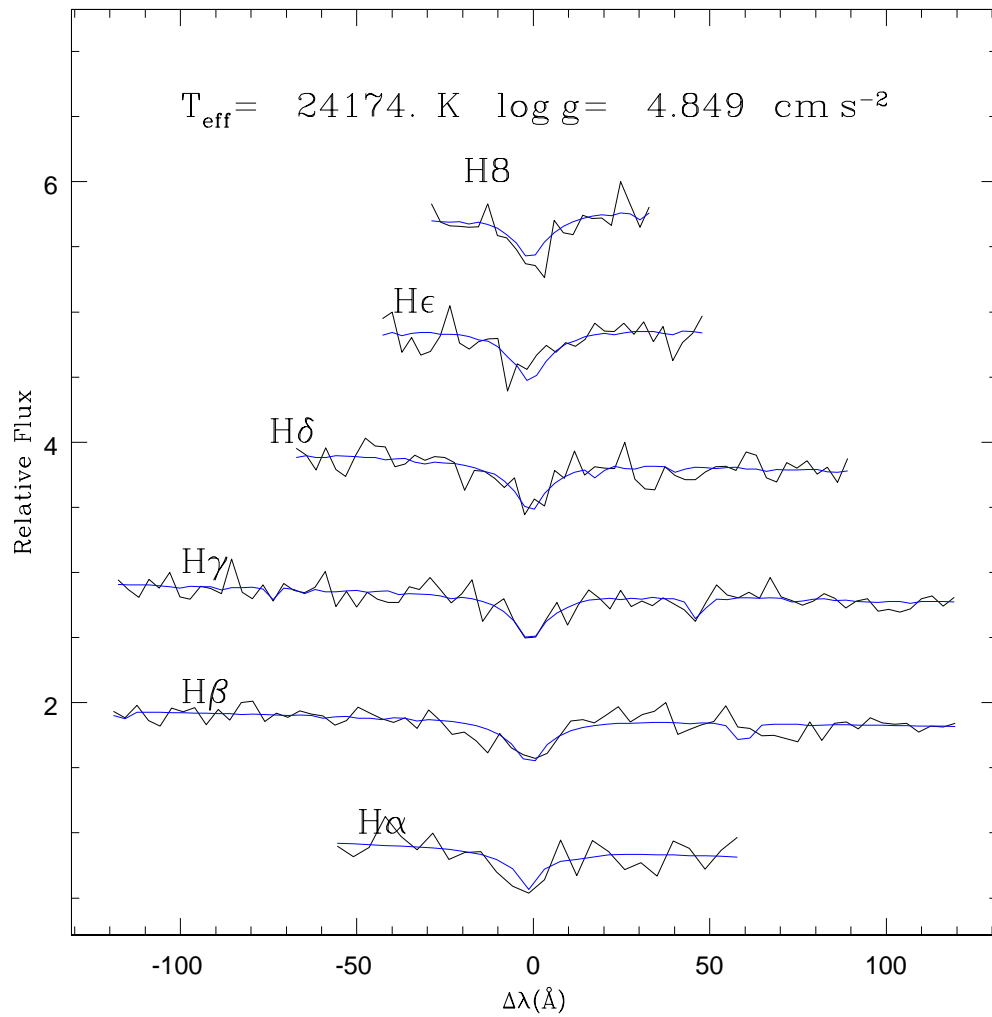
Figure C.24: The best Balmer Line fit of spSpec-53534-1852-016.
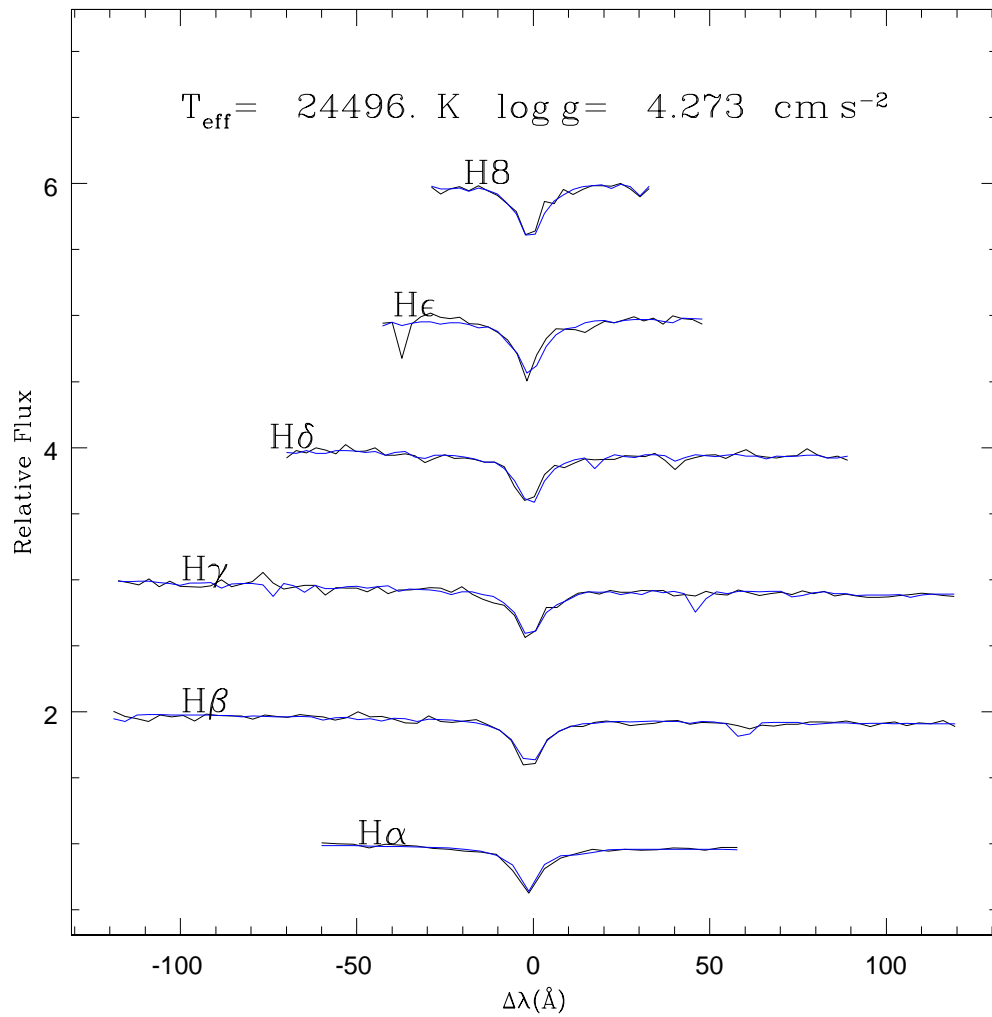
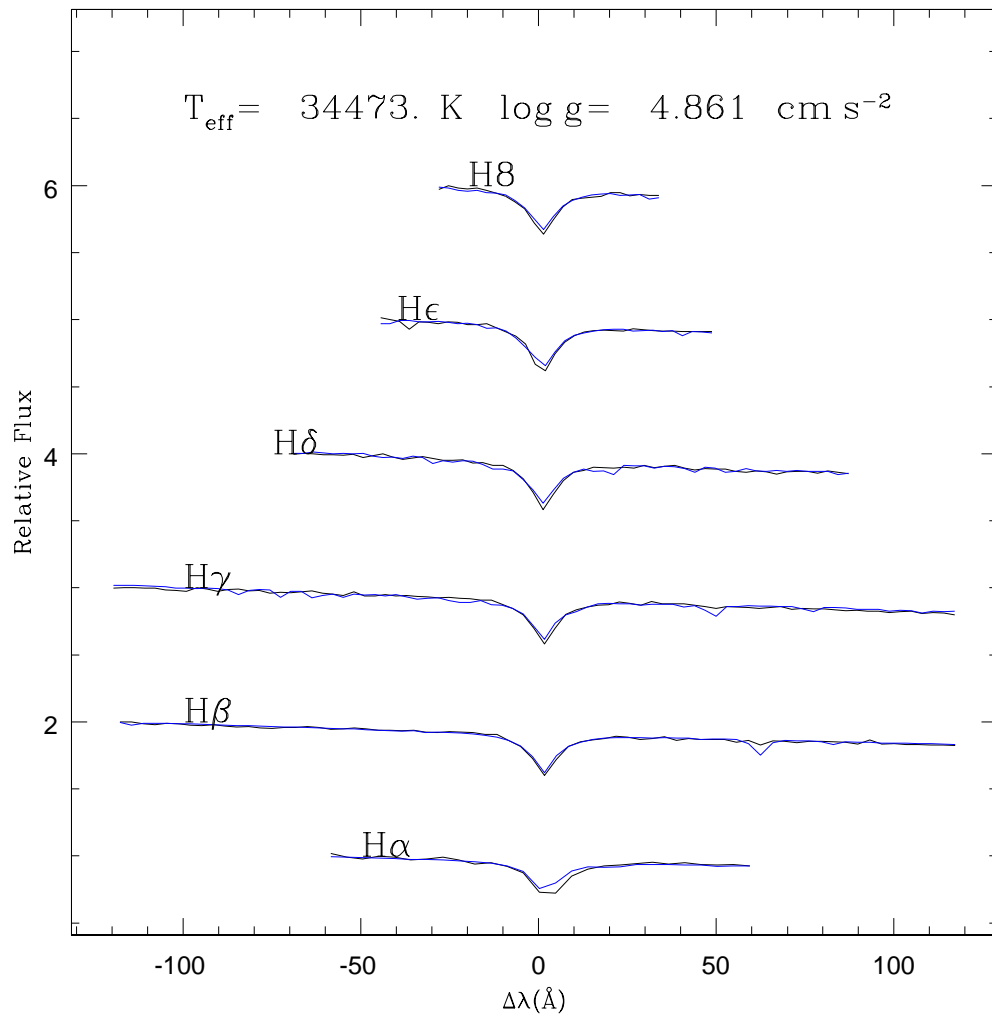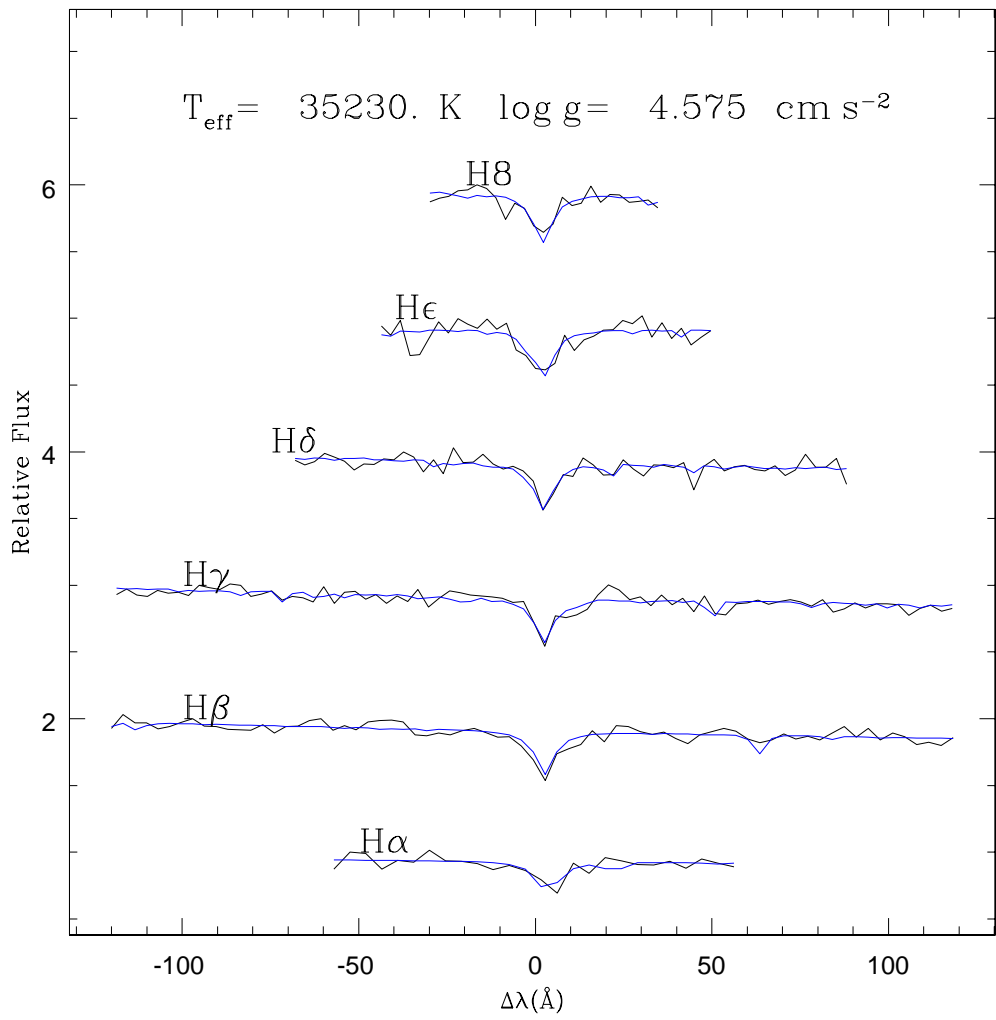Figure C.25: The best Balmer Line fit of spSpec-54554-2776-176.
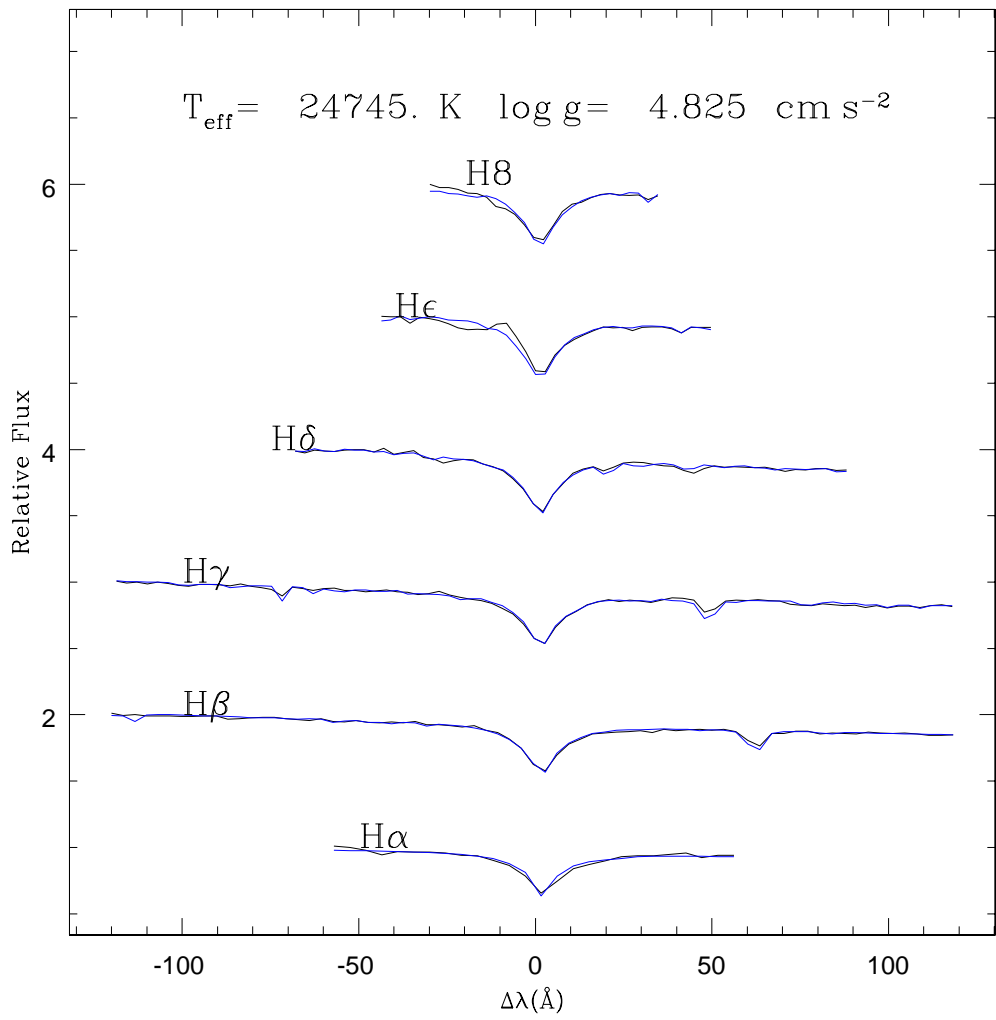
Figure C.26: The best Balmer Line fit of spSpec-53318-1868-029.
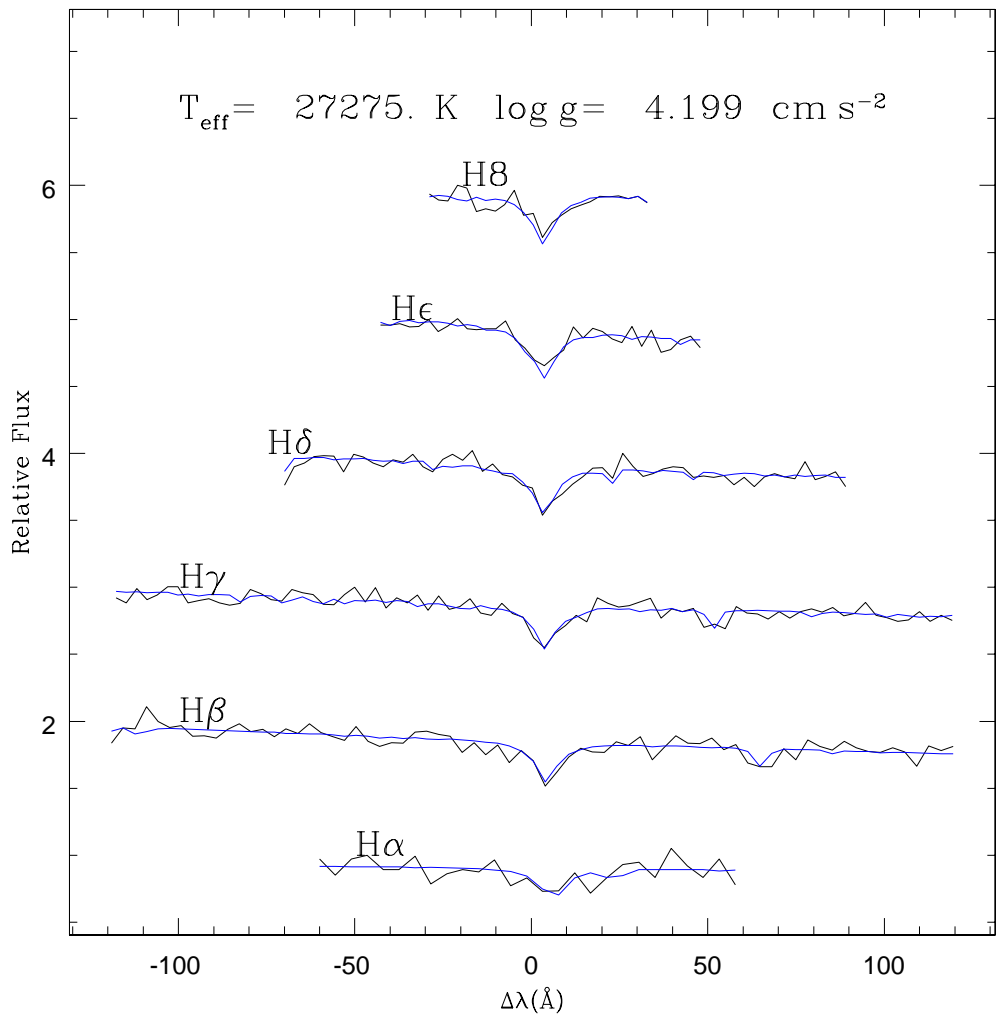
Figure C.27: The best Balmer Line fit of spSpec-52295-0525-423.
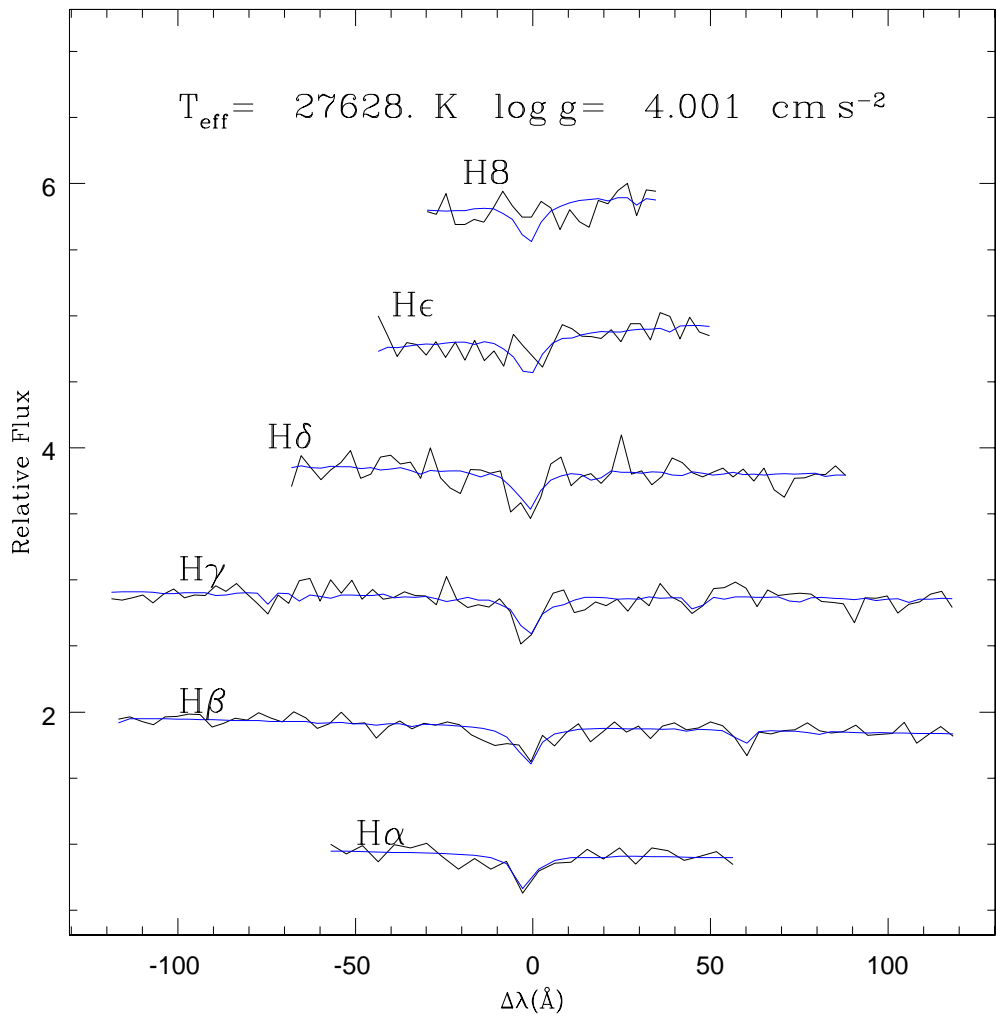
Figure C.28: The best Balmer Line fit of spSpec-53471-2002-285.
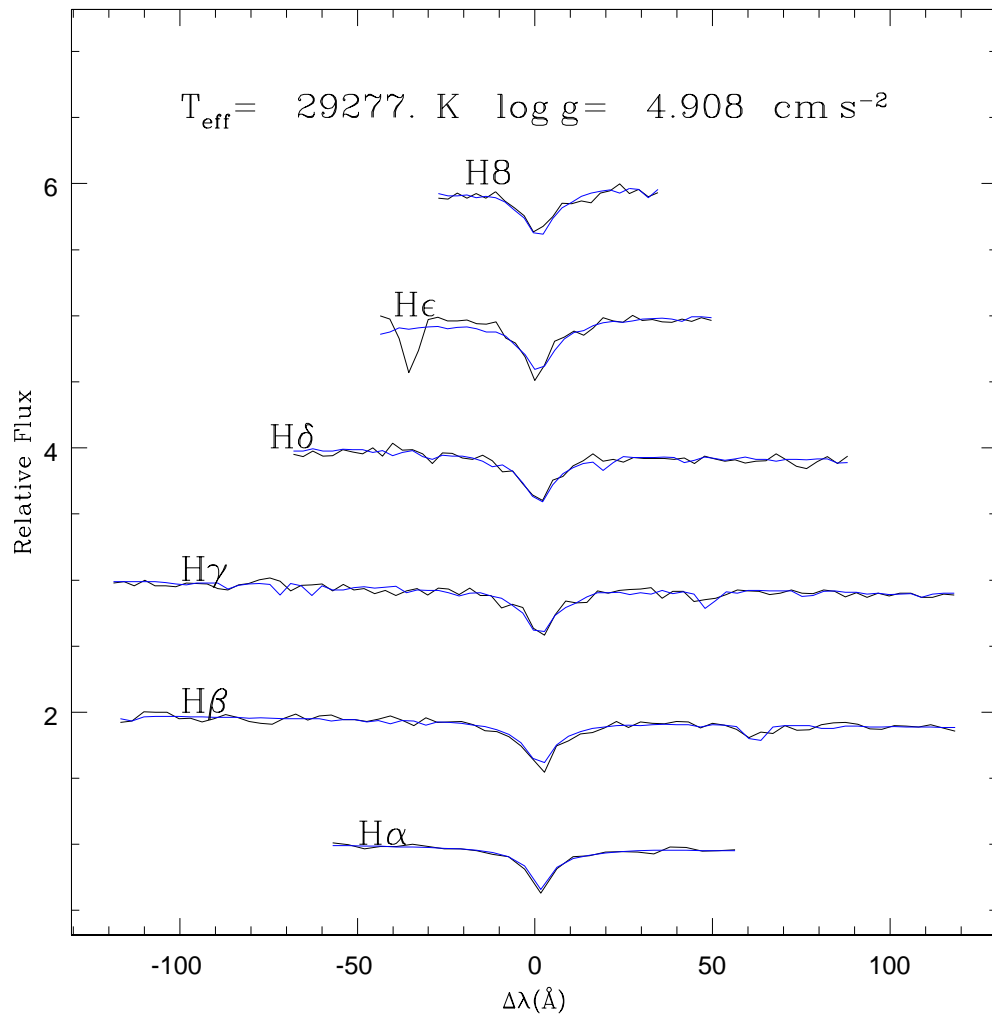
Figure C.29: The best Balmer Line fit of spSpec-52176-0636-605.
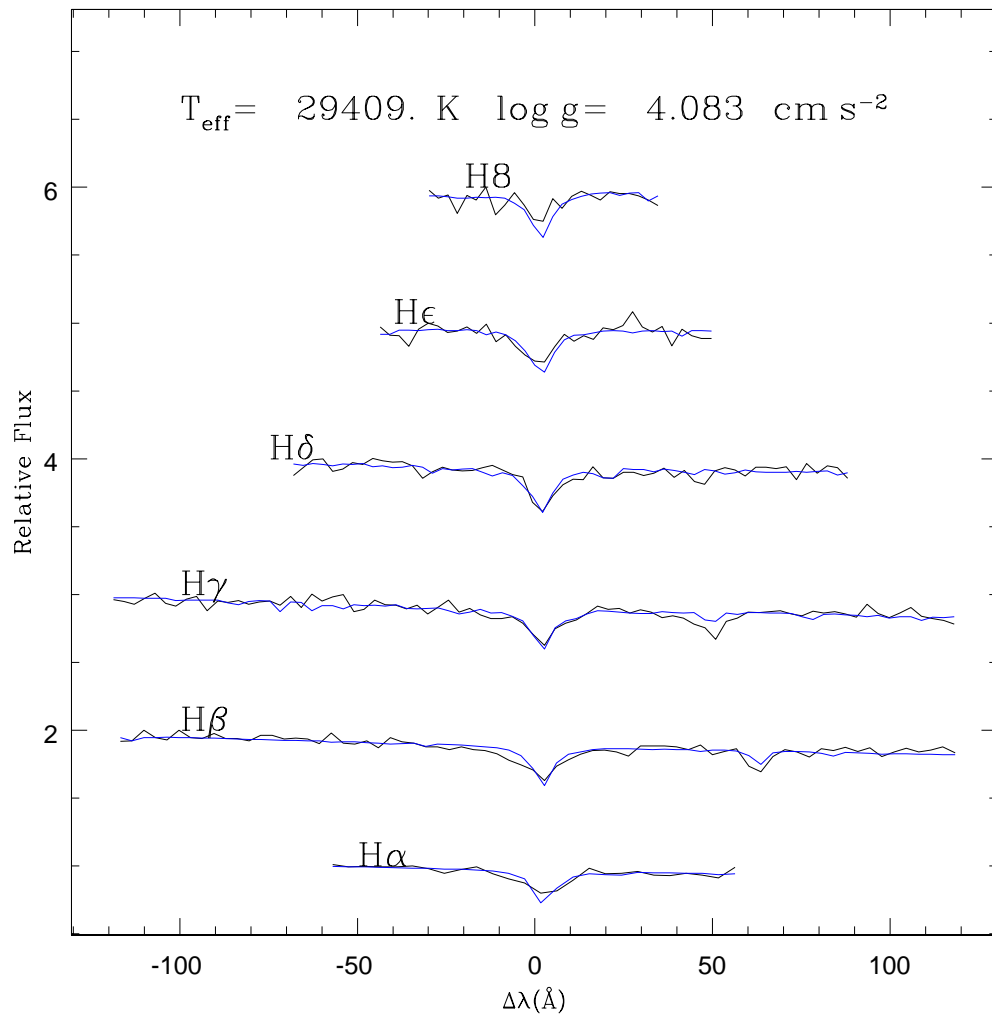
Figure C.30: The best Balmer Line fit of spSpec-54624-2189-620.
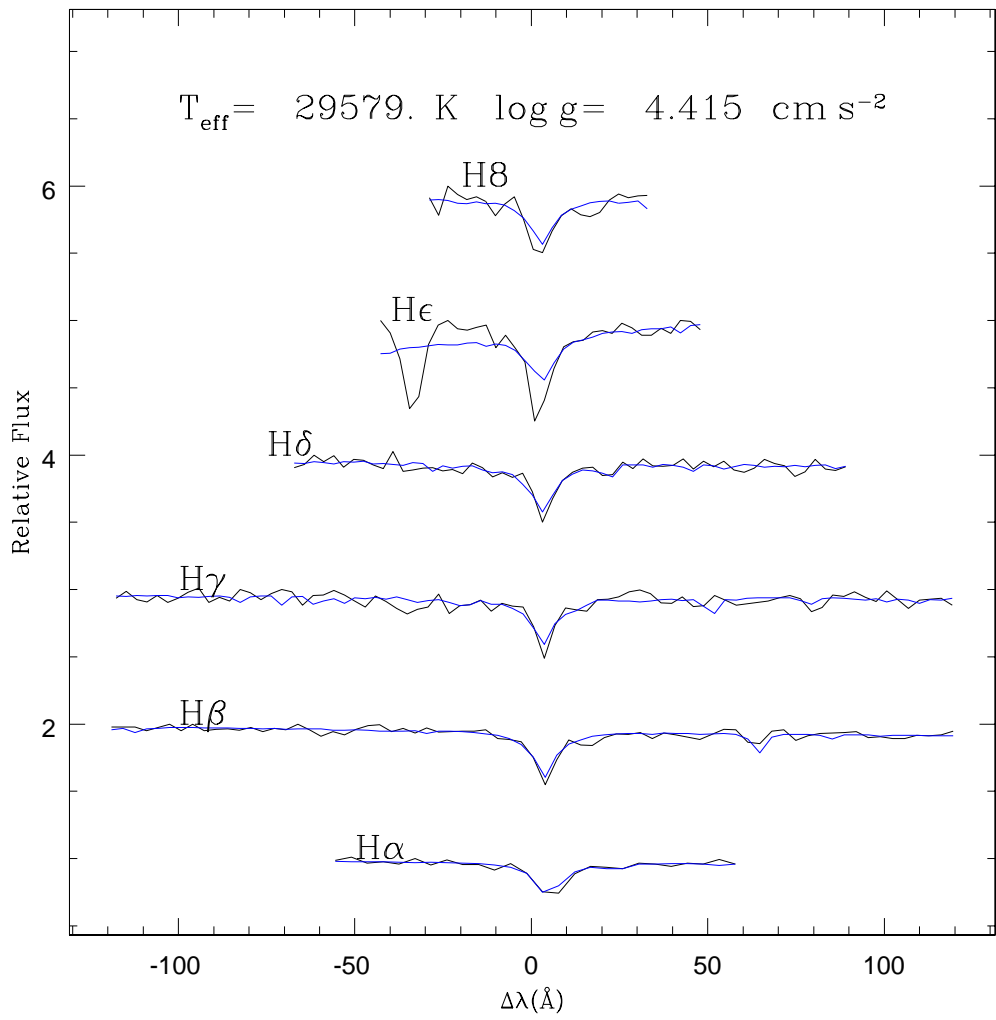
Figure C.31: The best Balmer Line fit of spSpec-53498-1771-097.
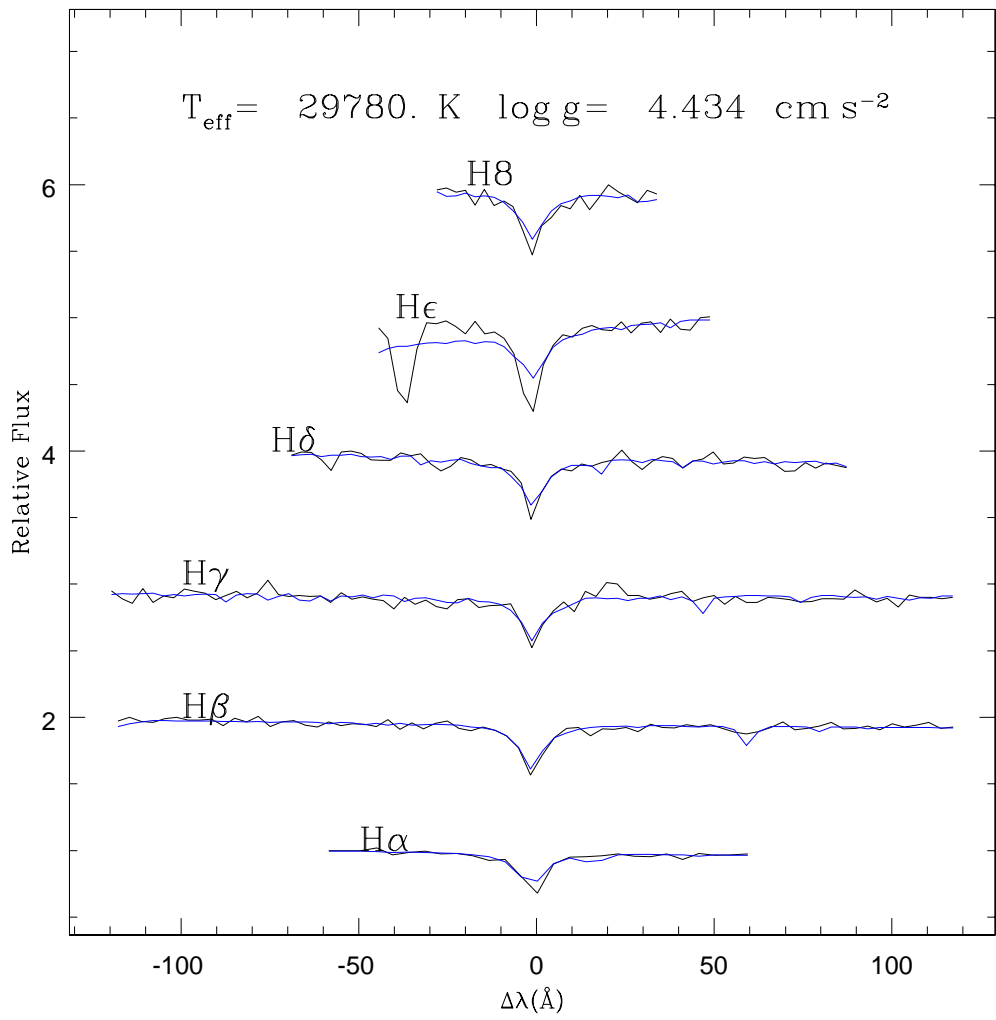
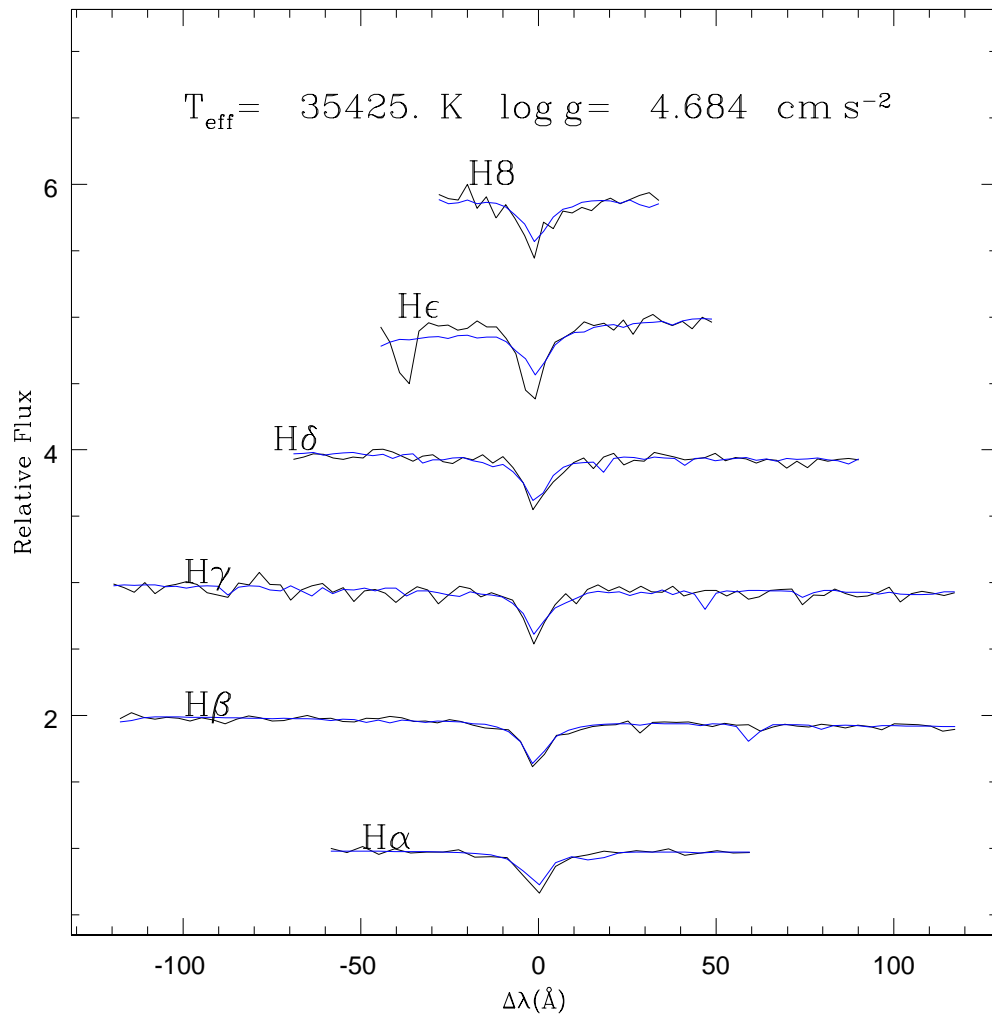Figure C.32: The best Balmer Line fit of spSpec-53799-2222-536.

Figure C.33: The best Balmer Line fit of spSpec-53172-1399-446.

Figure C.34: The best Balmer Line fit of spSpec-54180-2121-499.

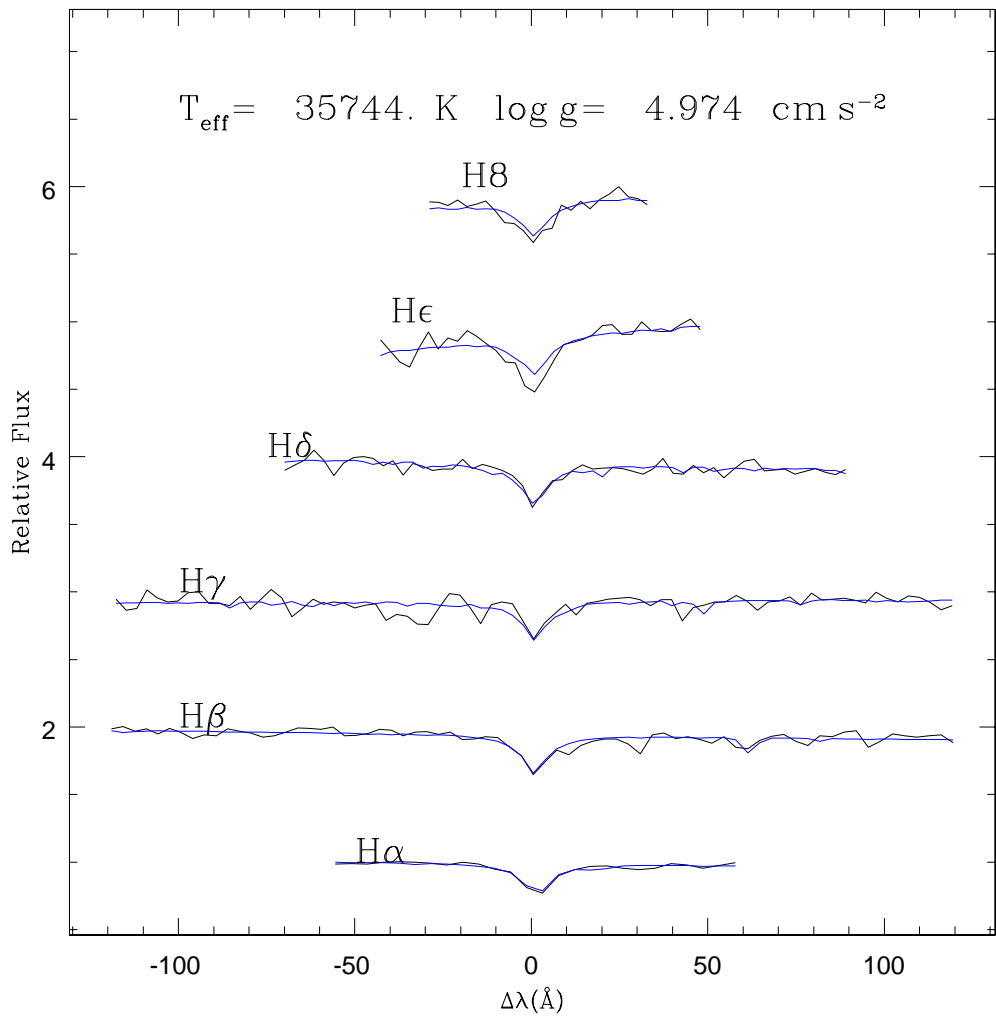Figure C.35: The best Balmer Line fit of spSpec-52674-1209-165.

Figure C.36: The best Balmer Line fit of spSpec-53464-1674-010.

Figure C.37: The best Balmer Line fit of spSpec-52370-0330-020.

Figure C.38: The best Balmer Line fit of spSpec-53917-2547-172.

Figure C.39: The best Balmer Line fit of spSpec-54589-2532-451.

Figure C.40: The best Balmer Line fit of spSpec-54140-2558-445.

Figure C.41: The best Balmer Line fit of spSpec-53786-2211-610.

Figure C.42: The best Balmer Line fit of spSpec-52023-0586-629.

Figure C.43: The best Balmer Line fit of spSpec-52782-1333-409.

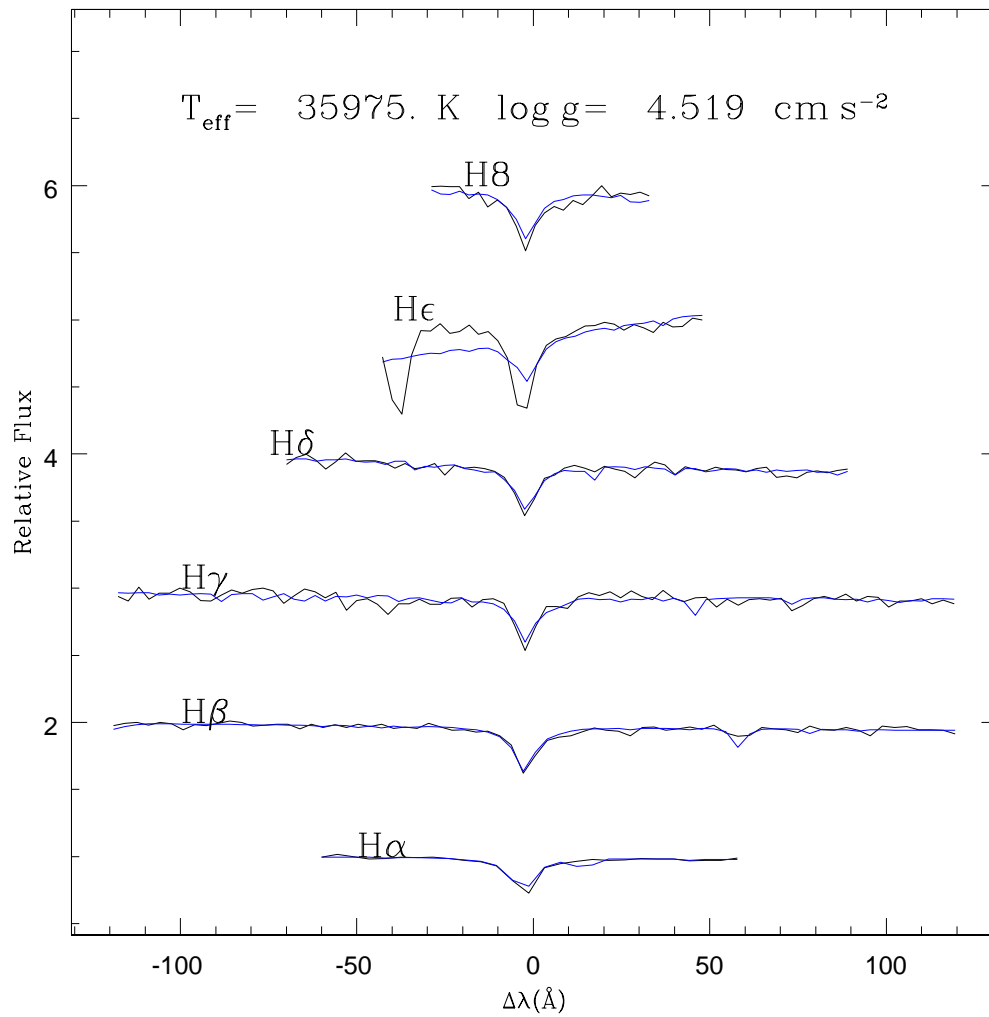Figure C.44: The best Balmer Line fit of spSpec-52316-0598-241.

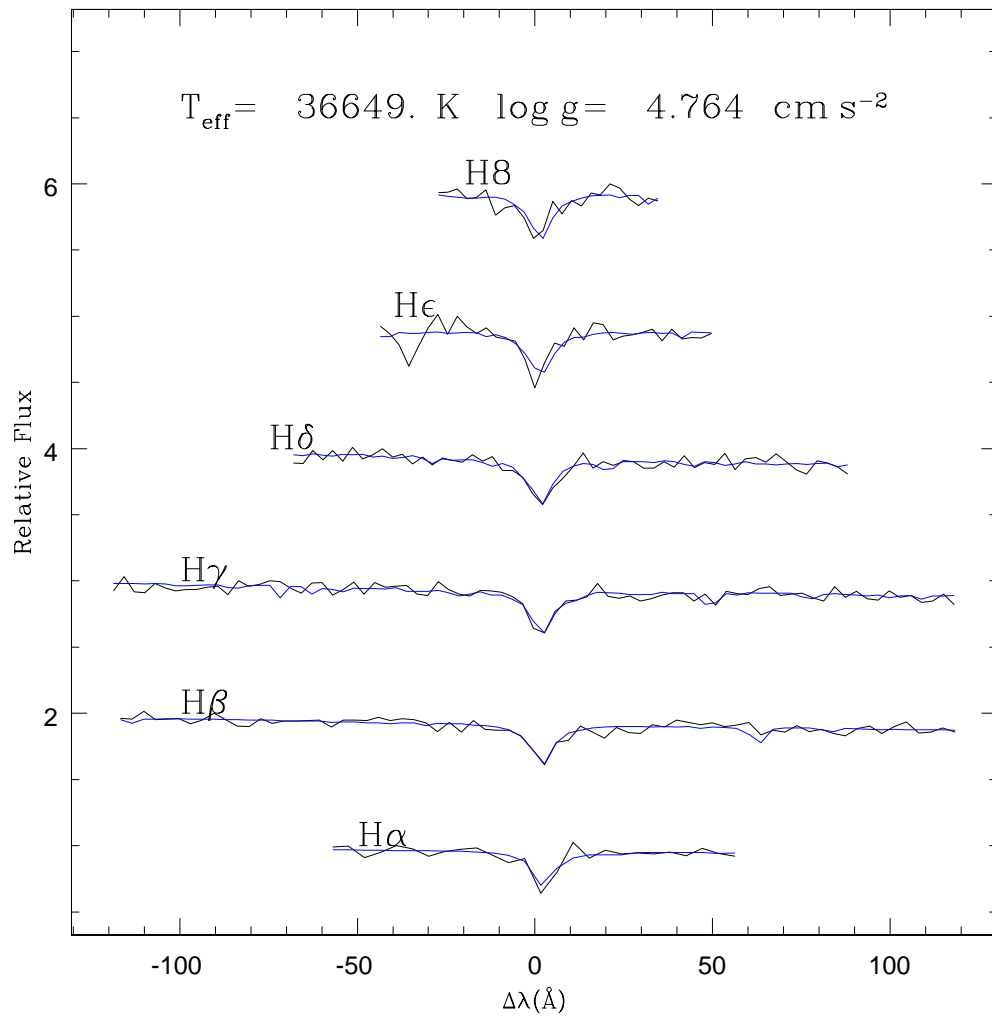Figure C.45: The best Balmer Line fit of spSpec-53033-1310-060.

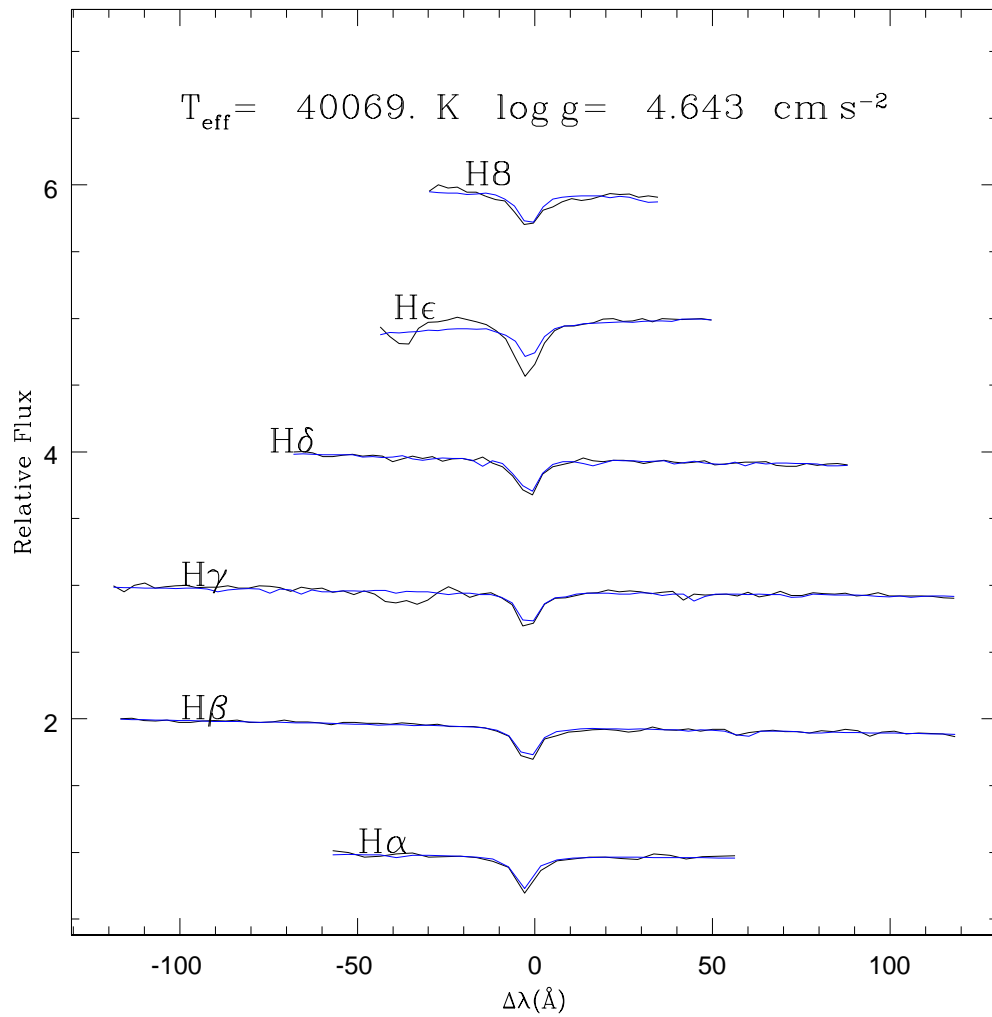Figure C.46: The best Balmer Line fit of spSpec-51690-0341-435.

Figure C.47: The best Balmer Line fit of spSpec-52079-0604-245.